



Friday, David (2023) *A time-integrated analysis of  $Bd \rightarrow \pi^+\pi^-\pi^+\pi^-$  at LHCb and simulations for Low Gain Avalanche Detectors (LGAD)*. PhD thesis.

<http://theses.gla.ac.uk/83485/>

Copyright and moral rights for this work are retained by the author

A copy can be downloaded for personal non-commercial research or study, without prior permission or charge

This work cannot be reproduced or quoted extensively from without first obtaining permission in writing from the author

The content must not be changed in any way or sold commercially in any format or medium without the formal permission of the author

When referring to this work, full bibliographic details including the author, title, awarding institution and date of the thesis must be given

Enlighten: Theses

<https://theses.gla.ac.uk/>  
[research-enlighten@glasgow.ac.uk](mailto:research-enlighten@glasgow.ac.uk)

A time-integrated analysis of  
 $B_d \rightarrow \pi^+ \pi^- \pi^+ \pi^-$  at LHCb and  
simulations for Low Gain Avalanche  
Detectors (LGAD)

David Friday

*Supervisors*

Dr. Paul SOLER

Dr. Lars EKLUND



University of Glasgow | School of Physics  
& Astronomy

University of Glasgow

Department of Physics and Astronomy

*Submitted in fulfilment of the requirements  
for the degree of Doctor of Philosophy*

© David Friday, 2022

# Abstract

This thesis presents the time-integrated amplitude analysis of  $B_d \rightarrow \pi^+\pi^-\pi^+\pi^-$  at the LHCb experiment during Run 2 data taking. It presents data selection of  $B_d$  mesons, with a yield of  $126725 \pm 504$ , and shows the amplitude model and full fits to the Run 2 (2015-2018) dataset. A longitudinal polarisation fraction of  $f_L = 0.721 \pm 0.01 \pm 0.03$  is reported with comparison to previous analyses. The extension of the analysis to a time and flavour-dependent analysis is discussed in the context of extracting a single solution to the unitarity angle  $\alpha$ . Novel simulations of Low Gain Avalanche Detectors (LGAD) for the high luminosity LHC are also presented. Work was completed showing consistent behaviour at the device edge using trench termination, and through new radiation simulations, the gain degradation of LGAD devices was reported. Gain recovery was shown not to be feasible at fluences in excess of  $1 \times 10^{15} \phi_{neq}$ .

# Acknowledgements

This document has been an experience, sometimes good, sometimes bad, but in every way defining. As such (that one's for you Paul), I have a few folk I would like to thank.

Firstly, I would like to thank my family for always having my back throughout this PhD. A special mention to my Gran, who told me explicitly to finish this document before she was 95, and to my Father and Amanda who, at the time of writing, have just got engaged, congratulations!

I would like to thank my supervisors Paul Soler and Lars Eklund for all their efforts over these four years. I hope in some small way I have done your supervision justice. Special thanks must be awarded to Jeremy Dalseno for being an irreplaceable guide through the murky depths of Amplitude Analysis, a subject where he is undoubtedly, the GOAT of  $\phi_2$ . I also wish Lucia and Mark many successes in Glasgow with their new students. I hope to meet again soon.

Similarly, thanks to those members of LHCb who have been around to keep me sane these 4 years. Andy, cheers for R1 beers and ping pong. Lakshan, cheers for your cooking and conversation and of course thanks to Dana, cheers for letting me sleep during CERN seminars on healthy work patterns.

Thanks to all my current and past colleagues here at Glasgow; Charlie, Murdo, Lauren, Michael, Manuel, John, Dima, Dwayne, Jonathan, Giuseppe and Evan who have tolerated me with grace and patience. I wish John luck at the University of Tohoku—a well deserved opportunity! Good luck to the writers club Adam, Bruno, Laurynas! I hope your submissions go well and that we all stay in touch long after this.

Thank you to Gordon, Sam and Jonathan for all your IT support throughout my PhD. You have put up with all the different ways I have stalled out—and possibly set fire to—the batch system. Your expertise on all things computing has been frankly invaluable.

Thanks to those in the Kelvin building who have made this place enjoyable these last

8 years, looking at you Frank, Claire and Tom. I hope to be back soon for more coffee, beers and complaining. Many thanks to Mike for late night gaming and life confirming chats. To the Santiago boys (Asier, Pablo, Ramon), I cannot thank you for the hangovers, but at least I can thank you for making me feel at home. Last but not least, Martha, never underestimate your contribution to this document, and to my life in general.

# Dedication

I dedicate this Thesis to the memory of my mum,  
Joanna Hazel Friday.

Always kind.

Always proud.

Forever loved.

# Declaration

The research results presented in this thesis are the product of my own work. Appropriate references are provided when results of third parties are mentioned. The research presented here was not submitted for another degree in any other department or university.

David Anthony Friday

# Preface

Chapter 1 is an introduction to the thesis. Chapter 2 is a review of the Standard Model of particle physics and amplitude analyses. In this chapter, I present my own work on calculating the channel couplings of the  $a_1(1640)^\pm$ , using a framework developed by Jeremy Dalseno (Instituto Galego de Física de Altas Enerxías). Chapter 3 is a review of the LHC and the LHCb experiment. Chapter 4 presents my simulations and work in understanding edge termination structures and radiation effects in Low Gain Avalanche Detectors. The basic simulation model was provided by Neil Moffat (Centro Nacional de Microelectrónica) before being extended by me to include a new radiation model and trench structures. In Chapter 5, I present my work for selecting  $B^0 \rightarrow \pi^+\pi^-\pi^+\pi^-$  candidates for analysis using multivariate techniques and my invariant mass fits. Chapter 6 contains my work on implementing a new Kernel Density Estimation (KDE) technique for calculating the phase space efficiency and my background parameterisation using a reweighting technique. I also present my extensions to the fit framework—developed initially by Jeremy Dalseno—to include the efficiencies, background and the  $a_1(1640)^\pm$  resonance. Chapter 7 presents my fits to data using the aforementioned frameworks, my extraction of all the fit parameters and a new result for the longitudinal polarisation fraction,  $f_L$ , and systematic uncertainty studies for this value.

# Contents

<b>Abstract</b>	<b>i</b>
<b>Acknowledgements</b>	<b>ii</b>
<b>Dedication</b>	<b>iv</b>
<b>Declaration</b>	<b>v</b>
<b>Preface</b>	<b>vi</b>
<b>1 Introduction</b>	<b>1</b>
<b>2 Theory and Motivations</b>	<b>4</b>
2.1 The Standard Model . . . . .	4
2.2 Symmetry . . . . .	7
2.2.1 The Wu Experiment (The Dawn of Parity) . . . . .	8
2.2.2 The Cabibbo-Kobayashi-Maskawa (CKM) Matrix . . . . .	10
2.3 CP violation . . . . .	14
2.4 Isospin Decompositon and Amplitude Analysis . . . . .	15
2.4.1 Isospin Decomposition of Charmless $B$ Decays . . . . .	15
2.4.1.1 Penguins . . . . .	15
2.4.1.2 Isospin . . . . .	18
2.4.1.3 $B^0 \rightarrow \rho\rho$ Isospin Models . . . . .	19
2.5 The Isobar Model . . . . .	24
2.5.1 Blatt-Weisskopf Barrier Factors . . . . .	24
2.5.2 Spin Factors . . . . .	26
2.5.3 Lineshapes . . . . .	31

2.6	Chapter Summary . . . . .	33
<b>3</b>	<b>The LHCb Experiment</b>	<b>36</b>
3.1	The Large Hadron Collider . . . . .	36
3.2	Experiment Overview . . . . .	38
3.3	Detectors . . . . .	42
3.3.1	Vertex Locator . . . . .	42
3.3.1.1	VELO Mapping Using Material Interaction . . . . .	45
3.3.1.2	Vertex Locator at High Luminosity . . . . .	46
3.3.2	Tracking Stations . . . . .	47
3.3.3	Spectrometer Magnet . . . . .	49
3.3.4	Ring Imaging Cherenkov Detectors . . . . .	50
3.3.5	Calorimeter System . . . . .	53
3.3.6	Muon Chambers . . . . .	55
3.4	Triggering at LHCb . . . . .	56
3.5	Offline Processing . . . . .	59
3.6	Simulation . . . . .	59
3.7	Chapter Summary . . . . .	61
<b>4</b>	<b>LGAD Simulation</b>	<b>62</b>
4.1	Motivation . . . . .	63
4.2	Silicon Detectors . . . . .	63
4.2.1	The p-n Junction . . . . .	64
4.2.1.1	Thermal Equilibrium . . . . .	65
4.2.1.2	Reverse Bias . . . . .	65
4.2.2	Carrier Transport and Multiplication . . . . .	66
4.2.2.1	Drift . . . . .	67
4.2.2.2	Diffusion . . . . .	67
4.2.2.3	Impact Ionisation . . . . .	68
4.2.3	Detector Operation . . . . .	68
4.2.4	LGAD . . . . .	69
4.3	Electrostatic Simulation . . . . .	74
4.3.1	Device Design . . . . .	77
4.3.2	Breakdown Scans . . . . .	78

4.3.3	Electrostatic Summary . . . . .	81
4.4	Radiation Model . . . . .	84
4.4.1	Deep Level Traps and Surface Charge Effects . . . . .	84
4.4.2	Donor Removal and Creation . . . . .	86
4.5	Transient Simulations . . . . .	87
4.5.1	Minimum Ionising Particles (MIPs) . . . . .	88
4.5.2	Gain Measurements . . . . .	89
4.5.3	Fill Factor . . . . .	90
4.5.4	Gain Recovery . . . . .	90
4.5.5	Transient Simulation Summary . . . . .	91
4.6	Chapter Summary . . . . .	92
<b>5</b>	<b>Reconstruction and Selection of <math>B^0</math> Mesons</b>	<b>95</b>
5.1	Reconstruction at LHCb . . . . .	95
5.2	Stripping and Offline Cuts . . . . .	96
5.3	Additional Selection Criteria . . . . .	96
5.4	BDT Training and Optimisation . . . . .	98
5.4.1	Optimisation . . . . .	103
5.5	Invariant Mass Fits . . . . .	103
5.5.1	PDFs (Probability Distribution Functions) . . . . .	104
5.6	Chapter Summary . . . . .	106
<b>6</b>	<b>Background Modelling and Efficiencies</b>	<b>111</b>
6.1	Kernel Density Estimation . . . . .	111
6.2	Training Samples and Method Validation . . . . .	113
6.3	Background Parameterisation . . . . .	122
6.4	Fit Model . . . . .	126
6.5	Chapter Summary . . . . .	128
<b>7</b>	<b>Results and Conclusions</b>	<b>129</b>
7.1	Fit Results . . . . .	129
7.2	Longitudinal Polarisation . . . . .	150
7.3	Conclusions and Outlook . . . . .	153
<b>8</b>	<b>Summary</b>	<b>154</b>

List of Tables	156
List of Figures	158

# Chapter 1

## Introduction

You don't have to test everything to destruction just to see if you made it right.

---

Neil Gaiman & Terry Pratchett

The LHCb experiment is one of the four major experiments that form part of the Large Hadron Collider at the European Laboratory for Particle Physics (CERN) that has been collecting data across two periods since 2009. The LHCb experiment was designed to make the most precise measurements of **CP** violation and exploration of heavy flavour phenomena. The work presented in this thesis covers two central topics. An exploration of the charmless time-independent amplitude structure of  $B^0 \rightarrow \pi^+\pi^-\pi^+\pi^-$ , the outputs of which will contribute to a single measurement of the unitarity angle  $\alpha$  through the measurement of the Longitudinal Polarisation Fraction of the  $\rho(770)^0\rho(770)^0$  decay channel; and simulation work for Low Gain Avalanche Detectors (LGAD), exploring device termination and radiation effects, that will direct the technologies development towards installation at the LHCb experiment for operation at the High Luminosity LHC from 2030 onward.

In Chapter 2, I present a theoretical overview of the Standard Model relevant to the LHCb physics program. Particular focus is given to the origin and structure of the Cabibbo-Kobayashi-Maskawa (CKM) matrix, which contains the definition of the unitarity angle  $\alpha$  that motivates this thesis. The chapter also describe the isospin decomposition of  $B \rightarrow hh$  systems, and the relevant extension that allows us to access  $\alpha$  directly. The lat-

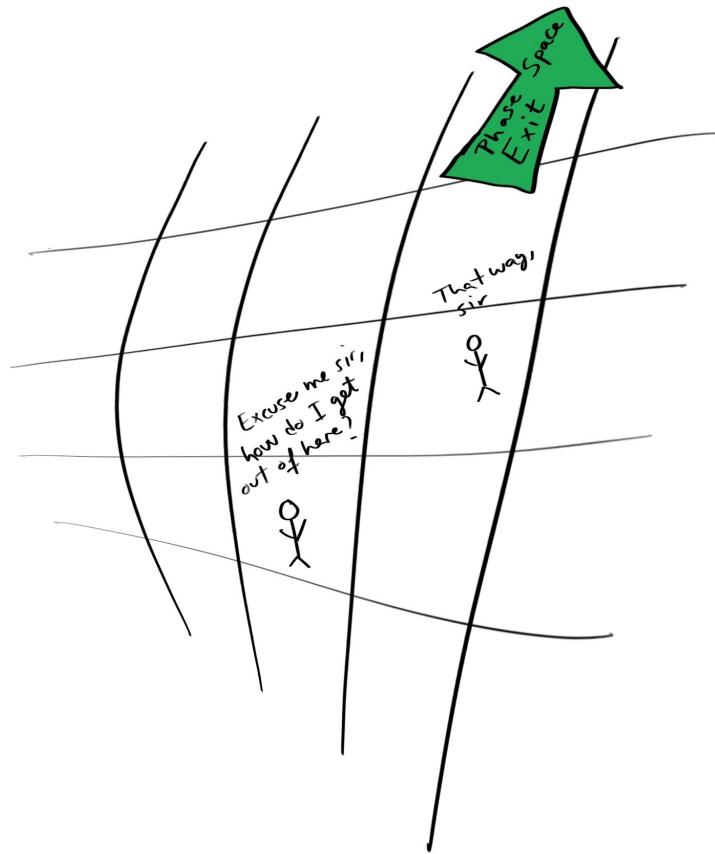


Figure 1.1: Asier Pereiro Castro, *Lost in phase space*.

ter stages of this chapter are concerned with amplitude analyses, and formalise the models used in this thesis, with particular care given to understanding our spin formalisation.

Chapter 3 gives an overview of the LHC before describing the LHCb experiment, with a description of each detector within the experiment. Particular emphasis is placed on describing the Vertex Locator (VELO) detector, an understanding of which motivates the simulation work presented in Chapter 3. This chapter also covers how physics data is extracted and stored by LHCb for use in physics analyses.

In Chapter 4, I present simulation work completed for Low Gain Avalanche Detectors (LGAD) research. The chapter first discusses the fundamentals of silicon detectors in terms of their composition, underlying physics and development. This forms the basis for the rest of the chapter. The simulation work is focused in two main topics, a discussion of pixel edge effects that can change breakdown, and fill factor characteristics, and the implementation of new radiation models to understand the operational limits under the

conditions of High Luminosity LHC.

Chapter 5 details a full description of data selection for the  $B^0 \rightarrow \pi^+\pi^-\pi^+\pi^-$  analysis. The selection is discussed in terms of physics cuts and multivariate selection, with particular care taken to discuss variable transforms and optimisation. The chapter then discusses the invariant mass fits that constrain the signal and background yields in our amplitude models. This section discusses the different physics models used to fit different contributions and presents the full fit model used.

In Chapter 6, I then present the efficiency and background modeling required as inputs for the amplitude analysis. There is particular focus on the efficiency studies that use a novel Kernel Density Estimation (KDE) technique to constrain the five-dimensional phase space (Figure 1.1). This is followed by a description of the background modeling used across all data samples. The closing part of the chapter discusses the full amplitude model, describing the fixed parameters and their physics motivations.

Chapter 7 presents the results extracted from the amplitude fits. These are the fit fractions of the various amplitude contributions modeled in this analysis, and model parameters. It will also present the time and flavour integrated fit for the Longitudinal Polarisation Fraction of the  $\rho(770)^0\rho(770)^0$  decay channel. The chapter closes with a discussion of how these fits will be extended into a single measurement of the angle  $\alpha$ .

Chapter 8 provides a short summary of the research presented in this thesis, highlighting key results from the relevant chapters.

# Chapter 2

## Theory and Motivations

I refuse to believe that God is a weak left-hander.

---

Wolfgang Pauli

This chapter seeks to take the reader from a light overview of the Standard Model of particle physics, through to understanding the amplitude models that underpin the  $B^0 \rightarrow \pi^+ \pi^- \pi^+ \pi^-$  analysis. The chapter will also seek to explain the current landscape of measuring the unitarity angle  $\alpha$  in this experimental channel, and the novel extension to resolve this ambiguity.

### 2.1 The Standard Model

The Standard Model (SM) of particle physics is a quantum field theory that encompasses all fundamental interactions, and particles observed in our universe. So far the SM has been extremely accurate and predictive, being supported with observation of the Higgs boson in 2012 [1, 2]. It also predicted a value of the anomalous magnetic dipole moment of the electron that is in agreement with the observed result to ten significant figures<sup>1</sup>; by far the most accurately verified theoretical prediction in the history of physics [4]. From the Standard Model, the fundamental particles so far discovered are shown in Figure 2.1

The particles of the Standard Model are broadly grouped into two categories based

---

<sup>1</sup>In contrast, recent results from the g-2 collaboration show evidence that the muon anomalous magnetic dipole moment may be inconsistent with the SM [3]. Current measurements show a  $3\sigma$  discrepancy with the SM expectation.

# Standard Model of Elementary Particles

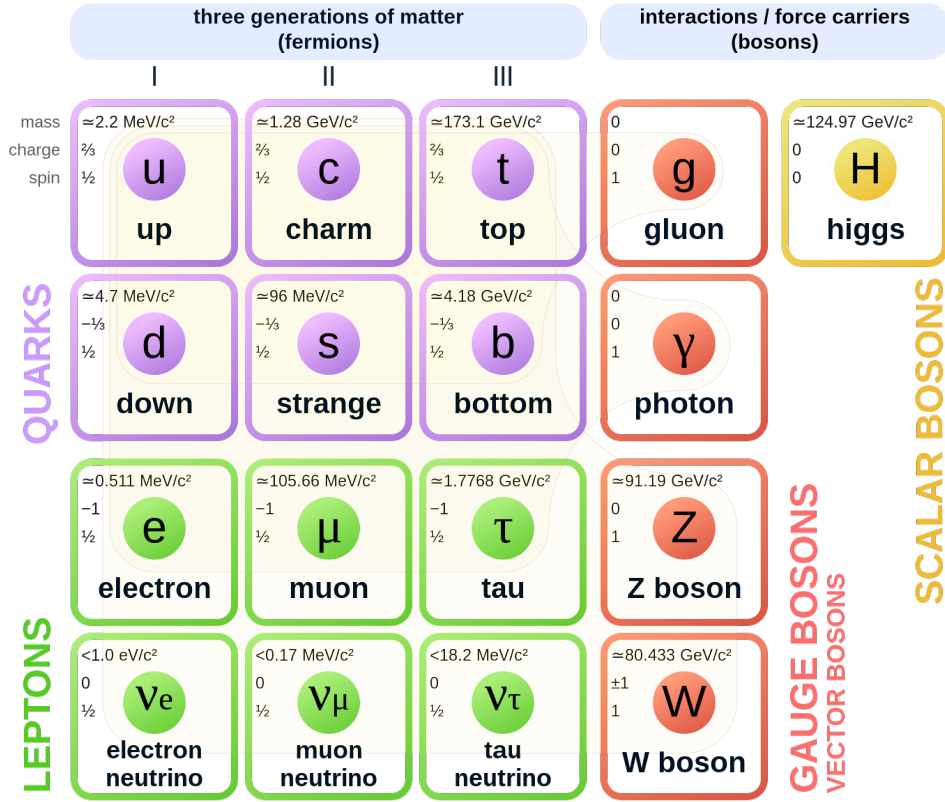


Figure 2.1: Standard Model of particle physics.

on their spin; either bosons, that have whole integer spin, or fermions, that have half integer spin. Looking now at the fermions; these account for all the visible matter in the universe and are subdivided into two further groups, the quarks and the leptons. For the leptons we find these exist in three distinct generations containing a charged and neutral particle (Table 2.1). Beyond the usual spin and charge quantities, leptons also carry another quantum number that is unique to each generation. This *flavour* is conserved in all interactions except neutrino oscillation [5]. However, recent flavour anomalies seen by LHCb are putting this conserved quantity under heavy scrutiny [6].

The other family of fermions are the quarks (Table 2.2) that also come in three distinct generations, where each generation contains a particle of  $+\frac{2}{3}$  electric charge, and one of  $-\frac{1}{3}$ . Similar to leptons the quarks also carry a quantum property called flavour. The quantities of flavour in the quark sector are Isospin ( $I$ ), where  $I_3$  denotes the  $z$  projection

Lepton	Generation	Mass (MeV)	Charge	e No.	$\mu$ No.	$\tau$ No.
Electron, $e$	I	0.511	-1	+1	0	0
Electron neutrino, $\nu_e$ ,	I	$< 2 \times 10^{-6}$	0	+1	0	0
Muon, $\mu$	II	105.66	-1	0	+1	0
Muon neutrino, $\nu_\mu$ ,	II	$< 0.9$	0	0	+1	0
Tau, $\tau$	III	$1776.86 \pm 0.12$	-1	0	0	+1
Tau neutrino, $\nu_\tau$ ,	III	$< 18.2$	0	0	0	+1

Table 2.1: Lepton content of the Standard Model [4].

of this isospin, charm ( $C$ ), strangeness ( $S$ ), topness ( $T$ ) and bottomness ( $B$ ). Unlike the lepton sector, these quantum numbers are not explicitly conserved. Quarks also carry another property in addition to flavour known as *colour*. Colour comes in three different forms red, green or blue for matter with respective anti-colours for the anti-quarks. These colours define the quark content of most matter as only neutral systems can exist freely due to a process known as colour-confinement [7]. It should be noted that although the author respects the current convention of referring to the  $b$ -quark as bottom, for the remainder of this thesis it shall be referred to by the name, beauty [8].

Finally we have the bosons which act as the mediators for electromagnetic, strong force, and weak force in the SM—gravity is omitted in the SM as it is many magnitudes weaker than the other forces. Electrically charged fermions can interact via the electromagnetic force, which is mediated by the photon ( $\gamma$ ). This force is extremely long range since the photon is massless, and does not readily self-interact or decay into other fundamental particles [9]. The nuclear strong force is mediated by the gluon ( $g$ ), which only interacts with fundamental particles that have a colour charge, hence gluons interact only with quarks and themselves [7]. Although the gluon, much like the photon, is massless, this self interaction limits the range of the strong force to be of the scale  $10^{-15}$  m [4]. The weak force is the only interaction that can change the flavour of quarks and leptons, a quantity that is conserved in all other decays. The weak force couples to left handed fermions via the charged  $W^\pm$ , and to left and right handed particles via the neutral  $Z^0$  boson. Since these bosons have mass, they operate on a very short scale of  $10^{-18}$  m [4].

The final piece of the Standard Model puzzle—for now—is the Higgs boson. In electroweak theory when the  $W^\pm$  and the  $Z^0$  were postulated as new bosons, their mass was required to be zero by  $SU(2)$  symmetry. To resolve this, while maintaining the zero mass

Quark	Generation	Mass (MeV)	Charge	$I_3$	$C$	$S$	$T$	$B$
Up, $u$	I	$2.2^{+0.5}_{-0.4}$	$+\frac{2}{3}$	$+\frac{1}{2}$	0	0	0	0
Down, $d$	I	$4.7^{+0.5}_{-0.3}$	$-\frac{1}{3}$	$-\frac{1}{2}$	0	0	0	0
Charm, $c$	II	$1.28^{+0.03}_{-0.04} \times 10^3$	$+\frac{2}{3}$	0	+1	0	0	0
Strange, $s$	II	$93^{+9}_{-3}$	$-\frac{1}{3}$	0	0	-1	0	0
Top, $t$	III	$173.0 \pm 0.4 \times 10^3$	$+\frac{2}{3}$	0	0	0	+1	0
Bottom, $b$	III	$4.18^{+0.04}_{-0.03}$	$-\frac{1}{3}$	0	0	0	0	-1

Table 2.2: Quark content of the Standard Model [4].

of the photon and gluon, a scalar field was predicted to exist, where the Higgs ( $H^0$ ) is the quantisation of this field [10, 11, 12]. This new field allowed for a breaking of  $SU(2)$  symmetry, allowing the  $W^\pm$  and  $Z^0$  to have mass. These new bosons were observed by the UA1 and UA2 experiments [13, 14, 15] providing the first experimental evidence of the Higgs field. In 2012 the final prediction of this theory, the Higgs itself, was discovered by CMS [1] and ATLAS [2].

## 2.2 Symmetry

The fundamental symmetries of the Standard Model are governed by local gauge symmetries. These are described by the unitary product group of the Standard Model,

$$G_{SM} = SU(3)_C \times SU(2)_L \times U(1)_Y, \quad (2.1)$$

which conserve colour charge ( $C$ ), weak-isospin ( $L$ )—specifically for left handed fields—and weak hyper-charge ( $Y$ ). These fields are represented mathematically within the Standard Model Lagrangian given by,

$$\mathcal{L}_{SM} = \mathcal{L}_{gauge} + \mathcal{L}_{Higgs} + \mathcal{L}_{Yukawa}, \quad (2.2)$$

where  $\mathcal{L}_{gauge}$  embodies the interaction terms of the electroweak force and QCD,  $\mathcal{L}_{Higgs}$  embodies the interaction terms with the Higgs field from spontaneous symmetry breaking and the  $\mathcal{L}_{Yukawa}$ , that couples the Higgs field to the quark and lepton fields. The latter of these (the Yukawa) is discussed in more detail later in the chapter.

Alongside these global symmetries, the SM also has a number of discrete symme-

tries that are conserved multiplicatively to ensure Lorentz invariance. These quantities are charge conjugation ( $C$ ), parity inversion ( $P$ ), and time reversal ( $T$ ). These interact uniquely with the weak force due to the differing gauge representations of left and right-handed fields.

### 2.2.1 The Wu Experiment (The Dawn of Parity)

The year is 1956 and Lee and Yang have published their paper reviewing recent experimental data on the  $\tau^+$  and  $\theta^+$  mesons [16]. The experimental landscape of the time showed that the  $\tau^+$ , which decays via,

$$\tau^+ \rightarrow \pi^+ \pi^+ \pi^-, \quad (2.3)$$

was a final state with negative parity and zero angular momentum. Similarly the  $\theta^+$ , which decays via,

$$\theta^+ \rightarrow \pi^+ \pi^0, \quad (2.4)$$

was found to be a final state with positive parity and zero angular momentum. This unto itself was not unusual, what was unusual is that all of the current experimental evidence was showing that the  $\tau^+$  and  $\theta^+$  had the same lifetime [17], and mass [18]. This implied—assuming the conservation of parity—that nature had contrived two distinct particles that had the same mass and lifetime. To resolve this  $\theta - \tau$  puzzle, Lee and Yang proposed investigating the weak interaction via  $\beta$ -decay interactions, or through the interactions of mesons and hyperons. The Wu experiment [19] investigated this through  $\beta$ -decay in 1956, specifically through the reaction,

$${}_{27}^{60}\text{Co} \rightarrow {}_{28}^{60}\text{Ni} + e^- + \bar{\nu}_e + 2\gamma. \quad (2.5)$$

This method worked by polarising  ${}_{27}^{60}\text{Co}$  in a magnetic field. This polarisation could be measured through gamma production, since gamma production is an electromagnetic interaction, and is inherently parity conserving. By comparing the polarisation of the nuclei to the direction of  $\beta$  production through the weak interaction it was possible to observe the first evidence of parity violation (Figure 2.2). An important historical footnote to this landmark observation is that Chien-Shiung Wu was denied the 1957 Nobel prize

with it only being awarded to her colleagues T.D. Lee and C.N. Yang.

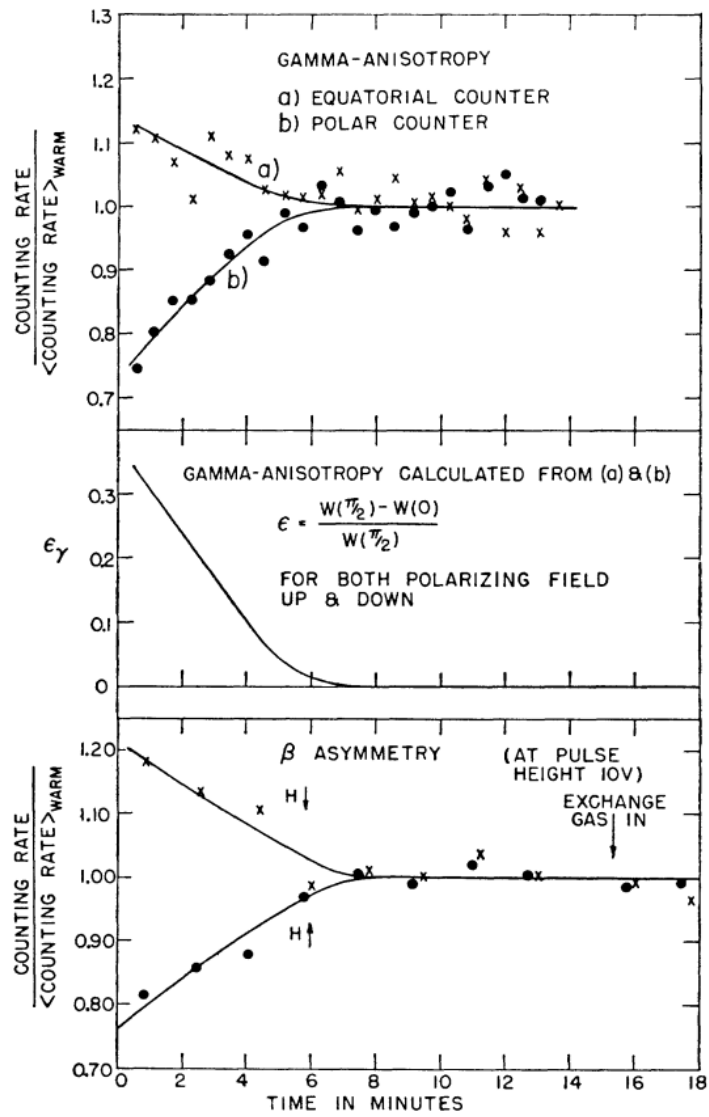


Figure 2.2: Gamma anisotropy and beta asymmetry for polarizing field pointing up and pointing down, reproduced from [19].

## 2.2.2 The Cabibbo-Kobayashi-Maskawa (CKM) Matrix

As discussed earlier, quark and lepton masses in the Standard Model depend on their Yukawa couplings to the  $\phi$ . These couplings allow for the quarks and leptons to interact via the Higgs mechanism and also embodies the physical observations of **CP** violation. The Yukawa Lagrangian is defined as,

$$\mathcal{L} = \begin{pmatrix} \bar{D}_{1L} \\ \bar{D}_{2L} \\ \bar{D}_{2L} \end{pmatrix}^T \left\{ \tilde{\phi} \begin{pmatrix} G_1^0 & G_2^0 & G_3^0 \\ G_4^0 & G_5^0 & G_6^0 \\ G_7^0 & G_8^0 & G_9^0 \end{pmatrix} \begin{pmatrix} u'_R \\ c'_R \\ t'_R \end{pmatrix} + \phi \begin{pmatrix} G_{10}^0 & G_{11}^0 & G_{12}^0 \\ G_{13}^0 & G_{14}^0 & G_{15}^0 \\ G_{16}^0 & G_{17}^0 & G_{18}^0 \end{pmatrix} \begin{pmatrix} d'_R \\ s'_R \\ b'_R \end{pmatrix} \right\} + h.c. \quad (2.6)$$

which is defined by three left handed  $SU(2)_L$  quark doublets,

$$D_{1L} = \begin{pmatrix} u' \\ d' \end{pmatrix}_L, \quad D_{2L} = \begin{pmatrix} c' \\ s' \end{pmatrix}_L, \quad D_{3L} = \begin{pmatrix} t' \\ b' \end{pmatrix}_L, \quad (2.7)$$

with the prime distinguishing these quark doublets from the quark mass eigenstates, six right handed singlets,

$$u'_R, d'_R, c'_R, s'_R, t'_R, b'_R, \quad (2.8)$$

and 18 independent coupling constants  $G_i^0, i = 1, 2 \dots 18$ , which are constrained by 36 parameters, and two fields defined by,

$$\tilde{\phi} = \begin{pmatrix} \phi^{0\dagger} \\ -\phi^- \end{pmatrix}, \quad \phi = \begin{pmatrix} \phi^+ \\ \phi^0 \end{pmatrix}. \quad (2.9)$$

The mass matrices of the up and down type quarks are then proportional to their corresponding Yukawa coupling and the vacuum expectation value  $v$ ,

$$\mathcal{M}_U = v \begin{pmatrix} G_1^0 & G_2^0 & G_3^0 \\ G_4^0 & G_5^0 & G_6^0 \\ G_7^0 & G_8^0 & G_9^0 \end{pmatrix}, \quad \mathcal{M}_D = v \begin{pmatrix} G_{10}^0 & G_{11}^0 & G_{12}^0 \\ G_{13}^0 & G_{14}^0 & G_{15}^0 \\ G_{16}^0 & G_{17}^0 & G_{18}^0 \end{pmatrix}, \quad (2.10)$$

where the bare quark masses can be recovered from the diagonalisation of these matrices,

$$T_{U,L} \mathcal{M}_U T_{U,R}^\dagger = \mathcal{M}_U^{diagonal}, \quad T_{D,L} \mathcal{M}_D T_{D,R}^\dagger = \mathcal{M}_D^{diagonal}. \quad (2.11)$$

This diagonalisation can then be used to transform left and right-handed quark fields into their respective mass eigenstates,

$$U_{L[R]}^m = T_{U,L[R]} U_{L[R]}, \quad D_{L[R]}^m = T_{D,L[R]} D_{L[R]}, \quad (2.12)$$

the implications of which can be seen in charge current interactions where,

$$\bar{U}_L \gamma_\mu D_L = \bar{U}_L^m T_{U,L} \gamma_\mu T_{D,L}^\dagger D_L^m = \bar{U}_L^m \gamma_\mu \mathbf{V} D_L^m, \quad (2.13)$$

where  $\mathbf{V}$ , the Cabbibo-Kobayashi-Maskawa matrix, is given by,

$$\mathbf{V} = T_{U,L} T_{D,L}^\dagger = \begin{pmatrix} \mathbf{V}_{ud} & \mathbf{V}_{us} & \mathbf{V}_{ub} \\ \mathbf{V}_{cd} & \mathbf{V}_{cs} & \mathbf{V}_{cb} \\ \mathbf{V}_{td} & \mathbf{V}_{ts} & \mathbf{V}_{tb} \end{pmatrix}. \quad (2.14)$$

In order to utilise this important matrix we must first understand the number of free parameters that can contribute to this matrix. A general  $n \times n$  matrix will contain  $2n^2$  real parameters. However the CKM matrix has a number of constraints which can reduce this number. The first of these is the requirement of unitarity,

$$\sum_J \mathbf{V}_{ij} \mathbf{V}_{jk}^* = \delta_{ik}, \quad (2.15)$$

which will yield  $n$  constraints for  $i = k$  and  $n^2 - n$  constraints for  $i \neq k$ . From this, the total number of parameters is reduced to  $n^2$ . The final constraints on the number of real parameters are from the phases of the quark fields that can be rotated freely through,

$$U_i^m \rightarrow e^{i\Phi_i^U} U_i^m, \quad D_j^m \rightarrow e^{j\Phi_j^D} D_j^m, \quad (2.16)$$

yielding the relation,

$$\mathbf{V} \rightarrow \begin{pmatrix} e^{-i\Phi_1^U} & \dots & 0 \\ \vdots & \ddots & \vdots \\ 0 & \dots & e^{-i\Phi_n^U} \end{pmatrix} \mathbf{V} \begin{pmatrix} e^{i\Phi_1^D} & \dots & 0 \\ \vdots & \ddots & \vdots \\ 0 & \dots & e^{i\Phi_n^D} \end{pmatrix}, \quad (2.17)$$

which lets us remove  $2n + 1$  relative phases. As such,  $\mathbf{V}$  contains  $n^2 - 2n + 1$  or  $(n - 1)^2$  independent physical parameters. However, using the properties of orthogonality held by the matrix we can define these parameters in terms of independent rotation angles and

phases with a general  $n \times n$  orthogonal matrix having,

$$N_{angles} = \frac{1}{2}n(n-1), \quad (2.18)$$

and,

$$N_{phases} = N_{free} - N_{angles} = (n-1)^2 - \frac{1}{2}n(n-1) = \frac{1}{2}(n-1)(n-2). \quad (2.19)$$

Just through this definition alone we can actually infer a lot about the possible physics at play in the CKM matrix. For example if we consider the case of *two* flavour families we instantly see that we can constrain this through a single angle, the Cabbibo angle [20], implying no **CP** violation in **V**. Luckily, the Standard Model actually contains *three* flavour families and from this we have 3 mixing angles and 1 phase introducing **CP** violation. The most common parameterisation is

$$\begin{pmatrix} c_{12}c_{13} & s_{12}c_{13} & s_{13}e^{-i\delta} \\ -s_{12}c_{23} - c_{12}s_{23}s_{13}e^{i\delta} & c_{12}c_{23} - s_{12}s_{23}s_{13}e^{i\delta} & s_{23}c_{13} \\ s_{12}s_{23} - c_{12}c_{23}s_{13}e^{i\delta} & -c_{12}s_{23} - s_{12}c_{23}s_{13}e^{i\delta} & c_{23}c_{13} \end{pmatrix}, \quad (2.20)$$

where  $s_{ij} = \sin \theta_{ij}$ ,  $c_{ij} = \cos \theta_{ij}$ , embody the Euler mixing angles, and  $\delta$  is the phase responsible for all CP-violating processes. From the experimental observation that  $s_{13} \ll s_{23} \ll s_{12} \ll 1$  the CKM matrix can be further parameterised as a power expansion in  $\sin \theta_C = \lambda$ . This is known as the Wolfenstein parameterisation [21], and is expressed as

$$\begin{pmatrix} 1 - \frac{1}{2}\lambda^2 & \lambda & A\lambda^3(\rho - i\eta + \frac{i}{2}\eta\lambda^2) \\ -\lambda & 1 - \frac{1}{2}\lambda^2 - i\eta A^2\lambda^4 & A\lambda^2(1 + i\eta\lambda^2) \\ A\lambda^3(1 - \rho - i\eta) & A\lambda^2 & 1 \end{pmatrix} \quad (2.21)$$

where  $A$ ,  $\rho$  and  $\eta$  are real quantities with magnitude of  $\mathcal{O}(1)$ , and  $\lambda$  has a value of approximately 0.22. A useful feature of this parameterisation is in characterising the six possible configurations of the unitarity triangle. These are defined by the unitarity condition of the CKM matrix. The different configurations and their magnitudes are given

as,

$$\mathbf{V}_{ud}^* \mathbf{V}_{us} + \mathbf{V}_{cd}^* \mathbf{V}_{cs} + \mathbf{V}_{td}^* \mathbf{V}_{ts} = 0, \quad (2.22)$$

$$\mathbf{V}_{ud}^* \mathbf{V}_{cd} + \mathbf{V}_{us}^* \mathbf{V}_{cs} + \mathbf{V}_{ub}^* \mathbf{V}_{cb} = 0, \quad (2.23)$$

$$\mathbf{V}_{us}^* \mathbf{V}_{ub} + \mathbf{V}_{cs}^* \mathbf{V}_{cb} + \mathbf{V}_{ts}^* \mathbf{V}_{tb} = 0, \quad (2.24)$$

$$\mathbf{V}_{td}^* \mathbf{V}_{cd} + \mathbf{V}_{ts}^* \mathbf{V}_{cs} + \mathbf{V}_{tb}^* \mathbf{V}_{cb} = 0, \quad (2.25)$$

$$\mathbf{V}_{td}^* \mathbf{V}_{ud} + \mathbf{V}_{ts}^* \mathbf{V}_{us} + \mathbf{V}_{tb}^* \mathbf{V}_{ub} = 0, \quad (2.26)$$

$$\mathbf{V}_{ud}^* \mathbf{V}_{ub} + \mathbf{V}_{cd}^* \mathbf{V}_{cb} + \mathbf{V}_{td}^* \mathbf{V}_{tb} = 0, \quad (2.27)$$

As can be inferred from the magnitudes of the triangular relations in terms of the coefficient  $\lambda$ , the largest measurable angles will be found in the final two parameterisations where  $\lambda$  is of the same order; although all are valid descriptions of the CKM matrix. Of these final two, the equation 2.26, is the preferred description of the CKM matrix with the unitarity triangle being that shown in Figure 2.3.

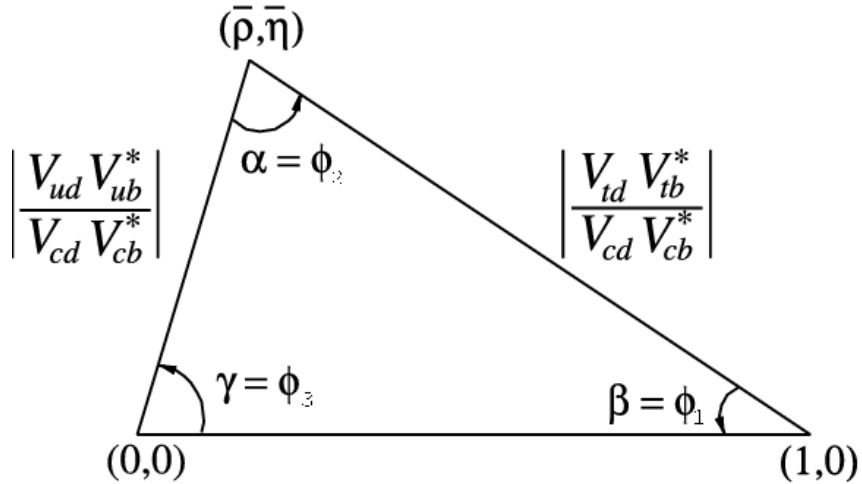


Figure 2.3: The CKM unitarity triangle in the  $(\bar{\rho}, \bar{\eta})$  plane [22].

The angles of the unitarity triangle are defined as,

$$\alpha = \arg \left( -\frac{V_{td} V_{tb}^*}{V_{ud} V_{ub}^*} \right), \quad \beta = \arg \left( -\frac{V_{cd} V_{cb}^*}{V_{td} V_{tb}^*} \right), \quad \gamma = \arg \left( -\frac{V_{ud} V_{ub}^*}{V_{cd} V_{cb}^*} \right), \quad (2.28)$$

CKM Angle	Central Value	Uncertainty
$\alpha$	91.98°	[+0.82 – 1.40]
$\beta$	22.42°	[+0.64 – 0.37]
$\gamma$	65.5°	[+1.3 – 1.2]

Table 2.3: CKM angle values [4].

with their current global fit values being presented in Table 2.3. Evidence of new physics would be seen through a constraint on these angles breaking the unitarity condition.

## 2.3 CP violation

In  $b$ -hadron decays the **CP** violation implied by the form of the CKM matrix can take one of three distinct forms. The first of these is **CP** violation in decay. For **CP**-violation in decay there must be at least two interfering amplitudes leading to the same final state. For example we can express the amplitudes of a decay and its **CP** conjugate as,

$$A = |A_1|e^{i(\delta_1+\phi_1)} + |A_2|e^{i(\delta_2+\phi_2)}, \quad (2.29)$$

$$\bar{A} = |A_1|e^{i(\delta_1-\phi_1)} + |A_2|e^{i(\delta_2-\phi_2)}, \quad (2.30)$$

where  $A_{1,2}$  refers to the interfering amplitude contributions,  $\phi_{1,2}$ , represents their weak phase (**CP**-odd) and  $\delta_{1,2}$ , represents their strong phase (**CP**-even). From these definitions it is possible to define a CP violating asymmetry,

$$\mathcal{A}_{CP} = \frac{\Gamma(\bar{B} \rightarrow \bar{f}) - \Gamma(B \rightarrow f)}{\Gamma(\bar{B} \rightarrow f) + \Gamma(B \rightarrow f)} \quad (2.31)$$

where  $\Gamma(B \rightarrow f)$  is the rate for a  $b$ -hadron decay to a final state  $f$ . In order to extract a measurement of  $\mathcal{A}_{CP}$  the strong and weak phases have to be both non-zero.

The next source of **CP** violation is from mixing. Mixing occurs when the mass eigenstate of a neutral particle is not equal to its flavour eigenstate. As such, the particle in our case, the  $B^0$ , will oscillate.

The final source of **CP** violation is through the interference of mixing and decay. This source of **CP** violation is defined as the interference between the decay  $B \rightarrow \bar{B} \rightarrow f$  with

mixing, and the decay  $B \rightarrow f$  without, where the final state  $f$  is common to both. This type occurs in the situation,

$$\arg(\lambda_f) - \arg(\lambda_{\bar{f}}) \neq 0, \quad (2.32)$$

where

$$\lambda_f = \frac{q}{p} \frac{\bar{A}_f}{A}. \quad (2.33)$$

## 2.4 Isospin Decomposition and Amplitude Analysis

In order to access the unitarity angle  $\alpha$  in this analysis, and disentangle the aforementioned sources of **CP** violation we use a technique called amplitude analysis. Amplitude analyses are useful for decoupling various resonant and non-resonant intermediate states in  $B^0$  decays. This allows us to investigate **CP** in specific channels such as  $B^0 \rightarrow \rho(770)^0 \rho(770)^0 \rightarrow \pi^+ \pi^- \pi^+ \pi^-$  without biasing our selection vetoing other resonant states. Our study of the  $B^0 \rightarrow \pi^+ \pi^- \pi^+ \pi^-$  utilises this technique to analyse the time independent rates and amplitudes of the  $B^0$ , and its intermediate resonances. This is used in conjunction with an extension to the isospin decomposition of neutral and charged mesons which will now be discussed.

### 2.4.1 Isospin Decomposition of Charmless $B$ Decays

Isospin decomposition concerns the decay of neutral  $B^0$  mesons, and charged  $B^+$  mesons, into pairs of light unflavoured isovector and pseudoscalar mesons, namely the  $\rho^0$  and the  $\pi$ . Analysts are specifically interested in the modes  $B^0 \rightarrow \pi^0 \pi^0$ ,  $B \rightarrow \rho \rho$  and  $B^0 \rightarrow \rho \pi$ . These modes are useful since under isospin symmetry, and by neglecting electroweak penguin contributions, the weak phase  $\beta + \gamma = \pi - \alpha$  [23] can be extracted from their amplitude level values.

#### 2.4.1.1 Penguins

Penguin transitions (Figure. 2.5), rather than the aquatic flightless bird [24], are a non-negligible contribution to the decay amplitudes observed in many charmless analyses. Unlike the biological penguin (Figure. 2.4), which is naturally suppressed by the detector



Figure 2.4: David Friday *Artistic depiction of penguins at CERN.*

geometry, and the geographical location of the experiment [25], transitions such as the flavour-changing neutral current penguin,  $\bar{b} \rightarrow \bar{d}(u\bar{u})$  can occur readily.

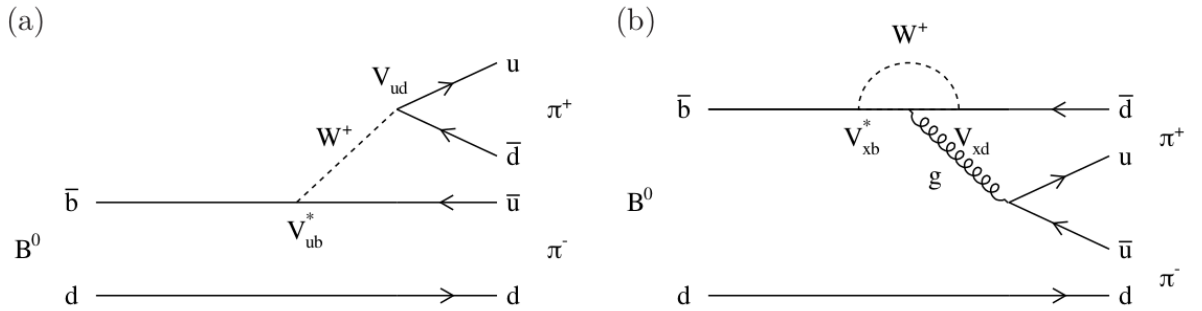


Figure 2.5: Tree (a) and Penguin (b) contributions in the  $B^0 \rightarrow \pi\pi$  process [26].

In order to quantify and thereby disentangle penguin contributions in our analysis it is important to consider the full transition amplitudes of our decay. This means including both the tree and penguin contributions for the three up-type quark flavours ( $uct$ ) that could occur in the  $W$  loop. As such, we can consider an amplitude of the form,

$$A^{ij} = \langle h_1^i h_2^j | (\mathcal{H}_{eff}) | B^0 \rangle = V_{ud} V_{ub}^* (T_u^{ij} + P_u^{ij}) + V_{cd} V_{cb}^* P_c^{ij} + V_{td} V_{tb}^* P_t^{ij} , \quad (2.34)$$

where  $\mathcal{H}_{eff}$ , is the effective Hamiltonian of the transition,  $T_u^{ij}$  represents contributions from tree-level transitions, and  $P_{u,c,t}^{ij}$  represent contributions from penguin transitions. Using the unitarity relation within the Cabibbo–Kobayashi–Maskawa (CKM) matrix it is possible to reduce this transition amplitude down to two terms rather than three. Since our analysis terminates on a determination of the CKM angle  $\alpha$ , the  $\mathcal{C}$ -convention will be adopted that yields the following simplification,

$$A^{ij} = V_{ud} V_{ub}^* (T_u^{ij} + P_u^{ij} - P_c^{ij}) + V_{td} V_{tb}^* (P_t^{ij} - P_c^{ij}) . \quad (2.35)$$

This  $\mathcal{C}$ -convention is then rewritten as,

$$\mathcal{A}^{ij} = V_{ud} V_{ub}^* \tilde{\mathcal{T}}^{ij} + V_{td} V_{tb}^* \tilde{\mathcal{P}}^{ij} . \quad (2.36)$$

with the terms  $\tilde{\mathcal{T}}^{ij} = T_u^{ij} + P_u^{ij} - P_c^{ij}$  and  $\tilde{\mathcal{P}}^{ij} = P_t^{ij} - P_c^{ij}$  representing the “tree” and “penguin” amplitudes respectively. These terms are not strictly pure amplitudes of either tree or penguin contributions. However, choosing this particular convention lets us fix our penguin-to-tree ratio with respect to other CKM transitions. Hence, in the  $\mathcal{C}$ -convention our penguin-to-tree ratio is given by,

$$\tilde{R}^{ij} = \frac{R_t \tilde{\mathcal{P}}^{ij}}{R_u \tilde{\mathcal{T}}^{ij}} , \quad (2.37)$$

where  $R_u = |V_{ud} V_{ub}^*|$ , and  $R_t = |V_{td} V_{tb}^*|$  are the magnitudes of their respective CKM products. These are also used in the redefined amplitudes  $T^{ij} = R_u \tilde{\mathcal{T}}^{ij}$ , and  $P^{ij} = R_t \tilde{\mathcal{P}}^{ij}$  that we will employ in this derivation.

From the properties of the unitarity triangle (Fig. 2.3) it is possible to pull the weak phases from equation 2.36. Using  $\gamma = \arg\left(-\frac{V_{ud} V_{ub}^*}{V_{cd} V_{cb}^*}\right)$  and  $\beta = \arg\left(-\frac{V_{cd} V_{cb}^*}{V_{td} V_{tb}^*}\right)$  we can rewrite our amplitudes as,

$$A^{ij} = -e^{i\gamma} T^{ij} + e^{-i\beta} P^{ij} . \quad (2.38)$$

Similarly in the case of the  $\mathbf{CP}$  conjugate states we can express their decay amplitude as,

$$\frac{p}{q}\bar{A}^{ij} = -e^{-i\gamma}T^{ij} + e^{i\beta}P^{ij} , \quad (2.39)$$

where  $p/q$  is the factor that defines the mixing phase for the parent mesons. In an isospin analysis, the **CP** invariance of the strong interaction means that the underlying hadronic processes ( $T$ ,  $P$ ) are applicable to **CP**-conjugate processes, the only difference being a complex conjugation of the weak phases. By rotating the amplitudes for the process and its **CP** conjugate by the weak phase  $\beta$ , the quantity  $\alpha$  can be derived from tree contributions,

$$e^{2i\alpha} = \frac{e^{i\alpha}T^{ij}}{e^{-i\alpha}T^{ij}} = \frac{\bar{A}^{ij} - P^{ij}}{A^{ij} - P^{ij}}. \quad (2.40)$$

Hence, in the absence of penguin contributions  $\alpha$  can then be related directly to the relative phase of the amplitudes describing  $B$  meson decays.

#### 2.4.1.2 Isospin

At this point, we have been discussing how  $\alpha$  can be extracted from the tree level amplitudes in the absence of penguin contributions. As can be seen in equation 2.40, in the case of non negligible penguin contributions, this is not so straightforward. However, it is possible to disentangle the penguin contributions using isospin amplitudes instead. Firstly, in all  $B \rightarrow hh$  decay processes we have the weak decay  $\bar{b} \rightarrow u\bar{u}\bar{d}$  which, when considering only the three valance quarks, corresponds to shift in  $\Delta I = \frac{1}{2}, \frac{3}{2}$ . The inclusion of the spectator quark gives final state isospins ( $I_f = 0, 1, 2$ ). From this we can use the Wigner-Eckart theorem to determine a general decomposition of decay amplitudes as in Table 2.4. The shift in isospin  $\Delta I = \frac{5}{2}$  which can come from re-scattering is included for completeness, but is suppressed by a factor  $\alpha_e m$  and therefore neglected in later discussion.

This general decomposition holds for any pair of distinguishable isovectors, and allows us to constrain the five decay amplitudes with the pentagonal relation,

$$A^{+-} + A^{-+} + 2A^{00} = \sqrt{2}(A^{+0} + A^{0+}). \quad (2.41)$$

The most useful quantity to analysts however is how these relations affect the penguin amplitudes. Since penguin amplitudes in the limit of  $\Delta I = \frac{3}{2}$  are expected to be small or negligible, the penguin amplitudes have the relation,

Amplitude	$A_{\frac{5}{2},2}$	$A_{\frac{3}{2},2}$	$A_{\frac{3}{2},1}$	$A_{\frac{1}{2},1}$	$A_{\frac{1}{2},0}$
$A^{+0} = \langle h_1^+ h_2^0   \mathcal{H}_s   u\bar{u}\bar{d}, u \rangle$	$-\sqrt{1/6}$	$+\sqrt{3/8}$	$-\sqrt{1/8}$	$+\sqrt{1/2}$	0
$A^{0+} = \langle h_1^0 h_2^+   \mathcal{H}_s   u\bar{u}\bar{d}, u \rangle$	$-\sqrt{1/6}$	$+\sqrt{3/8}$	$+\sqrt{1/8}$	$-\sqrt{1/2}$	0
$A^{+-} = \langle h_1^+ h_2^-   \mathcal{H}_s   u\bar{u}\bar{d}, d \rangle$	$+\sqrt{1/12}$	$+\sqrt{1/12}$	$+1/2$	$+1/2$	$+\sqrt{1/6}$
$A^{-+} = \langle h_1^- h_2^+   \mathcal{H}_s   u\bar{u}\bar{d}, d \rangle$	$+\sqrt{1/12}$	$+\sqrt{1/12}$	$-1/2$	$-1/2$	$+\sqrt{1/6}$
$A^{00} = \langle h_1^0 h_2^0   \mathcal{H}_s   u\bar{u}\bar{d}, d \rangle$	$+\sqrt{1/3}$	$+\sqrt{1/3}$	0	0	$-\sqrt{1/6}$

Table 2.4: General Decomposition of the amplitudes observed in the  $B \rightarrow hh$  decay modes for distinguishable mesons.

$$P^{+-} + P^{-+} + 2P^{00} = \sqrt{2}(P^{+0} + P^{0+}) = 0. \quad (2.42)$$

Under this isospin model the penguin amplitudes sum to zero. Hence, it follows that certain combinations of the decay amplitudes also have no penguin contributions. In contrast to equation 2.40, and using these isospin relations, we can create a penguin free constraint on  $\alpha$ ,

$$e^{2i\alpha} = \frac{\bar{A}^{+0} - \bar{A}^{0+}}{A^{+0} - A^{0+}}. \quad (2.43)$$

However, this is not enough to fully constrain  $\alpha$  since this still leads to a number of solutions that are dependent of the effective alpha,  $\alpha_{eff}$ , between the other components of the pentagonal system.  $\alpha_{eff}$  is a phase shift in the observed  $\alpha$ , caused by penguin contamination, and changes the phase of the observed amplitudes. An example of this offset in the amplitudes is shown in Figure 2.7 for the reduced decomposition described in Section 2.4.1.3. Even with a large number of solutions, a  $B \rightarrow hh$  analysis of distinguishable isovectors can still yield constraints on  $\alpha$ .

### 2.4.1.3 $B^0 \rightarrow \rho\rho$ Isospin Models

The  $B \rightarrow \rho\rho$  decay (along with the  $B \rightarrow \pi\pi$ ) offers a unique basis to constrain our isospin models further, since the two isovector mesons in the final state are indistinguishable. In this scenario, only the  $I_f = 0, 2$  are permitted. This leads to a greatly reduced amplitude decomposition that can be seen in Table 2.5.

This simplifies the identity from equation 2.41 into the triangular identity,

Amplitude	$A_{\frac{3}{2},2}$	$A_{\frac{1}{2},1}$	$A_{\frac{1}{2},0}$
$A^{+0} = \langle h_1^+ h_2^0   \mathcal{H}_s   u\bar{u}d, u \rangle$	-1	+3/2	0
$A^{+-} = \langle h_1^+ h_2^-   \mathcal{H}_s   u\bar{u}d, d \rangle$	$+\sqrt{1/2}$	$+\sqrt{1/2}$	+1
$A^{00} = \langle h_1^0 h_2^0   \mathcal{H}_s   u\bar{u}d, d \rangle$	+1	+1	$-\sqrt{1/2}$

Table 2.5: General Decomposition of the amplitudes observed in the  $B \rightarrow hh$  decay modes for indistinguishable mesons.

$$A^{+0} = \frac{A^{+-}}{\sqrt{2}} + A^{00}. \quad (2.44)$$

Following the same logic as in the general isospin model for distinguishable isovector states, we can find a penguin-free mode based on negligible penguin contributions in the limit of  $\Delta I = \frac{3}{2}$ ,

$$e^{2i\alpha} = \frac{\bar{A}^{+0}}{A^{+0}}. \quad (2.45)$$

Again, this ratio cannot be determined from a single measurement. However, analysing the triangular relationship in equation 2.44 is far more favourable. In the most general case, a measurement of  $\alpha$  (Figure 2.7) in this framework will lead to the reconstruction of two isospin triangles and their mirror solutions. This leads to a possible eightfold ambiguity in  $\alpha$  (Figure 2.7). This ambiguity can be reduced in two possible ways. Firstly, if one or both of these triangles are flat, the mirror solutions of these become degenerate. Secondly, a favourable measurement of  $\mathcal{S}^{00}$ , which represents the time-dependent CP asymmetry of the  $B \rightarrow h^0 h^0$  decay mode restricts the phase-transformed solutions. In the  $B \rightarrow \pi\pi$  decay mode since neither isospin triangle is flat and a measure of  $\mathcal{S}^{00}$  in LHCb is unfeasible due to a four-photon final state,  $\alpha$  can only be determined with an eightfold ambiguity as seen in figure 2.6.

The  $B \rightarrow \rho\rho$  decay mode however has much larger amplitudes in the  $A^{+-}$  and  $A^{+0}$  modes than in  $A^{00}$ . This means that the mirrored solutions that appear in the  $B \rightarrow \pi\pi$  system do not arise, leading to a twofold degeneracy that can be observed in figure 2.8. This is currently limited by the current measurement of  $\mathcal{S}^{00}$ , which although accessible through the  $\pi^+\pi^-$  final state has extremely high uncertainties. Hence by using  $B^0 \rightarrow \pi^+\pi^-\pi^+\pi^-$  we seek to go beyond the results reported in figure 2.8 by using direct amplitude-level observables. Instead, we intend to instead measure  $\mathcal{A}_{CP}^{00}$  through  $\lambda_{CP}^{00} = \left| \frac{\bar{A}^{00}}{A^{00}} \right|$  and  $\mathcal{S}_{CP}^{00}$

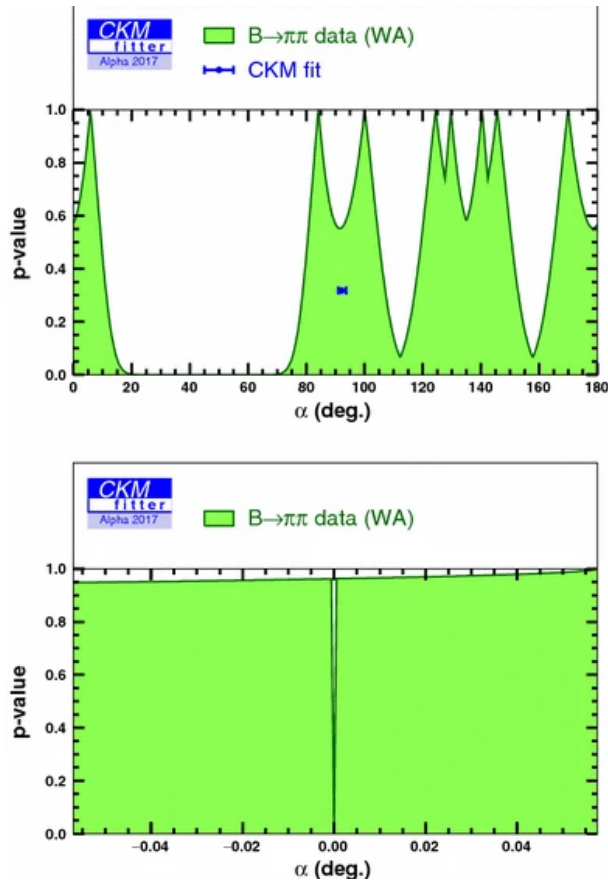


Figure 2.6: One-dimensional scan of  $\alpha$  in the  $[0,180]$  range (top) isospin analysis of the  $B \rightarrow \pi\pi$  system. The zoom in the vicinity of 0 (bottom figure) displays the punctual discontinuity, whose width due to the scan binning has no physical meaning [27]. This is extracted from the branching fractions of each amplitude and their CP violating phases.

through  $\phi_{CP}^{00} = \frac{\arg(\bar{A}^{00}A^{00*})}{2}$  to constrain the  $\alpha_{eff}$  in  $B^0 \rightarrow \rho^0\rho^0$ , where  $\alpha_{eff}$  is a phase shift in the observed  $\alpha$ , caused by penguin contamination, and changes the phase of the observed amplitudes (Figure 2.7). The statistical distance of these solutions from the no-penguin solution allows us to approach a single constraint on  $\alpha$ . As such, the work presented in this thesis contributes to a constraint for a single solution to  $\alpha$  as proposed in Ref. [26].

In the analysis presented in this thesis, time and flavour integrated fits will be used to improve our constraints on  $\lambda_{CP}^{00}$  by measuring the Longitudinal Polarisation fraction,  $f_L$ . This amplitude-level observable requires the Longitudinal Polarisation fraction to be fully constrained since isospin measurements are made only using longitudinally polarised

$\rho$  mesons, which are represented by the amplitude  $A^{00}$  in figure 2.7. The expansion of the phase space for this thesis permits a higher  $\rho(770)^0$  yield, reducing our statistical uncertainty on this quantity compared to previous measurements [28, 29, 30]. Access to this quantity is discussed in Chapter 7.

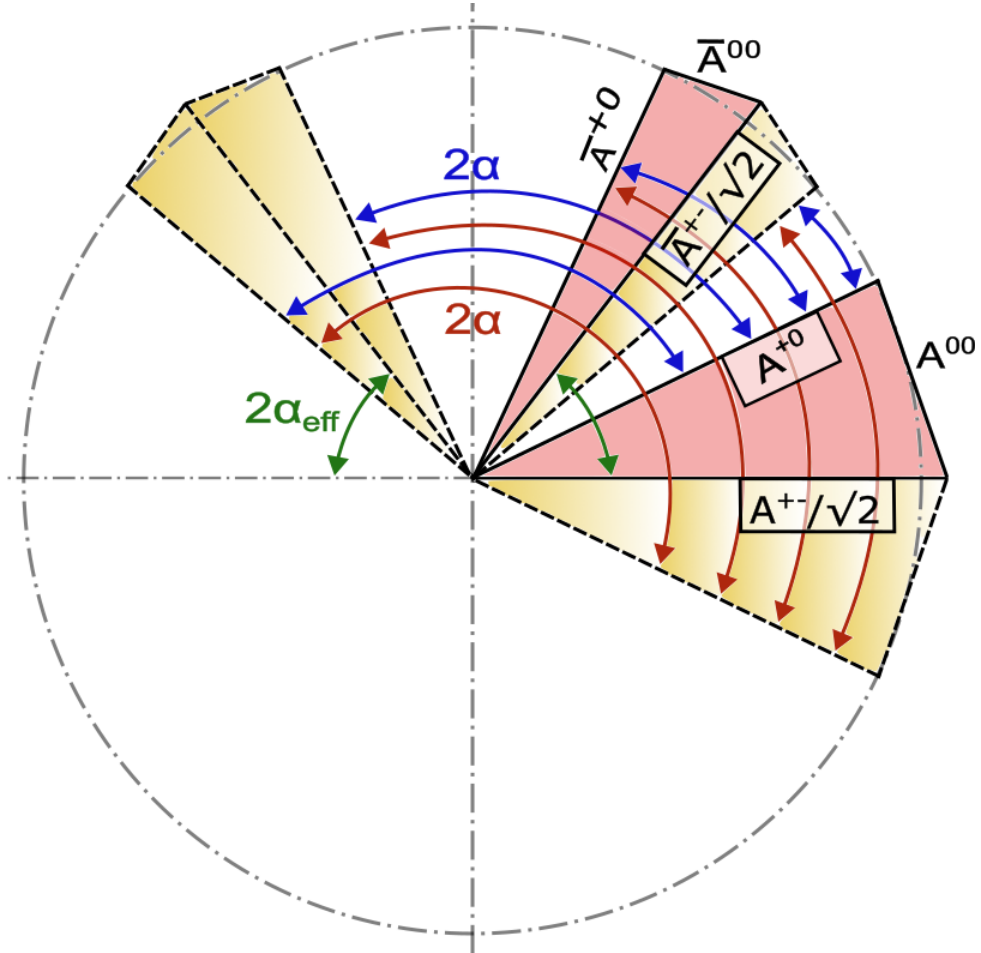


Figure 2.7: Isopin decomposition of the indistinguishable  $B \rightarrow hh$  system. The red and blue arrows indicate the eight-fold degeneracy of the system while the green arrows indicate the phase offset due to penguin contributions in the system. In the  $\rho\rho$  system this system collapses to a two-fold degeneracy.

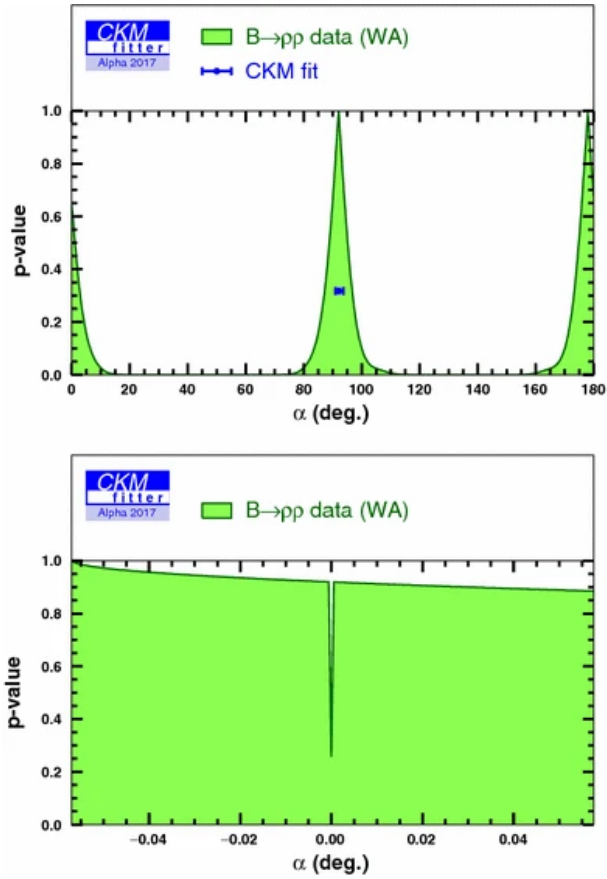


Figure 2.8: One-dimensional scan of  $\alpha$  in the  $[0,180]$  range (top) isospin analysis of the  $B \rightarrow \rho\rho$  system. The zoom in the vicinity of 0 (bottom figure) displays the punctual discontinuity, whose width due to the scan binning has no physical meaning [27].

## 2.5 The Isobar Model

In order to measure the quantities needed to derive  $\alpha$ , we need access to amplitude-level quantities. This section will provide a working understanding of the isobar approach and discuss its application in the amplitude models for use in the  $B^0 \rightarrow \pi^+\pi^-\pi^+\pi^-$  analysis.

The amplitude of a decay in an  $n$ -body phase space,  $A(\Phi_n)$ , can be described as the sum of all interfering resonances of the decay in the form,

$$A(\Phi_n) = \sum c_i A_i(\Phi_n) \quad (2.46)$$

where  $c_i$  is a complex number extracted from fits to data that represent contributions from strong and weak phase components, and  $A_i$  is the amplitude for the individual resonances. In the isobar approach to summing amplitudes we assume that the decay and its intermediate resonances can be constructed as a set of *independent* two-body decays. Figure 2.9 shows two possible quasi-two-body decay paths for the  $B^0$  meson.

The total amplitude for each intermediate state is parameterised as

$$A_i(\Phi_4) = B_i(\Phi_4) S_i(\Phi_4) \prod_j B_j(\Phi_4) T_j(\Phi_4), \quad (2.47)$$

where  $B_i$  represents the Blatt-Weisskopf barrier factor of  $B^0$  decays, while  $S_i$  is the spin amplitude of the overall decay chain. The specific  $j$  intermediate states are comprised of their respective decay barrier factors and a propagator,  $T$ . The Bose-symmetry of different decay paths due to the exchange of like-signed pions must be considered in the final sum to avoid underestimation of resonant contributions.

### 2.5.1 Blatt-Weisskopf Barrier Factors

The Blatt-Weisskopf Barrier [31] Factors correct for unphysical divergences in the amplitude induced by spin amplitudes at high energies. The correction is done by assuming a square-well interaction potential with radius  $r$ . For all states, the barrier radius is taken to be  $4.0 \text{ GeV}^{-1}$  ( $\approx 0.8 \text{ fm}$ ). These barrier factors are also dependent on the momentum transfer (break up momentum) between the decay products that is given by,

$$q^2(M, m_1, m_2) = \frac{M}{4} - \frac{m_1 + m_2}{2} + \frac{(m_1 - m_2)^2}{4M}, \quad (2.48)$$

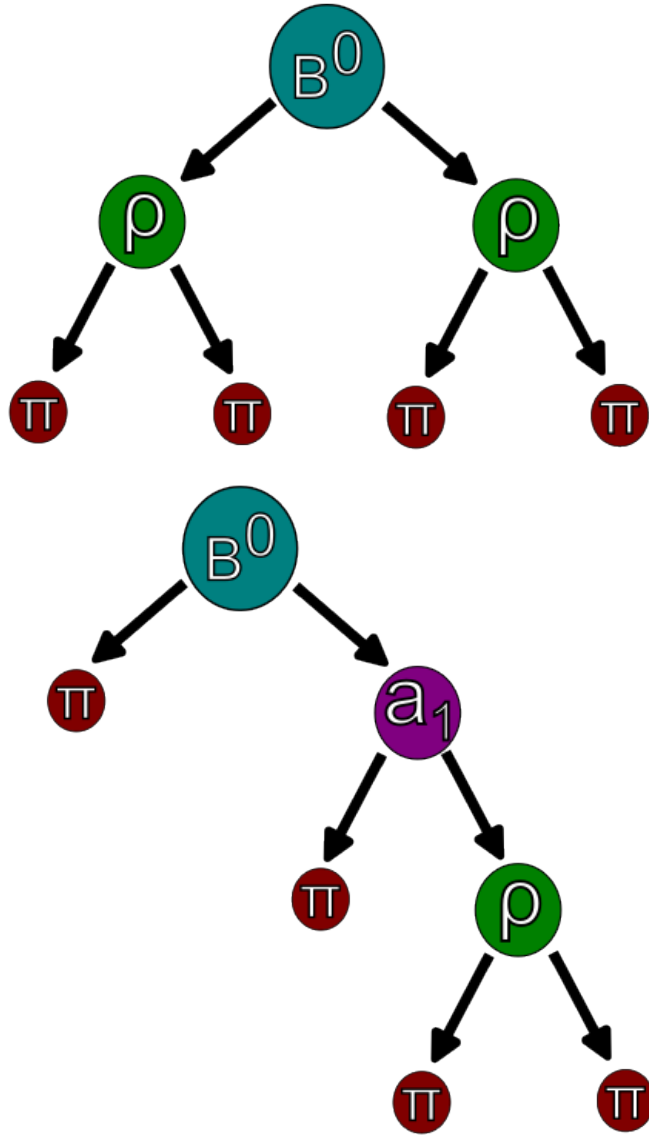


Figure 2.9: Two quasi-two-body decay paths for the  $B^0$ , proceeding via either  $B^0 \rightarrow \rho(770)^0\rho(770)^0$ , or  $B^0 \rightarrow a_1(1260)^\pm\pi^\mp$ .

where  $M$  is the mass of the particle and  $m_{1,2}$  are the masses of the respective decay products. The final term in understanding the Blatt-Weisskopf barrier factors is  $L$ , which represents the orbital angular momentum. Their explicit expressions used in this analysis are

$$\begin{aligned}
B_0(q) &= 1, \\
B_1(q) &= \frac{1}{\sqrt{1+(qr)^2}}, \\
B_2(q) &= \frac{1}{\sqrt{9+3(qr)^2+(qr)^4}}, \\
B_3(q) &= \frac{1}{\sqrt{225+45(qr)^2+6(qr)^4+(qr)^6}},
\end{aligned} \tag{2.49}$$

with  $B_L$  denoting the orbital angular momentum of the contribution.

### 2.5.2 Spin Factors

The helicity formalism forms the basis for many amplitude analyses. However, while it describes narrow resonant states to some level of precision, it has some limitations. One of these limitations is that the spin formalism is non-relativistic, which could lead to some misinterpretation of lineshapes in relativistic conditions. The other factor is that helicity amplitudes are not eigenstates of relative angular momentum between decay products. As such, it becomes much more difficult to assign suitable barrier factors to the decay. In the case of this analysis we get around these issues by using a covariant tensor formalism based on the Rarita-Schwinger conditions [32]. The first Rarita-Schwinger condition

$$\epsilon^\mu(p; \lambda)p_\mu = 0, \tag{2.50}$$

defines that the polarisation vector of some state should be orthogonal to its momentum. This condition is stipulated since spin represents how a particle at rest behaves under spatial rotation. As such, when viewed in the rest frame of the particle the time component must vanish. In order to maintain this condition we can require that the polarisation vector is orthogonal when  $p_\mu$  is time-like. If we select the  $z$ -axis as a convention it is possible to generate three independent solutions to the equation, which we can interpret as three distinct spin projections of a spin-1 particle along the axis, with the longitudinal polarisation being defined as,

$$\epsilon^\mu(\lambda = 0) = (0, 0, 0, 1),$$

and the right-handed (+) and left-handed (−) transverse polarisation being defined as,

$$\epsilon^\mu(\lambda = \pm 1) = \mp \frac{1}{\sqrt{2}}(0, 1, \pm i, 0). \quad (2.51)$$

This definition however is only valid in the rest frame of the initial state. In order to remove this restriction, we adjust our definitions by boosting them into an arbitrary frame. Therefore, a Lorentz transformation is applied to boost the polarisation vectors into this,

$$\begin{aligned} \epsilon^\mu(p, \lambda = 0) &= \frac{1}{M} \begin{pmatrix} p_z \\ p_z p_x / (E + M) \\ p_z p_y / (E + M) \\ M + p_z^2 / (E + M) \end{pmatrix}, \\ \epsilon^\mu(p, \lambda = \pm 1) &= \frac{\mp 1}{M\sqrt{2}} \begin{pmatrix} p_x \pm ip_y \\ M + p_x(p_x \pm ip_y) / (E + M) \\ \pm iM + p_y(p_x \pm ip_y) / (E + M) \\ p_z(p_x \pm ip_y) / (E + M) \end{pmatrix}. \end{aligned} \quad (2.52)$$

Considering  $2S + 1$  degrees of freedom are available to a spin- $S$  state to fully constrain our spin-1 case, two additional conditions are needed. We require that the polarisation vector should be symmetric under index exchange,

$$\epsilon^{\dots\mu_i\dots\mu_j\dots}(p, \lambda) = \epsilon^{\dots\mu_j\dots\mu_i\dots}(p, s_z), \quad (2.53)$$

and that the polarisation tensor should be traceless,

$$g_{\mu_i\mu_j}\epsilon^{\dots\mu_i\dots\mu_j\dots}(p, \lambda) = 0. \quad (2.54)$$

These conditions are automatically satisfied by the underlying Lie algebra of the Clebsch-Gordon coefficients that couple angular momentum states in quantum mechanics. For example, the spin-2 polarisation tensor can be constructed by coupling two spin-1 states together as,

$$\epsilon^{\mu\nu}(p, \lambda) = \sum_{\lambda_1, \lambda_2} \langle 1\lambda_1, 1\lambda_2 | 2\lambda \rangle \epsilon^\mu(p, \lambda_1) \epsilon^\nu(p, \lambda_2), \quad (2.55)$$

where  $\langle 1\lambda_1, 1\lambda_2 | 2\lambda \rangle$  are the Clebsch-Gordon coefficients. Higher-order spin polarisation tensors can be generated recursively in a similar fashion.

The most important construct of the covariant tensor formalism is the projection operator,

$$P^{\mu\nu}(p) = \sum_{\lambda} \epsilon^{\mu}(p, \lambda) \epsilon^{*\nu}(p, \lambda) = -g^{\mu\nu} + \frac{p^{\mu} p^{\nu}}{M^2}, \quad (2.56)$$

which has the property of being able to project an arbitrary 4-vector into the spin-1 subspace spanned by the polarisation vectors  $\epsilon^{\mu}(p, s_z)$ .

Another particularly useful object is the relative orbital angular momentum spin tensor  $L$ , which for some process  $R \rightarrow P_1 P_2$ , is the relative momenta of the decay products  $q_R \equiv p_1 - p_2$  projected to align with the spin of  $R$ ,

$$L_{\mu_1 \mu_2 \dots \mu_L}(p_R, q_R) = (-1)^L P_{\mu_1 \mu_2 \dots \mu_L \nu_1 \nu_2 \dots \nu_L}(p_R) q_R^{\nu_1} q_R^{\nu_2} \dots q_R^{\nu_L}, \quad (2.57)$$

where the number of indices representing the tensor rank is equal to the value of  $L$ . Finally, to ensure that the spin amplitude behaves correctly under parity transformation, it is sometimes necessary to include the Levi-Cevita totally antisymmetric tensor  $\epsilon_{abcd} p_R^d$ . Each stage of a decay is represented by a Lorentz scalar obtained by contracting an orbital tensor between the decay products with a spin wavefunction of equal rank representing the final state.

So the first thing we want to understand is how a particle of arbitrary spin  $X$  decays into two pseudoscalars,  $s_1, s_2$  under this scheme. This case is quite simple since the relative wave between  $s_1, s_2$  must carry the spin of  $X$ . As such,  $s_1, s_2$  must also by extension have no polarisation tensors orthogonal to  $X$ . These constraints leave only a single viable solution for the  $X \rightarrow s_1 s_2$  system,

$$\langle s_1, s_2, L = X | M | X \rangle = \sum_{s_{zX}} \epsilon^{a, b \dots X}(p_X, s_{zX}) L_{Xab \dots X}(p_X, q_X). \quad (2.58)$$

For the specific case of  $\rho(770)^0 \rightarrow \pi^+ \pi^-$  which satisfies this topological case we can express the spin 1 case as,

$$\langle \pi^+, \pi^-, L = 1 | M | \rho \rangle = \sum_{s_{z\rho}} \epsilon^a(p_{\rho}, s_{z\rho}) L_{1a}(p_{\rho}, q_{\rho}). \quad (2.59)$$

However, what about other cases such as  $S_- \rightarrow V_1 V_2$  which form the first 2-body structure of  $B^0 \rightarrow \rho(770)^0 \rho(770)^0 \rightarrow \pi^+ \pi^- \pi^+ \pi^-$ ? In order to better understand this case we will examine the  $L = 0, 1, 2$  cases. For  $L = 0$ ,

$$\langle V_1, V_2, L = 0 | M | S_- \rangle = \sum_{s_{z1}, s_{z2}} \epsilon_a^*(p_{V_1}, s_{zV_1}) \epsilon^{*a}(p_{V_2}, s_{zV_2}), \quad (2.60)$$

where the polarisation tensors act in some arbitrary direction since there is no orbital angular momentum between the  $V_1, V_2$  daughter particles. Now in the case of  $L = 1$  the situation is slightly more complex since there is now some intrinsic spin related to the  $S_-$ . In this case the spin formalism evolves in the following way,

$$\langle V_1, V_2, L = 1 | M | S_- \rangle = \sum_{s_{z1}, s_{z2}} L_{1a}(p_{S_-}, q_{S_-}) \phi_1^a(p_{V_1}, p_{V_2}, s_{zV_1}, s_{zV_2}), \quad (2.61)$$

where  $\phi$  is some general spin-1 waveform that couples the two spin-1 daughters. However  $\phi$  must also be orthogonal to the decaying  $S_-$ . In order to contract this, we need to include a rank-3 Levi-Civita operator  $\epsilon_{abcd} p_{S_-}^d$  to preserve parity. Therefore we can express  $\phi$  as

$$\phi_1^a(p_{V_1}, p_{V_2}, s_{zV_1}, s_{zV_2}) = P_1^{ab}(p_{S_-}) \epsilon_{abcd} \epsilon^{*b}(p_{V_1}, s_{zV_1}) \epsilon^{*c}(p_{V_2}, s_{zV_2}) p_{S_-}^d. \quad (2.62)$$

By substituting this into our original formalism definition and contracting the orbital angular momentum relation with the identity

$$p_1^{\mu\nu}(p) L_{1\nu}(p, q) = L_1^\mu(p, q), \quad (2.63)$$

yields the P-Wave solution to this decay topology,

$$\langle V_1, V_2, L = 1 | M | S_- \rangle = L_1^b(p_{S_-}, q_{S_-}) \epsilon_{abcd} \epsilon^{*b}(p_{V_1}, s_{zV_1}) \epsilon^{*c}(p_{V_2}, s_{zV_2}) p_{S_-}^d. \quad (2.64)$$

The final decay topology we will cover before applying this to a decay tree used in the analysis is the D-Wave case where  $L = 2$ . Once again we consider the decay in terms of some orbital angular momentum tensor and—in this case—some spin 2 wavefunction,

$$\langle V_1, V_2, L = 2 | M | S_- \rangle = \sum_{s_{z1}, s_{z2}} L_{2ab}(p_{S_-}, q_{S_-}) \phi_2^{ab}(p_{V_1}, p_{V_2}, s_{zV_1}, s_{zV_2}). \quad (2.65)$$

As for the  $L = 1$  example we need to project the  $\phi$  into a suitable subspace. In this case, however, we can contract this in terms of a rank-2 projection vector,

$$\phi_2^{ab} = P_2^{abcd}(p_{S_-})\epsilon^{*c}(p_{V_1}, S_{z_{V_1}})\epsilon^{*d}(p_{V_2}, S_{z_{V_2}}). \quad (2.66)$$

Finally making use of the identity.

$$P_2^{\mu\nu\alpha\beta}(p)L_{2\alpha\beta} = L_2^{\mu\nu}(p, q), \quad (2.67)$$

we can reach the final form for the  $L = 2$  case,

$$\langle V_1, V_2, L = 2 | M | S_- \rangle = \sum_{s_{z_1}, s_{z_2}} L_{2cd}(p_{S_-}, q_{S_-})\epsilon^{*c}(p_{V_1}, S_{z_{V_1}})\epsilon^{*d}(p_{V_2}, S_{z_{V_2}}). \quad (2.68)$$

With access to all these cases, it is possible to construct the decay topology for any decay  $S_- \rightarrow [V_1 V_2]_{s,p,d}, V \rightarrow s_1 s_2$ . The full set of topologies used in the amplitude analysis are presented in Table 2.6.

Topology	Spin amplitude
$P_0 \rightarrow AP_1, A \rightarrow [VP_2]_S, V \rightarrow P_3 P_4$	$L_a(p_{P_0}, q_{P_0})P^{ab}(p_A)L_b(p_V, q_V)$
$P_0 \rightarrow AP_1, A \rightarrow [VP_2]_D, V \rightarrow P_3 P_4$	$L_a(p_{P_0}, q_{P_0})L^{ab}(p_A, q_A)L_b(p_V, q_V)$
$P_0 \rightarrow AP_1, A \rightarrow SP_2, S \rightarrow P_3 P_4$	$L_a(p_{P_0}, q_{P_0})L^a(p_A, q_A)$
$P_0 \rightarrow TP_1, T \rightarrow VP_2, V \rightarrow P_3 P_4$	$\epsilon_{abcd}L^{de}(p_{P_0}, q_{P_0})L_c^e(p_T, q_T)p_T^b L^a(p_V, q_V)$
$P_0 \rightarrow [V_1 V_2]_S, V_1 \rightarrow P_1 P_2, V_2 \rightarrow P_3 P_4$	$L^a(p_{V_1}, q_{V_1})L^a(p_{V_2}, q_{V_2})$
$P_0 \rightarrow [V_1 V_2]_P, V_1 \rightarrow P_1 P_2, V_2 \rightarrow P_3 P_4$	$\epsilon_{abcd}L^d(p_{P_0}, q_{P_0})L^c(p_{V_1}, q_{V_1})L^b(p_{V_2}, q_{V_2})p_{P_0}^a$
$P_0 \rightarrow [V_1 V_2]_D, V_1 \rightarrow P_1 P_2, V_2 \rightarrow P_3 P_4$	$L_{ab}(p_{P_0}, q_{P_0})L^b(p_{V_1}, q_{V_1})L^a(p_{V_2}, q_{V_2})$
$P_0 \rightarrow [TV]_P, T \rightarrow P_1 P_2, V \rightarrow P_3 P_4$	$L_a(p_{P_0}, q_{P_0})L^{ab}(p_T, q_T)L_b(p_V, q_V)$
$P_0 \rightarrow VS, V \rightarrow P_1 P_2, S \rightarrow P_3 P_4$	$L_a(p_{P_0}, q_{P_0})L^a(p_V, q_V)$
$P_0 \rightarrow TS, T \rightarrow P_1 P_2, S \rightarrow P_3 P_4$	$L_{ab}(p_{P_0}, q_{P_0})L^{ba}(p_T, q_T)$
$P_0 \rightarrow [T_1 T_2]_S, T_1 \rightarrow P_1 P_2, T_2 \rightarrow P_3 P_4$	$L_{ab}(p_{T_1}, q_{T_1})L^{ba}(p_{T_2}, q_{T_2})$

Table 2.6: Spin amplitudes for each decay topology considered in this analysis, where  $P$  is a pseudoscalar,  $S$  a scalar,  $V$  a vector,  $A$  an axial-vector and  $T$  a tensor state. In cases where multiple orbital angular momentum configurations are present between states, the wave is indicated by a subscript. Note that the particle ordering is important as it sets the phase convention.

### 2.5.3 Lineshapes

The final piece of the analysis puzzle are the lineshapes. In order to properly describe the lineshapes for the analysis in general, we describe them with the Breit-Wigner propagator,

$$T(s) = \frac{1}{M^2(s) - s - i\sqrt{s}\Gamma(s)}, \quad (2.69)$$

where  $T(s)$  is the energy-dependent propagator,  $M^2(s)$  is the energy-dependent mass—usually approximated by the pole mass—and  $\Gamma(s)$  is the total energy-dependent width. Generally, in amplitude analyses this decay width is approximated as the width of the decay channel being studied. However, in the case of resonances with higher masses, and/or greater numbers of daughters, this approximation can reduce the sensitivity of the model. For this analysis we use a Monte Carlo method to calculate the total energy-dependent width by summing the partial widths over the phase space,

$$\Gamma(s) = \sum_i \Gamma_i(s) = \Gamma_0 \sum_i g_i \rho_i(s), \quad (2.70)$$

where  $i$  represents each known decay mode,  $g_i$  represents a coupling and  $\rho_i(s)$  represents the phase space available at the energy. It is assumed for normalisation that the couplings will sum to 1 over the full range of the phase space. Since for many resonant states we do not have theoretical access to these couplings, we have to reverse engineer them from the known branching fractions of these resonances,

$$\mathcal{B}_i^{\text{pred}} \propto \int_{s_{\text{min}}}^{\infty} \frac{\sqrt{s}\Gamma_i(s)}{|m_0^2 - s - i\sqrt{s}\Gamma(s)|^2} ds = \int_{s_{\text{min}}}^{\infty} \frac{\sqrt{s}g_i\rho_i(s)}{|m_0^2 - s - i\sqrt{s}\Gamma(s)|^2} ds, \quad (2.71)$$

where the couplings are found by minimising the  $\chi^2$ ,

$$\chi^2 = \sum_i \left[ \frac{\mathcal{B}_i^{\text{exp}} - \mathcal{B}_i^{\text{pred}}(g_i)}{\Delta\mathcal{B}_i^{\text{exp}}} \right]^2, \quad (2.72)$$

where  $\mathcal{B}_i^{\text{exp}}$  represents the central value of the branching fraction and  $\Delta\mathcal{B}_i^{\text{exp}}$  represents experimental uncertainty. The energy-dependent phase space volume of each decay is proportional to,

$$\rho_n(s) \propto \frac{1}{\sqrt{s}} \int \sum_{\lambda} |A_{\lambda}(\Phi_n)|^2 d\Phi_n(s), \quad (2.73)$$

where  $A$  is the transition amplitude of the decay summed over the available polarisations of the initial state,  $\lambda$ , and  $d\Phi_n$  is the differential phase space density for  $n$ -body decays given by,

$$d\Phi_n(s, p_1, \dots, p_n) = \delta^4(P - \sum_{i=1}^n p_i) \prod_{i=1}^n \frac{d^3 p_i}{(2\pi)^3 2E_i}. \quad (2.74)$$

This phase space density is derived using Monte Carlo with the amplitudes being derived from their barrier factors, lineshapes and spin densities. This method is used to derive the final line shape for the  $\omega(782)$ ,  $f_2(1270)$ ,  $a_2(1320)$  and the  $a_1(1640)$ . For the  $a_1(1640)$ , the energy-dependent widths and total width can be seen in Figures 2.10 and 2.11 respectively.

In the special case of topologies containing a  $\rho(770)^0$ , the Breit-Wigner propagator is substituted for a Gounaris–Sakuri model [33]. This model was determined experimentally through  $ee \rightarrow \pi\pi$  decays and has reduced uncertainty in the description of the  $\rho(770)^0$ . The model effectively extends the Breit-Wigner with the inclusion of an analytical dispersion term  $f(s)$ , that better describes the  $\rho(770)^0$  lineshape,

$$T_{\rho}(s) = \frac{1}{M^2(s) + f(s) - s - i\sqrt{s}\Gamma(s)}, \quad (2.75)$$

where the additional mass dependence,  $f(s)$ , is defined as,

$$f(s) = \Gamma \left[ q^2 [h(s) - h(m_0^2)] + (m_0^2 - s) q_0^2 \frac{dh}{ds} \Big|_{m_0^2} \right], \quad (2.76)$$

where,

$$h(s) = \frac{2}{\pi} \frac{q}{\sqrt{s}} \log \left( \frac{\sqrt{s} + 2q}{2m_{\pi}} \right), \quad (2.77)$$

and,

$$\frac{dh}{ds} \Big|_{m_0^2} = h(m_0^2) [(8q_0^2)^{-1} - (2m_0^2)^{-1}] + (2\pi m_0^2)^{-1}. \quad (2.78)$$

This dispersion increases the accuracy of the propagator in the context of the amplitude analysis, increasing the quality of the latter fits. For the  $\rho(770)^0$  we also need to consider

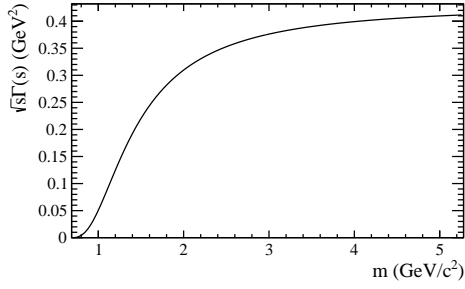
isospin-violating  $\omega(782)$  decays to two charged pions via the mechanism of  $\omega(782)$  mixing with the  $\rho(770)^0$ . To account for this interference effect, a model is constructed that directly parameterises the interference between these two contributions following Ref. [34],

$$T_{\rho\omega}(s) = T_\rho(s) \left[ \frac{1 + a_\omega \Delta_{\text{EM}} T_\omega(s)}{1 - \Delta_{\text{EM}}^2 T_\rho(s) T_\omega(s)} \right], \quad (2.79)$$

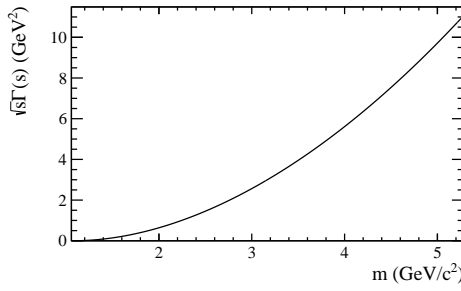
where  $T_\omega(m)$  is the relativistic Breit–Wigner  $\omega(782)$  lineshape,  $T_\rho(m)$  is the Gounaris–Sakuri lineshape,  $a_\omega$  are the complex free parameters of the model that denote the relative magnitude and phase of the  $\omega(782)$  production amplitude with respect to the  $\rho(770)^0$  state,  $\Delta_{\text{EM}} \equiv \delta_{\text{EM}} (m_\rho + m_\omega)$ , where  $\delta$  governs the electromagnetic mixing between  $\rho(770)^0$  and  $\omega(782)$ , with  $m_\rho$  and  $m_\omega$  representing the known particle masses [4].

## 2.6 Chapter Summary

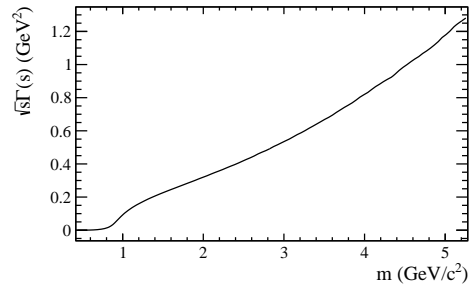
The underlying physics and techniques that have been presented in this chapter are used to access important experimental constraints on the unitarity angle  $\alpha$ . This chapter has outlined access to this angle from first principles of the CKM matrix, through the extended isospin model, finishing with a discussion of amplitude analysis. The fits and values accessed by these techniques will be discussed in subsequent chapters.



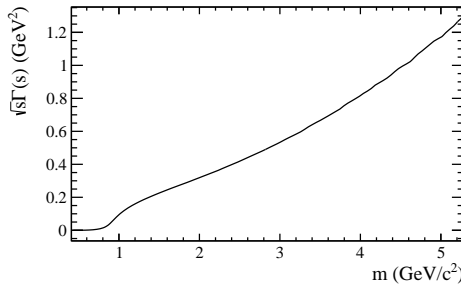
(a)  $a_1(1640) \rightarrow f_0\pi$  energy-dependent width.



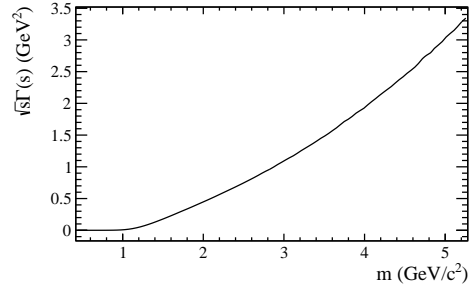
(b)  $a_1(1640) \rightarrow \omega(782)\pi^+\pi^0$  energy-dependent width.



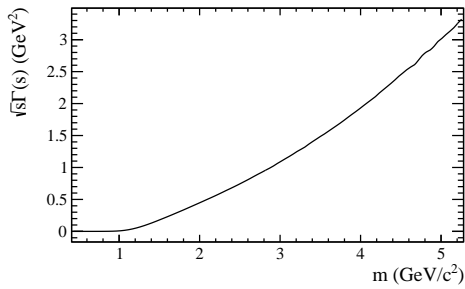
(c)  $a_1(1640) \rightarrow \rho(770)^0\pi^+$  energy-dependent width (S-wave).



(d)  $a_1(1640) \rightarrow \rho(770)^+\pi^0$  energy-dependent width (S-wave).



(e)  $a_1(1640) \rightarrow \rho(770)^0\pi^+$  energy-dependent width (D-wave).



(f)  $a_1(1640) \rightarrow \rho(770)^+\pi^0$  energy-dependent width (D-wave).

Figure 2.10: energy-dependent partial width of the  $a_1(1640)$ .

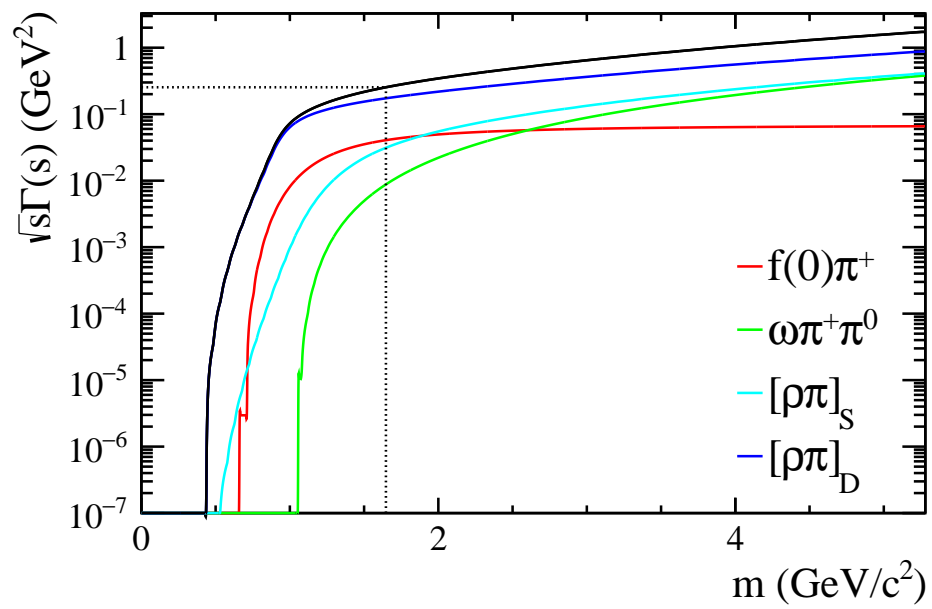


Figure 2.11: energy-dependent width of the  $a_1(1640)$ .

# Chapter 3

## The LHCb Experiment

The powercut was caused by a (poor) fouine (weasel in English, furetto in Italian) who decided to chew on the 66kV transformer at point 8...

---

LHCb Logbook

The LHCb (Large Hadron Collider Beauty) experiment is a flavour physics experiment at the Large Hadron Collider (LHC) in Geneva, Switzerland. LHCb, as the name suggests, was originally designed to perform heavy-flavour physics measurements centred on the beauty quark. However, its physics case has widened to include a comprehensive charm physics program [35], heavy baryon searches [36, 37], and semi leptonic measurements [38]. In this chapter I will discuss the experimental setup itself, starting with a description of the accelerator complex responsible for  $pp$  collisions at LHCb, before discussing the various sub-detector elements, and ending on a description of the data flow and offline data handling strategies employed by the collaboration. This chapter does not cover the recent upgrades and changes to the LHC and the LHCb experiment for Run III of data taking.

### 3.1 The Large Hadron Collider

The LHC is the core experimental complex for 23 member states situated at the European Laboratory for Particle Physics (CERN). The collider itself is located 100 m underground

and has a circumference of 27 km. The tunnel itself originally housed the Large Electron Positron (LEP) collider, which was later replaced by the LHC.

The first run of recorded data was taken with protons in 2010, which marked the start of the first full data taking period at the LHC. This was known to as Run I which concluded in 2012 before the first shutdown for upgrades and repairs to both the LHC, and its experiments. Run II subsequently happened between 2015 to 2018. Currently—and moving forward—the LHC is the most powerful particle accelerator in the world with centre of mass energies,  $\sqrt{s}$ , of 14 TeV where  $\sqrt{s}$  is the invariant mass of the two colliding proton beams. However, accessing proton-proton collisions at these energies is not the work of a single machine, and protons are in fact accelerated across 5 distinct stages (Figure 3.1).

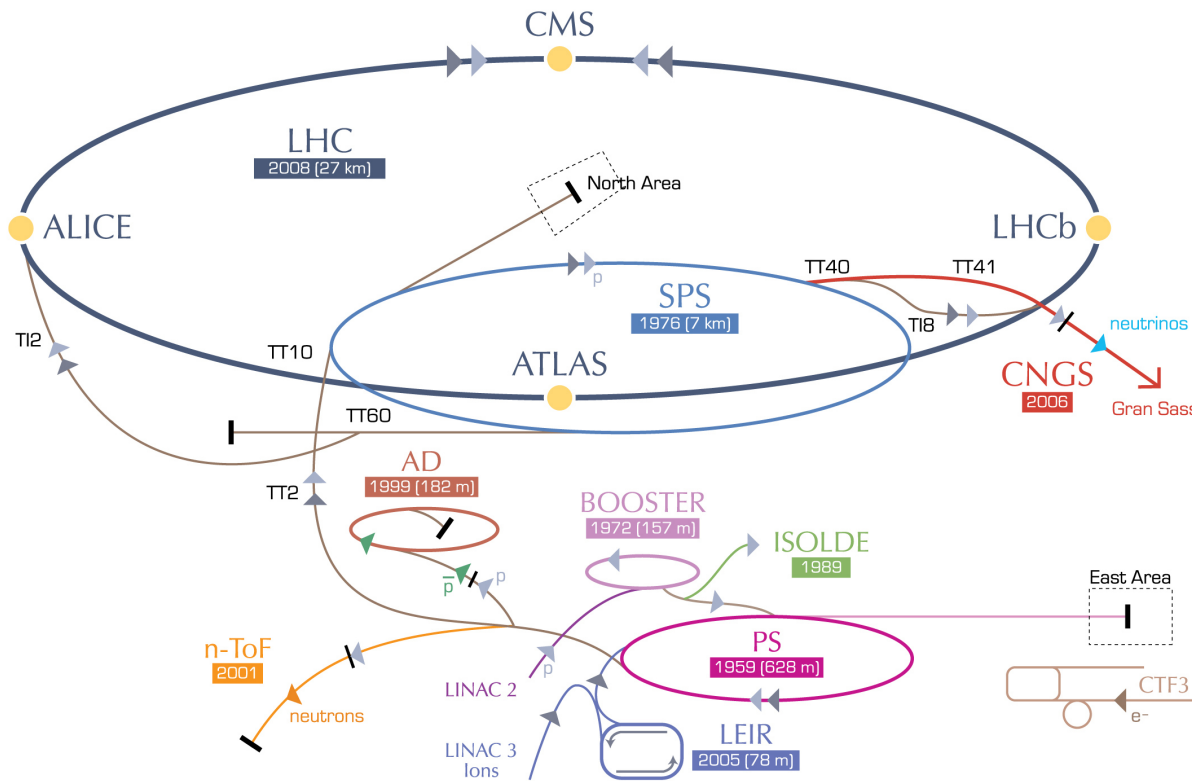


Figure 3.1: Map of the CERN accelerator complex. Reproduced from [39].

The first accelerator stage is the Linear Accelerator 2 (LINAC 2) that accelerates protons from a hydrogen gas source. Once accelerated, they are injected into the Proton Synchrotron Booster (PSB) that uses a pulsed kicker magnet to arrange the spacing of

the protons. The protons exit this booster stage in groups of  $\approx 1 \times 10^{11}$ , at an energy of 1.4 GeV. These bunches then enter the Proton Synchrotron (PS), the first circular accelerator stage, where they are accelerated up to an energy of 26 GeV. They are then injected into the final pre-accelerator stage, the Super Proton Synchrotron (SPS), the second largest machine in the CERN complex which has a circumference of 7 km. This stage accelerates the bunches up to 450 GeV before final injection into the LHC where they are split into two counter-rotating beams.

The LHC maintains beam quality and integrity with an ultra-high vacuum—maintaining pressures below  $10^{-8}$  mbar—to reduce degradation, and uses super-cooled quadrupole magnets that maintain beam focus. There are also a further 16 Radio-Frequency (RF) cavities that accelerate the proton bunches to the final collision energies. The beams are brought together at four points around the ring such that they collide and generate new particles for the large scale experiments. These experiments are ATLAS (A Toroidal LHC Apparatus) [40], CMS (Compact Muon Solenoid) [41], ALICE (A Lead Ion Collision Experiment) [42] and of course LHCb [43]—writers bias acknowledged at this point. ATLAS and CMS are both general purpose barrel detectors designed to measure all detectable products for a variety of SM and new physics searches. It is important—and rightfully so—to mention that the LHC was primarily commissioned to confirm the existence of the Higgs Boson, which was jointly discovered by ATLAS and CMS in 2012 [1, 2]. ALICE is designed slightly differently to exploit lead-ion collisions that happen at the LHC during special run periods. ALICE has recently made significant steps in understanding SM (Standard Model) physics with the first published observation of the dead cone effect [44]. The purpose of this thesis is to describe an analysis using data taken at the LHCb experiment and, as such, will be discussed in the subsequent sections.

## 3.2 Experiment Overview

The LHCb experiment is a forward-facing spectrometer designed for the study of CP-violation through  $pp$  collisions (Figure 3.2). This is the first experiment designed specifically to study CP-violation and heavy flavour physics in this environment, with the previous iterations of *B-factory* experiments, such as BaBar [45], and Belle [46] utilising clean  $b\bar{b}$  pair production through  $e^+e^- \rightarrow \Upsilon(4S)$ .

In contrast to the *B-factories*, LHCb utilises the unique properties of gluon-gluon

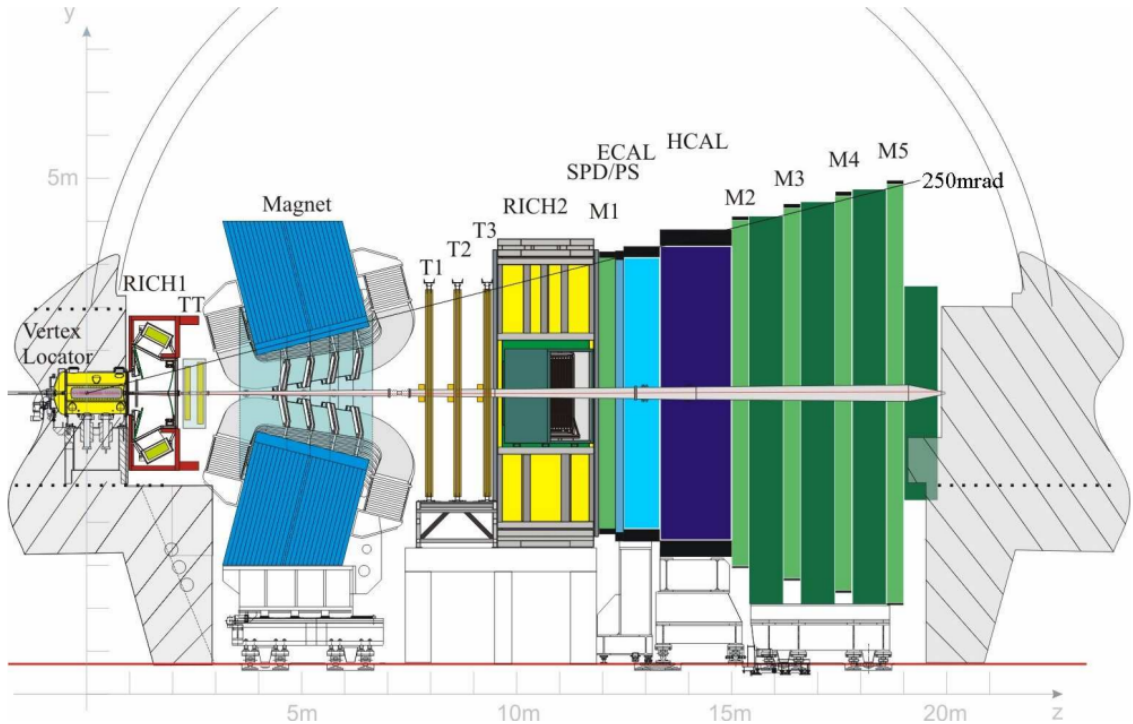


Figure 3.2: The LHCb detector layout, with the beam axis ( $z$ ) going from left to right, the  $y$ -axis going from bottom to top, and the  $x$ -axis going into the page. Reproduced from [47].

fusion, with the  $b\bar{b}$  pair being boosted along the beamline, as can be seen in Figure 3.3. This is a consequence of the asymmetry in momentum between interacting gluon pairs from the  $pp$  collision.

The other consequence of this  $b\bar{b}$  production mechanism is that the events of interest are produced in a much narrower region of pseudorapidity than other experiments. For this reason the LHCb detector operates purely in the forward region with an acceptance of  $1.8 < \eta < 4.9$ , with the pseudorapidity  $\eta$  defined as

$$\eta = \ln \left( \tan \frac{\theta}{2} \right), \quad (3.1)$$

where  $\theta$  is the angle in the transverse plane of the  $b$  or  $\bar{b}$  with respect to the beamline. This acceptance means that although the LHCb experiment covers only 1.8% of the solid angle, approximately 27% of all  $b\bar{b}$  pairs produced from  $pp$  collisions were accessible for reconstruction in Run I [49].

In order to reconstruct events for use in flavour analyses, the LHCb experiment is

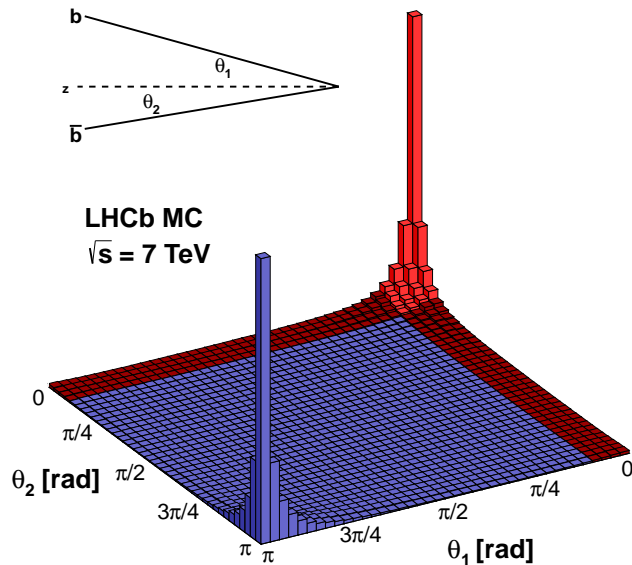


Figure 3.3: Angular distribution of the  $b\bar{b}$  pair produced in  $pp$  collisions at LHCb. The acceptance of the LHCb experiment appears as red on the plot. Reproduced from [48].

divided into a series of subdetectors. In Figure 3.2 the initial  $pp$  interaction takes place in the VELO (VERTex LOcator) which provides initial tracking information for particles produced in the detector. Particles that fall within the LHCb acceptance then travel through the first of the RICH (Ring Imaging CHerenkov) subdetectors that contribute towards particle identification in LHCb. From here, the particles proceed through the TT (Tracker Turicensis) into a dipole magnet that bends the path of charged particles. From the radius of curvature derived from subsequent hits in the tracking stations (T1 - T3) their momenta can be determined. The final stage of the LHCb experiment is made of several calorimeters, the preshower detectors SPD/PS, the ECAL (Electron CALorimeter) and the HCAL (Hadron CALorimeter). Finally we have muon chambers that are used for muon tracking and identification. These calorimetry stages and muon chambers provide further information for the identification of photons, electrons, hadrons and muons that traverse the detector.

For flavour analyses LHCb needs to accurately reconstruct event tracks within its acceptance. However, in high luminosity environments where large numbers of  $pp$  collisions are creating tracks within the acceptance, LHCb can have difficulty resolving individual

events. This is known as pile-up and is an extremely important metric in determining the efficiency of the detector. The pile-up in the detector is related directly to the Luminosity,  $\mathcal{L}$ . Unlike the general purpose detectors ATLAS and CMS, LHCb cannot perform at the nominal LHC operating luminosity which amounts to  $\mathcal{O}(50)$  interactions per bunch crossing under Run II conditions.

This is overcome in LHCb using a technique called *Luminosity Leveling* to reduce the  $\mathcal{L}$  delivered to LHCb by a factor of 10-50. Although there were a number of possible leveling techniques available at the LHC [50], LHCb uses two quadrupole magnets to vary the overlap of the colliding beams in the transverse direction ( $y - z$ ). An algorithm is then used to ensure that the LHCb receives a constant level of  $\mathcal{L}$  during a LHC Fill. A LHC Fill is the period in which the beams are considered stable enough for use in the experiments, since, due to the imperfect vacuum, there is a natural degradation in the delivered luminosity. A comparison of the luminosity delivered to ATLAS, CMS and LHCb is presented in Figure 3.4

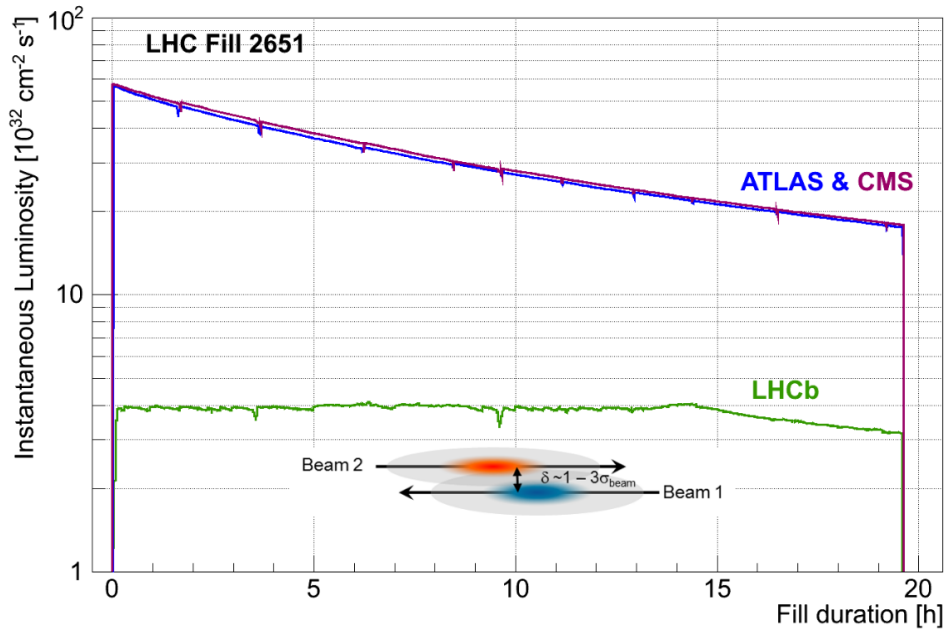


Figure 3.4: Instantaneous luminosity plot against time(hours) for ATLAS, CMS and LHCb during LHC fill 2651. Reproduced from [51].

Over six years of operation, LHCb has taken an integrated luminosity of  $9.1 fb^{-1}$  of data with the luminosity being calculated via two statistically independent methods—Beam Gas Imaging and Van der Meer scans—with a combined precision of 1.12%, making

its luminosity measurements the most precise of any bunch-beamed hadron collider [52]. A full breakdown of the luminosity and centre-of-mass energy by year can be seen in Table 3.1. Between Run I and Run II the main change was an increase of centre-of-mass energy from  $\approx 7$  TeV to 13 TeV. This increase in centre-of-mass energy led to an effective doubling of the  $b\bar{b}$  cross section in LHCb with  $\approx 1 \times 10^{12}$   $b\bar{b}$  pairs being produced in each year of Run II [53].

Year	Luminosity ( $fb^{-1}$ )	$\sqrt{s}$ (TeV)
2011	1.0	7
2012	2.0	8
2015	0.3	13
2016	1.6	13
2017	1.7	13
2018	2.1	13

Table 3.1: Integrated luminosity per year at LHCb [54].

The analysis presented in this thesis utilises data from Run II. The LGAD (Low Gain Avalanche Detector) radiation studies are based on projections of the LHCb environment after the high luminosity upgrade. Details for the aforementioned detectors that make up the LHCb experiment will now be presented as they play an essential role in interpreting the collisions within LHCb.

### 3.3 Detectors

The LHCb experiment is made up of a number of detectors that allow it to access key physics quantities. This section covers the main detector systems that make up the LHCb experiment and directly influence the analysis outputs in this thesis.

#### 3.3.1 Vertex Locator

The VELO (VERTex LOcator) is a silicon microstrip detector designed to cover the forward region of the  $pp$  interaction point. This detector was designed such that tracks within the nominal acceptance of LHCb ( $15 - 300$  mrad), cross at least 3 VELO planes. Under these conditions, the VELO is capable of reconstructing approximately 27% of all  $b\bar{b}$  produced within  $pp$  collisions in LHCb [49]. The VELO also reconstructs tracks in the backward direction to better constrain the primary vertex of the interaction.

Since  $B^0$  mesons have a comparatively short lifetime compared to the stable particles observed further down the experiment, it is important that the VELO sensors sit as close to the beamline as possible. However, while the beam is undergoing orbital corrections before a physics fill, small deviations in the location of the beam could damage the VELO sensors. As a consequence, the VELO is constructed in two halves (Figure 3.5) that can be retracted to 29 mm from the beamline until stable beam conditions are met. At that point the VELO is closed bringing the two halves together, with its aperture situated 7 mm from the beamline, and the first active components at 8.2 mm.

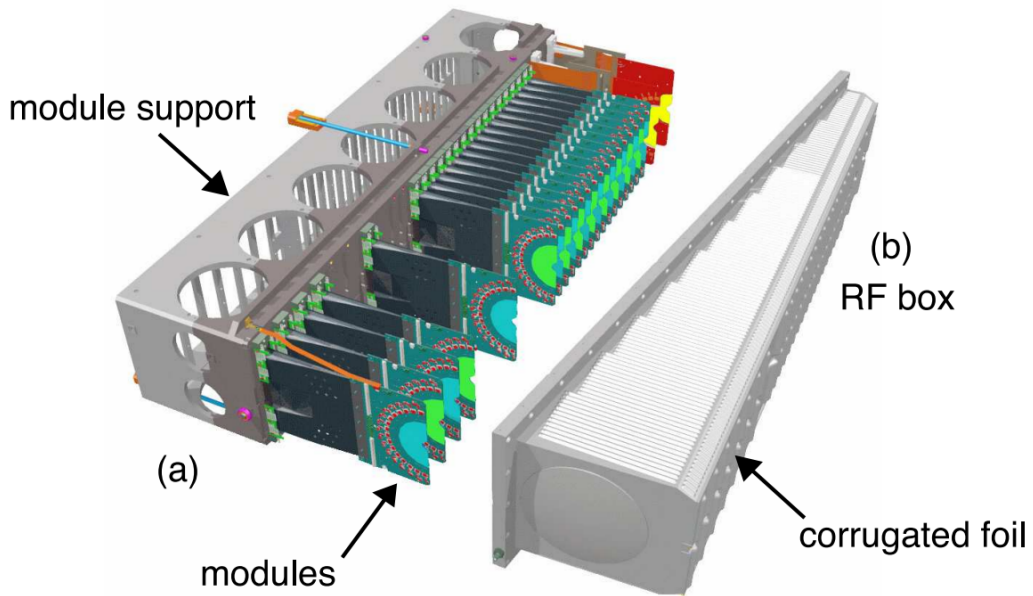


Figure 3.5: A schematic of a VELO half showing the general configuration of the modules and RF foil. Note the module spacing increases as you move away from the interaction point (back of image). Reproduced from [47].

In terms of construction, each half of the VELO contains twenty-one detector modules positioned along the beamline. These modules are then housed within an aluminium box known as the Radio Frequency (RF) box. This RF box has a two-fold purpose within the VELO detector. One purpose is to maintain a good vacuum with the beampipe, and the second is to shield the VELO from spurious electromagnetic activity from the beams. The RF box and the beampipe are separated by  $300\ \mu\text{m}$  of aluminium, which isolates the beampipe and VELO, while reducing the material between the beam and the VELO sensors. The VELO itself is held at a vacuum pressure of approximately  $10^{-7}$  mbar during operation.

Each VELO module contains two semi-circular silicon sensors implanted with aluminium micro-strips. In each plane of  $z$  that the sensor inhabits, a hit in the silicon can be assigned a value of its radial coordinate  $R$ , and its azimuth angle  $\phi$ , to be read off through the micro-strips. The pitch of the aluminium micro-strips starts at around  $40\ \mu\text{m}$  and goes up to around  $100\ \mu\text{m}$ . The purpose of this spacing is to reduce the cost and readout rate of the VELO, since a VELO with only a  $40\ \mu\text{m}$  pitch would contain nearly twice the number of channels. That being said, each VELO sensor still has 2,048 individual readout channels.

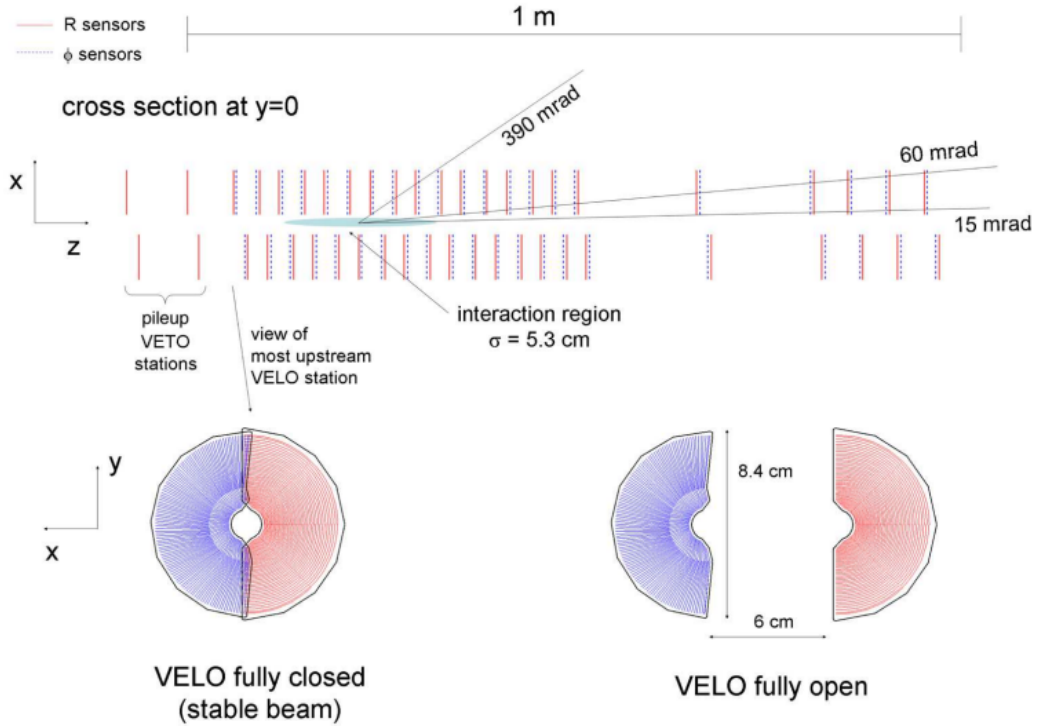


Figure 3.6: An overview of the layout of the VELO modules with the R sensors (red) and  $\phi$  sensors (blue). Reproduced from [47].

Similar to the pitch of the readout strips, the VELO modules are spaced such that there is a higher density around the primary interaction point. This has the effect that measurements of the IP (Impact Parameter) of a track are measured with approximately equal precision along the VELO. The IP is a useful parameter that quantifies the distance of closest approach of a track relative to the primary vertex. This is an important parameter for 4-body decays since low IP parameters can be used to ensure a good vertex resolution, and by extension identify better  $B_d \rightarrow \pi^+\pi^-\pi^+\pi^-$  candidates. As such, the

IP also allows us to quantify the performance of the VELO with a typical  $pp$  collisions having a resolution between 10 and  $20\mu\text{m}$  (Figure 3.7).

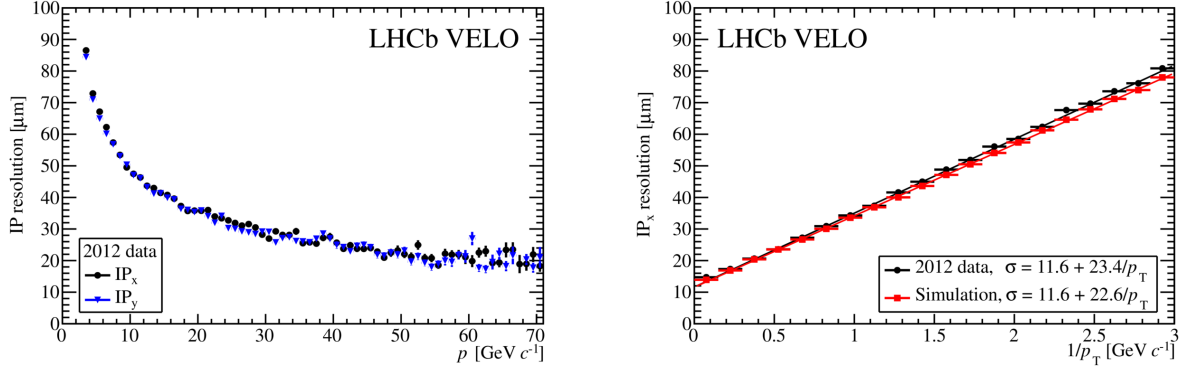


Figure 3.7:  $IP_x$  and  $IP_y$  resolution as a function of momentum (left) and  $IP_x$  as a function of  $1/p_T$  and compared with simulation (right). Determined with 2012 data. Reproduced from [47].

### 3.3.1.1 VELO Mapping Using Material Interaction

For precise measurements of secondary vertices within the VELO detector, knowledge of the material in the VELO is required to reduce the uncertainty on tracks and vertices. However, the location of VELO material differs between fills because of small misalignments during the opening and closing of the VELO. Therefore, the location of the  $pp$  collision region changes by  $\mathcal{O}(1)$  mm from year to year [55].

The VELO is aligned to account for these differences using a software-based alignment procedure that determines the location of each active VELO module (Figure 3.8) [56].

However, this alignment procedure can only take account of active sensors in the VELO so information regarding the passive structure is lost. As of 2018, an alternate procedure has been developed that creates a high-precision map of the VELO using beam-gas imaging techniques [55]. The technique uses data collected during beam-gas collisions, when the VELO is injected with helium and neon gas. As opposed to the nominal running of the detector, material interactions can then happen along the full length of the VELO. By relaxing the requirements for the primary vertex to originate from the  $pp$  interaction region, it is possible to map the VELO using only the secondary material interactions (Figure 3.9).

This high precision mapping of the VELO can then be used to weight secondary

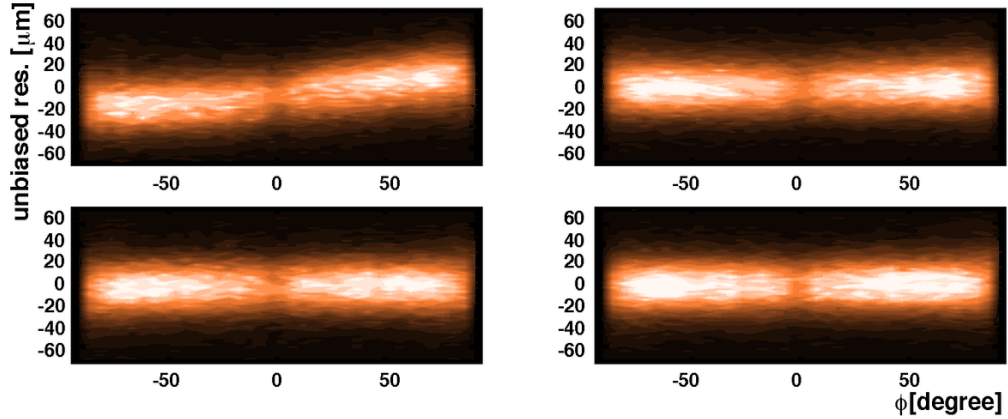


Figure 3.8: Example of unbiased sensor residuals as a function of the  $\phi$  coordinate using only the survey information (left) and using the track-based software alignment (right). Results are given for two different example sensors. Reproduced from [49].

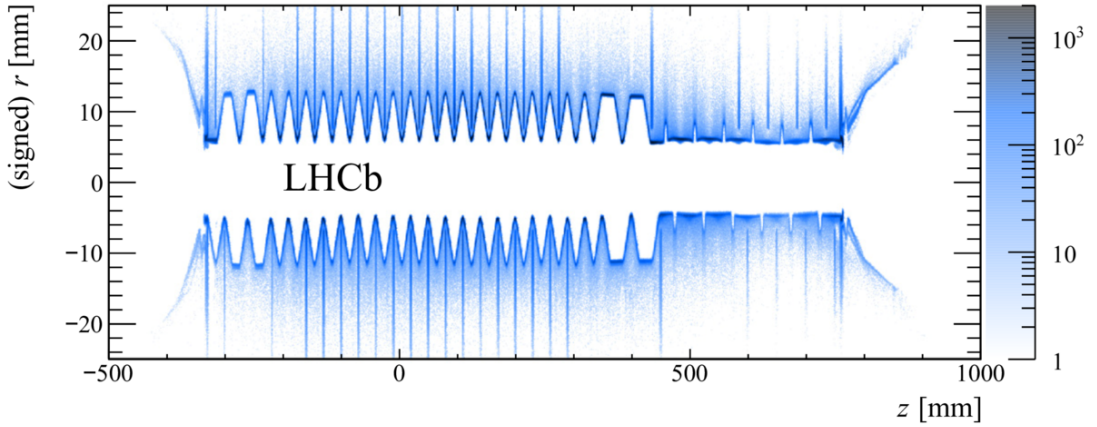


Figure 3.9: Reconstructed secondary vertices (SV) in the Run 1 data sample showing the  $zr$  plane integrated over  $\phi$ , where a positive (negative)  $r$  value denotes that the SV is closest to material in the right (left) half of the VELO. Reproduced from [55].

vertices with a likelihood of coming from a material interaction. This approach was most notably used to veto photon conversion to  $\mu^+\mu^-$  during dark photon searches at LHCb [57]. More advanced material mapping such as this will also improve the selection efficiency for short-lived resonant modes such as the  $\rho(770)$  in future analyses at LHCb.

### 3.3.1.2 Vertex Locator at High Luminosity

After the high luminosity upgrade for the LHC scheduled in 2027 there will be a yearly increase in luminosity seen in LHCb from  $2.1fb^{-1}$  up to  $\mathcal{O}(50)fb^{-1}$ . This increase in

luminosity will offer distinct challenges, both in event timing resolution and radiation hardness. The feasibility of silicon detectors with good timing resolution is explored further in the LGAD chapter (Chapter 3).

### 3.3.2 Tracking Stations

Past the VELO detector there are a series of tracking planes designed to aid the VELO in reconstructing longer tracks as they propagate through the detector [58]. There are three planar detectors downstream of the magnet known as the tracking stations (T1-T3), and one upstream, the Tracker Turicensis (TT).

The TT is composed purely of silicon. This sub-detector element is composed of 4 sub planes with a total depth of  $\approx 30\text{cm}$  per plane. The first and last sub-planes are orientated vertically whereas the intermediate planes are orientated at  $\pm 5^\circ$  from the horizontal, as seen in Figure 3.10. This sensor orientation maximises the resolution in the  $x$ -direction of the detector since this improves the momentum resolution of intersecting tracks.

Due to extreme changes of flux over the pseudorapidity of LHCb after the magnet, the tracking stations are made up of two distinct components. The first of these is the inner tracker (IT). These are situated at the centre of the tracking stations close to the beamline and are made of radiation-hard silicon strips. In order to keep hit occupancy low enough for reconstruction, these sensors have a high granularity for track reconstruction. Further out from this central region, we have the outer tracker (OT). Since the OT is further out from the beamline, the particle flux observed in this region is much lower. Hence, the OT constitutes of a cost-effective drift time detector. This detector design ultimately allows for precision measurements of track trajectory across a range of pseudorapidities. As mentioned, the inner regions of the tracking stations (T1 - T3) are similar in construction to the TT with the inner region being a silicon strip detector. As can be seen in Figure 3.11, the inner region of the tracking stations (T1 - T3) has greater horizontal coverage to account for the magnet. This orientation leads to a spatial hit resolution of  $50\ \mu\text{m}$  [59] within the inner tracker. The outer tracker elements on these planes consist of two layers of drift tubes. These tubes contain a mix of Argon and  $\text{CO}_2$  gas, which was optimised to achieve a spatial resolution of  $200\ \mu\text{m}$  and a drift time of  $50\ \text{ns}$

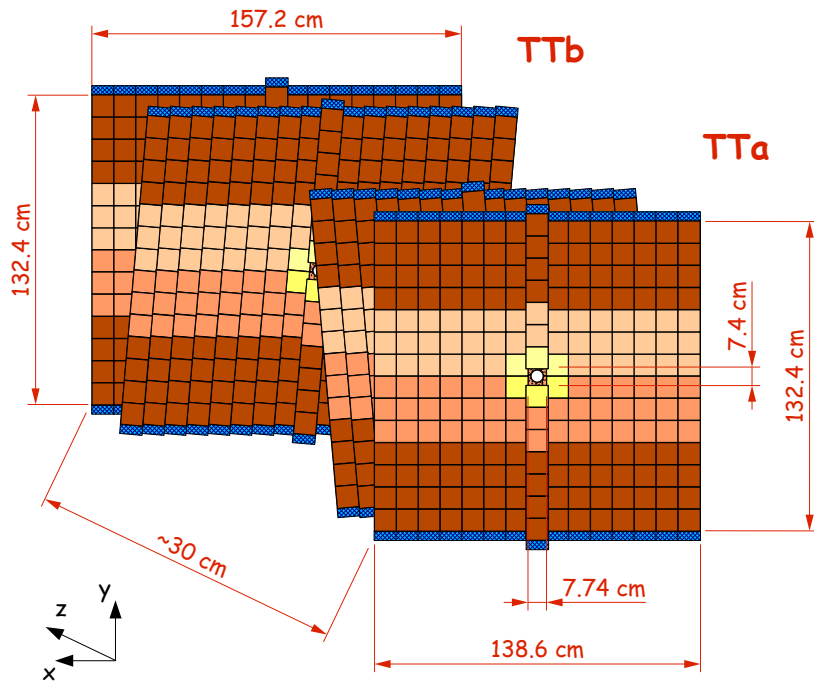


Figure 3.10: Orientation of the sub planes of the TT. Reproduced from [60].

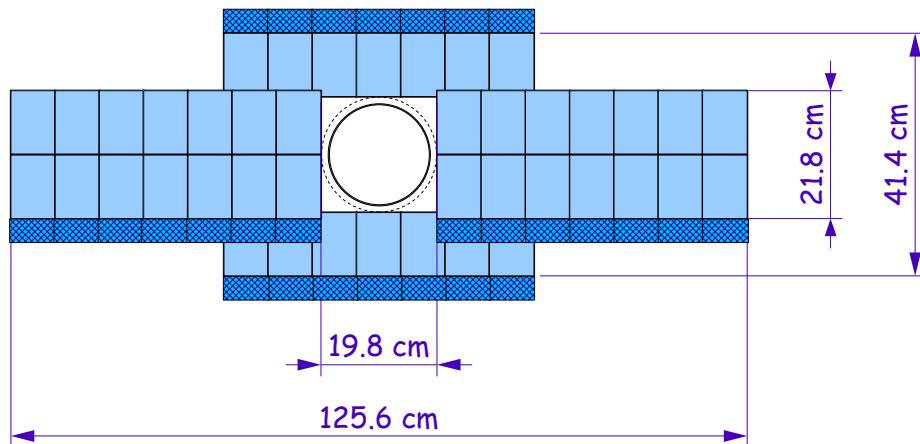


Figure 3.11: Schematic of the tracking station (T1 - T3) inner silicon tracker. Reproduced from [60].

### 3.3.3 Spectrometer Magnet

In order to identify and characterise charged particles, LHCb uses a dipole magnet to bend their tracks. This curvature, when precisely measured in the VELO and TT, allows the momentum of the particles to be determined. With the magnet and tracking detectors, LHCb has achieved a relative uncertainty on momentum resolution of 0.5% at low momentum, and 1.0% at high momentum [51]. This translates to a mass resolution of approximately  $10 \text{ MeV}/c^2$ .

The magnet itself is situated directly after the TT (Figure 3.2) 5.3 m along the beam-line. The magnet itself is composed of two 27 ton aluminium coils surrounded by an iron yoke, as can be seen in Figure 3.12. This magnet generates an integrated magnetic field of approximately 4 Tm.

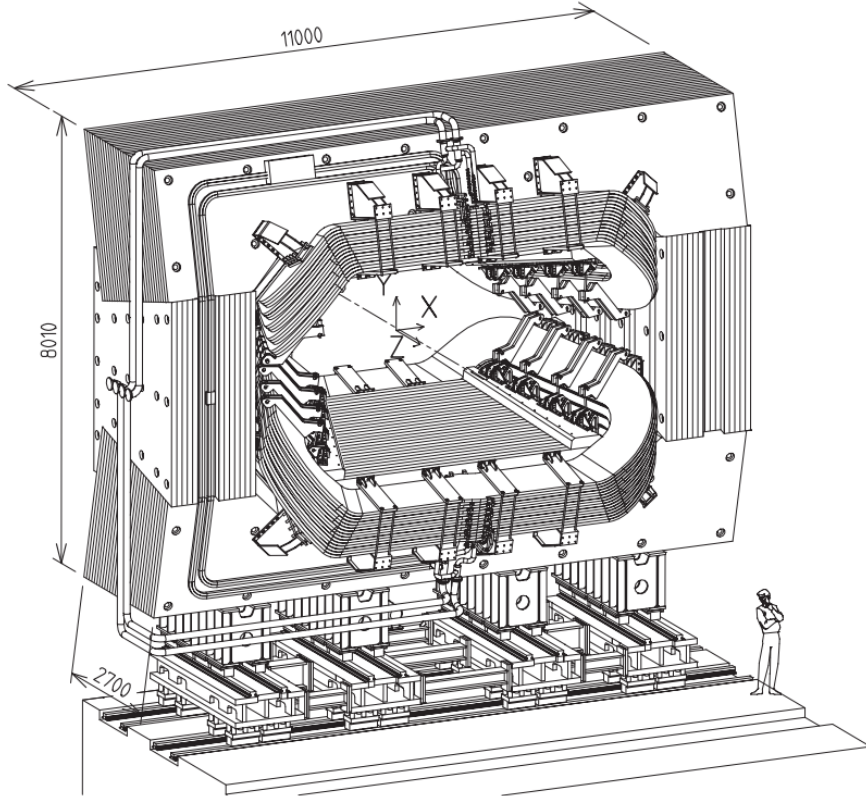


Figure 3.12: Perspective view of the LHCb magnet Reproduced from [47].

A precise knowledge of how this field evolves across the detector elements is important to ensure accurate momentum measurements. During commissioning, measurements of

the integrated field across the volume were found to give a high precision of up to  $4 \times 10^{-4}$ . However, some sensor elements such as the outer tracker drift tubes are sensitive to magnetic field distortions. In order to account for these asymmetries, LHCb takes data in two modes, either ‘MagUp’ where the field is in the  $+y$  direction, or ‘MagDown’ where the field is in the  $-y$  direction. Both of these magnet conditions are run for approximately equal periods of data taking to reduce asymmetries as much as possible.

### 3.3.4 Ring Imaging Cherenkov Detectors

In LHCb there are two Ring Imaging Cherenkov detectors, the RICH-1 and RICH-2, that provide key input to particle identification (PID) at LHCb. PID is the determination of the type of particle track that has been reconstructed by the detector. The RICH system itself is primarily used for the separation of pion, kaon and proton tracks within LHCb. The calorimeter systems HCAL (Hadron Calorimeter), and ECAL (Electron Calorimeter), in addition to the muon chambers help compliment the RICH system, but the RICH is the primary source of PID for our analysis.

Functionally, the RICH detectors use Cherenkov radiation to extract PID information. Cherenkov radiation is emitted when a charged particle travels through a medium with a velocity greater than the velocity of light in that medium. This light is produced in a cone which obeys the relation

$$\cos \theta_c = \frac{1}{n\beta}, \quad (3.2)$$

where  $\theta_c$  is the opening angle of the light cone,  $n$  is the refractive index of the incident medium and  $\beta$  is the ratio of the velocity of the particles to the speed of light in vacuum,  $v/c$ . Therefore the opening angle is intrinsically related to the particle trajectory through the detector. However, instead of thinking about the velocity, we can instead express our opening angle in terms of the particle momentum

$$\cos \theta_c = \frac{1}{n} \sqrt{1 + \left(\frac{mc}{p}\right)^2}. \quad (3.3)$$

This means that if we can measure both the particle momentum and the opening angle of the light cone we can infer the rest mass  $m$  of the particle. However, as can be seen in equation 3.3, when the momentum reaches a critical point  $p \gg mc$ , the tracks will all

have the same opening angle of  $1/n$  regardless of the rest mass of the particle. Figure 3.13 shows how depending on the species of particle, and medium of interaction, the momenta where PID can be distinguished can vary greatly. It should be noted that lighter particles saturate at a much lower momentum since  $p \gg mc$  is much lower.

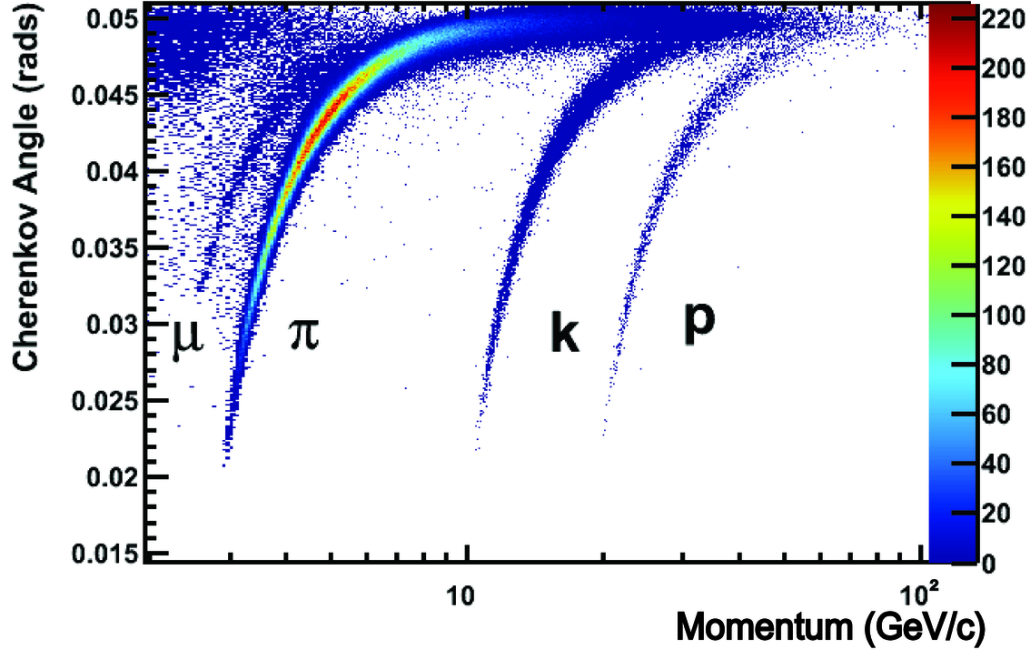


Figure 3.13: Reconstructed Cherenkov angle as a function of track momentum in the  $C_4F_{10}$  radiator of RICH-1. Reproduced from [61].

The RICH-1 and RICH-2 detectors are positioned and designed to maximise the energy range over which PID can be correctly reconstructed. The RICH-1—located between the VELO and TT—covers the full angular acceptance of LHCb, and has been optimised to resolve PID in tracks between 1 and 60 GeV. It is located before the magnet to capture low momentum tracks that could fall out of the LHCb acceptance later in the detector. RICH-2 however, is designed to cover high momentum tracks up to a maximum of approximately 100 GeV. These high momentum tracks are unlikely to be perturbed too much by the spectrometer magnet so the RICH-2 is also optimised over a smaller angular acceptance of 15-100 (120) in the vertical (horizontal) plane.

To capture particle information at different data ranges the RICH-1 and RICH-2 use different dielectrics, with RICH-1 using  $C_4F_{10}$ , and RICH-2 using  $CF_4$  gas. As a particle enters the dielectric material, light cones are produced depending on the material. These

cones are reflected via a series of flat and spherical mirrors before impacting Hybrid Photon Detectors (HPDs). Within the HPDs, the cones are imaged as rings and the expected  $\theta_c$  is calculated under the 5 available mass hypothesis ( $e, K, \mu, \pi$  and  $p$ ). The ring radius for each track is then fit to the ring imaged in the HPDs. This is done using a difference in log-likelihood method where the log-likelihood is calculated between the pion hypothesis, and the remaining mass options. Using pions as the reference point is arbitrary in this context but is the standard method used within LHCb.

In order to quantify the ability of the RICH to discriminate particles, two control channels are used. These control channels can be reconstructed purely from kinematic information. These control samples are  $D^{*+} \rightarrow D^0(K^-\pi^+)\pi^+$  for pion and kaon track reconstruction, and  $\Lambda^0 \rightarrow p\pi^-$  or  $\Lambda_c \rightarrow K^-\pi^+p$  for proton reconstruction. The PID performance of the RICH is excellent at low momentum, having efficiencies over 80% until over 60 GeV (Figure 3.14).

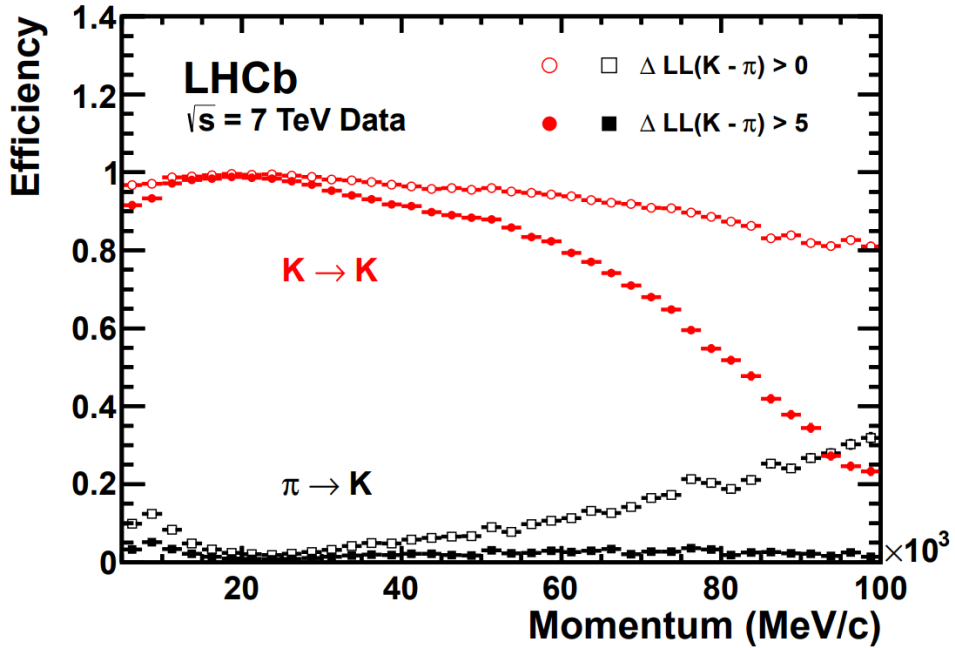


Figure 3.14: Kaon identification efficiency (red) and kaon-pion misidentification rate (black) as a function of track momentum, in GeV/c, from 2011 data. The plot was reproduced from [61]. The two  $\Delta LL$  ranges demonstrate the trade off between identification efficiency and misidentification within the RICH.

However, although the RICH has good performance in data, modelling it for simulation is a non-trivial task. This is because the refractive index of the RICH radiators has to

be averaged, since during data taking it fluctuates with pressure and temperature. As a consequence of this averaging, current Monte Carlo generated for LHCb has a different PID performance. The LHCb collaboration has developed tools such as PIDCalib [62] to correct for these differences to allow for PID variables to be used in classifiers for analysis.

### 3.3.5 Calorimeter System

Identification of electron and hadron candidates can also be achieved through the calorimetry system. The calorimetry also provides a vital input for flavour tagging, with reconstruction of prompt photons and  $\pi^0$  candidates for events. The system is composed of a scintillating pad detector (SPD), a pre-shower detector (PS), an electromagnetic calorimeter (ECAL) and finally a hadronic calorimeter (HCAL). These components when used together allow for the identification of electrons, hadrons and photons originating from  $pp$  collisions. The ECAL and HCAL are positioned just behind the first of the Muon chambers as can be seen in Figure 3.2.

One of the most demanding identifications is that of electrons within the calorimetry system. This is because the electron trigger is required to reject 99% of the inelastic  $pp$  interactions within the LHCb experiment by identifying electrons with high transverse energy. To support the ECAL in identifying electrons the PS and SPD systems are used. The PS rejects charged pions while the SPD rejects neutral pions. These systems are highly efficient, with pion rejection factors of 99.6%, 99.6% and 99.7% and electron retention rates of 91%, 92% and 97% for 10, 20 and 50 GeV/ $c$  particle momentum [47]. Figure 3.15 shows the different energy deposition between electron and pion candidates for discrimination in the ECAL.

The ECAL itself is a sampling scintillator/lead structure read out by plastic wavelength-shifting (WLS) fibres. The lead layer (2 mm) of the ECAL is used to induce electromagnetic showers that are then captured by the scintillating material (4 mm). The total depth of the ECAL is 42 cm to capture all the energy from incident photons and electrons at this stage.

The HCAL works slightly differently, being constructed of layers of iron absorbers (1 cm) and scintillating material (3 mm). The most unique part of the HCAL is that the scintillating tiles run parallel to the beam axis rather than perpendicular as in the case of the ECAL. This configuration can be seen in Figure 3.16.

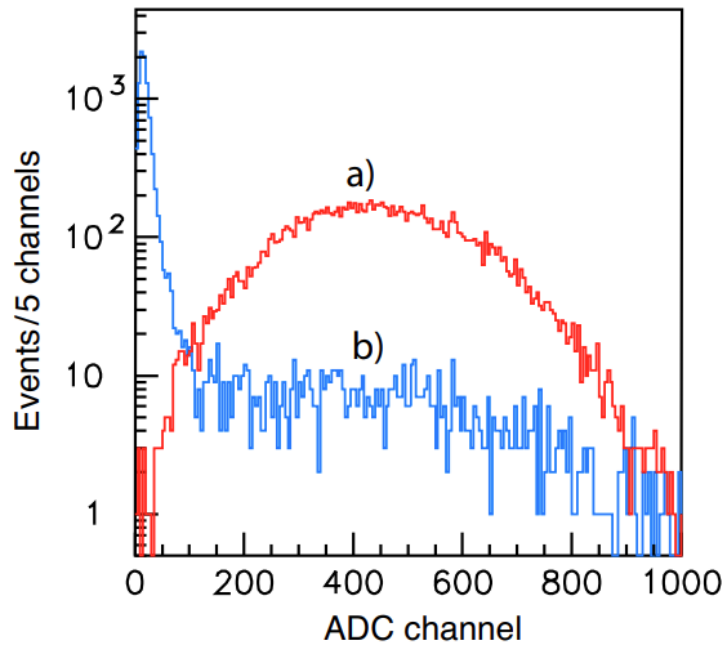


Figure 3.15: Energy deposition of (a) 50 GeV electrons and (b) pions in the PS. The plot was reproduced from [47].

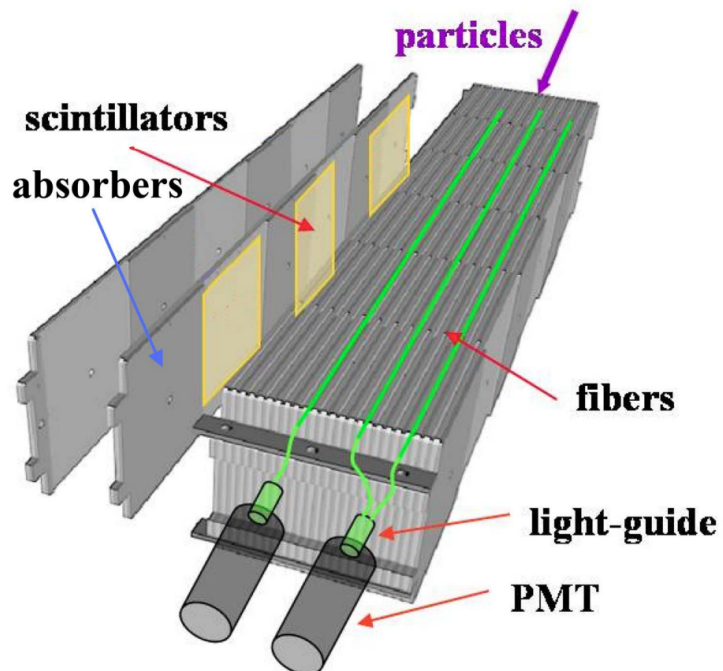


Figure 3.16: The layout of an HCAL module. Reproduced from [47].

### 3.3.6 Muon Chambers

The final system in the LHCb experiment is the muon system [47]. The muon system is an important part of the experiment, giving access to many CP-sensitive decays involving muons. However, in the context of this thesis these properties are not exploited. The muon system is used as an input to the first trigger level (L0) where high- $p_T$  muon candidates are used to identify promising events.

The muon system is comprised of five stations (M1-M5). M1 is located before the calorimeters, whereas the subsequent stations are at the very back of the detector (Figure 3.17). The full system is made up of 1380 chambers containing a mix of CO<sub>2</sub>, Ar and CF<sub>4</sub> gas. It also utilises two different detection technologies, the multi-wire proportional chambers (MWPC) and Gas Electron Multiplier (GEM) chambers.

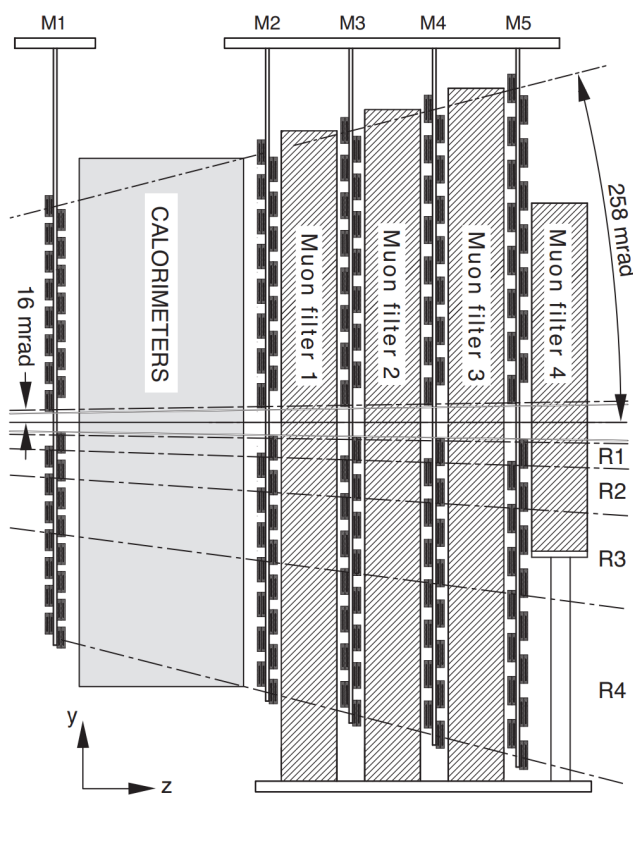


Figure 3.17: Side view of the muon system. Reproduced from [47].

The chambers in stations M2-M5 are multi-wire proportional chambers. The chambers are made of two spaced cathodes containing a gas composition of CO<sub>2</sub>/Ar/CF<sub>4</sub> (40:55:5).

Readout is achieved using gold plated tungsten wires running through the chambers. Drift time resolution is 5 ns within these chambers.

The M1 station is slightly different since it experiences much greater muon flux than the later stations. To function in this environment, the M1 stations use radiation hard Gas Electron Multiplier (GEM) chambers—in lieu of MWPC chambers—with a gas composition of  $\text{CO}_2/\text{Ar}/\text{CF}_4$  (15:45:40). These chambers are constructed with a cathode and anode surrounding three GEM foils as can be seen in Figure 3.18. The gas mixture used is less ionising which lends to the radiation hardness of this station. However, when an electron in the gas is ionised, it is multiplied by the GEM layers, and read out with a time resolution of 3 ns.

Stations M1-M3 are built with a higher spatial resolution than M4-M5 and are used to define the track direction and calculate the  $p_T$  of muon candidates in the detector. M4 and M5 are primarily built to identify penetrating particles.

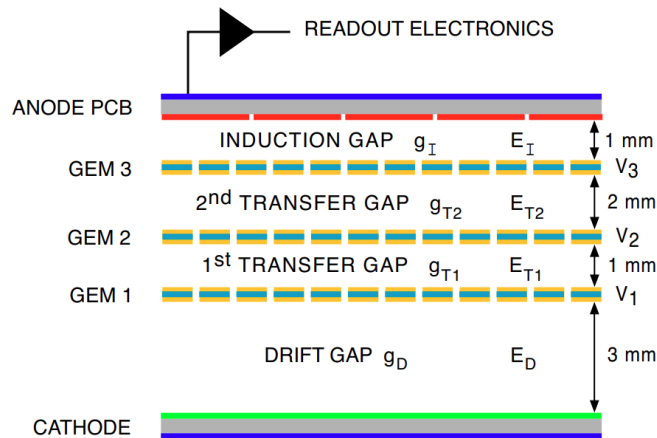


Figure 3.18: Schematic cross section of a triple-GEM detector. Reproduced from [47].

### 3.4 Triggering at LHCb

The LHC operates at a very high crossing rate, the rate at which  $pp$  collisions take place inside LHCb. During Run 2 of the LHCb experiment a rate of around 40 MHz was achieved at the interaction point. For LHCb only  $\approx 25\%$  of these crossings contain Beauty or Charm events that would be of interest for flavour analyses. However, that being said,

to record all this data would be overwhelming for both the detector and permanent storage available to the experiment. Therefore, the LHCb experiment needs to reduce its data rate while maintaining the greatest amount of physics data. This is done using a three-level trigger with a hardware trigger followed by two high-level software triggers [63]. It should be noted for completeness that this discussion is only relevant for Run 1 and 2 of the LHCb detector as Run 3 will be using a software-only trigger system.

The first trigger is the Level-0 hardware trigger that reduces the data rate from 40 MHz down to 1 MHz which can be handled by the software triggers. This translates to the hardware trigger vetoing approximately 97% of inelastic  $pp$  collisions. The hardware trigger makes decisions using the VELO, calorimeters and muon systems. The L0 trigger uses the following properties in order to decide whether an event should be retained. The first of these are measurements of  $E_T$ , Transverse Energy, in the calorimeters with only high energy events being kept. The L0 also checks for the presence of at least 2 high  $p_T$  muons in the muon chambers. This is because high  $E_T$  and  $p_T$  indicate the likely presence of heavy flavour events. Finally, the L0 vetoes events with extremely high track multiplicity since these events are difficult to reconstruct within the LHCb software. These decisions are made in the front-end electronics by the L0 Decision Unit (L0DU). Events that pass the L0 then go to the High Level Trigger stages.

The first high-level trigger stage (HLT1) (Figure 3.19) is implemented in the software package MOORE [64]. This software is run on the event filter farm, which is where the L0 triggered outputs are transferred. HLT1 uses simple reconstruction algorithms to confirm that the hits identified by the L0 represent particles that pass the L0. It primarily does this by matching tracks seen in the VELO and reconstructing neutral candidates (photons and neutral hadrons) in the absence of tracks. This first level of the software trigger reduces the input rate to the second high-level trigger by approximately 90%, on top of the L0 output, with a rate of 30 kHz, and 110 kHz, for Run 1 and 2 respectively.

The second high-level trigger (HLT2) (Figure 3.20) takes the HLT1 output and then performs a more advanced reconstruction taking into account all the detector information available to the event. These full reconstructions make use of the software package DAVINCI. HLT2 trigger lines make use of topological, and loose particle identification information, to determine whether an event is likely to contain a decay path of interest. Every event is passed over by all the inclusive and exclusive trigger lines and is saved if it passes any HLT2 triggers. The final output of these trigger decisions reduces the data

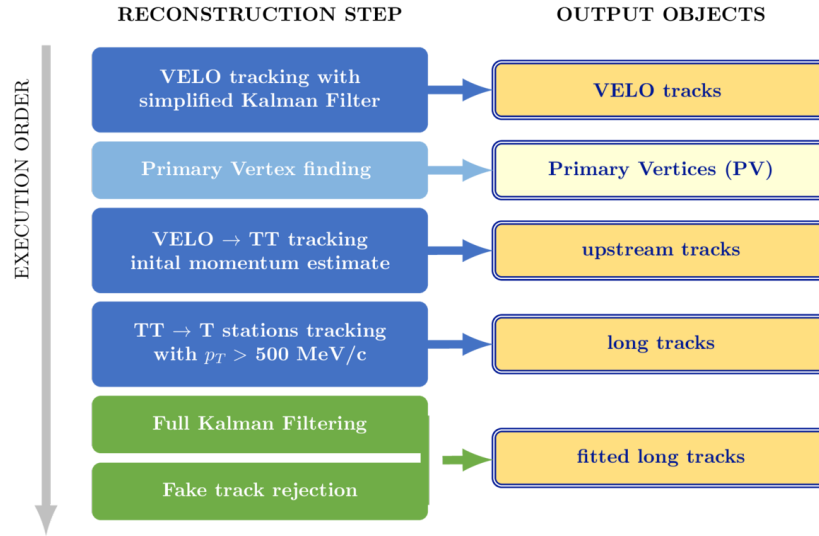


Figure 3.19: HLT1 track and vertex reconstruction [63].

rate to a manageable 5kHz/12.5KHz for Run 1 and 2 respectively. For understanding rates for branching fraction measurements it is possible to inspect what line combinations were passed by each event saved at LHCb.

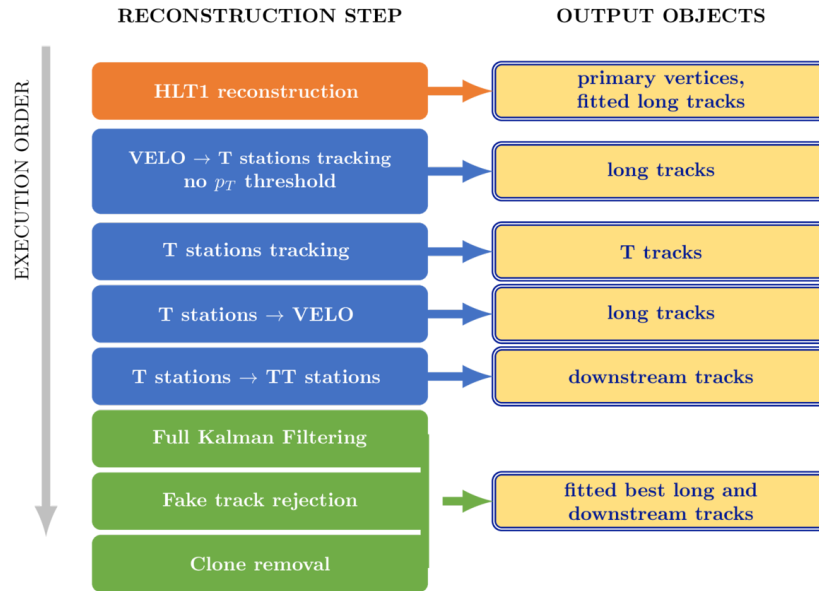


Figure 3.20: HLT2 track and vertex reconstruction [63].

## 3.5 Offline Processing

Data that has been selected by the trigger system is written to durable tape storage devices and stored offline. These file objects contain all the relevant detector and trigger information needed to fully define an event. However, this is still a long way from anything that can be used in physics analysis. In order to process the data and provide extra information, such as PID and track reconstruction, to the analyst the BRUNEL package is used [65]. BRUNEL runs over the raw hit and cluster data and constructs vertex and track objects. This process is much more robust than in the online trigger taking inputs from detector alignment, and running the most up to date versions of the reconstruction algorithms. Along with PID information, from the RICH discussed above, and this track information, BRUNEL saves these fully reconstructed particles to file. However, since BRUNEL takes up to 2 seconds per event it is run infrequently over the whole dataset, and only when stable updates to the reconstruction are released. In order to save on disk space and simplify analyses, BRUNEL outputs are filtered using HLT2 into more useful data streams for analysts. This process is called stripping and is the final stage of data processing before analysis.

Once these tracks and clusters have been grouped, and high level reconstruction has assigned the relevant stripping flags, they can be processed by DAVINCI [66]. DAVINCI is an offline analysis tool that reconstructs BRUNEL events under different decay descriptors. This software allows the user to apply cuts and decisions unique to their analysis and to reconstruct data under various hypotheses to understand systematic issues that may arise in the analysis.

## 3.6 Simulation

In order to validate and train our models in preparation for real data, the LHC uses various Monte Carlo generators. Using these generators it is possible to produce large samples of particle decays without having to deal with the complexities of QCD. This is important since most of the relevant decay amplitudes of interest are currently just too complex, or are intrinsically non-perturbative to model analytically.

The LHCb experiment uses the MC generator PYTHIA [67] inside the GAUSS [68] framework, which contains the full GEANT4 [69] simulation of the LHCb experiment.

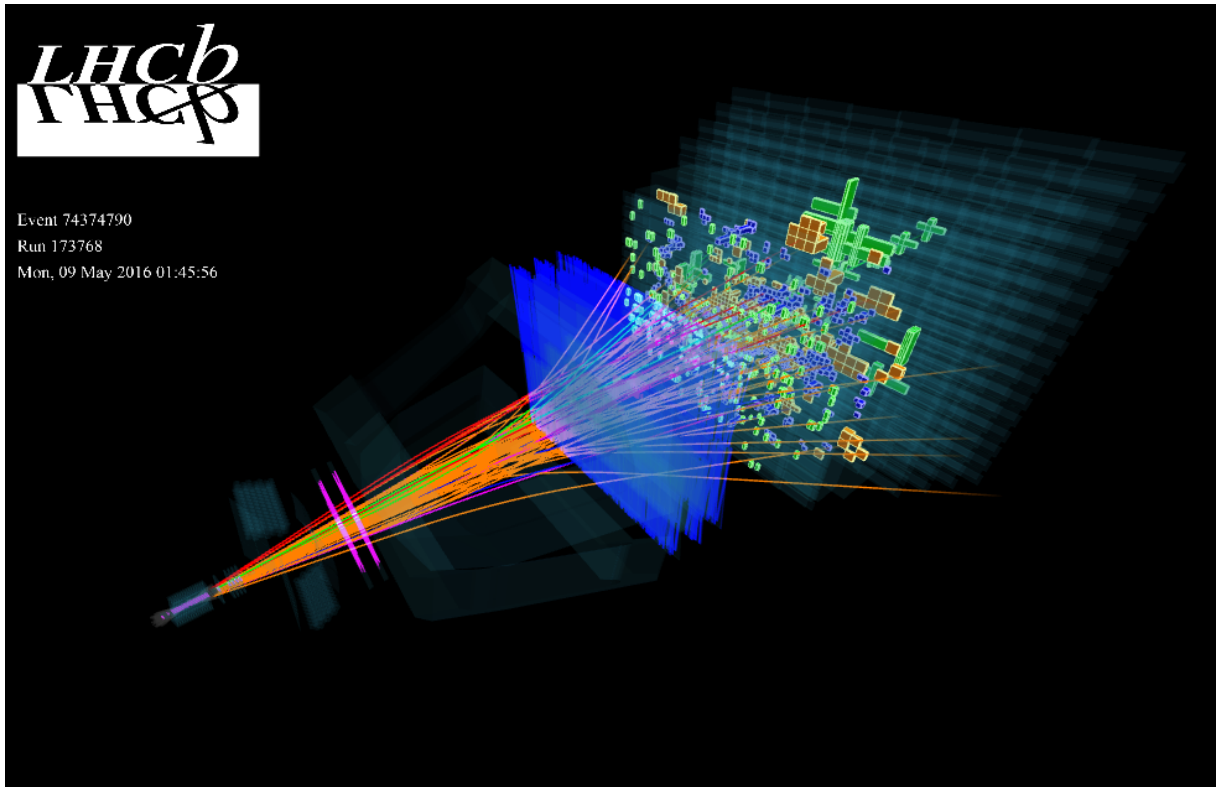


Figure 3.21: LHCb Event Display reconstructing a real event using the GEANT4 framework. Image provided by CERN.

Events from PYTHIA are further specified with EVTGEN [70] allowing the analyst to define characteristics of the decay. In the context of this thesis we use a specific EVTGEN model to produce flat-phase space data for efficiency training. Any extra final state radiations are generated by the PHOTOS [71] package, although this package is unused in the analysis presented as no final state radiation is reconstructed. These events are then digitised using the BOOLE package creating hits in a virtual detector. An example of a real event projected in the GEANT4 LHCb can be seen in Figure 3.21.

By generating accurate  $pp$  collisions in this way, LHCb analyses can use these Monte Carlo simulated collisions for a number of applications. For example, they allow for the optimisation of particle selection, and for the calculation of experimental efficiencies within the detector. Both of the above uses are applied to this analysis.

## 3.7 Chapter Summary

Access to flavour physics parameters is only made possible through the use of the LHC and LHCb machinery. This chapter has outlined the mechanism by which proton collisions are sustained and recorded within the LHCb experiment. Extra care has been taken to describe the operational and mechanical characteristics of the VELO, future developments of which are discussed in the subsequent chapter.

# Chapter 4

## LGAD Simulation

Right or wrong, it's very pleasant to  
break something from time to time

---

Fyodor Dostoevsky

Detector development is a vital area of physics research, enabling analysts to access areas of physics that have been previously unreachable by experiment. Advancements in accelerator physics have unlocked the opportunity to explore particle interactions at energy frontiers and with luminosity unseen by earlier HEP physics experiments. But to access this new scale of physics we need to develop new technologies to survive the environment and return usable data for future analyses.

In this chapter we will cover the basics of semiconductor detector technologies before moving on to specific simulation studies for a new silicon detector technology called LGADs (Low Gain Avalanche Detectors). These studies will be separated into electrostatic and transient simulations for clarity of presentation.

In this chapter, to compare radiation sources, radiation damage is scaled using the non-ionising energy loss (NIEL) [72]. The NIEL allows the physical fluence  $\phi_{phys}$  to be converted to the neutron equivalent dose, which is denoted as  $\phi_{eq}$ , and that is benchmarked against a 1 MeV neutron. For the duration of the chapter it should be assumed that all fluences are given in  $\phi_{eq}/\text{cm}^2$ .

## 4.1 Motivation

Silicon detectors - without dwelling too much on their history - have seen a wide array of applications within experimental particle physics. Silicon detectors can offer high spatial resolution and high ionisation over short distances when compared to gaseous detectors. These properties have seen this technology widely used in inner detector structures across CERN.

Ultra fast silicon detectors will be a cornerstone of the upgraded experiments at the high-luminosity LHC (Large Hadron Collider). As part of future upgrades, the LHCb experiment will see an integrated luminosity increase to  $\mathcal{O}(50)\text{fb}^{-1}$  per year, leading to increased ambiguity in vertex resolution. The LHCb VELO (VERtEX LOcator) (see previous chapter) identifies the best candidate for the PV (Primary Vertex) by minimising the impact parameter of all possible track configurations from a given event.

Recent studies of the upgrade 2 environment predict poor performance, with PV misidentification rates of up to 20%. This is primarily due to the poor timing performance of the upgrade 2 VELO, which has timing performance  $\mathcal{O}(25)\text{ns}$  [73]. To reduce this misidentification LGADs (Low Gain Avalanche Detectors) are being developed for use in the VELO with timing resolution of order  $\mathcal{O}(50)\text{ps}$  [74]. Early studies predict that silicon detectors with timing resolution in the range 50–100 ps used in the inner most layer of the VELO can reduce misidentification to  $\sim 5\%$ . The simulations presented in this chapter are to determine whether LGAD can be segmented suitably using oxide trenches to fulfil this use case and if the technology can operate at the fluences predicted during Run V of the LHCb experiment ( $1 \times 10^{16} \phi_{eq}$ ). The technology proposed in this chapter would be installed during LS4 (Long Shutdown 4), which is currently scheduled to take place in 2031.

## 4.2 Silicon Detectors

Silicon is a versatile material with a number of core properties that make it ideal for applications in high energy physics [75]. The first of these is that, compared to other semiconductor materials such as diamond, it has a low ionisation energy,  $\mathcal{O}(4)\text{eV}$ , making it sensitive over large energy ranges. It also has a reasonable bandgap of 1.12 eV at 300 K which opens up the opportunity for room temperature operation. It should be noted that

this energy band is temperature dependent and varies with the equation,

$$E_g(T) = 1.17 - \frac{(4.73 \times 10^{-4})T^2}{T + 636}, \quad (4.1)$$

where  $T$  is the temperature. Silicon can also be grown in crystal orientations that reduce radiation damage. From crystal orientations given by the Miller indices of the crystal seeds denoted as  $(h,k,l)$  there are 3 primary orientations of crystal. These orientations are  $\langle 100 \rangle$ ,  $\langle 110 \rangle$  and  $\langle 111 \rangle$ , which can be seen in Figure 4.1. These configurations can change the electrical characteristics of the device and in general only  $\langle 100 \rangle$  and  $\langle 111 \rangle$  are used in HEP applications since they are more radiation hard when compared with  $\langle 110 \rangle$  silicon [76].

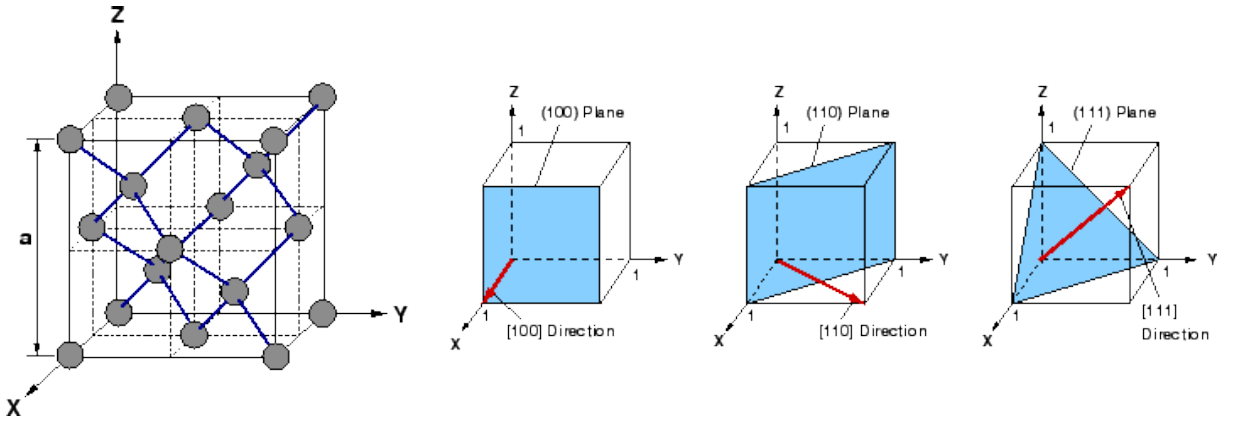


Figure 4.1: Silicon Miller index orientations for HEP, reproduced from [77].

### 4.2.1 The p-n Junction

In order to discuss the general transport mechanisms at play in silicon detectors, it is now important to understand how these act with respect to the p-n junction, a fundamental building block of these detectors. n-type semiconductor materials are materials that have been *doped* with donor impurities such as boron, while p-type are doped with acceptor impurities such as phosphorus. In order to understand the interplay between these materials we must discuss how this junction performs at thermal equilibrium.

### 4.2.1.1 Thermal Equilibrium

At the transition between n-doped and p-doped material through diffusion, some of the charge carriers will diffuse across the boundary due to the difference in concentration between the regions. Recombination over this boundary with free carriers *depletes* this region. A depletion zone is formed where acceptor and donor ions are left without their respective free charge carriers. In this region an electric field will build directly counter-acting this diffusion. This diffusion can then be characterised by a built-in voltage defined as

$$V_{bi} = \frac{kT}{e} \ln \left( \frac{n_{0,n} p_{0,p}}{n_i^2} \right) \approx \frac{kT}{e} \ln \left( \frac{N_D N_A}{n_i^2} \right), \quad (4.2)$$

with  $n_{0,n}$  being the electron concentration on the n-doped side,  $p_{0,p}$  being the hole concentration on the p-doped side and  $n_i$  being the intrinsic carrier concentration. In the case of complete ionisation of donors and acceptors in this region, the electron and hole concentrations can be substituted for the concentration of donors and acceptors,  $N_{D,A}$ .  $V_{bi}$  in this situation is the difference in Fermi potential between the doped materials (Figure 4.2).

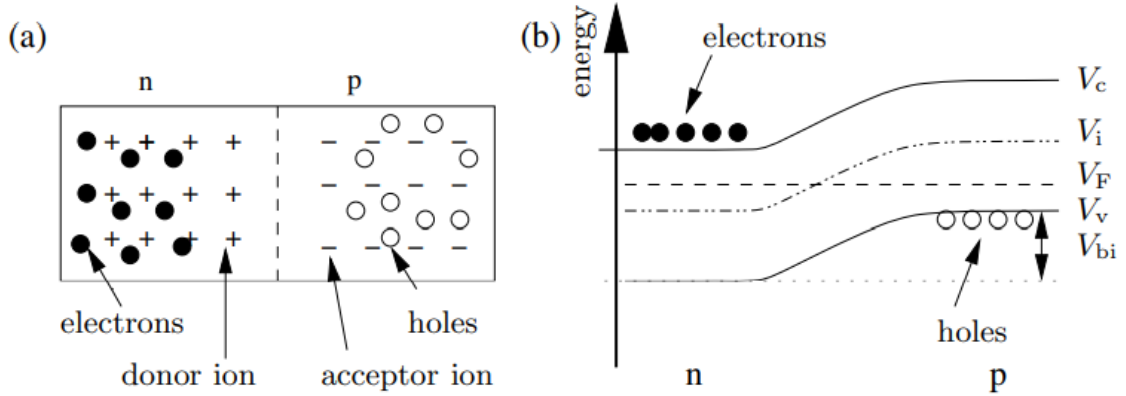


Figure 4.2: Schematic illustration of a p-n junction (a) and its band diagram to illustrate built-in voltage. Reproduced from [78].

### 4.2.1.2 Reverse Bias

In order to use the semiconductor device as a sensor, a further voltage is applied in the same direction as the built-in voltage. This reverse bias continues to extend the space

charge region. For convenience, in this section we define the reverse bias as positive. The total width of the depletion region—for the case of an abrupt p-n junction—can be calculated as

$$W = x_n + x_p = \sqrt{\frac{2\epsilon_0\epsilon_{si}}{e} \left( \frac{1}{N_A} + \frac{1}{N_D} \right) (V + V_{bi})}, \quad (4.3)$$

where  $W$  is the total width of the depletion zone,  $x_{n,p}$  are the widths of the n and p sides,  $\epsilon_{0,si}$  are the electric permittivities of the vacuum and silicon, and  $V$  is the reverse bias voltage. In most cases it is feasible to assume that on a boundary  $N_A \gg N_D$  and that  $V \gg V_{bi}$ . Under these conditions the width is simplified to

$$W = x_n = \sqrt{\frac{2\epsilon_0\epsilon_{si}}{eN_D} V}, \quad (4.4)$$

which is widely used to estimate the depletion depth at various voltages. LGAD devices (Figure 4.10) can be simplified into two independent zones to deplete; a bulk of lightly doped silicon and a highly doped multiplication implant. As such, we expect to see depletion of the bulk silicon at  $\approx 10$  V and a second depletion at  $\approx 50$  V for the multiplication implant. For exact measurements of the depletion voltage for actual devices,  $CV$  (Capacitance/Voltage) measurements are used since at full depletion the volume current no longer increases. Hence, by measuring the p-n diode as 2-conductive plates separated by a depletion zone of width  $W(V)$  we can plot two distinct regions,

$$C(V) = \frac{\epsilon_0\epsilon_{si}}{W(V)} \approx \begin{cases} \sqrt{\frac{\epsilon_0\epsilon_{si}N_D}{2V}}, & \text{for } V < V_{depletion}, \\ \frac{\epsilon_0\epsilon_{si}}{d}, & \text{for } V > V_{depletion}, \end{cases} \quad (4.5)$$

where  $d$  is the sensor thickness. The full depletion voltage is at the intersection between these regions.

## 4.2.2 Carrier Transport and Multiplication

Semiconductor devices primarily work by an interplay of several transport mechanisms that move free charge through the device. The most important three of these are drift, diffusion and impact ionisation, which will now be discussed.

#### 4.2.2.1 Drift

Although electrons in a semiconductor at thermal equilibrium have some motion—due to scattering from lattice and impurities—in the absence of an electric field  $E$  the net movement of charge carriers in a semiconductor is zero. In this scenario the average time between collisions can be thought of as a mean free time,  $\tau_c$ . However, in the presence of an electric field these charge carriers will start to *drift* in relation to the field. Since the electrons in this field will experience a force equal to  $-qE$  the electrons will acquire some average drift velocity that can be defined as,

$$v_n = - \left( \frac{q \cdot \tau_c}{m_n} \right) E = -\mu_n E, \quad (4.6)$$

$$v_p = - \left( \frac{q \cdot \tau_c}{m_p} \right) E = \mu_p E. \quad (4.7)$$

Here the equations have been presented in terms of electron drift velocity  $v_n$  and hole drift  $v_p$  respectively, where  $q$  is the electron charge,  $m_n$  is the effective mass of the electron,  $\mu_n$  and  $\mu_p$  are the electron and hole mobilities, and  $m_p$  is the effective hole mass.

#### 4.2.2.2 Diffusion

Diffusion is the process by which, given some gradient in the charge concentration, charge carriers will prefer to move between high concentration and low concentration regions. This effect will naturally spread the distribution of charge carriers over time and is called diffusion. The diffusion current per unit area can be defined as

$$\mathbf{J}_{n,diff} = -D_n \nabla n = -\frac{kT}{e} \mu_n \nabla n, \quad (4.8)$$

$$\mathbf{J}_{p,diff} = -D_p \nabla p = \frac{kT}{e} \mu_p \nabla p, \quad (4.9)$$

where  $\nabla n$  and  $\nabla p$  are the gradient of electron and hole concentrations respectively. The diffusion constant  $D_{n,p}$  is related to the mobility of charge defined via the Einstein equation  $D_{n,p}/\mu_{n,p} = kT/e$ . This process is independent of any electric field induced in the device.

### 4.2.2.3 Impact Ionisation

Once the electric field in a device reaches a high enough level, *avalanche processes* can occur in the device where carriers have sufficient energy to create electron-hole pairs without external input. In terms of its mechanics, if we have a free electron in the conduction band of our lattice then, given a strong enough electric field (inducing a high enough drift velocity), it can transfer energy to an electron in a valence band such that it becomes excited to the conduction band—that is free to drift itself. This ionisation of an electron from the conduction to valence band, creates a new electron-hole pair. The acceleration of this new charge carrier can then lead to an *avalanche* of free electrons in the conduction band. In order for this impact ionisation process to occur, the required kinetic energy of the process is given by [79]

$$E_0 = \frac{1}{2}mv_s^2 = 1.5E_g, \quad (4.10)$$

where  $m$  is the mass of the charge carrier,  $v_s$  is the saturation velocity and  $E_g$  is the minimum energy to produce an electron hole pair. However, this is with the assumption that the carrier masses are the same, and that there is no bandgap. In reality the bandgap increases the minimum energy with electrons and holes needing  $3.2E_g$  and  $4.4E_g$  respectively due to varying saturation velocities and effective masses [80]. The electron-hole generation rate itself is defined as,

$$G = \alpha_n n \mu_n + \alpha_p p \mu_p, \quad (4.11)$$

where  $\mu_{n,p}$  is the electron (hole) mobility as before, and  $(n, p)$  is the species density. The ionisation rates  $\alpha_{n,p}$ , are very sensitive to electric field changes with high fields lowering the ionisation threshold. This is one of the key factors contributing to device breakdown.

## 4.2.3 Detector Operation

Silicon detectors for use in HEP are operated under reverse bias conditions, where the depletion region of the device will be either several micrometers as in the case of Silicon Photomultipliers (SiPM), or the entire device structure as in the case of Low Gain Avalanche Detectors (LGAD), depending on detector structure. The proposed LGAD detectors would be operated in the full depletion mode. For a LGAD under full depletion

there will always be an electric field present across the device that will contribute to the carrier transport mechanisms previously mentioned. Inside a HEP detector, particles or photons will impact the device and deposit some or all of their incident energy, depending on the parameters of the detector creating electron-hole pairs. These pairs will drift across the detector with drift velocities  $v_n$  and  $v_p$  to the anode and cathode respectively, with the transient current generated being described by Ramo's theorem [81]

$$i = E_v q v_{n,p}, \quad (4.12)$$

where  $q$  is the charge of the electron or hole,  $v_{n,p}$  is the drift—or instantaneous—velocity of the electron or hole and  $E_v$  is the component of the electric field acting in direction  $v$  that would exist assuming the following conditions.

- The electron is removed.
- The electron is raised to unit potential.
- All other conductors in the system are grounded.

If the entire energy of the particle is deposited in the detector, then from this transient current measurement it is possible to recover the incident particle energy. However, in the case of LGAD—which is a tracking sensor—we are more interested in rapidly resolving hits that penetrate the whole sensor.

#### 4.2.4 LGAD

LGADs are a new fast timing detector being developed across several institutions first proposed by CNM (Centro Nacional de Microelectronica) and Giulio Pellegrini [82]. In principle they are similar in design to Avalanche Photodiodes (APD), but have a significantly lower gain of  $\mathcal{O}(10)$  as opposed to  $\mathcal{O}(100)$ . This is desirable as higher gain detectors are more prone to sensor noise, and are often difficult to segment due to cross talk, reducing their ability to discriminate true signal at high luminosity. As such, the ideal operating mode of an LGAD is with a gain of  $\approx 10$ , and a time resolution of  $\approx 30$  ps. The latter of these two properties comes from the unique combination of a uniform drift region, and high field avalanche region, which gives the signal a very fast rising edge.

LGADs were primarily developed from studies completed at CNM, and were fabricated to overcome issues faced when operating traditional p-in-n silicon detectors under heavy

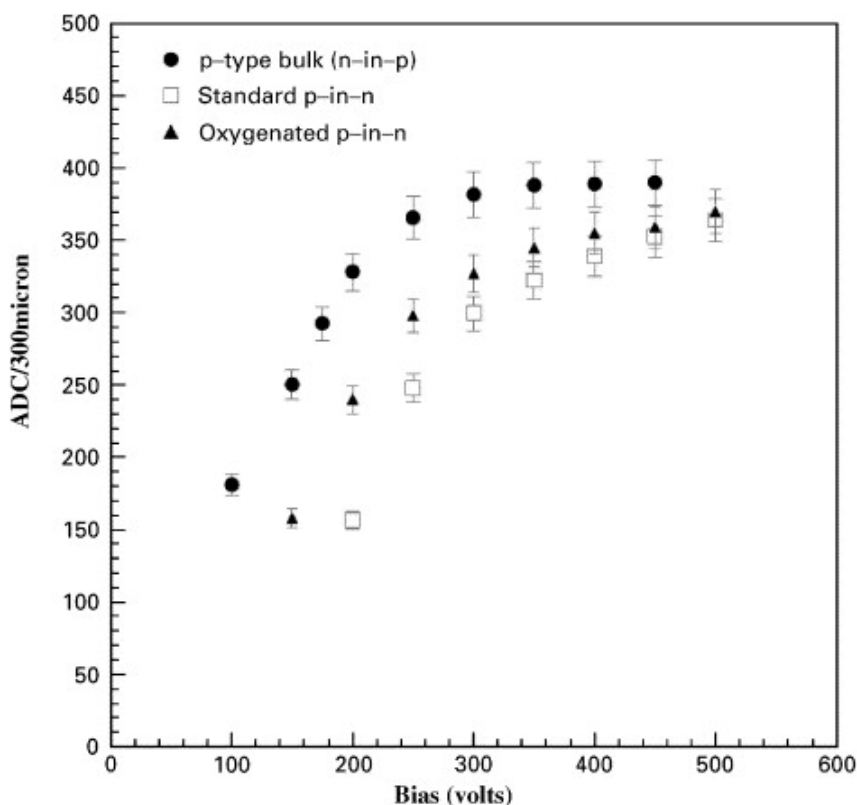


Figure 4.3: Comparison of CCE between n-in-p detector (non-oxygenated p-bulk), oxygenated and non-oxygenated p-in-n detectors. Reproduced from [83].

hadron radiation [84] [83]. One of these is the *type inversion* of n-type silicon after exposure to fluences of approximately  $10^{13} \phi_{eq}/\text{cm}^2$ . This type inversion changes the charge collection regions of the detector. A possible modification to the device to overcome this is to use a p-type bulk that will not invert under these conditions. Similarly, embedding the n-type implant in a heavily doped p-implant can generate large electric fields, which reduces the expected trapping, and by extension, the overall damage to the profile [83]. This property can be observed in Figure 4.3, where after being irradiated to a fluence of  $3 \times 10^{14} \text{cm}^{-2}$ , charge collection in the n-in-p case remained higher than all n-type bulk samples.

This more radiation-hard structure was implemented in the first generation of LGAD devices. These devices were  $50 \mu\text{m}$  pad sensors, with a substrate depth of  $300 \mu\text{m}$  (Figure 4.4). The deep  $n^+$  region, where the + denotes a high doping concentration, is present to reduce breakdown at the pad edges. The effectiveness of different pad isolation techniques is discussed later in the chapter.

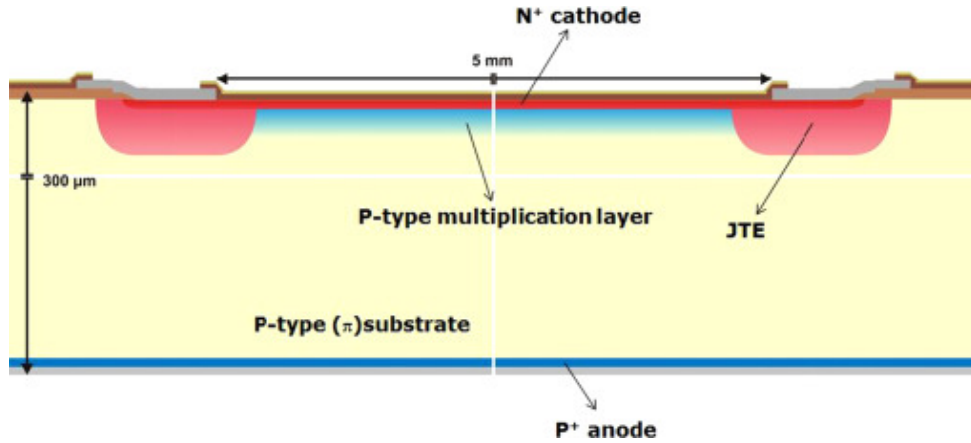


Figure 4.4: Schematic cross-section of the LGAD pad design. Reproduced from [82].

These devices formed the basis of initial testing to understand performance of LGAD devices. Investigating charge collection at different fluences, these devices were irradiated to a fluence of  $2 \times 10^{15} \phi_{eq}/\text{cm}^2$ . Up to this fluence limit it was observed that the multiplication factor of the devices was severely inhibited (Figure 4.5). Simulation of charge recovery in highly irradiated LGAD devices is discussed later in this chapter with relation to recent device designs.

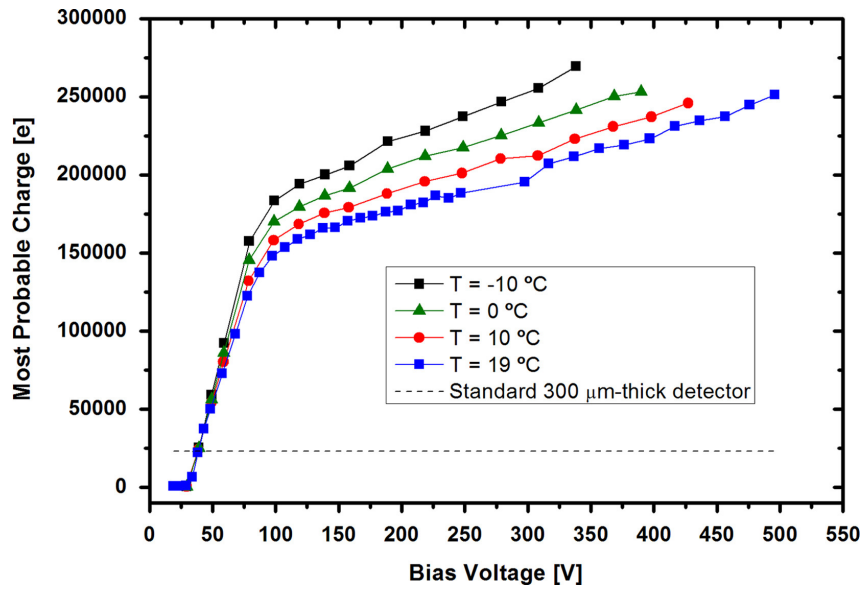


Figure 4.5: Measured absolute collected charge as a function of the applied bias for a LGAD sample irradiated to different fluences. Reproduced from [82].

Another device consideration is the noise level of a detector. In tightly segmented,

high gain detectors, noise is a significant issue. It contributes not only to the detection of spurious signals but can reduce resolution through cross-talk. This is much reduced in low gain detector systems where the general noise response is much lower. As can be seen in Figure 4.6, when compared to non-multiplying (no gain) detectors even when irradiated, LGADs have a low and consistent noise profile making them good candidates for HEP applications.

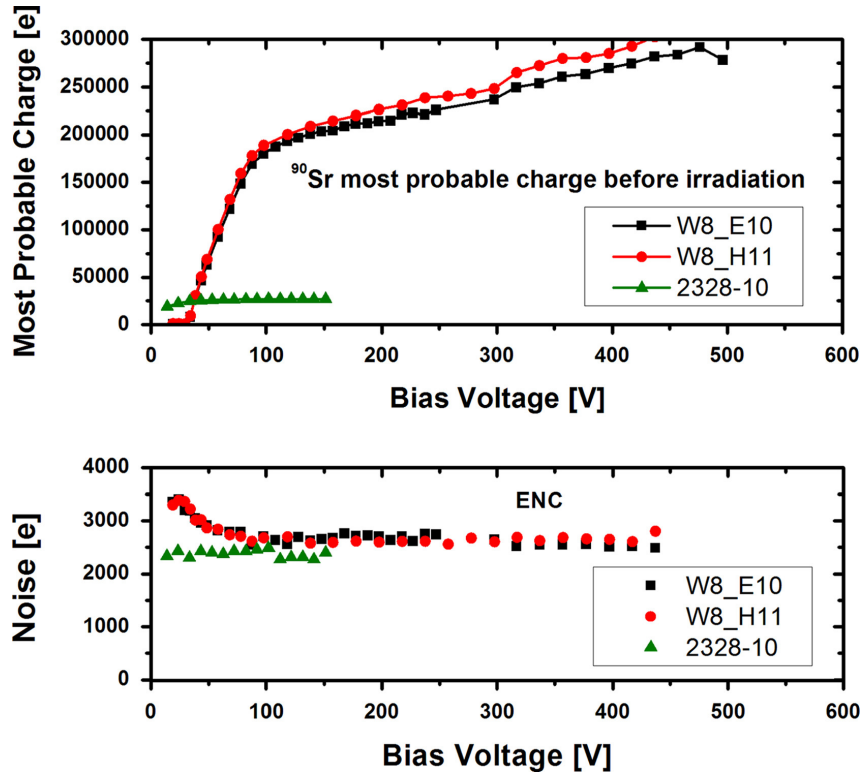


Figure 4.6: Absolute collected charge (up) and noise (bottom) signals for two LGAD samples after Sr-90 source MIPs exposure. Measurements are compared with the response of a conventional non-multiplying pad diode (2328-10). Reproduced from [82].

From these early studies LGAD technology has continued to be refined with new designs; looking to increase granularity and radiation response. Specifically, much work has gone into understanding the inter-pixel region of LGAD devices. This has culminated in a body of simulation work comparing the response for various oxide and p-stop combinations. As can be seen in Figure 4.7, a wide variety of designs were investigated to understand how intrinsic properties such as fill-factor, gain and breakdown vary with different terminations.

This is where the current body of work picks up, seeking to understand edge effects of

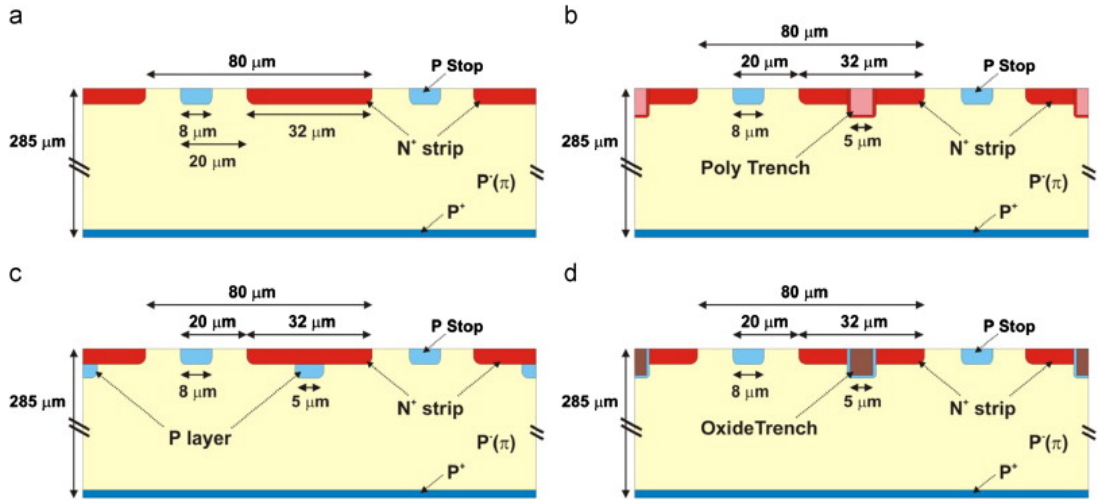


Figure 4.7: Schematic view of the pixel structures studied in this work. (a) Conventional p-type stripped detector. (b) “Polytrench” variation, including a polysilicon trench, doped with phosphorus, along the centre of the strip pitch. (c) “P-layer” variation, including a p-type diffusion below the  $N^+$  electrode; (d) “OxideTrench” variation, including an oxide filled trench along the centre of the strip and a p-type implantation through the trench. Reproduced from [85].

the device in addition to the inter-pixel region, and continuing to expand the simulation base of how LGAD devices respond in irradiated environments.

### 4.3 Electrostatic Simulation

For the development of LGAD devices for use in LHCb Run V—which is the intended installation point for this technology, a body of electrostatic simulations was carried out to model device edge effects. Previous studies looked primarily at pixel isolation investigating both JTE (Junction Termination Extension) and trench isolation techniques between pixels [86].

A JTE is a deep  $n^+$  type implant that extends through the multiplication layer. The operating principle of this implant is that it allows for control of the peak surface and bulk electric fields at the pixel edges [87]. This reduction of the field at the device edge, reduces the risk of unwanted breakdown. In order to approximate the doping profile of the JTE implant, we use sparse data from a Scanning Capacitance Microscopy (SCM) scan [88], supplied to the University of Glasgow group by Micron Semiconductors Ltd, and a fit using a sum of Gaussian functions of the form

$$\sum_{i=1}^n N_i \exp\left(-\frac{(x - \mu_i)^2}{2(\sigma_i)^2}\right), \quad (4.13)$$

where  $n$  is the number of Gaussian contributions,  $N_i$  is the fraction of that contribution,  $\mu_i$  is the contribution mean and  $\sigma_i$  is the contribution variance. This strategy was conducted using  $n = 3$  to produce Figure 4.8. This was used in the TCAD<sup>1</sup> simulations to fully define the JTE.

Oxide trench termination (Figure 4.9) is the other main termination method to be modelled. The operating principle of the trench is to reduce the *dead* area between pixels, where either no charge collection or multiplication takes place. The general concern with this type of termination is that it will reduce breakdown due to sharp electric field changes at the interface. However, there is a large body of research suggesting that this is not the case, with oxide trench devices breaking down in excess of 500 V [86].

In order to validate the core performance of proposed LGAD devices, these termination techniques were used in a variety of combinations at the edge of the devices. In contrast to previous studies this means that, rather than the device continuing into another pixel, it terminates into the undoped silicon. The following subsection looks into several design

---

<sup>1</sup>TCAD refers to Sentaurus Device [89], an advanced multidimensional device simulator capable of simulating electrical, thermal, and optical characteristics of silicon-based and compound semiconductor devices. Devices in this thesis are represented in the simulator as a ‘virtual’ device whose physical properties are discretized onto a nonuniform ‘mesh’ of nodes.

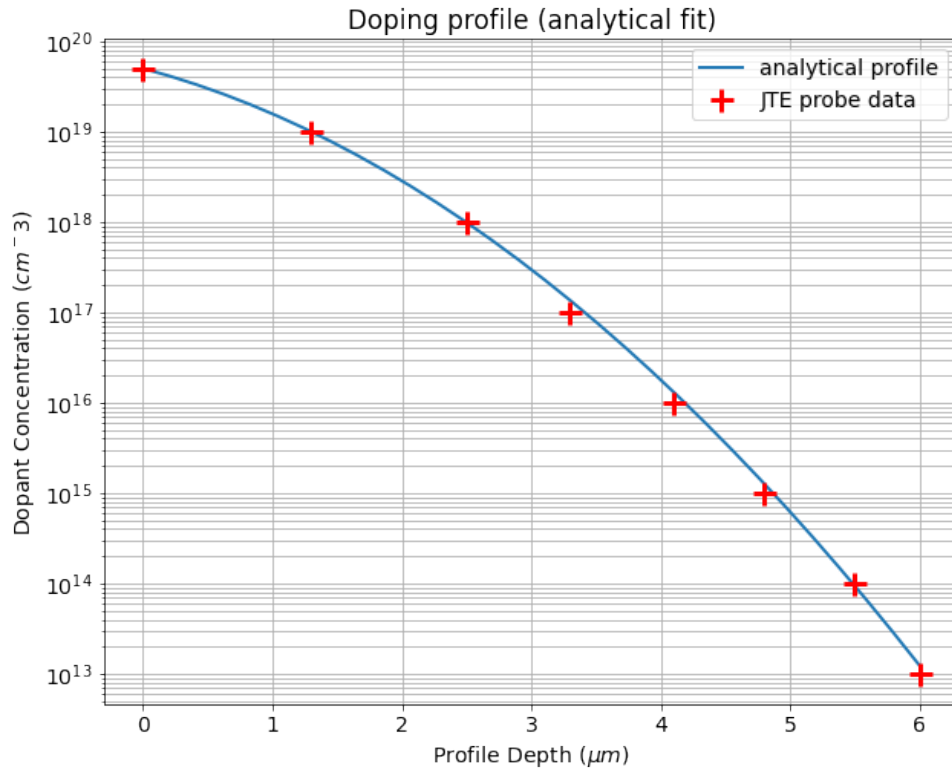


Figure 4.8: JTE probe dopant concentration fit with a sum of Gaussian functions used to approximate the JTE structure in TCAD simulations.

combinations and their outputs.

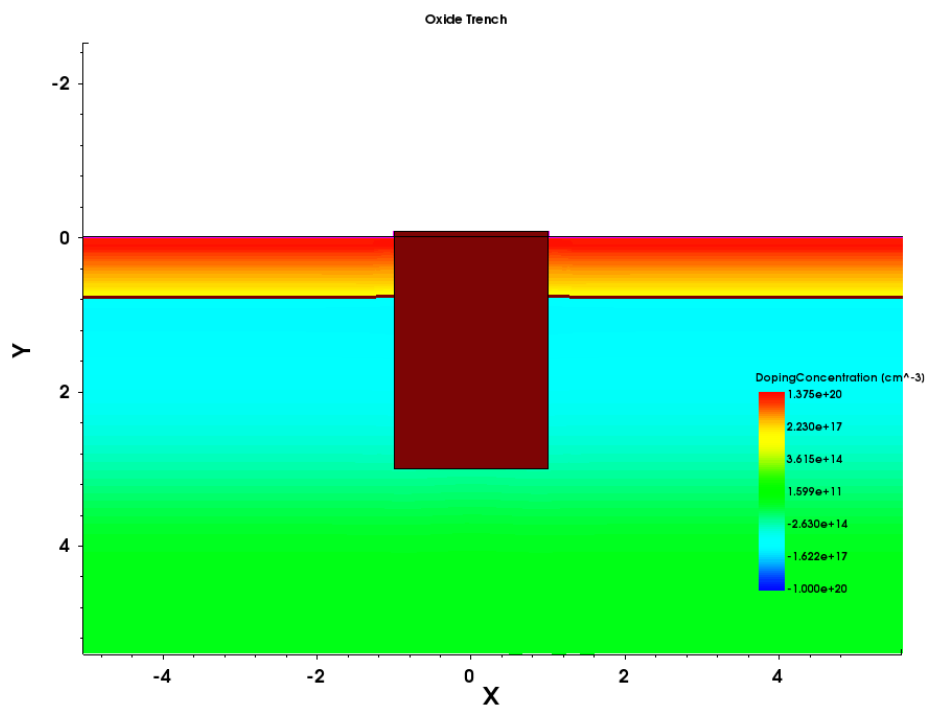


Figure 4.9: Oxide trench used in an inter-pixel region.

### 4.3.1 Device Design

Along with modelling the termination objects used in the LGAD design, a general device simulation needed to be constructed to investigate edge effects. Figure 4.10 represents one of the final designs used in transient simulations. It should be noted that guard ring simulation has been omitted due to computational limits.

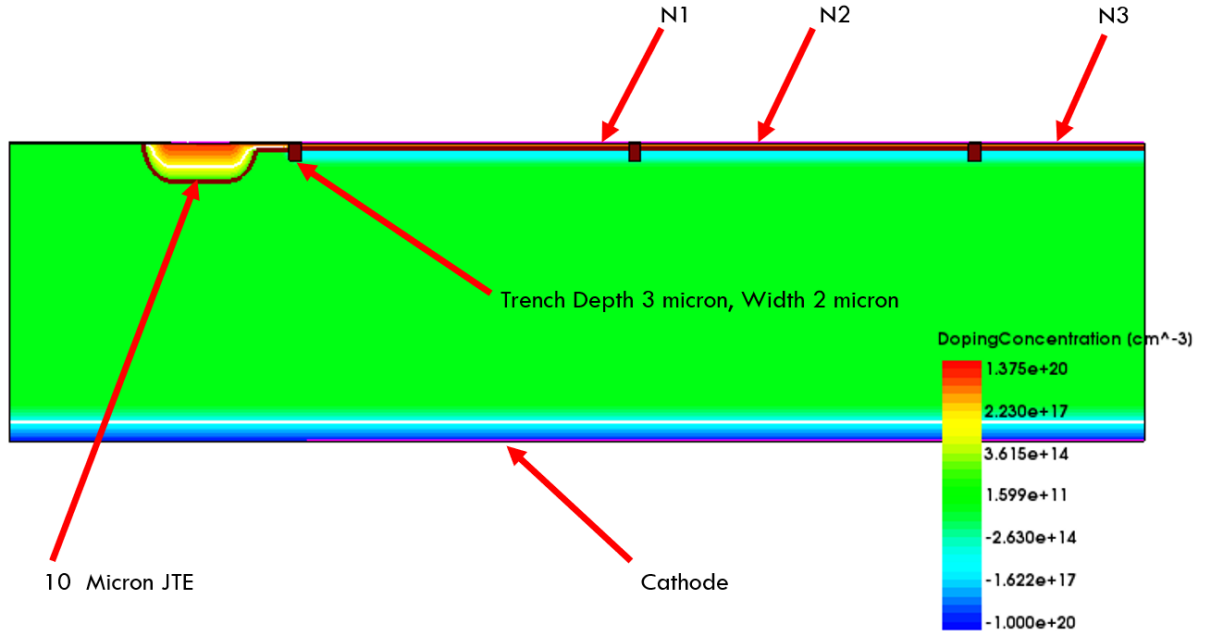


Figure 4.10: Doping profile for a general LGAD device using both JTE and oxide trench termination for use in electrostatic and transient device simulation. N1, N2 and N3 each represent individual pixels.

However, to appreciate the unique doping profile of an LGAD device ( $n^{++}, p^+, p^-, p^{++}$ ) and its effect on charge collection, it is more instructive to view its electric field characteristics at breakdown. In this regime it can be seen that the LGAD has a distinct high field region due to the  $n^{++} \rightarrow p^+$  profile. This region is known as the multiplication region and responsible for the  $\mathcal{O}(10)$  gain in the device. This differs from the PiN diode which lacks the secondary  $P^+$  implant and as such has unitary gain. Comparison between these device types can be seen in Figure 4.11.

These doping profiles and field simulations form a key input into the electrostatic and transient simulations detailed beyond this point in the chapter.

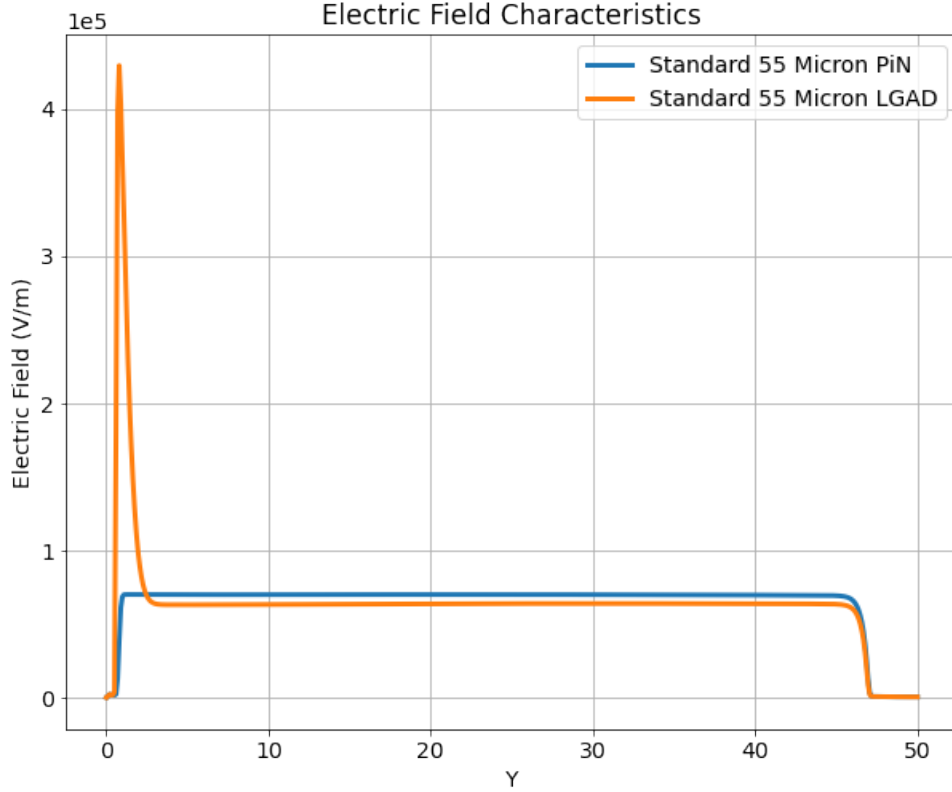


Figure 4.11: Electric field simulations at 320V for an LGAD device and a PiN Diode. Simulated in TCAD [89].

### 4.3.2 Breakdown Scans

Device breakdown is characterised by a sudden, almost exponential rise in the current across the device often referred to as an avalanche current. This occurs when the electric field across the device becomes strong enough to spontaneously ionise electrons. Further impact ionisation—as discussed prior—from these electrons then leads to a dramatic increase in current. This can be characterised by running  $IV$  scans over simulated devices, as can be seen in Figure 4.12.

In order for the gain to remain proportional to the incident signal it is important to operate the device below this threshold. Prior studies have already found that for both JTE (Junction Termination Extension) and Trench terminated devices that breakdown happens at around 400 V for a  $50\ \mu\text{m}$  device [90]. However, this study has not taken place at the wafer termination beyond which there are no further  $n^+$  implants. In order to fully quantify and investigate whether we expect any edge effects, studies have been completed

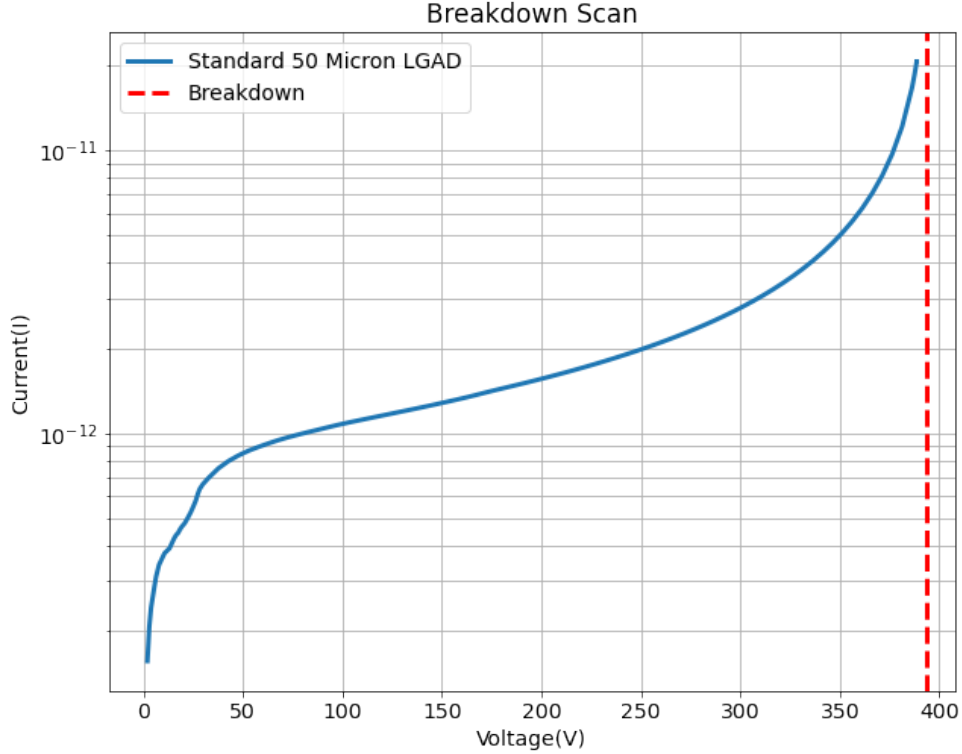


Figure 4.12: Breakdown Scan of a simulated LGAD device. The device design has a generic  $50\ \mu\text{m}$  thickness. The dashed line indicates the estimated point of device breakdown. Simulated in TCAD [89].

over a variety of edge structures (Figure 4.13).

These edge structures can be classified into two broad groups and these are.

- **JTE Characteristics**—The JTE can either be biased with a centrally bonded anode in the same way as a traditional pixel (floating) or alternatively covered in oxide. The offset of the JTE from the final trench termination can also be varied.
- **Trench Characteristics**—The trenching of the device can be varied in both depth width and whether it forms part of the final device termination.

With this in mind, electrostatic simulations were carried out using TCAD [89] on various configurations, to assess the breakdown characteristics of the designs. Many of the models used to describe the electrostatic behaviour are native to TCAD. However, some extensions were implemented from Ref. [91] for consistency between electrostatic and transient results. The electrostatic simulation was carried out in the following way. The pixels N1, N2 and N3 had a target DC bias of 1000 V set at 248 K. A scan was then

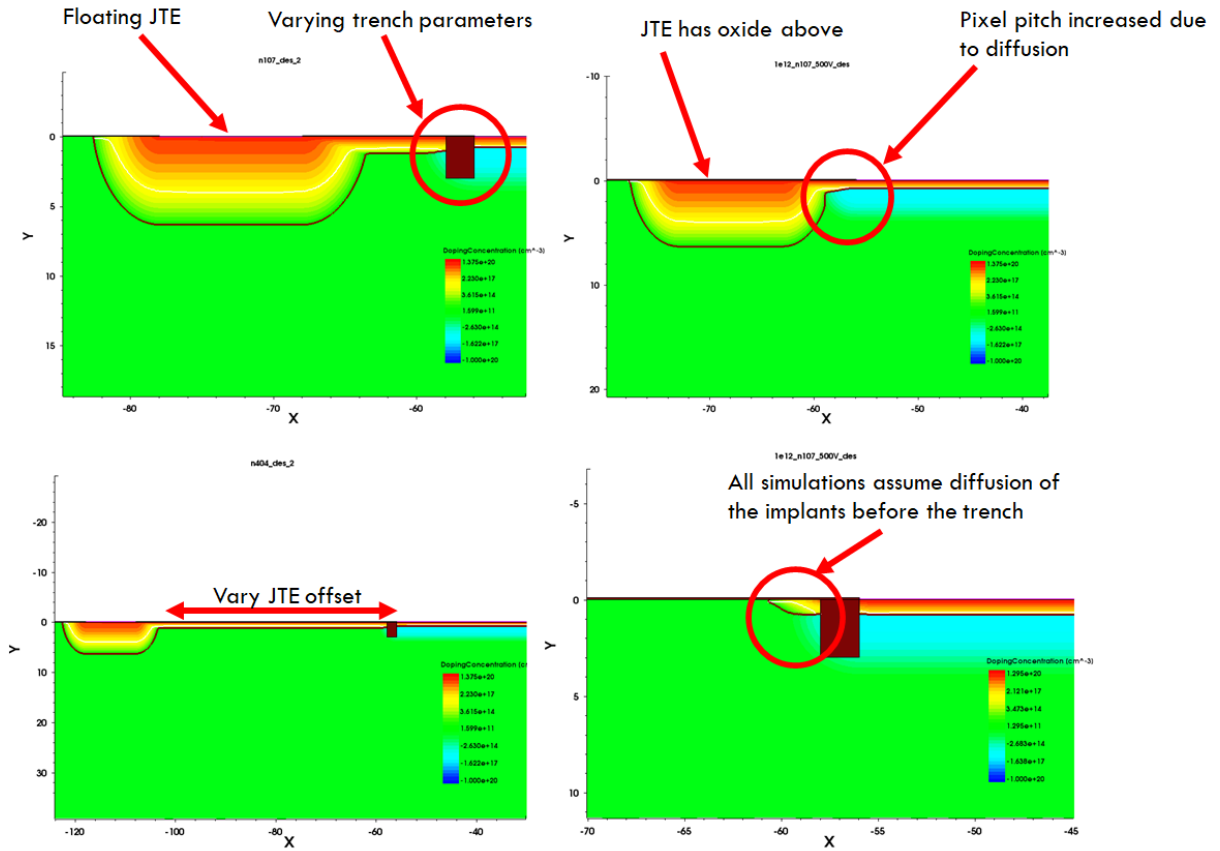


Figure 4.13: Sample of LGAD termination scenarios: floating JTE (top left), oxide covered JTE with no termination trench (top right), variable JTE offset (bottom left), terminated with only a trench (bottom right). Simulated in TCAD [89].

carried out towards this target with a current break point at  $6 \times 10^{-8}$  A to account for the exponential current increase at breakdown. The resulting  $IV$  scans were checked across pixels N1 and N2 to ensure similar breakdown characteristics regardless of termination method. Figure 4.14 shows the scan with a floating JTE where the current across the JTE was also monitored for stability.

Looking across the other main configurations with this method showed consistent device behaviour regardless of termination method (Figure 4.15). The exception to this was the device without a JTE. In this configuration, although breakdown was unaffected, the pixel N1 showed a higher leakage current at low bias. This is likely due to undepleted  $p^+$  that extends beyond the trench boundary.

Trench parameters were then varied with the general device design specified in Figure 4.10. This was to assess the trench parameters, independent of the device termination.

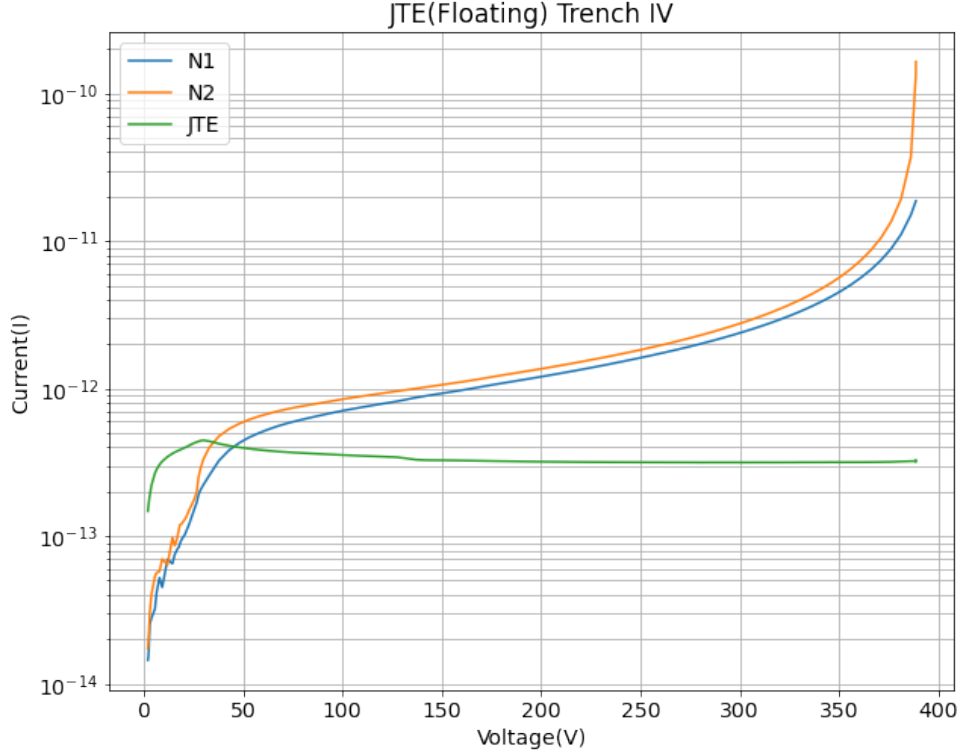


Figure 4.14: *IV* Scan of a simulated LGAD device with floating JTE and oxide trench termination. The breakdown is consistent between pixels N1 and N2. Simulated in TCAD [89].

From this, both trench width and depth were varied. From breakdown scans it became apparent that the device breakdown was relatively independent of the trench parameters for reasonable dimensions (Figure 4.16). Further studies of these characteristics would be of value after irradiation to investigate surface charge effects with different oxide depths.

### 4.3.3 Electrostatic Summary

From the electrostatic simulations that were carried out, consistent behaviour was observed regardless of the termination conditions. It was also observed that trench parameters had little to no effect on breakdown characteristics. However, given the increase in leakage current, and change in characteristics between pixels N1 and N2 in the *No JTE* case it was decided that the next generation of physical wafers should be inclusive of a JTE. This decision has also influenced the subsequent transient simulations that were carried out, with the design specified in Figure 4.10. In terms of future electrostatic stud-

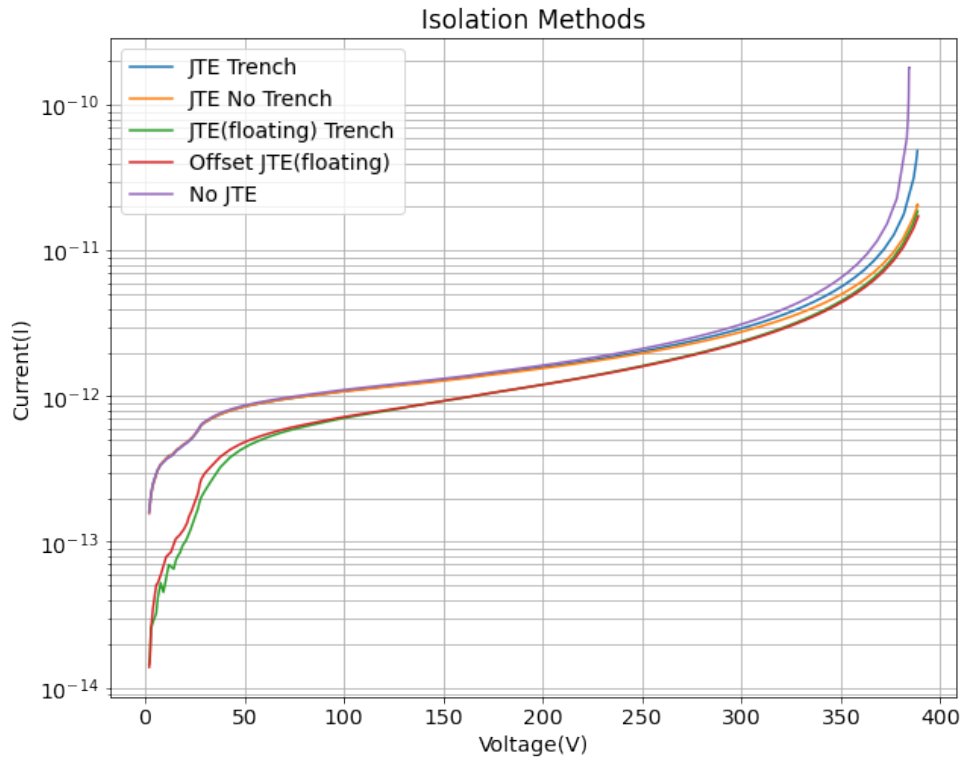


Figure 4.15: Comparison of main termination configurations across edge pixel N1. Trench parameters were kept constant between termination modes for meaningful comparison. Simulated in TCAD [89].

ies, comprehensive studies and comparisons to the next physical wafers manufactured at Micron Semiconductors Ltd could confirm the simulated behaviour. Beyond this study, investigations into the effect of trench parameters on irradiated device breakdown would be the next step in defining a full description of LGAD devices.

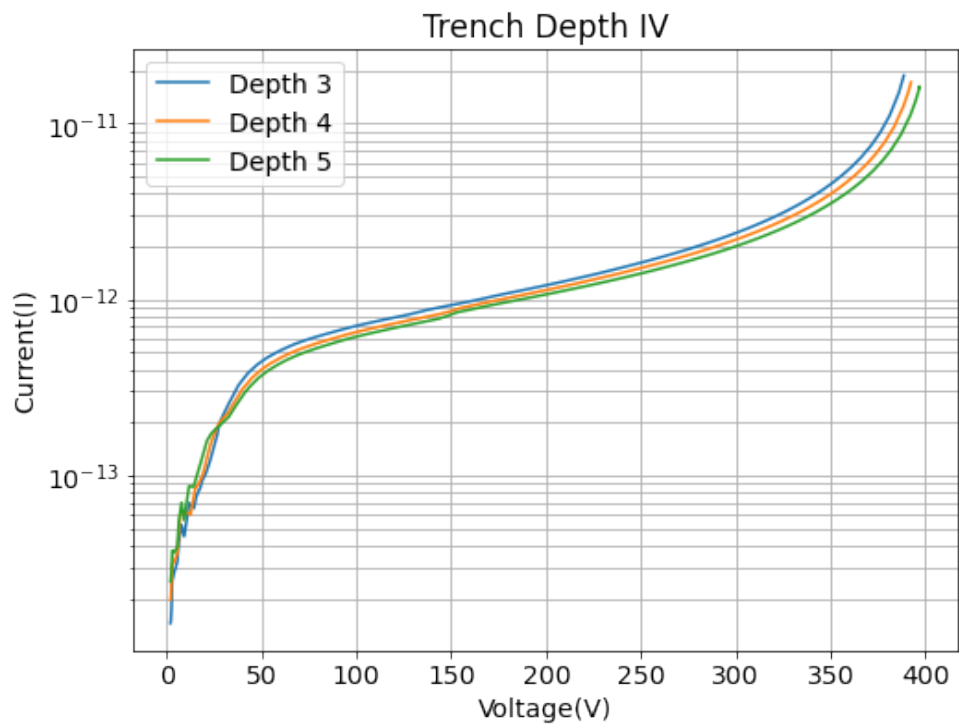


Figure 4.16: Comparison of breakdown voltage across different trench depths with constant width of  $2 \mu\text{m}$ . Simulated in TCAD [89].

## 4.4 Radiation Model

Since LGAD based detectors will be used as tracking devices close to the beam, it is vital to consider the effects of radiation on such devices. At the LHC the contribution of radiation to sensor and electronic degradation is significant and will become more important with the High-Luminosity upgrade. Radiation effects can primarily be thought of in terms of surface and bulk defects. Bulk effects primarily concern the displacement of atoms in the lattice whereas surface effects cover damage at the interfaces. The primary surface effect discussed in this body of work and chapter is the increase in oxide charge. The main effects observed in the presence of high fluence are an increase in leakage current, increase in depletion voltage, due to changes in space charge, and charge trapping in the bulk.

### 4.4.1 Deep Level Traps and Surface Charge Effects

Bulk damage effects are caused by the interaction of incident particles with lattice atoms with the dissociation leading to reduced performance. To remove a silicon atom from its position in the lattice a minimum recoil energy,  $E_d$ , of about 25 eV. This seems low but it is important to consider that electrons require an energy of  $\approx 260$  keV to generate this recoil energy in collision. Similarly protons and neutrons only require  $\approx 190$  keV due to their higher mass.

These defects in the bulk are responsible for two main effects. The first of these is an increase in leakage current due to extra available energy levels in the band gap. This increases the availability of generation-recombination centres in the silicon, leading to an increase in leakage current. The change in the volume generation current  $I_{vol}$  can be expressed as

$$\frac{I_{vol}}{V} = \frac{I_{vol,\phi=0}}{V} + \alpha\phi, \quad (4.14)$$

where  $V$  is the depleted volume and  $\alpha$  is the current related damage rate. It should be noted that the parameter  $\alpha$  is dependent on the intrinsic charge carrier concentration of the silicon. Conversely, while increasing the diversity of energy levels in the band gap increases the leakage current, it also depletes certain regions of available charge carriers. These regions in the depletion zone can *trap* charge for longer than the charge collection time. These effects can drastically reduce signal height. After exposure to a fluence of  $10^{14} \phi_{eq}/\text{cm}^2$  a standard device will still collect about 90% of charge. However, this

drastically falls off with exposure to  $10^{15} \phi_{eq}/\text{cm}^2$  reducing this to around 50%. Similar to the idea of mean-free time, this effect is generally parameterised as a mean trapping time,  $\tau_t$ , which is inversely proportional to the trap concentration

$$\frac{1}{\tau_t(\phi)} = \frac{1}{\tau_t(\phi = 0)} + \gamma\phi, \quad (4.15)$$

where  $\gamma$  is a coefficient unique to the material being irradiated. Similarly, the surface region of the device is also sensitive to high fluences. Silicon oxide—which will be used in LGAD trench designs—can experience impact ionisation in a similar fashion to the bulk. However, when electron-hole pairs are created in the oxide, the electrons can rapidly be collected by an electrode due to their high mobility in the oxide. Holes however have very low mobility and can build up within the oxide as they become trapped on the boundary [92]. These charges can generate a change in the oxide flat-band voltage,  $V_{FB}$  changing device performance.

These effects are modeled in TCAD using a general model that optimises device level effects for both the bulk and surface [91]. The model works by generating two simplified trap distributions with respect to the surface and the bulk as can be seen in Figure 4.17.

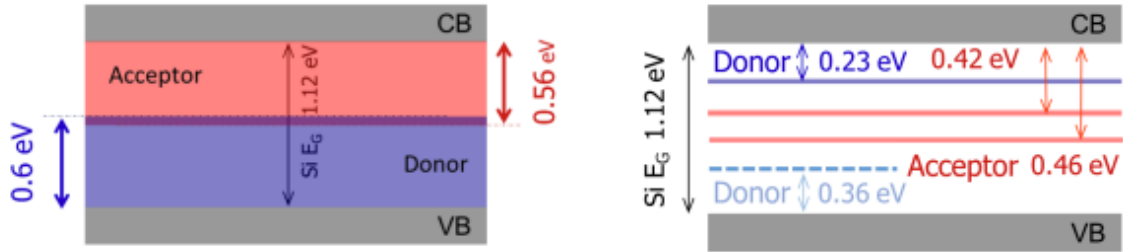


Figure 4.17: Interface level trap distributions (left), bulk trap level distributions (right). Reproduced from [91].

For the bulk, the trap states are all considered separately, with trap concentrations being derived from experimental analysis of  $\langle 100 \rangle$  silicon devices from various companies. The effects on charge collection are also qualitatively confirmed comparing device gain at  $10^{14} \phi_{eq}$  and  $10^{15} \phi_{eq}$  in section 4.5.2. The only surface effect modeled in this study was charge build up in the oxide. The parameters that govern the trap levels and surface charge for different fluence levels were derived from Ref. [91].

## 4.4.2 Donor Removal and Creation

Bulk and surface effects look closely into the importance of the material on radiation damage. However, they do deal with the effects of radiation on the doping concentration of the multiplication region. We deal with this using an adapted version of the *Hamburg model* which describes the effects of donor removal in semiconductors [93]

$$N_{eff} = N_{eff,\phi=0} - [N_c(\phi) + N_a(\phi, T_a, t) + N_Y(\phi, T_a, t)], \quad (4.16)$$

where  $N_c(\phi)$  describes the fluence dependence of the effective doping, and the other two terms describe the short term annealing  $N_a(\phi, T_a, t)$ , and reverse annealing,  $N_Y(\phi, T_a, t)$ , in terms of time,  $t$  and the storage temperature  $T_a$ . For the simulated case, these later terms are neglected as we are primarily interested in the fluence dependence only.

The Hamburg equation is then simplified using the Torino parameterisation that considers only acceptor generation and initial acceptor removal [94, 95]. This parameterisation yields

$$N_{eff}(\phi) = g_{eff}\phi + N_{eff}(0)e^{-c\phi}, \quad (4.17)$$

where  $g_{eff}$  is an acceptor generation constant ( $\approx 0.02 \text{ cm}^{-2}$ ) and  $c$  is a constant that depends on the initial acceptor concentration. Hence,  $c$  is more correctly parameterised as

$$c(N_{eff}(\phi)) = \alpha N_{eff}(0, x)^\beta, \quad (4.18)$$

for varying acceptor concentrations, where  $\alpha$  and  $\beta$  can be extracted directly from material studies. With this parameterisation it is possible to model how the multiplication layer will change with increased fluence, as seen in Figure 4.18.

By combining the bulk models and these analytical profiles it is then possible to run transient simulations on irradiated LGAD devices, which will be the topic of the next section.

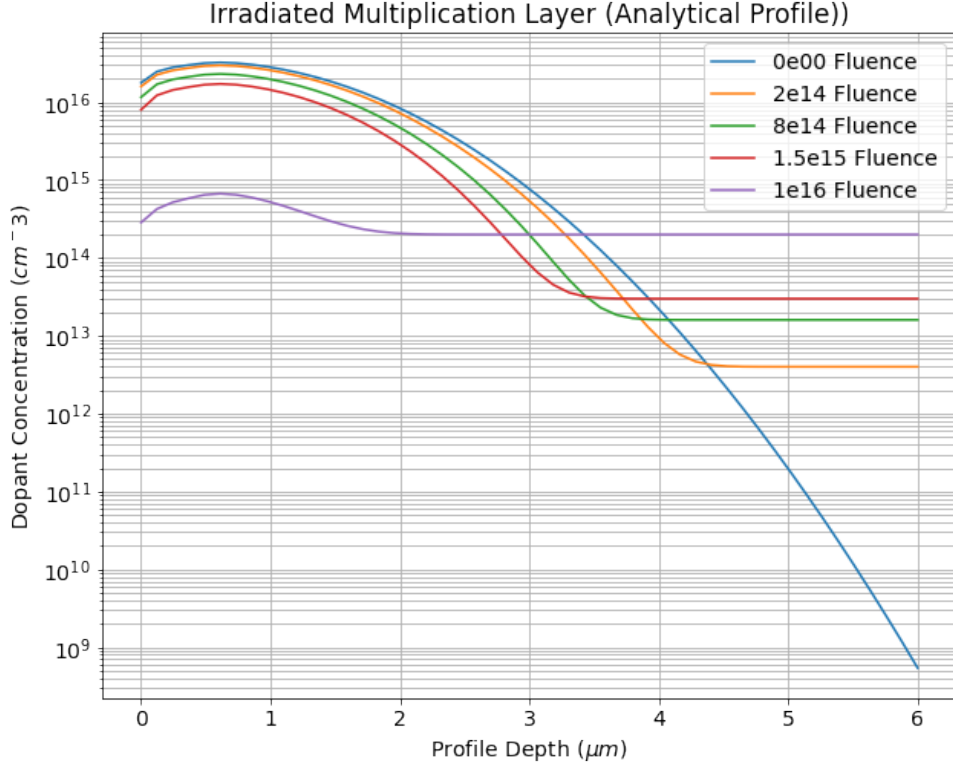


Figure 4.18: Analytical multiplication profiles in high fluence environments, optimised for phosphorous doping using values extracted from [94].

## 4.5 Transient Simulations

Transient simulations are used in determining device properties that are unavailable in time-independent studies. The main target quantities of these analyses are gain and fill factor, where gain is defined as

$$Gain = \frac{CC_{LGAD}}{CC_{PiN}}, \quad (4.19)$$

where  $CC_{LGAD}$  and  $CC_{PiN}$  define the total collected charge across a set time period for an LGAD device and PiN device respectively. Hence, rather than a measure of absolute gain all provided terms are a measure of relative gain for the device under test. Similarly, fill factor is the percentage of each pixel under which a gain threshold is met. The studies for fill factor also give some qualitative analysis of cross-talk between neighbouring pixels.

### 4.5.1 Minimum Ionising Particles (MIPs)

In order to carry out transient simulations, the device under test must be impacted by a minimum ionising particle. When one of these particles penetrates a device it loses energy and leaves a trail of electron-hole pairs. In the case of the MIP this is constant across the depth of the device. These MIPs were modeled using a TCAD Heavy Ion model, which can be adapted to simulate MIP interactions, since it is a general tool for modeling how charge is deposited in a device.

The TCAD Heavy Ion model describes this by defining an electron-hole pair generation rate depending on various factors. The simplest generation model being defined as

$$G(l, w, t) = G_{LET}(l)R(w, l)T(t), \quad (4.20)$$

where  $G_{LET}(l)$  is the LET (Linear Energy Transfer) generation density for defining the raw number of pairs created as a function of the track length,  $l$ .  $R(w, l)$  is the spatial distribution of the generator and is defined as

$$R(w, l) = \exp\left(-\left(\frac{w}{w_t(l)}\right)^2\right), \quad (4.21)$$

for the Gaussian case, and is a function of track length,  $l$ , and characteristic distance  $w_t$ . Finally  $T(t)$  is the function defining the temporal variations in the generation rate. This is predefined within the TCAD package and is omitted here for clarity. For all the transient simulations the MIP parameters in table 4.1 were used with the MIP impacting normal to the pixel plane.

Parameter	Value
$G_{LET}$	$1.282 \times 10^{-5} \text{ pC}/\mu\text{m}$
$w_t$	$1 \mu\text{m}$
Distribution	Gaussian
Length	$50 \mu\text{m}$

Table 4.1: Heavy Ion parameters for use in transient simulations.

It should be noted that  $G_{LET}$  and  $w_t$  are described as constants across the length of the track to ensure uniform generation. The value of  $G_{LET}$  is also relatively low compared to other simulated experiments of this type, since recent studies have shown gain suppression linked to charge density in the multiplication layer [96].

## 4.5.2 Gain Measurements

Gain measurements were primarily carried out to investigate the effects of large radiation doses on the performance of LGAD devices. For these measurements we used a Heavy Ion model that impacted the device at the centre of pixel N1 (Figure 4.10) after the device had been depleted and held at a bias of 320 V.

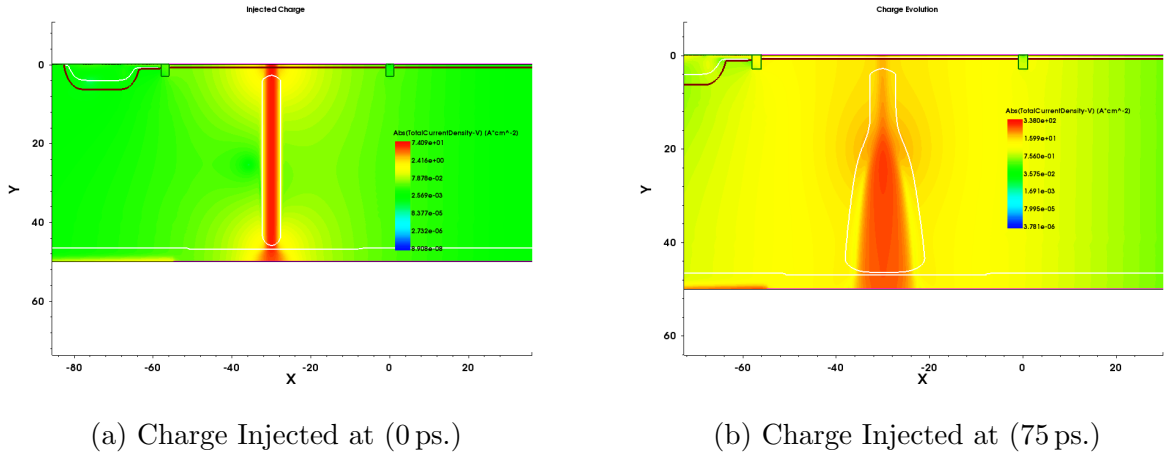


Figure 4.19: Evolution of charge density during transient device simulation. Simulated in TCAD [89].

As can be seen in Figure 4.19, the charge is deposited linearly through the centre of the pixel and the initial charge density is constant along this track. After 75 ps it can be seen that the charge deposited in the multiplication region has rapidly been collected due to the high field in the multiplication region, while the remaining charge drifts across the device more slowly. This can be seen prominently in transient current charge plots (Figure 4.20) where LGAD devices are characterised by this extremely fast rise time.

Radiation effects were modeled as specified in the previous section. Importantly, all simulations were completed at a temperature of 248 K since the TCAD radiation model has only been validated at this temperature. The fluences were limited to the parameters measured in Ref. [91] to ensure realistic device performance. For a selection of fluences the relative gain was recorded, as can be seen in Figure 4.21, where the gain drops off in a non linear fashion. This is likely due to the interplay between the acceptor removal effects modeled for the multiplication layer, and trap formation for the bulk; each having a different evolution with fluence. However, it would be nonphysical to model these effects separately.

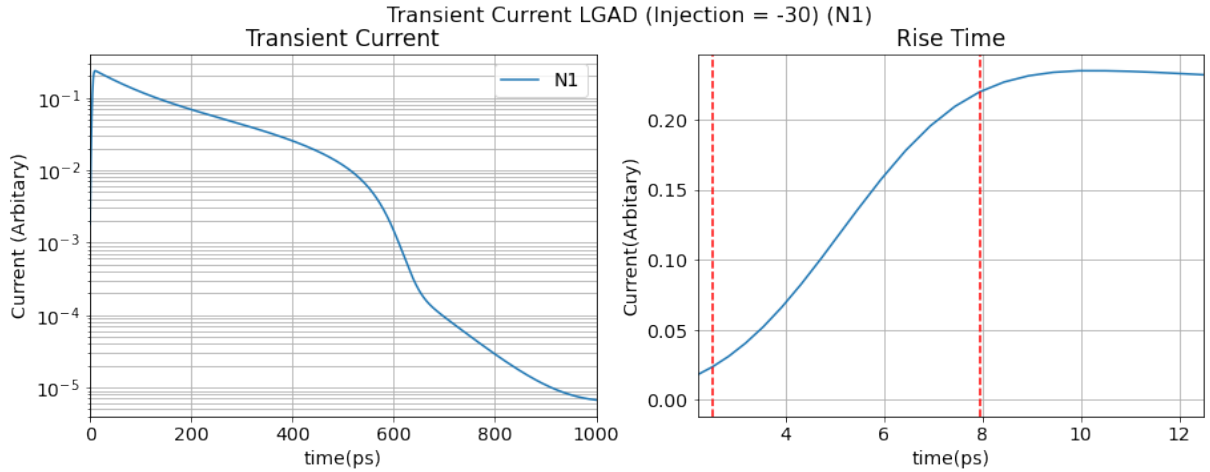


Figure 4.20: Transient current plots for a MIP charge injected at 0 ps in the centre of pixel N1. The simulation terminates after 1000 ps. The current is given in arbitrary units to blind true charge characteristics. Simulated in TCAD [89].

### 4.5.3 Fill Factor

In order to qualitatively analyse the fill factor of the device, charge was injected at small intervals. The charge was always injected perpendicular to the pixel plane to reduce numerical error and to observe charge sharing effects. It was observed in Figure 4.22 that even close to the trench boundary there was minimal cross-talk between the pixels, implying good isolation with the trenching. Charge profiles were also mostly symmetric even at the JTE boundary, implying consistent device behaviour in this region.

### 4.5.4 Gain Recovery

Under LHCb upgrade conditions, the VELO sensors will undergo exposure to the aforementioned fluences. From the simulated studies into the response to this radiation it is therefore important to consider if the detector response can be recovered in some way. Generally, for silicon detectors to recover their performance, the electric field of the device needs to be enhanced to overcome trap effects. To do this, the bias voltage of the sensor can be raised, which is made possible by the enhancements to the breakdown voltage observed in irradiated devices (Figure 4.23). This has been done with early iterations of the LGAD devices, however this is the first time the effect has been simulated [82].

The simulation strategy was carried out in a similar manner to the gain measurement studies using same heavy ion parameters. However, in contrast to this study, multiple

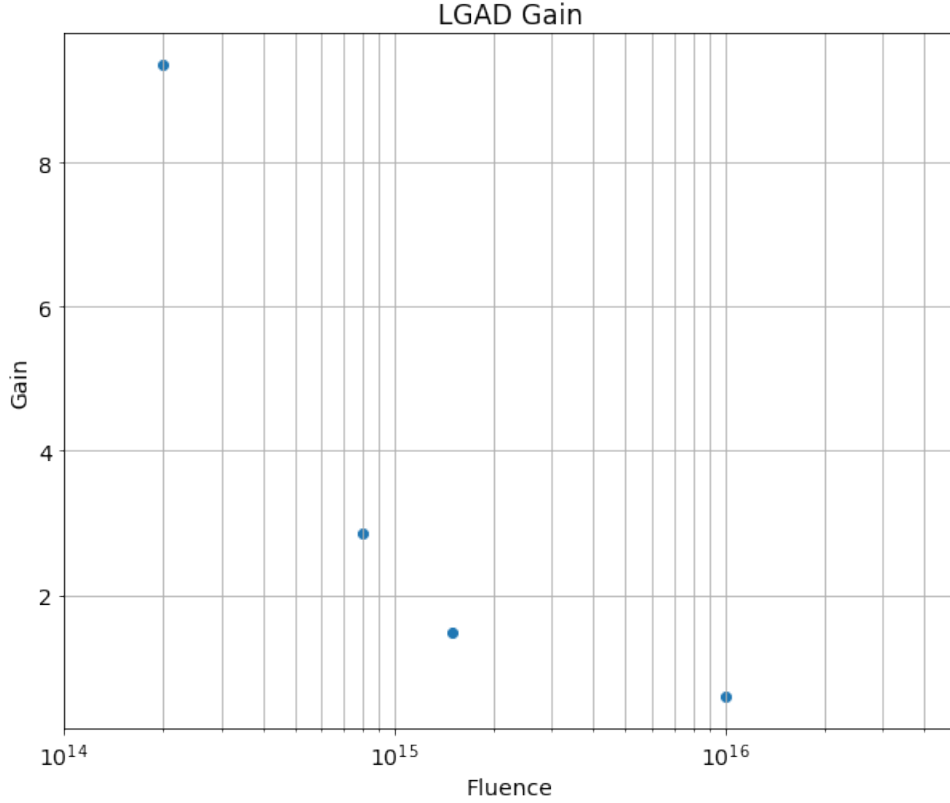


Figure 4.21: Relative gain for different a device simulated at varying fluences. Simulated in TCAD [89].

measurements were taken at increasing bias voltages up to the breakdown of the devices. This was then expressed as a function of gain, where we observed for low fluences the ability to recover gain to some level (Figure 4.24). However, the inability to recover the gain in the high fluence case is a feature of the technological challenges faced by the high-luminosity LHC. Further study and the comparison to test beam data will be vital in quantifying this effect, and by extension validating LGAD for use in the LHCb upgrade.

#### 4.5.5 Transient Simulation Summary

Transient simulations of LGAD devices have shown a good consistency of operation across the pixels with a well defined fill factor even at high fluences. However, even though the fill factor and operational consistency between pixels were good, the reduction of gain and the subsequent difficulty of recovery could be an issue for this type of fast timing detector in high-luminosity LHC. In the short term, the production and test of physical irradiated

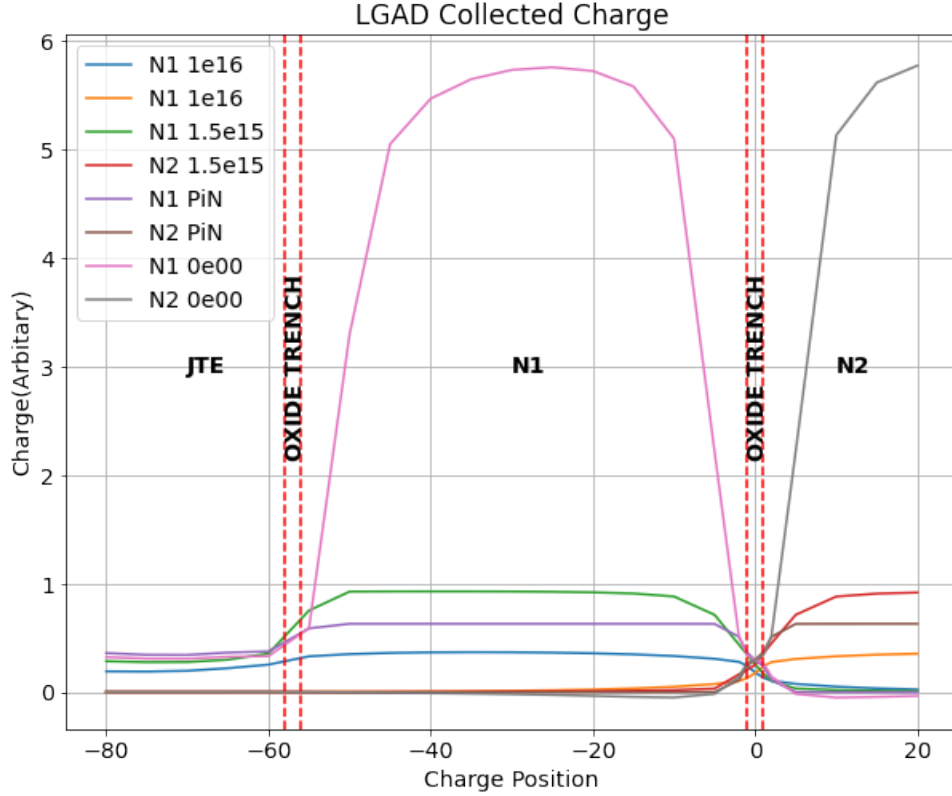


Figure 4.22: Simulated charge collection in LGAD devices with profile outlined in Figure 4.10. Scans are carried out from the JTE over pixels N1 and N2. Fluences are given in  $\phi_{eq}/\text{cm}^{-2}$ . Simulated in TCAD [89].

devices will be important to quantify the simulation results. Beyond this, there is also scope to develop more radiation hard LGAD designs with studies into carbonated boron doping, suggesting a factor of 2 improvement in radiation hardness [97]. However, changes to the doping must be considered carefully as diffusion, and by extension the electric field characteristics, can be substantially altered. There is also interest in simulating gain suppression effects in LGAD devices to understand how this will limit future developments [96].

## 4.6 Chapter Summary

LGAD simulations have formed a core input into designs and consideration for the next generation of fast-timing detectors at both LHCb and the LHC as a whole, with similar detector technologies being developed for ATLAS and CMS. With the drastic changes

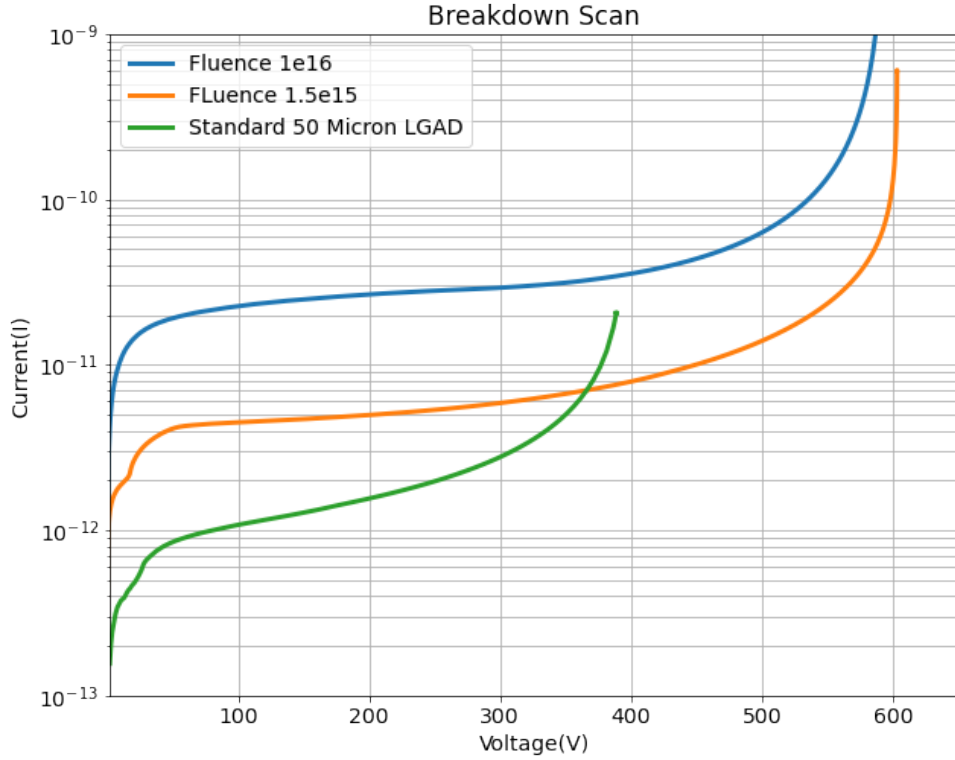


Figure 4.23: Simulated breakdown characteristics of LGAD devices. Simulated in TCAD [89].

foreseen to the integrated luminosity simulations of device radiation profiles in both electrostatic and transient regimes, these will determine the viability of LGAD as a viable detector candidate. The work carried out in this thesis has demonstrated the viability of segmentation using oxide trenches and justified the inclusion of a JTE at the edge of the device. The radiation studies have provided some direction in understanding how the device may evolve over time, but study of irradiated wafers will be needed both to validate the modeling and to define future simulation developments.

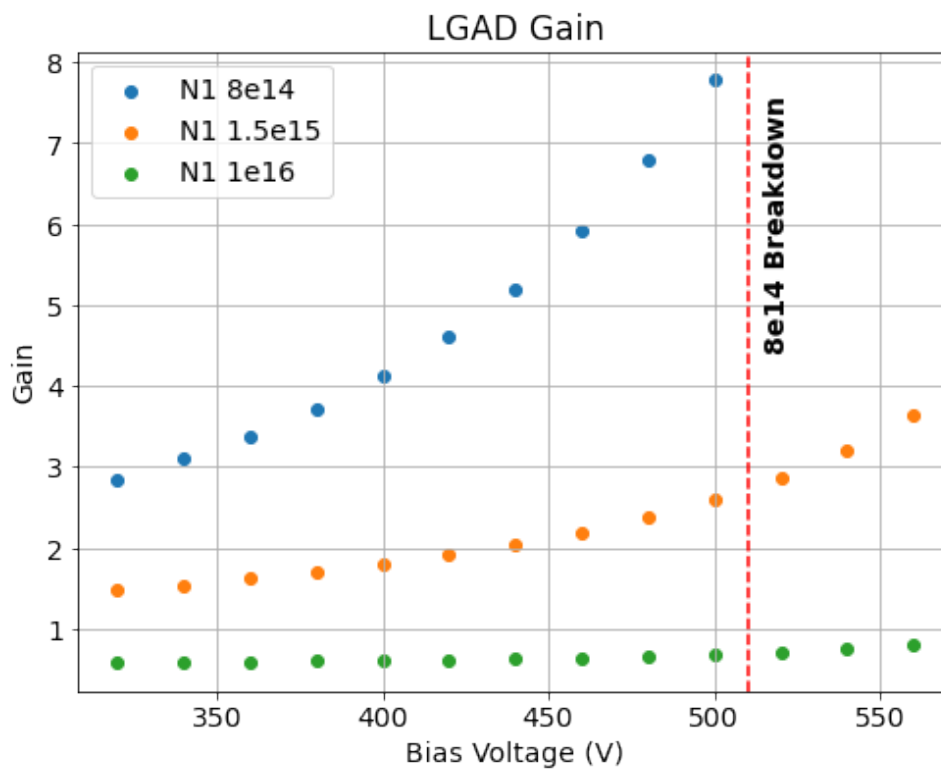


Figure 4.24: Simulated gain recovery for a selection of fluences. The device breakdown at a fluence of  $8 \times 10^{14} \phi$  is at a approximately 510 V limiting the range of this experiment. Simulated in TCAD [89].

# Chapter 5

## Reconstruction and Selection of $B^0$ Mesons

Gentlemen, we can rebuild him. We have the technology. We have the capability to make the world's first...[Unbiased  $B^0$  Selection]

---

The Six Million Dollar Man (Edited)

Much like assembling LEGO in the dark, the daunting task of reconstructing detector outputs into meaningful physics, via reconstruction and selection, is one of the most important tasks of the LHCb experiment. This chapter is concerned with how LHCb reconstructs its particles, and how we interpret this data using novel machine learning techniques to build signal candidates for our analysis.

### 5.1 Reconstruction at LHCb

Reconstruction takes place within the LHCb software packages of BRUNEL and DAVINCI. In order to reconstruct an event, the hits in the detector are collected into clusters, for neutrals, and into tracks, for charged particles. These tracks and clusters are then combined later in the algorithm to reconstruct specific decays. The LHCb experiment reconstructs these tracks and clusters into full events based on the following high level information.

- The momentum of a particle derived from the deflection in the  $B$  field produced by the spectrometer magnet.
- The position and direction of the track in the VELO (Vertex Locator) detector.
- The position and direction of the track in the RICH (Ring Imaging Cherenkov) detectors.
- The predicted production direction of the clusters in the calorimetry and muon systems.

This reconstruction is then used to apply flags to data samples to indicate the type of events that they most likely contain in BRUNEL, with the full reconstruction taking place offline in DAVINCI during tuple production. The rest of the chapter is concerned with the selection of the  $B_d \rightarrow \pi^+ \pi^- \pi^+ \pi^-$  sample.

## 5.2 Stripping and Offline Cuts

In order to reduce the amount of data, our algorithms loop over stripping decisions that are used to pre-select our data. In the case of this analysis, a dedicated stripping line specified in Table 5.1 is used. This stripping line was written to avoid biases induced in previous analyses of this channel, namely, by changing the limitations imposed on the 2-body and 3-body cuts. Previous analyses in this channel have imposed strict cuts below the  $a_1(1260)$  meson mass for the 2-body combination. These cuts were beneficial when looking purely at the  $\rho$  meson (Vector-Vector channel), however, they cut out an extremely important interference with respect to this amplitude analysis. As such, there are only cuts below the charm threshold for the  $D^0$  and  $D^{*0}$ , and loose cuts to ensure a suitable vertex fit.

## 5.3 Additional Selection Criteria

In addition to the reconstruction carried out as input to the BDT (Boosted Decision Tree) all events are also reconstructed with the  $B^0$  Mass constrained to the PDG (Particle Data Group) value. This means that the 4-body tracks are constrained to have come from a primary vertex of exactly this value. Another easily discriminated background

Variable Definition	StrippingB2hhpipiPhsSpcCut4piLine
B candidates selection cuts	
Mass of B	$5.0 < M_B < 5.6$ GeV
Distance of closest approach	$AMAXDOCA < 0.2$ mm
B vertex $\chi^2$	$BPVCHI2 < 30$
B minimal $P_T$	$P_T > 2$ GeV
B IP $\chi^2$	$BPVIPCHI2 < 30$
B separation $\chi^2$	$BPVVDCHI2 > 10$
Flight w.r.t best PV	$BPVDIRA > 0.9999$
Pion selection cuts	
Minimal $P_T$	$P_T > 200$ MeV
Track ghost probability	$GhostProb < 0.4$
2-Body Combination Cut	$[\pi^+\pi^-]cc < 1864.83$ MeV
3-Body Combination Cut	$[\pi^+\pi^-\pi^+]cc < 1869.65$ MeV

Table 5.1: StrippingB2hhpipiPhsSpcCut4piLine selection criteria.

contribution comes from secondary VELO interactions. As mentioned in the Detector chapter, secondary hadronic showers from material interactions in the VELO can lead to fake signals. As such, to discriminate against these we impose a radial flight distance cut of 4 mm to constrain the  $B^0$  production to the centre of the VELO; as can be seen in Figure 5.1.

We also impose a cut on the IPCHI2 of the  $B^0$  meson to ensure that, after the refit to the PDG value, the fit has converged. Physically the IPCHI2 is the minimum distance of a track to the primary vertex. This is done by imposing that the returned value is greater than 0 since negative values imply non convergence. Finally, to reduce uncertainty on the daughter particles we enforce two conditions. The first is that any tracks that leave signals in the Muon chambers at the furthest point of the experiment are removed ("isMuon==0"). The second is that they have a low *ghost probability*, where the *ghost probability* is the chance that a track is made up of unrelated clusters in the VELO. This probability is low when tracks are well isolated in low multiplicity events.

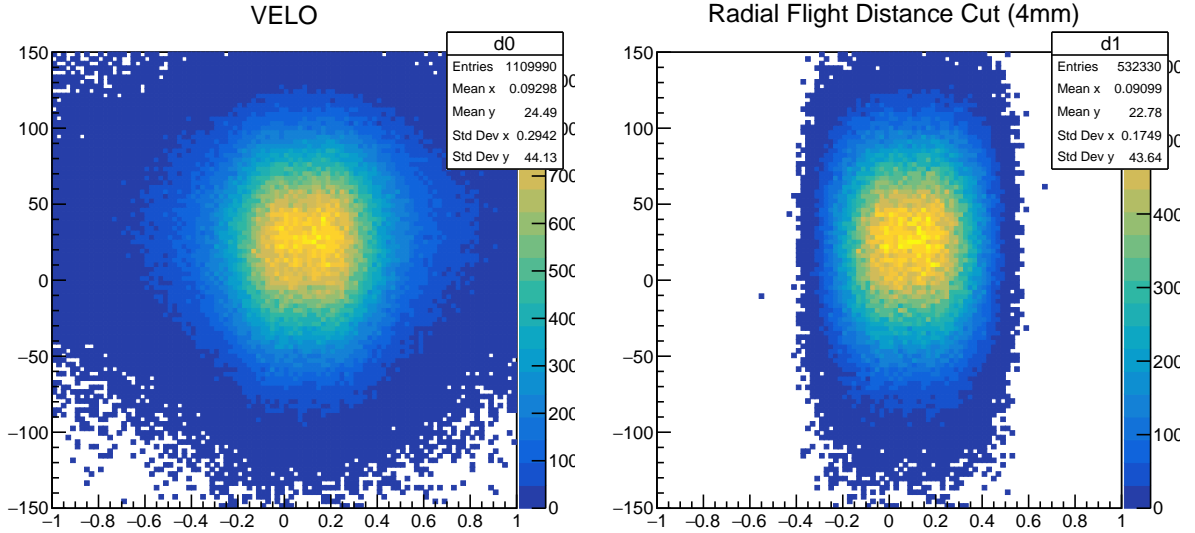


Figure 5.1: 2012 dataset without radial flight distance cuts (left). Radial flight distance cut applied to the 2012 dataset. Units of both axis are cm.

## 5.4 BDT Training and Optimisation

In addition to the offline cuts, a BDT was trained to discriminate between signal and backgrounds that exist in the same mass window. BDT methods generate *decision trees* that impose different sets of cuts that allow for discrimination between channels. For this analysis a gradient boosted method was implemented from the XGBoost python package [98]. In methods such as these, it is important to use a reasonable set of variables that will not bias later analysis steps, and can also provide some level of discrimination. As such, for this analysis the variables shown in table 5.2 were selected.

These variables were chosen as the majority are focused on reconstruction quality rather than physics characteristics of the decay. They are also focused on the origin and end products of the decay to avoid biasing the selection towards certain physics channels such as the  $\rho(770)^0\rho(770)^0$  decay. Once these variables were selected we then conditioned the variables to improve their performance.

Traditionally, to reduce the bias that can be caused by local maxima in training, logarithmic transforms are used to condition variables. However, many machine learning packages such as the XGBoost package have demonstrated increased performance with more Gaussian variables [98]. In an attempt to improve model performance we run the training with logarithmic, Box-Cox and Yeo-Johnson power transforms. The Yeo-Johnson

Variables
B0 ETA
B0 FD $\chi^2$
B0 Vertex Fit
B0 $P_T$
B0 DIRA
B0 AMAXDOCA
B0 IP $\chi^2$
Daughter IP $\chi^2$

Table 5.2: Decision Tree Variables used in the  $B_d$  analysis. B0 ETA is the B0 pseudorapidity, B0 FD is the B0 Flight Distance, B0 Vertex Fit is a measure of the fit quality to the B0 vertex, B0  $P_T$  is the transverse momentum of the B0, B0 DIRA is the direction angle of the B0 with respect to the Primary Vertex, B0 AMAXDOCA is the maximum distance of closest approach from the daughter tracks, B0 IP is the impact parameter of the B0 with respect to the primary vertex and Daughter IP is the impact parameter of the daughters with respect to the B0.

transform is given by,

$$x_i^{(\lambda)} = \begin{cases} [(x_i + 1)^\lambda - 1]/\lambda & \text{if } \lambda \neq 0, x_i \geq 0, \\ \ln(x_i + 1) & \text{if } \lambda = 0, x_i \geq 0, \\ -[(-x_i + 1)^{2-\lambda} - 1]/(2 - \lambda) & \text{if } \lambda \neq 2, x_i < 0, \\ -\ln(-x_i + 1) & \text{if } \lambda = 2, x_i < 0, \end{cases} \quad (5.1)$$

where  $x$  is the original data, and  $\lambda$  is the parameterisation term of the transform.  $\lambda$  is calculated by running a maximum likelihood fit with a Gaussian PDF on Monte Carlo data, with the maximised  $\lambda$  being recorded. For the transform to be valid in data, once the optimum  $\lambda$  value is calculated in Monte Carlo, it is fixed. Similarly, the Box-Cox transform is given by,

$$x_i^{(\lambda)} = \begin{cases} \frac{x_i^\lambda - 1}{\lambda} & \text{if } \lambda \neq 0, \\ \ln(x_i) & \text{if } \lambda = 0, \end{cases} \quad (5.2)$$

where the parameters are identical. However, the Box-Cox transform can only transform positive data, so it is unsuitable for any quantities that go negative. Figure 5.2 shows the transforms applied to three of the training variables, as a set of possible inputs for the BDT training.

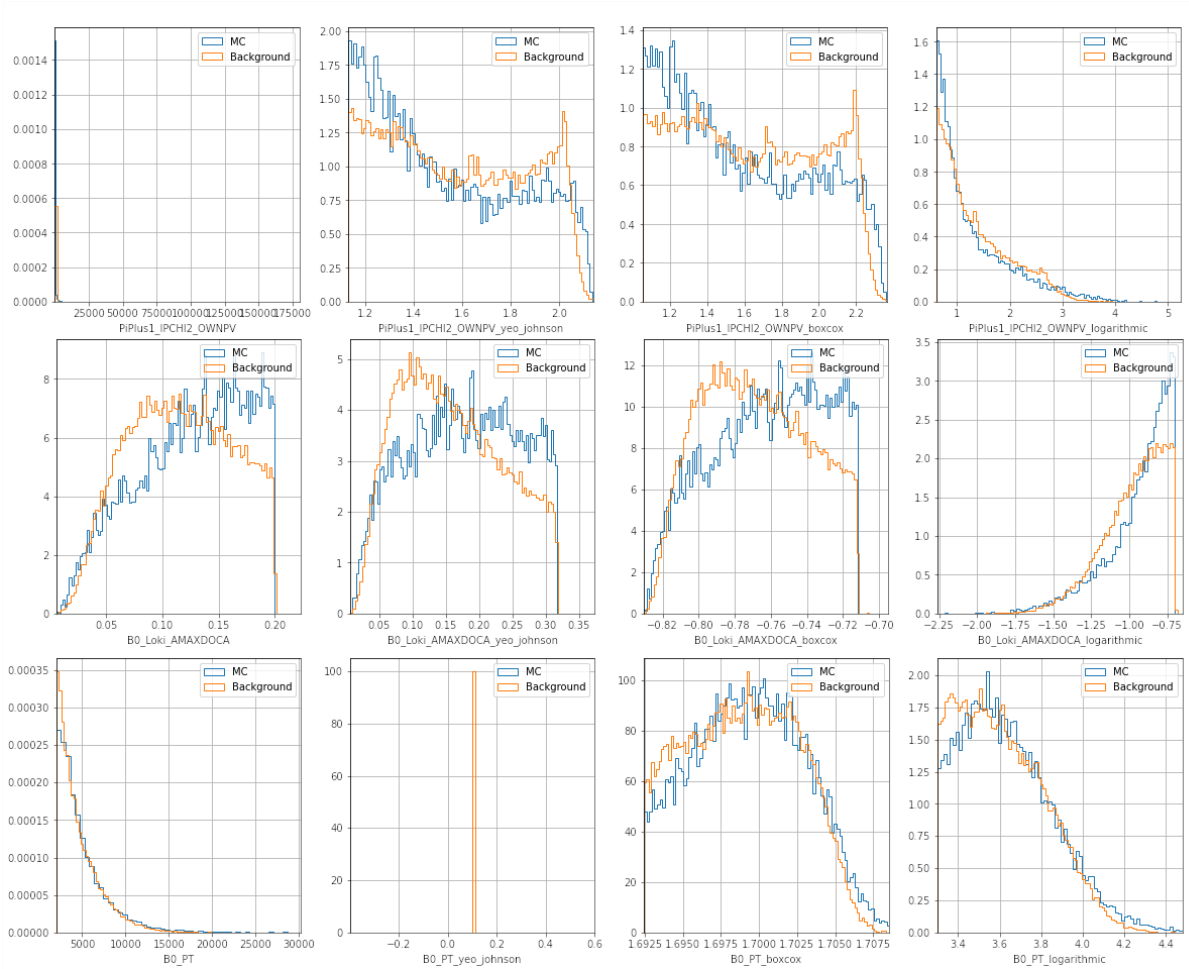


Figure 5.2: Logarithmic and power transforms applied to several training variables. The left plots are the original variables, the second from the left are the same variables with a Yeo-Johnson transform, the third column consists of the Box-Cox transform and the right plots are the logarithmic transforms of the variables. As can be seen, transform efficiency varies by variable. In the case of  $B0_{PT}$  a suitable  $\lambda$  could not be resolved to run the Yeo Johnson transform.

Further to this, the models generated were validated using a k-folding technique, while tuning a number of model hyperparameters. These hyperparameters define the learning characteristics of the model, dictating how much decisions can vary and the minimum number of passing events to generate new decisions. Parameter stability was determined

by running the same hyperparameter sets with different random seeds and inspecting the pulls of variable significance; an example of which can be seen in Figure 5.3. This automated parameter folding was used not only on the hyperparameter sets but also on the variable transforms previously discussed. The models with the best response were transformed in table 5.3.

Variables	
B0 ETA	None
B0 FD $\chi^2$	LOG
B0 Vertex Fit	None
B0 $P_T$	LOG
B0 DIRA	None
B0 AMAXDOCA	None
B0 IP $\chi^2$	BOXCOS
Daughter IP $\chi^2$	LOG

Table 5.3: Decision Tree Variables transforms used in the analysis.

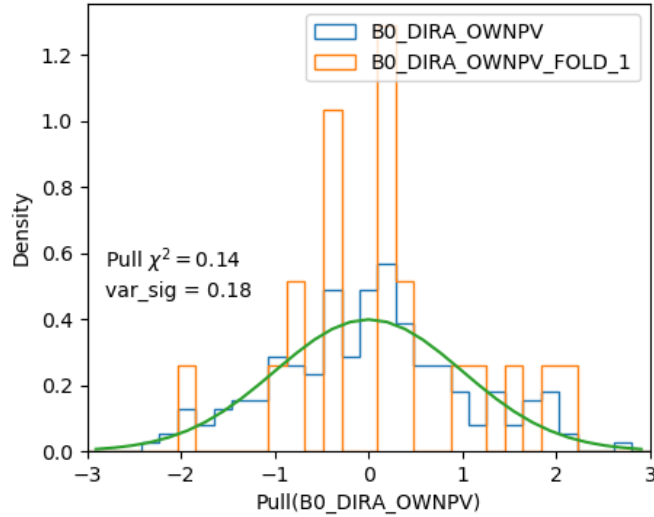


Figure 5.3: Pull plot of B0 DIRA OWNPV significance over random training seeds to monitor stability. Fold 1 refers to the variable significance extracted from a single k-fold.

Once model stability is identified, the model performance is validated using receiver operator characteristic curves (ROC). ROC curves are a graphical technique that plots the true positive rate and false positive rate of a classifier against a single continuous

variable; in our case the BDT value. The area under the ROC curve is a measure of total performance. Figure 5.4 shows the performance of the final classifier against a random coin flip approach in discriminating signal and background. The central value for the significance of each variable is given in table 5.4.

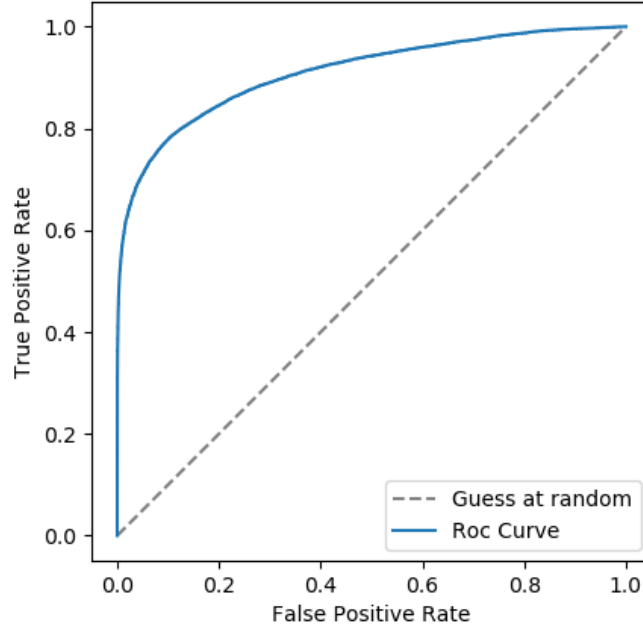


Figure 5.4: ROC curve showing the performance of the selected XDGBoost classifier.

Variables	Significance
B0 ETA	0.08
B0 FD $\chi^2$	0.10
B0 Vertex Fit	0.11
B0 $P_T$	0.06
B0 DIRA	0.2
B0 AMAXDOCA	0.11
B0 IP $\chi^2$	0.14
Daughter IP $\chi^2$	[0.05, 0.05, 0.05, 0.05]

Table 5.4: BDT variable significance as calculated by the XDGBoost python library. The significance is an internal measure of a variables discrimination power with respect to the other variables. Significance always sums to unity.

From this process the final model is selected. However, rather than optimising the

BDT at this stage, the optimised cut location was determined across a two-dimensional scan of BDT and particle ID of the final state pions.

### 5.4.1 Optimisation

Optimisation is achieved in two dimensions with BDT and ProbNNk, where ProbNNk is the neural network response of the LHCb PID tagger, with response being modeled across a number of parameters. These parameters are yield, the figure-of-merit (FoM), purity and fit quality. The yield is an estimate of raw events from a preliminary fit to the data using a simple Gaussian (signal), Exponential (combinatorial background) and ARGUS (partially reconstructed background) model [99]. The figure-of-merit is the standard,

$$FoM = \frac{S}{\sqrt{S+B}}, \quad (5.3)$$

figure-of-merit where  $S$  is the signal yield, and  $B$  is the background yield within  $3\sigma$  of the PDG  $B^0$  mass. This general figure-of-merit balances purity and yield with lower values at low yield and low purity. Purity is simply the ratio of  $S/B$  within  $3\sigma$  of the PDG  $B^0$  mass, and fit quality is the model  $\chi^2$  inclusive of all backgrounds. As can be seen in figure 5.5, the response across different success criteria is varied. In general though, it was observed that without too much loss in purity, looser BDT and ProbNNk cuts provide higher yield samples.

The main balancing criteria for this optimisation was the fit quality, which has a peaking structure in the low ProbNNk, high BDT region. This structure is primarily caused by model uncertainties in the understanding of single misidentification backgrounds, such as  $B^0 \rightarrow K\pi\pi\pi$ ; where mismodeling of these backgrounds above the combinatorial can lead to serious deviations. As such, a point around the BDT  $> 0.7$ , ProbNNk  $< 0.18$ , mark was chosen to reduce model uncertainties while balancing purity and yield. These cuts are kept constant between samples.

## 5.5 Invariant Mass Fits

The invariant mass fits provide an input into the amplitude analysis, allowing us to constrain the yields of background and signal events in our sample. In order to constrain these, we complete an extended maximum likelihood fit to the unconstrained data. Within

the scope of the analysis, this section will detail the components and the fit strategy used to quantify the signal and background yields of our fit.

### 5.5.1 PDFs (Probability Distribution Functions)

In order to correctly model the invariant mass we need to utilise different PDFs that model contributions correctly. For the  $B^0 \rightarrow \pi^+\pi^-\pi^+\pi^-$ ,  $B_s^0 \rightarrow \pi^+\pi^-\pi^+\pi^-$ ,  $B^0 \rightarrow K^\pm\pi^\mp\pi^+\pi^-$  and  $B^0 \rightarrow K^+K^-\pi^+\pi^-$  decay channels a Double Crystal Ball function is used [100]. The generic Double Crystal Ball (DCB) function with respect to the mass variable  $m$  is given by,

$$\text{DCB}(m; m_0, \sigma_L, \sigma_R, \alpha_L, n_L, \alpha_R, n_R) = \begin{cases} A_L \cdot (B_L - \frac{m-m_0}{\sigma_L})^{-n_L}, & \text{for } \frac{m-m_0}{\sigma_L} < -\alpha_L, \\ \exp\left(-\frac{1}{2} \cdot \left[\frac{m-m_0}{\sigma_L}\right]^2\right), & \text{for } \frac{m-m_0}{\sigma_L} \leq 0, \\ \exp\left(-\frac{1}{2} \cdot \left[\frac{m-m_0}{\sigma_R}\right]^2\right), & \text{for } \frac{m-m_0}{\sigma_R} \leq \alpha_R, \\ A_R \cdot (B_R + \frac{m-m_0}{\sigma_R})^{-n_R}, & \text{otherwise,} \end{cases} \quad (5.4)$$

with the normalisation factors defined by,

$$A_i = \left(\frac{n_i}{|\alpha_i|}\right)^{n_i} \cdot \exp\left(-\frac{|\alpha_i|^2}{2}\right),$$

$$B_i = \frac{n_i}{|\alpha_i|} - |\alpha_i|,$$

where the seven parameters are the mass,  $m_{B_d, B_s}$ , the resolution of the left,  $\sigma_L$ , and right,  $\sigma_R$ , Crystal Ball halves, and the tail parameters  $\alpha_{L,R}$ ,  $n_{L,R}$ . In the fits,  $\sigma$  is further parameterised as  $\sigma^2 = (\sigma_{MC}^2 + \sigma_{Data}^2)$  where  $\sigma_{MC}$  is the resolution of each individual MC (Monte Carlo) channel fixed from MC, and  $\sigma_{Data}$  is a detector resolution term left to float in the final fit. The tail parameters  $\alpha_{L,R}$ ,  $n_{L,R}$  are also fixed from MC. The fits to the misidentification regions can be seen in Figure 5.6. It should be noted that all MC samples used for modeling have been corrected using the LHCb tool PIDGen for resolving particle ID discrepancies between data and MC samples.

The fixed parameters from the fit to the  $B^0 \rightarrow K\pi\pi\pi$ , the  $B^0 \rightarrow KK\pi\pi$  and  $B_{d,s}^0 \rightarrow \pi\pi\pi\pi$  can be seen in tables 5.5, 5.6 and 5.7 respectively.

$B^0 \rightarrow K\pi\pi\pi$ fixed parameters	Value	Uncertainty
$\alpha_1$	0.308	$\pm 0.035$
$\alpha_2$	-2.216	$\pm 0.082$
$n_1$	3.558	$\pm 1.021$
$n_2$	2.130	$\pm 0.304$
$\sigma_{1(MC)}$	16.962	$\pm 0.839$
$\sigma_{2(MC)}$	28.360	$\pm 0.440$

Table 5.5: Fixed parameters for the  $B^0 \rightarrow K\pi\pi\pi$  signal model.

$B^0 \rightarrow KK\pi\pi$ fixed parameters	Value	Uncertainty
$\alpha_1$	0.231	$\pm 0.053$
$\alpha_2$	-1.902	$\pm 0.165$
$n_1$	20.000	$\pm 2.585$
$n_2$	3.567	$\pm 1.186$
$\sigma_{1(MC)}$	28.441	$\pm 2.585$
$\sigma_{2(MC)}$	34.475	$\pm 1.734$

Table 5.6: Fixed parameters for the  $B^0 \rightarrow KK\pi\pi$  signal model.

For the partially reconstructed background, where we reconstruct a  $B^0$  with missing pion and  $\gamma$  contributions, we use an Argus function [99] defined with respect to variable  $m$ , and some numerical normalisation  $\mathcal{N}$ ,

$$A(m, m_0, c, p) = \mathcal{N} \cdot m \cdot \left[ 1 - \left( \frac{m}{m_0} \right)^2 \right]^p \cdot \exp \left[ c \cdot \left( 1 - \left( \frac{m}{m_0} \right)^2 \right) \right], \quad (5.5)$$

where  $m_0$  is the mass of the  $m_{B^0} - (m_K - m_\pi)$  to set the limit on the reconstructed shape, the power term  $p$  is fixed to 0.5 and the curvature term  $c$  is left to float in the final fit. This shape is then convoluted with a Gaussian defined with respect to  $m$ ,

$$G(m, \mu, \sigma) = \frac{1}{\sigma\sqrt{2\pi}} e^{-(m-\mu)^2/2\sigma^2}, \quad (5.6)$$

where  $\mu$  is fixed at zero since this is a resolution term and  $\sigma$  is the same  $\sigma_{L,R}$  from the  $B^0$  Double Crystal Ball fit. The full description of the partially reconstructed background is given by the convolution,

$$R(m, m_0, c, p, \mu, \sigma) = A(m, m_0, c, p) \otimes G(m, \mu, \sigma). \quad (5.7)$$

The final fit component is the combinatorial background, which is comprised of unrelated

$B_{d,s}^0 \rightarrow \pi\pi\pi\pi$ fixed parameters	Value	Uncertainty
$\alpha_1$	1.610	$\pm 0.009$
$\alpha_2$	-1.450	$\pm 0.012$
$n_1$	2.433	$\pm 0.034$
$n_2$	4.120	$\pm 0.075$
$\sigma_{(MC)}$	16.292	$\pm 0.031$

Table 5.7: Fixed parameters for the  $B^0 \rightarrow \pi\pi\pi\pi$  signal model. The value of  $\sigma$  is not split in this DCB function as the reconstructed signal mode should be symmetric.

pions that can fulfill the  $B^0$  4-body vector requirements. This forms a substantial part of our backgrounds since our selection was made loose, to be inclusive of intermediate resonant states. The background was modeled with an exponential function defined with respect to  $m$ , and some normalisation  $\mathcal{N}$ ,

$$E(m, c) = \mathcal{N} \cdot \exp(c \cdot m), \quad (5.8)$$

where  $c$  is the decay constant of the exponential. Studies were completed to check the viability of using different background parameterisations such as Chebychev polynomials, however, they offered no improvement in the final fits. From these components, the final fit model can be written as,

$$\begin{aligned} Model = & N_{BKG} E_{combinatorial} + N_{ARGUS} R_{reconstructed} + \dots \\ & N_{BD} DCB_{B^0 \rightarrow \pi\pi\pi\pi} + N_{BS} DCB_{B_s \rightarrow \pi\pi\pi\pi} + \dots \\ & N_K DCB_{B^0 \rightarrow K\pi\pi\pi} + N_{KK} DCB_{B^0 \rightarrow KK\pi\pi}, \end{aligned}$$

where  $N_i$  is the number of events observed under each normalised PDF as part of the negative log-likelihood fit. These fits were done for each year of data taking, since efficiencies will be calculated independently for each sample due to changing run conditions. The final fits can be seen in Figure 5.7 with their respective yields and uncertainties presented in Table 5.8. The total yield of  $B_d \rightarrow \pi^+\pi^-\pi^+\pi^-$  events for Run 2 is found to be:  $126725 \pm 504$ .

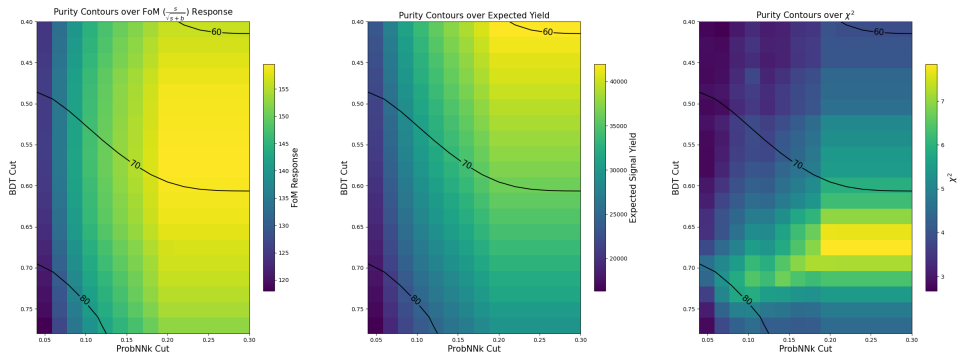
## 5.6 Chapter Summary

The  $B^0 \rightarrow \pi^+\pi^-\pi^+\pi^-$  selection is complete, using a combination of a dedicated stripping selection, a series of offline cuts, a tuned BDT—utilising novel variable transforms—and a

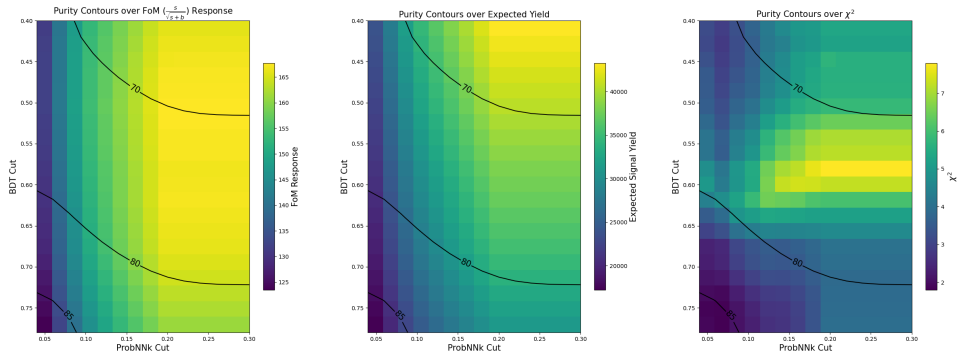
Year	Signal Yield	Background Yield	Mis-ID Yield
2015	$6681 \pm 117$	$2176 \pm 209$	$605 \pm 102$
2016	$36930 \pm 278$	$12940 \pm 513$	$3427 \pm 247$
2017	$38300 \pm 274$	$11250 \pm 512$	$3102 \pm 241$
2018	$44810 \pm 297$	$13400 \pm 545$	$3430 \pm 257$

Table 5.8: Yields of the three main contributions inside the  $B_d$  mass window used for the analysis.

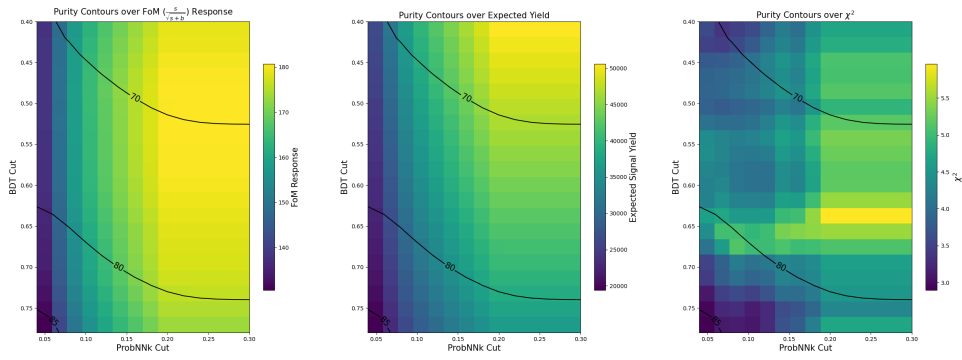
multi-dimensional optimisation with PID to select the data. From this, invariant mass fits have been completed to data inclusive of several misidentification backgrounds, and with an extended Crystal Ball function to include detector resolution effects. This has been carried out on all LHCb Run 2 data which will be used for the remaining chapters of this thesis. Run 1 data is currently omitted due to a data fault at the BRUNEL level suppressing flavour tagging information, which is required for the proposed time-dependent section of the analysis.



(a)

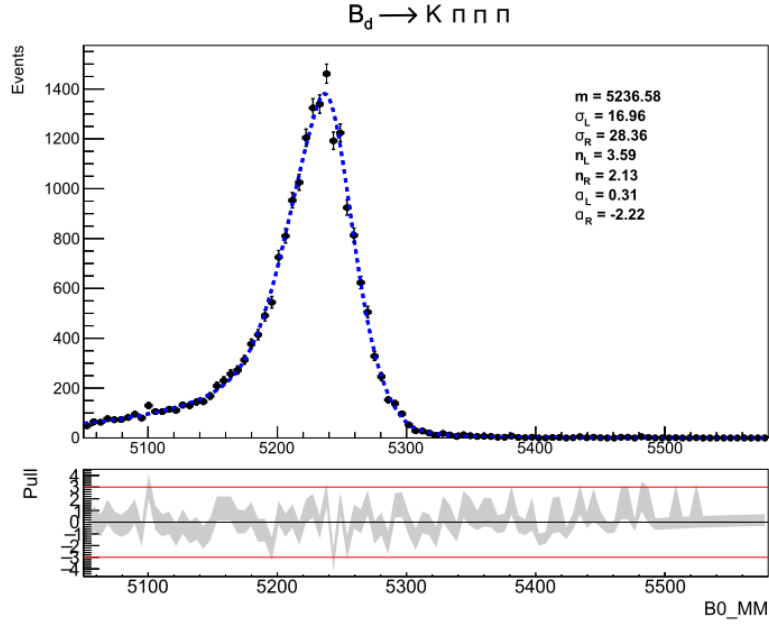


(b)

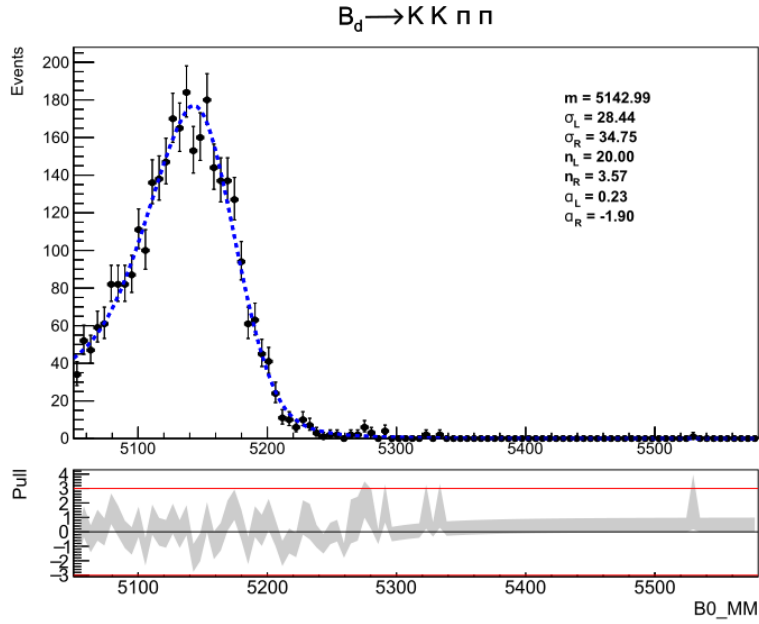


(c)

Figure 5.5: Three panel optimisations for the 2016 (a), 2017 (b) and 2018 (c) datasets. The left plots are optimised for the  $S/\sqrt{S+B}$  FoM, the middle plots are optimised for the purity  $S/B$  and the right plots are optimised for  $\chi^2$ , where a lower  $\chi^2$  indicates a better convergence with a simplified invariant mass model. Characteristics of the optimisation are consistent between samples.

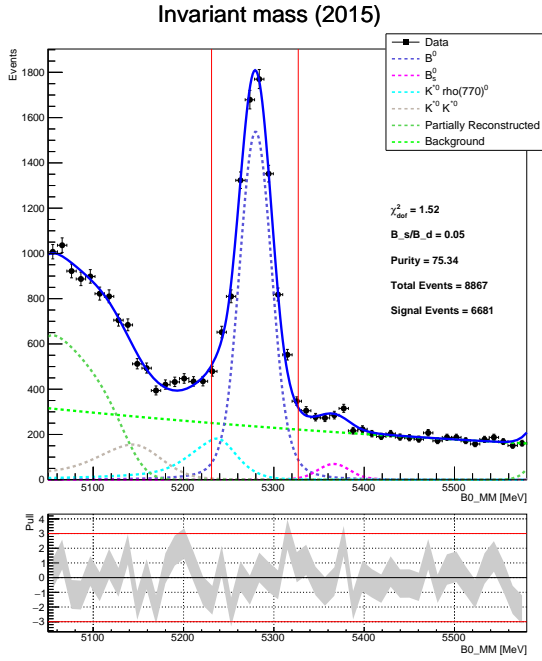


(a)  $B^0 \rightarrow K\pi\pi\pi$  (2016 MC) events reconstructed under a  $B^0 \rightarrow \pi\pi\pi\pi$  hypothesis and fit with a DCB function. Tail  $\alpha_{L,R}n_{L,R}$  and MC resolution parameters  $\sigma_{MC_{L,R}}$  were fixed from these fits.

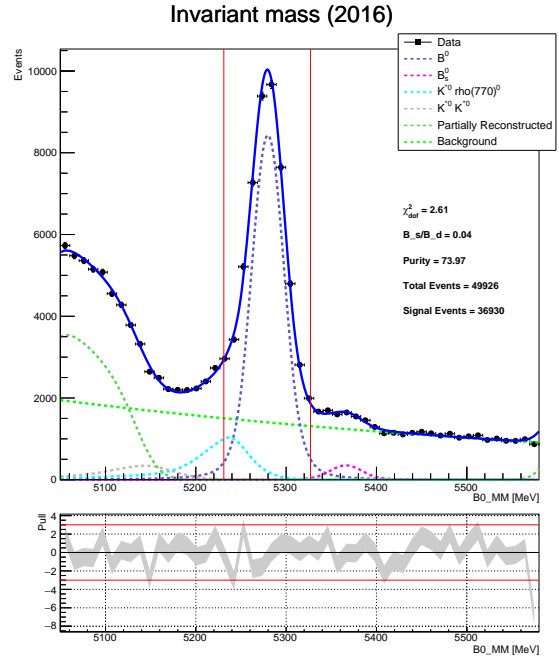


(b)  $B^0 \rightarrow KK\pi\pi$  (2016 MC) events reconstructed under a  $B^0 \rightarrow \pi\pi\pi\pi$  hypothesis and fit with a DCB function. Tail  $\alpha_{L,R}n_{L,R}$  and MC resolution parameters  $\sigma_{MC_{L,R}}$  were fixed from these fits.

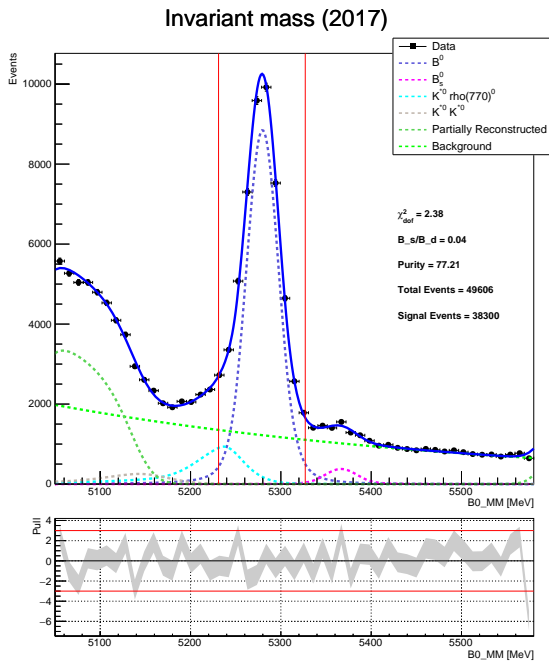
Figure 5.6: Misidentified MC events reconstructed under a  $B^0 \rightarrow \pi\pi\pi\pi$  hypothesis.



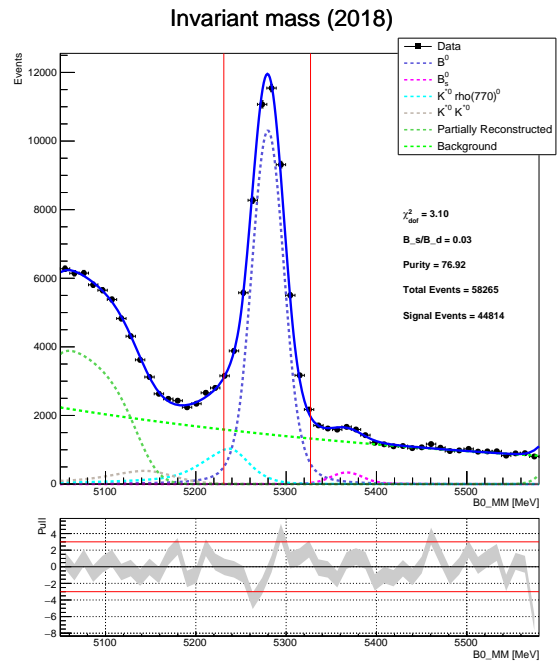
(a) 2015 invariant mass fit.



(b) 2016 invariant mass fit.



(c) 2017 invariant mass fit.



(d) 2018 invariant mass fit.

Figure 5.7: Invariant mass fits for the full 2015 (a), 2016 (b), 2017 (c) and 2018 (d) datasets.

# Chapter 6

## Background Modelling and Efficiencies

I'm doing badly, I'm doing well,  
whichever you prefer.

---

Franz Kafka (On Machine Learning)

It is no easy thing to quantify empirical backgrounds within an analysis, and to model the varying efficiencies caused by variations in experimental setup. However, with simulated samples and the correct application of machine learning algorithms it is possible to quantify both of these in a minimally biased way.

In this chapter we will discuss the machine learning model approach used to define our empirical background, and phase space efficiencies before assessing the applications to data. The final part of the chapter will concern how these models are included in our fits.

### 6.1 Kernel Density Estimation

Ideally when characterising our background and efficiency models we would do so with some model derived from a previous analysis of interfering channels. However, with the complexities of our phase space and with the difficulties associated with quantifying certain data cuts in our backgrounds, a data-driven approach to the problem is required. For this analysis we have chosen to apply a Kernel Density Estimation technique from the

scikit-learn python package to derive an efficiency model from LHCb Monte Carlo data [101].

Kernel Density Estimation (KDE) methods at their heart allow us to derive models from binned data while reducing the loss of model sensitivity associated with using the wrong binning. This can be seen in Figure 6.1 where the underlying kernel model - seen using both a Tophat and Gaussian kernel - captures features more efficiently than the initial binning choices.

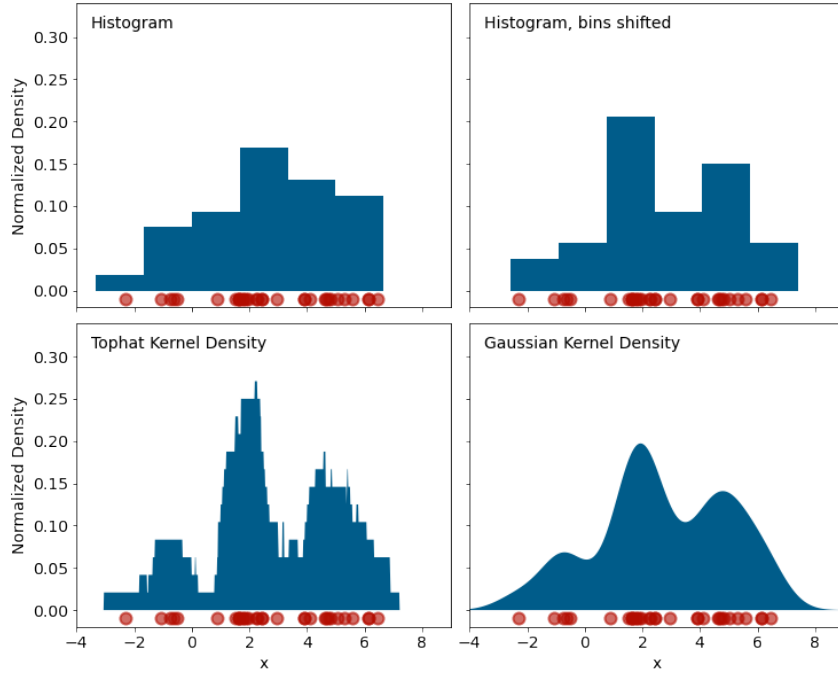


Figure 6.1: Demonstration of a 1D KDE method compared to alternative binning schemes. Underlying data is given in red.

The kernel itself used in these estimations is defined as a positive function  $K(x; h)$  which is modulated by some bandwidth value  $h$  that strikes the balance between distribution variance and bias, with low bandwidth kernels returning smooth but highly biased distributions. Equally, if the bandwidth is too low, the variance in the underlying structure is overestimated, as can be seen in Figure 6.2, where the underlying data is generated from three Gaussian distributions. As such, given this kernel structure, we can calculate the density of some point  $y$  within a group of points  $x_n$  by the equation,

$$\rho_K(y) = \sum_{n=1}^N K(y - x_n; h), \quad (6.1)$$

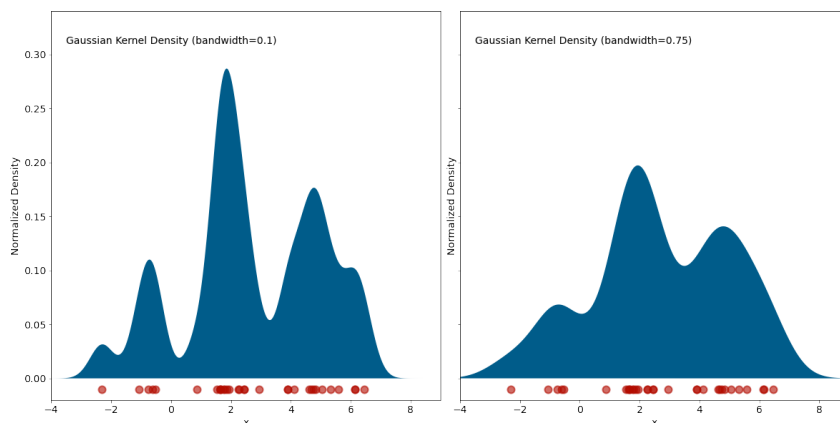


Figure 6.2: Demonstration of a 1D KDE method overestimating variance in data generated from three distinct Gaussian distributions.

where  $N$ , is the total number of points within the training sample. This means, that for a given Kernel Distribution, maximising this equation—with respect to the usual over training conditions—will give us the best estimation of the underlying distribution.

The final consideration with KDE methodologies are boundary conditions. In order to quickly converge on effective solutions across the phase space, most KDE packages will compute a FFT (Fast Fourier Transform) of the space to break up signal frequency components. However, since the procedure effectively forces periodicity outside of the boundaries, most methods pad each dimension with zeros above and below the primary range. Since this is nonphysical it leads to discrepancies at the edges of the phase space.

In order to get resolve this issue, the KDE can be trained with forced reflections at the boundaries to reduce the edge effects. These are especially important in the modelling of the angular variables, which are otherwise forced to zero by the KDE.

## 6.2 Training Samples and Method Validation

The distributions in the previous section were produced from training data, and then applied to a flat distribution across the one-dimensional space. In order to normalise this output correctly across a multi-dimensional phase space (as is required of our analysis) we need to generate a flat phase space distribution across these dimensions, free of detector effects, as these will be modeled from a flat phase space LHCb Monte Carlo sample. The flatness of a space can be thought of in terms of density in dalitz space, which is

parameterised by partial decay widths. So for a 3 body decay the partial decay width,  $d\Gamma$ , is related to the decay of particle,  $M$ , into dalitz elements,  $dm_{12}, dm_{13}$ , by the equation

$$d\Gamma = \frac{1}{(2\pi)^3} \frac{1}{8M} \|M\|^2 dm_{12} dm_{13}. \quad (6.2)$$

In the non resonant case where the B meson decays directly to  $\pi^+\pi^-\pi^+\pi^-$  this differential rate, and by extension the density, will be constant (or flat) across the whole kinematic space. As such, we generate flat phase space Monte Carlo using the `TGENPHASESPACE` package from `ROOT` to generate in excess of one million flat candidates to validate the background model. In order for this normalisation sample to be consistent in phase space in our data, we have to apply the same set of kinematic cuts, as these veto entire regions of the phase space. These are given in Table 6.1.

Parameter
$[\pi\pi]_M < 1.1 GeV$
$[\pi\pi\pi]_M < 1.75 GeV$

Table 6.1: Kinematic selection cuts for MC particles.

To ensure that our phase space is correctly being modelled by the LHCb flat phase space Monte Carlo simulated sample and `TGENPHASESPACE` normalisation sample, we first check that the variable correlations are consistent (Figures 6.3, 6.4, 6.5).

What we expect to see is that the correlations are the same in the normalisation against flat phase space data. This indicates that the only difference between the samples is the efficiency, and hence the sample is suitable for efficiency training. Similarly, we expect that they vary more in the sideband data since that also contains resonant contributions and features unique to the background. Once these samples are validated, we train our KDE models against flat phase Monte Carlo sample data using variables that are presented in in Table 6.2.

Before training we also check the efficiency projections between data-taking periods for consistency. This is done using a Kolmogorov–Smirnov test to compare projections between data-taking periods [102]. As can be seen in Figure 6.6, all of the distributions fall within good statistical agreement of each other, implying similar phase space efficiencies across Run II. This has the consequence that the KDE efficiency model will have good agreement across periods of data-taking.

Parameter	Description
$s(\pi_1^+ \pi_1^-)$	Invariant mass of the $\rho(770)_1^0$ system
$s(\pi_2^+ \pi_2^-)$	Invariant mass of the $\rho(770)_2^0$ system
$\theta(\pi_1^+, \pi_1^-)$	Helicity angle in the $\rho(770)_1^0$ decay plane
$\theta(\pi_2^+, \pi_2^-)$	Helicity angle in the $\rho(770)_2^0$ decay plane
$\phi(\rho(770)_1^0, \rho(770)_2^0)$	Helicity angle between the $\rho(770)_1^0$ and $\rho(770)_2^0$ planes

Table 6.2: Training variables for the KDE efficiency training.

Finally, to validate this method of efficiency training we complete a null test where a KDE model is training and validated against the TGENPHASESPACE normalisation sample used in this analysis. The results that are presented in Figures 6.7 and 6.8 show that the technique performs well and is used to model the efficiency in the final plots presented in Chapter 7.

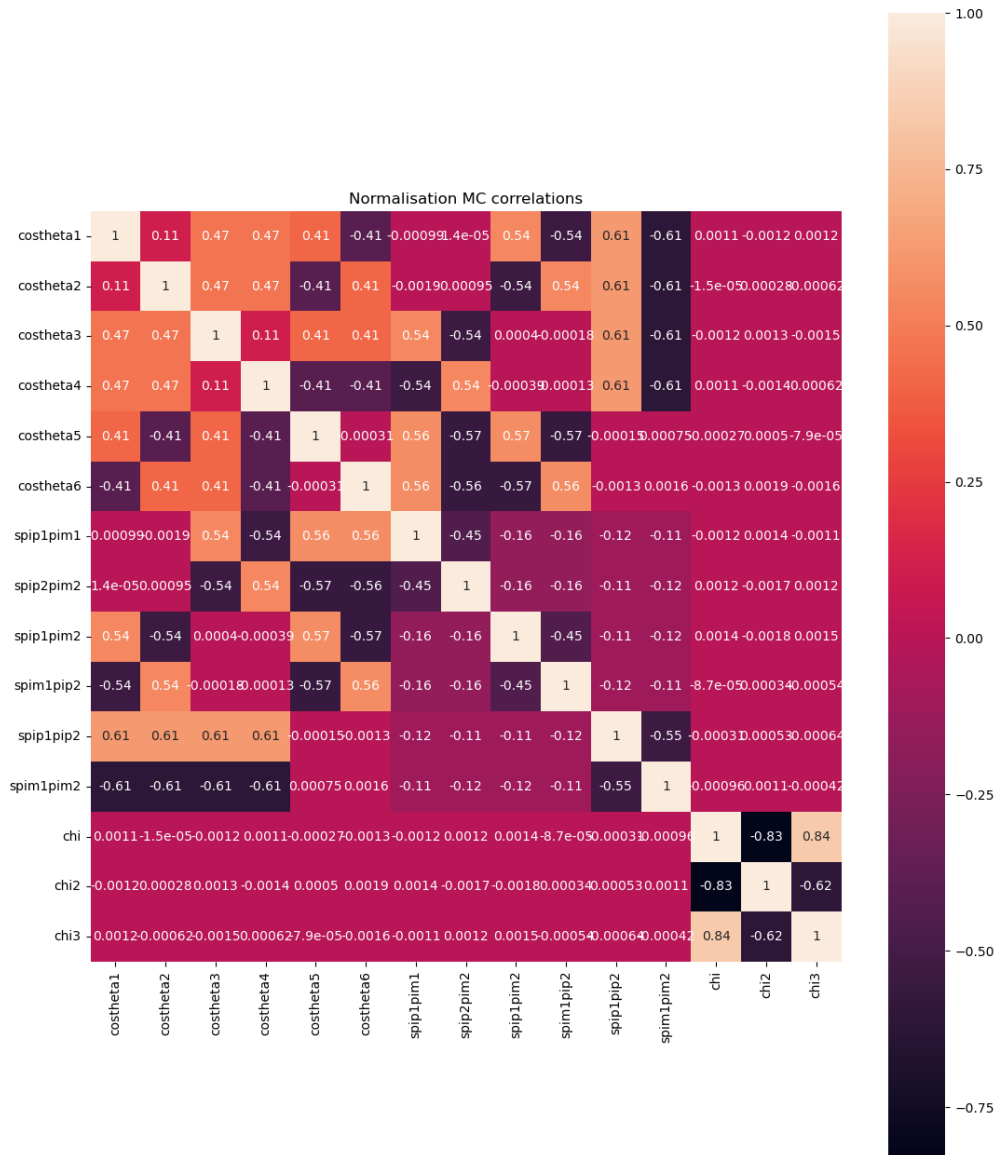


Figure 6.3: Correlation plot for the normalisation sample.

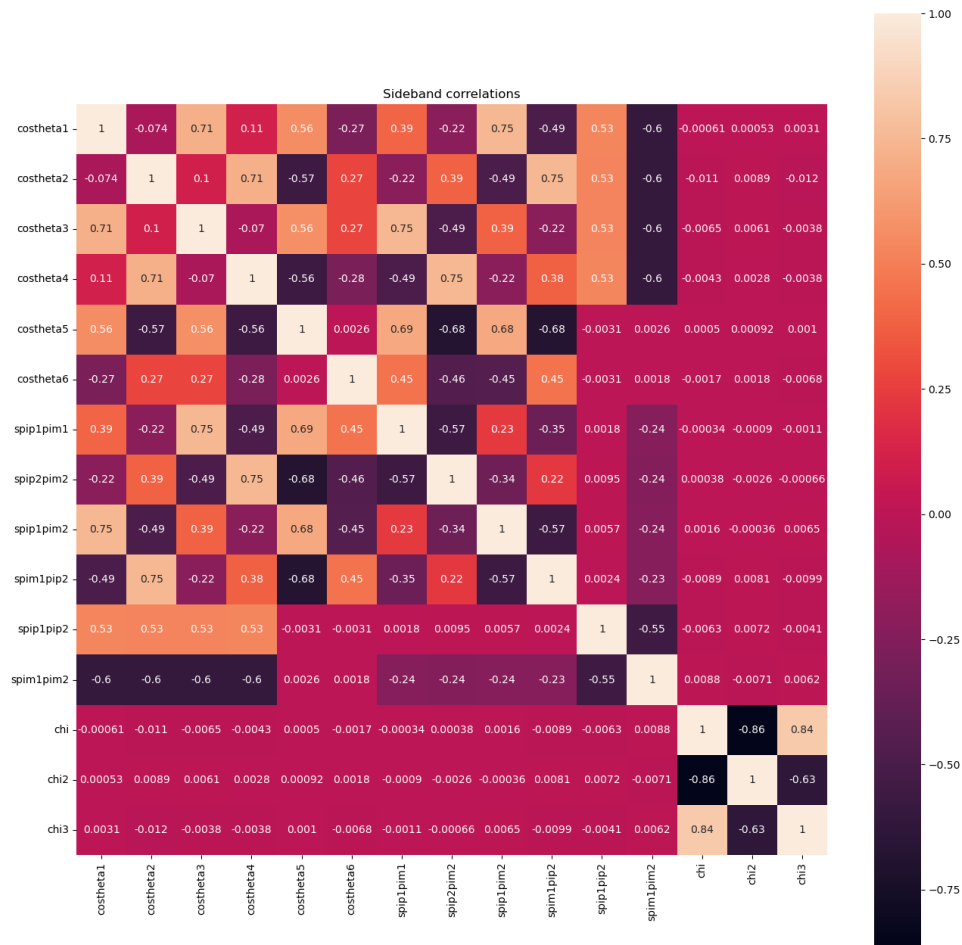


Figure 6.4: Correlation plot for the sideband sample.

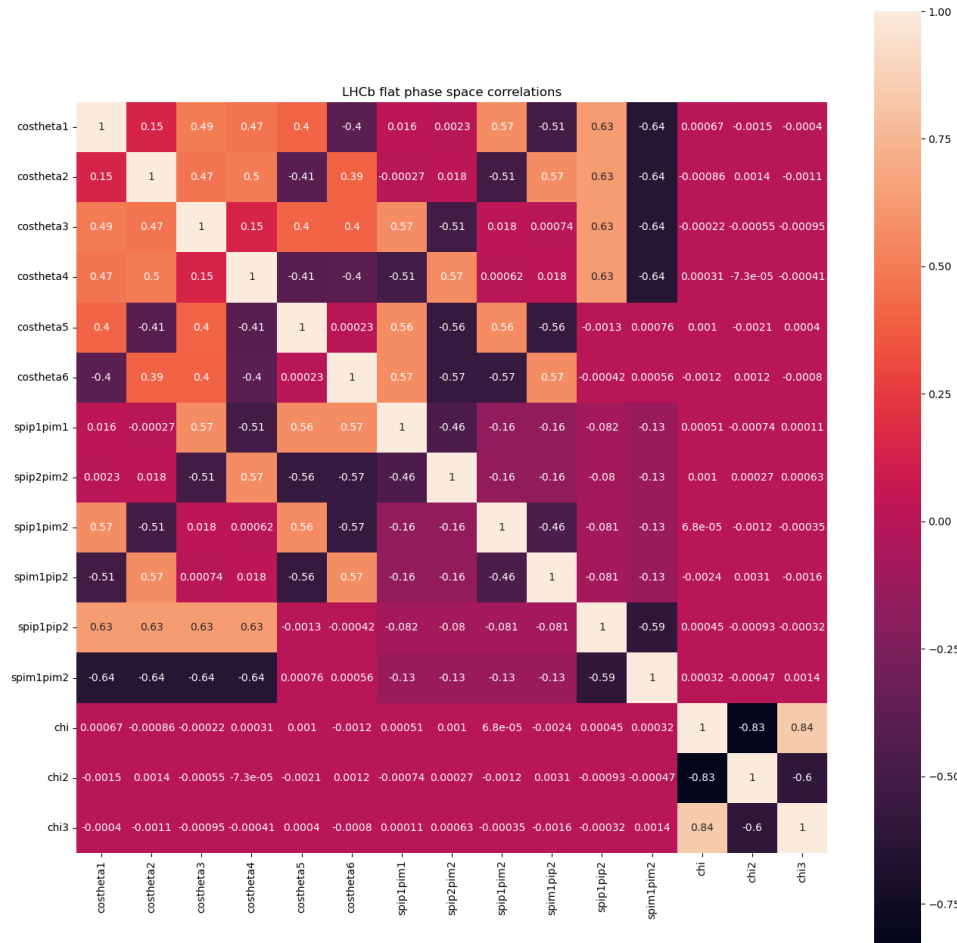
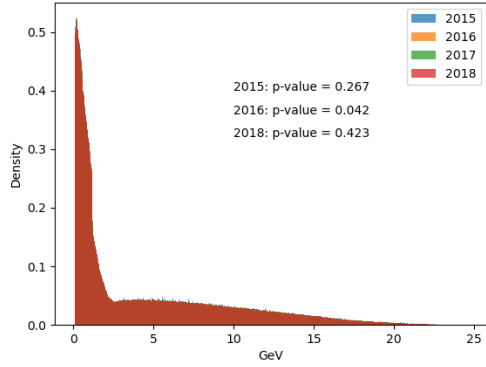
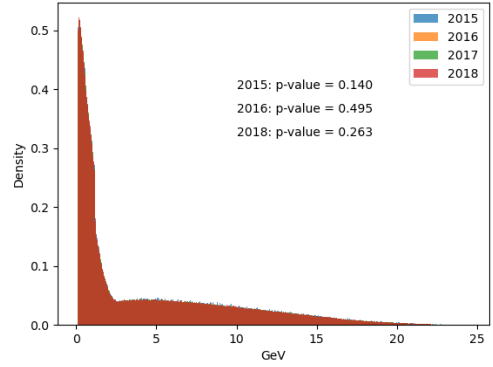


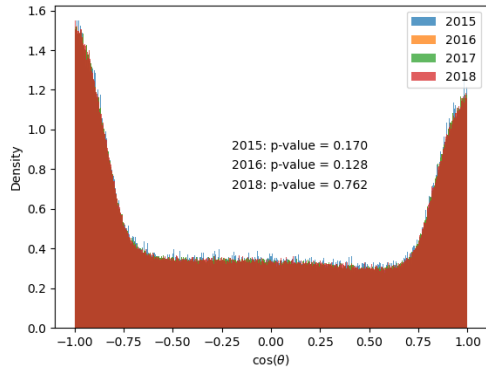
Figure 6.5: Correlation plot for the LHCb flat phase space sample.



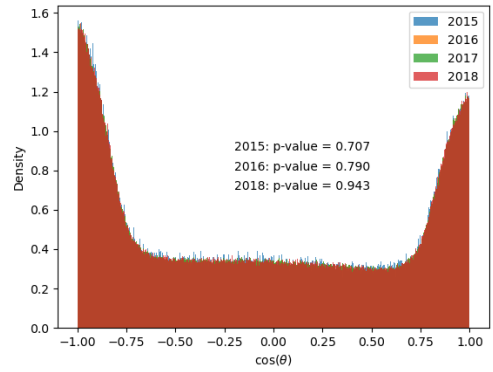
(a) KS test for  $s(\pi_1^+ \pi_1^-)$  training variable.



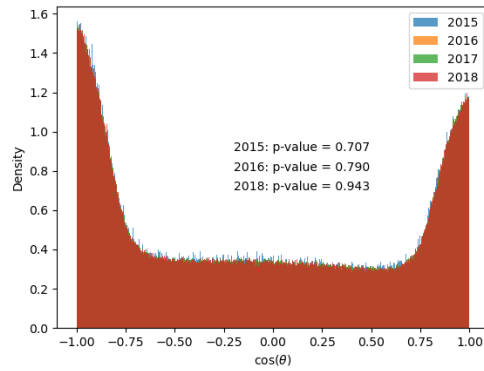
(b) KS test for  $s(\pi_2^+ \pi_2^-)$  training variable.



(c) KS test for  $\theta(\pi_1^+ \pi_1^-)$  training variable.



(d) KS test for  $\theta(\pi_2^+ \pi_2^-)$  training variable.



(e) KS test for  $\phi(\rho(770)_1^0 \rho(770)_2^0)$  training variable.

Figure 6.6: KS tests for the training variables used in the KDE efficiency training.

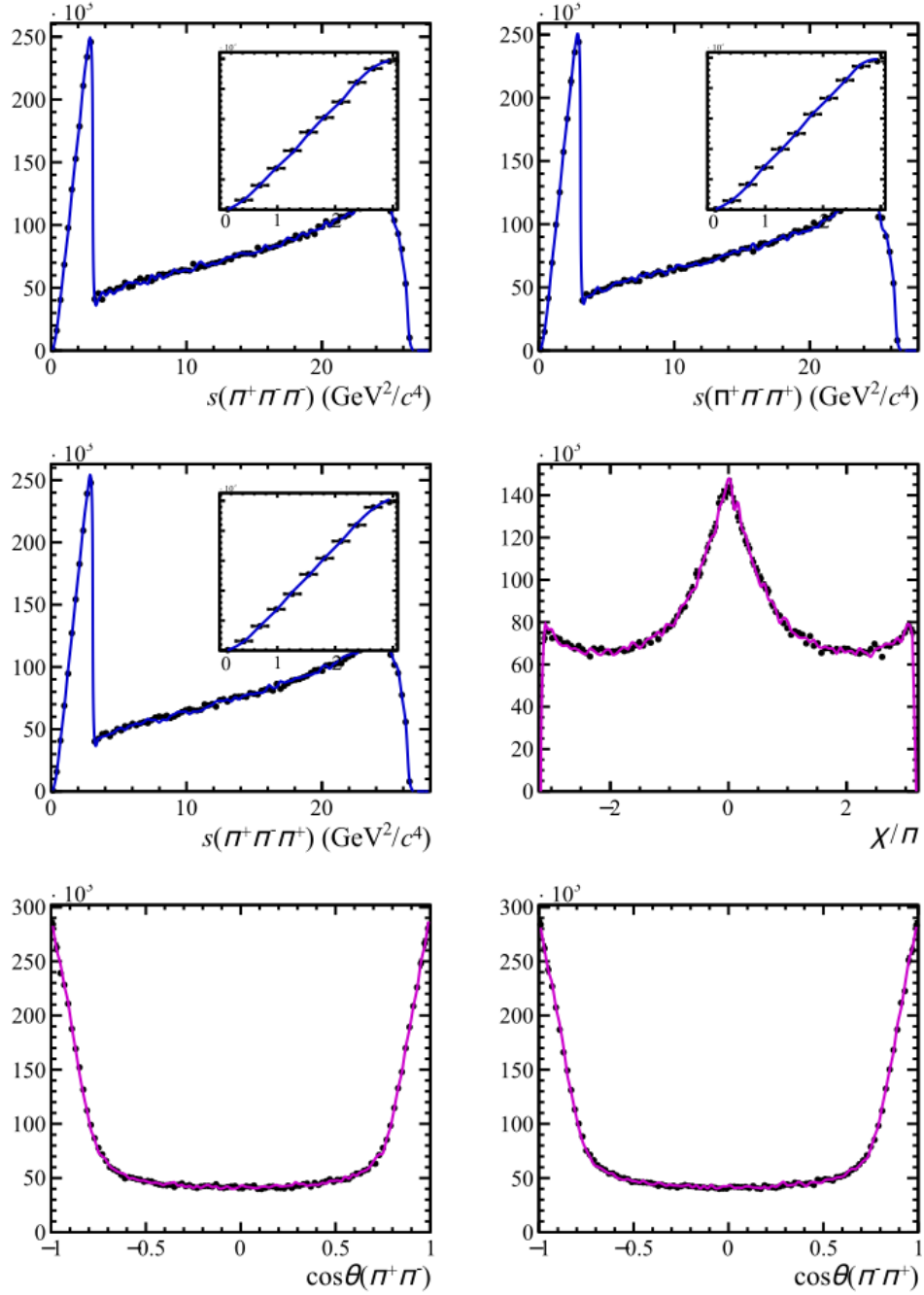


Figure 6.7: Null test validation plots (pt 1). The magenta plots indicate the training variables and the blue plots indicate the reconstructed projections. The overlay plots represent the kinematic cuts  $[\pi\pi]_S < 1.1\text{ GeV}$  and  $[\pi\pi\pi]_S < 3.06\text{ GeV}$ .

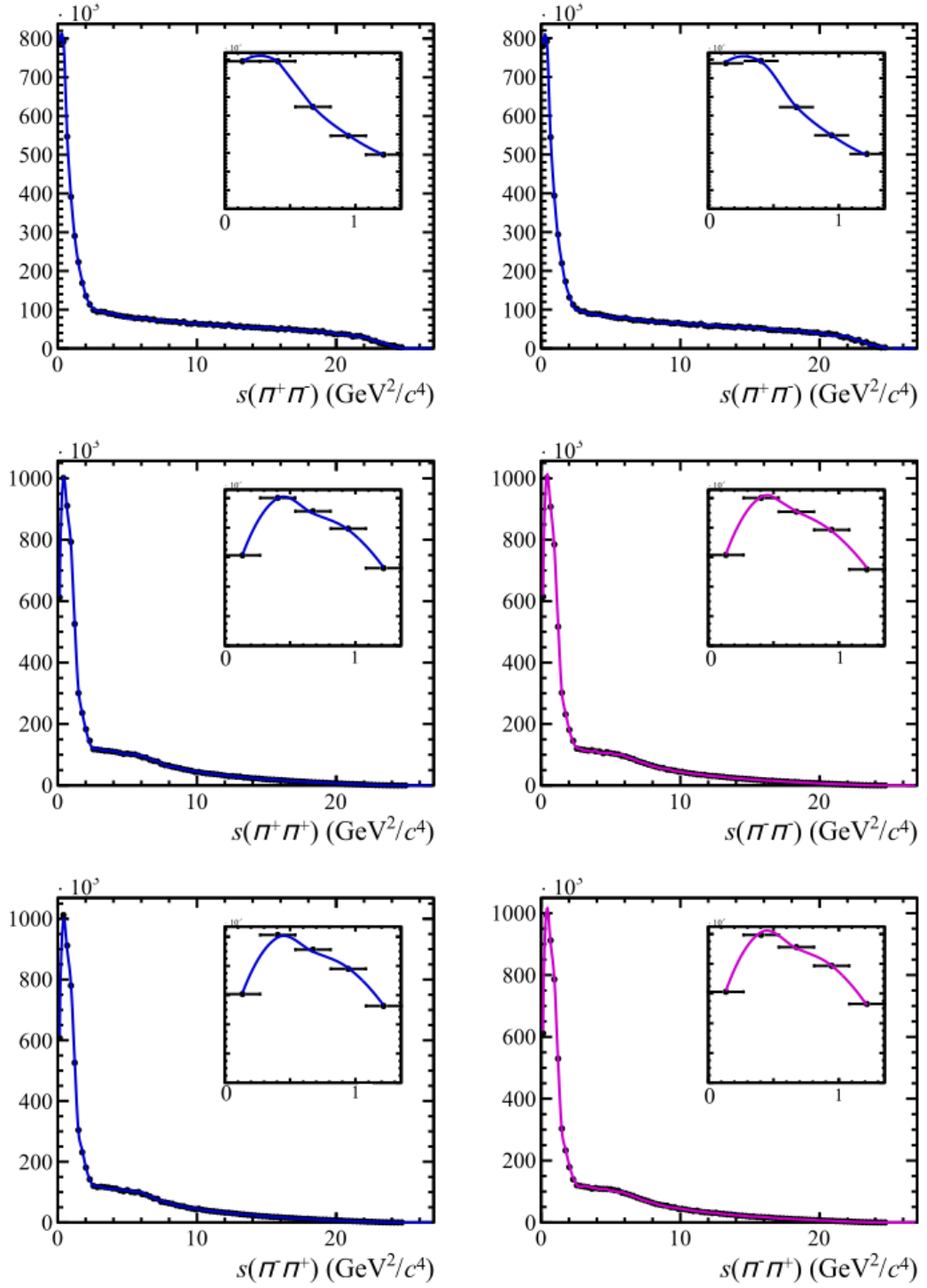


Figure 6.8: Null test validation plots (pt 2). The magenta plots indicate the training variables and the blue plots indicate the reconstructed projections. The overlay plots represent the kinematic cuts  $[\pi\pi]_S < 1.1 \text{ GeV}$  and  $[\pi\pi\pi]_S < 3.06 \text{ GeV}$

## 6.3 Background Parameterisation

Unlike the efficiencies, due to the increased complexity of the phase space, the background is parameterised using a folding reweighter that matches the normalisation sample to the sideband data. In essence, the reweighter calculates a correction to the weight of an event in flat phase space. For a one-dimensional space this can be simply calculated using,

$$m_{bin} = \frac{w_{target}}{w_{original}}, \quad (6.3)$$

where  $w_{target}$  is the weight of the target distribution, and  $w_{original}$  is the original weight of the original distribution. However, this method is overly simplistic for describing a multidimensional space and prone to large biases. For a multi-dimensional case such as ours we employ a Gradient Boosted Reweigher (GBReweigher) from the HEP-ML [103] project. This method extends the classical method with decision trees that can apply different weightings based on location in the phase space.

Using HEP-ML, the background model is trained across the overconstrained space of all the 2-body invariant mass distributions, and available helicity angles (Figure 6.9). All helicity angles used in the training are calculated in the centre of mass frame. The full list of training variables is given in Table 6.3.

Parameter	Description
$s(\pi_1^+ \pi_1^-)$	Invariant mass of the $\rho(770)_1^0$ system
$s(\pi_2^+ \pi_2^-)$	Invariant mass of the $\rho(770)_2^0$ system
$s(\pi_1^+ \pi_2^-)$	Invariant mass of the $\rho(770)_3^0$ system
$s(\pi_2^+ \pi_1^-)$	Invariant mass of the $\rho(770)_4^0$ system
$s(\pi_1^+ \pi_2^+)$	Invariant mass of the nonphysical $\pi_1^+ \pi_2^+$ system
$s(\pi_1^- \pi_2^-)$	Invariant mass of the nonphysical $\pi_1^- \pi_2^-$ system
$\theta(\pi_1^+, \pi_1^-)$	Helicity angle in the $\rho(770)_1^0$ decay plane
$\theta(\pi_2^+, \pi_2^-)$	Helicity angle in the $\rho(770)_2^0$ decay plane
$\theta(\pi_1^+, \pi_2^-)$	Helicity angle in the $\rho(770)_3^0$ decay plane
$\theta(\pi_2^+, \pi_1^-)$	Helicity angle in the $\rho(770)_4^0$ decay plane
$\theta(\pi_1^+, \pi_2^+)$	Helicity angle in the nonphysical $\pi_1^+ \pi_2^+$ system
$\theta(\pi_1^-, \pi_2^-)$	Helicity angle in the nonphysical $\pi_1^- \pi_2^-$ system
$\phi(\rho(770)_1^0, \rho(770)_2^0)$	Helicity angle between the $\rho(770)_1^0$ and $\rho(770)_2^0$ planes
$\phi(\rho(770)_3^0, \rho(770)_4^0)$	Helicity angle between the $\rho(770)_3^0$ and $\rho(770)_4^0$ planes
$\phi(\pi_1^+ \pi_2^+, \pi_1^- \pi_2^-)$	Helicity angle between the nonphysical $\pi\pi$ planes

Table 6.3: Training variables for the hep-ml background reweighter.

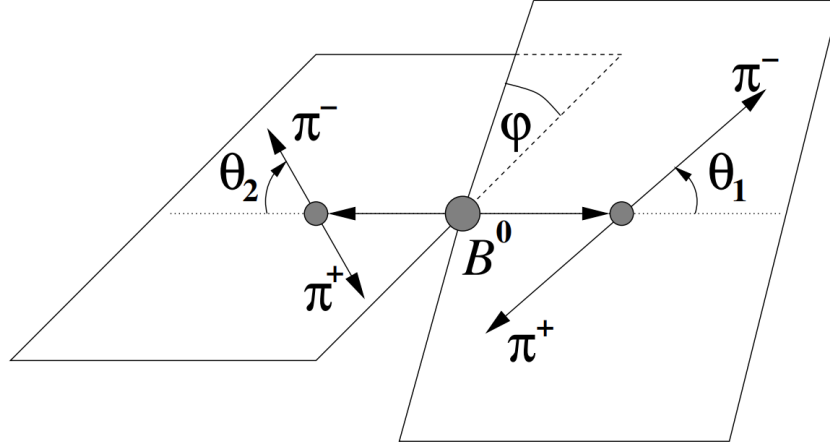


Figure 6.9: Helicity formalism for the  $B_d \rightarrow \rho(770)^0 \rho(770)^0$  system reproduced from [30]. The  $\theta$  angles represent the decay topology of the  $\rho$ , while the angle  $\phi$  represents the angle between the decay planes. Angles used in the reweighting are considered over all possible pion combinations.

The correct reproduction of the 3-body distributions were used to validate this approach to the background modelling. The training plots are presented in Figure 6.10, while the validation outputs are presented in Figure 6.11. The trained model for the background is based on a combined Run II sideband sample, where changes in background characteristics are assumed to be negligible between years.

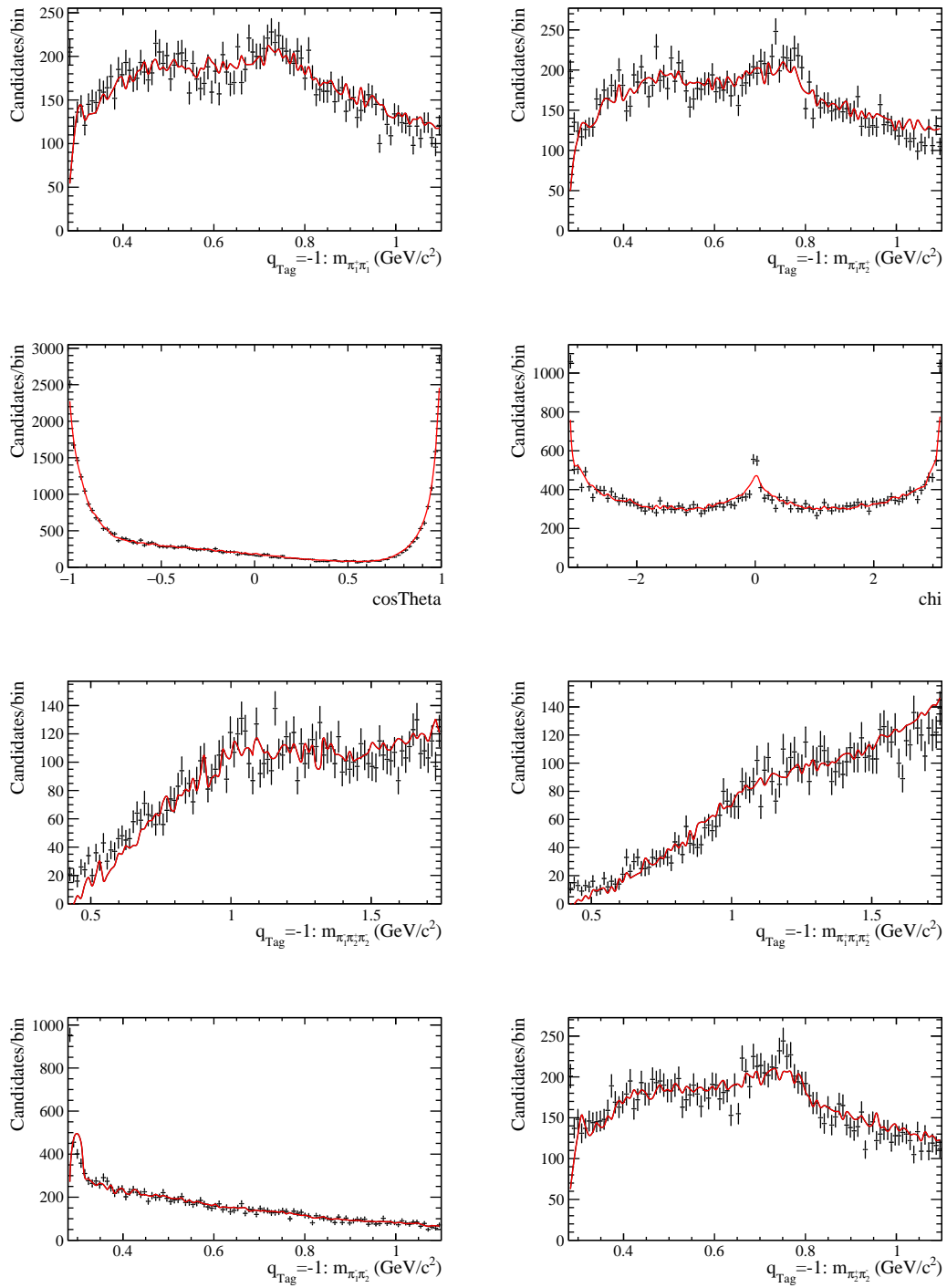


Figure 6.10: Sample of the training variables used in the multivariate reweighting to model the background

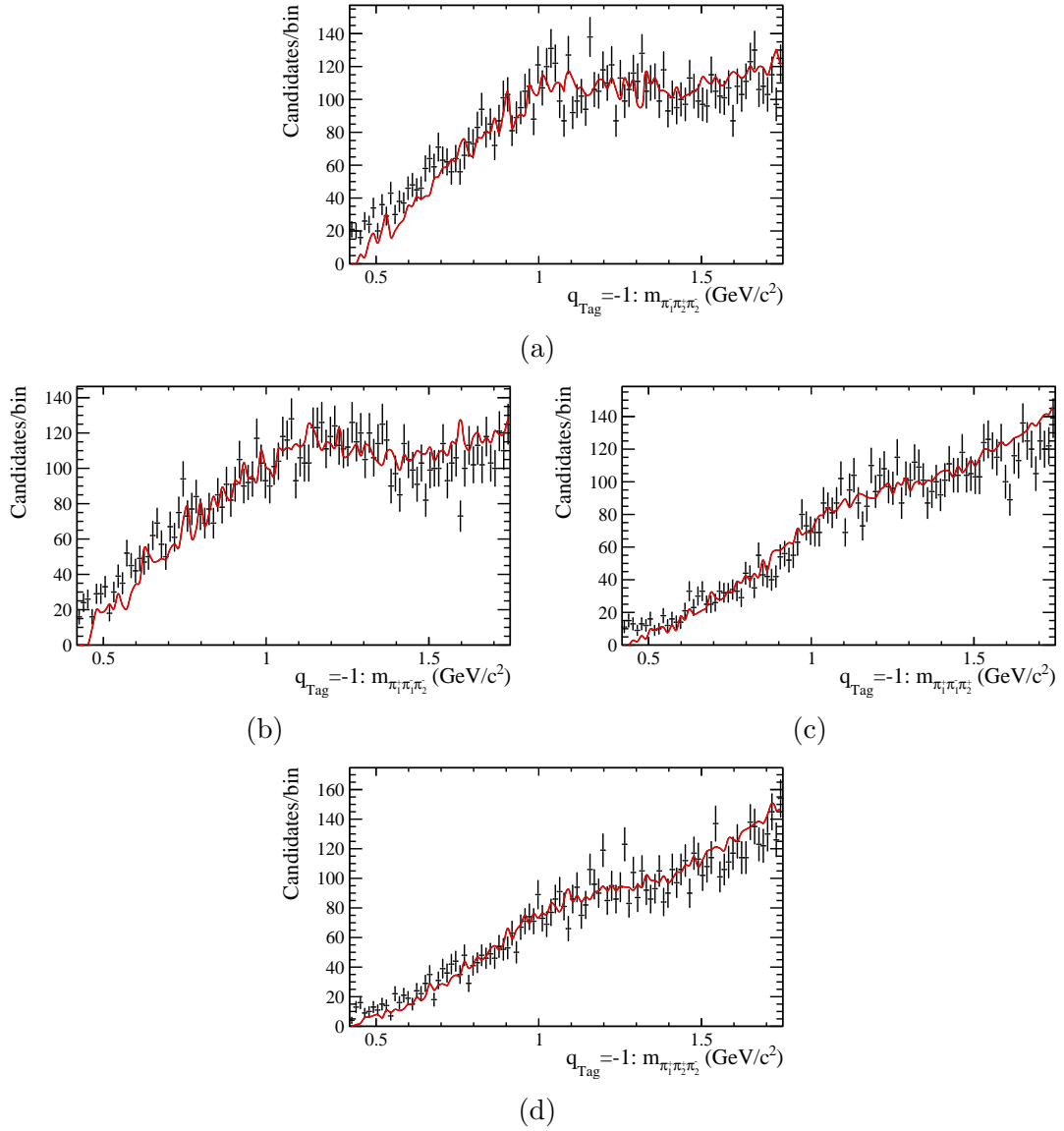


Figure 6.11: Background model reproduced from the training variables in the four possible 3-body combinations, (a)  $\pi_1^- \pi_2^+ \pi_3^+$ , (b)  $\pi_1^+ \pi_1^- \pi_2^-$ , (c)  $\pi_1^+ \pi_1^- \pi_2^+$  and (d)  $\pi_1^+ \pi_2^+ \pi_2^-$ . The fit is completed to Run 2 upper sideband data.

## 6.4 Fit Model

The full fit is calculated using an extended maximum likelihood function, where we use a custom implementation of MINUT2 [104] to find the function minimum. The likelihood function for a single PDF is given by,

$$\mathcal{L} = \frac{N_{pred}^{N_{obs}} e^{-N_{pred}}}{N_{obs}!} \prod_{i=1}^{N_{obs}} P(x_i; \theta), \quad (6.4)$$

where  $N_{pred}$  is the number of predicted events under the PDF and  $N_{obs}$  is the number of events in the sample  $x_i$ . Within the PDF  $P(x_i; \theta)$ , then  $x_i$  denotes each event for which to calculate each PDF, and  $\theta$  determines the input parameters. The best fit to this PDF is then given by the minimum of this function. For a likelihood function defined by multiple PDFs we can extend the likelihood function in the following way,

$$\mathcal{L} = \frac{\sum N_{pred}^{N_{obs}} e^{-\sum N_{pred}}}{N_{obs}!} \prod_{i=1}^{N_{obs}} \sum_{k=1} f_k P_k(x_i; \theta), \quad (6.5)$$

where  $f_k$  determines the fraction of the PDF  $k$  in the final fit. For ease of computation and convenience we usually work with this in the log-likelihood form making use of the relation,

$$f_i = \frac{N_{pred_i}}{N_{pred_i} + N_{pred_{i+1}} \dots N_{pred_n}}, \quad (6.6)$$

with the log-likelihood fit being fully described by,

$$\log(\mathcal{L}) = \log \left( \sum_{i=1} \sum_{k=1} N_k P_k(x_i, \theta) \right) - \sum_{k=1} N_k. \quad (6.7)$$

For the data fits completed in this analysis we consider two main contributions: that of a signal PDF constructed of multiple isobar structures and of a background PDF derived empirically from data. In the context of the full fit, the log-likelihood function is given by,

$$\log(\mathcal{L}) = \log \left( \sum_{i=1} \left( \frac{N_{sig} [\sum_{k=1} P_k(x_i, \theta)] \sigma_{sig}}{Norm_{sig}} + \frac{N_{bkg} P_{bkg}(x_i)}{Norm_{bkg}} \right) \right) - (N_{sig} + N_{bkg}), \quad (6.8)$$

where  $N_{sig,bkg}$  are the signal and background yields,  $\sigma_{sig}$  is the KDE calculated signal efficiencies,  $P_{bkg}$  is the reweighted background calculation independent of the fit parameters,  $P_k(x_i, \theta)$  represent the individual isobars that make up the signal model with respect to model parameters  $\theta$ , and  $Norm_{sig,bkg}$  represents the signal and background normalisation functions respectively. It is important to note that the amplitude normalisation is with respect to the calculated efficiencies. This is not needed in the background normalisation as the model already includes the efficiency. The full set of amplitudes  $P_k(x_i, \theta)$  are described as,

$$\begin{aligned}
P_{total} = & \lambda_{\rho_S^0 \rho_S^0} a_{\rho_S^0 \rho_S^0} A(\theta)_{\rho_S^0 \rho_S^0} + \lambda_{\rho_P^0 \rho_P^0} a_{\rho_P^0 \rho_P^0} A(\theta)_{\rho_P^0 \rho_P^0} + \\
& \lambda_{\rho_D^0 \rho_D^0} a_{\rho_D^0 \rho_D^0} A(\theta)_{\rho_D^0 \rho_D^0} + \\
& \lambda_{a_1(1260) \pm \pi^\mp} a_{a_1(1260) \pm \pi^\mp} A(\theta)_{a_1(1260) \pm \pi^\mp} + \\
& \lambda_{a_1(1640) \pm \pi^\mp} a_{a_1(1640) \pm \pi^\mp} A(\theta)_{a_1(1640) \pm \pi^\mp} + \\
& \lambda_{a_2(1320) \pm \pi^\mp} a_{a_2(1320) \pm \pi^\mp} A(\theta)_{a_2(1320) \pm \pi^\mp} + \\
& \lambda_{\rho_S^0 \pi \pi} a_{\rho_S^0 \pi \pi} A(\theta)_{\rho_S^0 \pi \pi} + \lambda_{\pi \pi \pi \pi} a_{\pi \pi \pi \pi} A(\theta)_{\pi \pi \pi \pi},
\end{aligned} \tag{6.9}$$

where  $\lambda_i$ , defines the complex CP violation coupling  $\{dx_i, dy_i\}$ , where  $dx_i$  is the real contribution, and  $dy_i$  is the imaginary contribution to this coupling,  $a_i$ , defines the complex amplitude coupling  $\{x_i, y_i\}$ , where  $x_i$  is the real contribution, and  $y_i$  is the imaginary contribution to this coupling, and  $A(\theta)$  embodies the full amplitude calculation inclusive of spin factors. Individual spin cases are represented by subscripts and are included individually within the fit and model. All  $\rho\rho$  amplitudes are inclusive of  $\rho - \omega$  mixing and use the Gounaris–Sakuri propagator. Similarly all  $\pi\pi$  modes have contributions from the K-matrix formalism as outlined in Ref. [105].

For the flavour and time integrated case  $\lambda_{contribution}$  is fixed to  $\{1, 0\}$  since we have no sensitivity to **CP** violation in this fit configuration. The direction of the coupling is arbitrary in the context of the fit as long as all contributions are aligned identically. Similarly, in order to fix the relative couplings of the final fit, we have fixed  $a_{[\rho(770)^0 \rho(770)^0]_S}$  to  $\{1, 0\}$  aligning it with the real axis. As such, all couplings reported from the fit are relative to this definition. Masses and widths of intermediates have been fixed from PDG values [4]. The  $\rho - \omega$  mixing parameters are fixed from Ref. [34]. Finally, the signal and background yields are fixed from the invariant mass fits compiled in Chapter 5. The fixed parameters in the fit are given in table 6.4. Floating parameters and their fit values are

quoted in the next chapter.

Parameter	Description	Value
NSig	Signal Events 2016(2017)(2018)	36930(38300)(44814)
NBkg	Background Events 2016(2017)(2018)	15389(13408)(15769)
m_rho0	$\rho(770)^0$ charmless pole mass	0.7690
w_rho0	$\rho(770)^0$ width	0.1509
m_omega	$\omega$ charmless pole mass	0.78265
w_omega	$\omega$ width	0.00849
m_a11260	$a_1(1260)$ charmless pole mass	1.225
w_a11260	$a_1(1260)$ width	0.430
m_a21320	$a_2(1320)$ charmless pole mass	1.3169
w_a21320	$a_2(1320)$ width	0.1050
rw_delta	$\rho - \omega$ electromagnetic coupling magnitude	0.00215
rw_pdelta	$\rho - \omega$ electromagnetic coupling phase	022
xrho0rho0_S	$[\rho(770)^0\rho(770)^0]_S$ amplitude real strong coupling	1
yrho0rho0_S	$[\rho(770)^0\rho(770)^0]_S$ amplitude imaginary strong coupling	0

Table 6.4: Parameters fixed in the amplitude fits.

## 6.5 Chapter Summary

This chapter has presented the two techniques required to fully parameterise the background and efficiencies of the fit model. These methods were the KDE method used to model the signal efficiencies, and the HEP-ML reweighter used to parameterise the background. Systematic studies into the choices of background sample and model still need to be investigated. Sideband data is used as a standard combinatorial proxy by LHCb [30]. However, the effects of varying both the BDT and particle identification cuts needs to be understood to constrain any uncertainties. There is also an argument to use an sWeights instead of an empirical model [106]. In the case of this analysis, this alternate method could propagate large uncertainties from the invariant mass fits so has not been investigated further. The chapter has also presented the full fit strategy with respect to the available model parameters. The model parameters that require fixing in to attain a meaningful amplitude model have been defined and discussed. The outputs from the full time and flavour integrated fits will be presented in the next chapter.

# Chapter 7

## Results and Conclusions

I always consider every place worth exploring once—just in case there’s a thirty foot flaming sign divulging the secret of life, that no one has told me about.

---

Tibor Fischer

All good experiments must come to some conclusion, and although this chapter will discuss the outlook beyond the measurements presented, it will be focused on outputs from the time and flavour-integrated analysis. This chapter will present the fit results, the fit fractions, and a measurement of the Longitudinal Polarisation Fraction,  $f_L$ , measurements for the  $B^0 \rightarrow \rho(770)^0 \rho(770)^0$  system. There will be some limited discussion of systematic uncertainties with respect to the final measurement, before summarising the result, and discussing the outlook for extension to a time and flavour-dependent fit.

### 7.1 Fit Results

The amplitude fits described in Chapter 6 were carried out across the 2016, 2017, 2018 and full Run 2 samples—2015 data was only included in the Run 2 sample as it was statistically limited for a standalone fit. For each fit, we float the parameters presented in Table 7.1.

For each of the samples we present a series of projections—including the non-physical 2-body projections constructed from same-sign pions. The full breakdown of the projec-

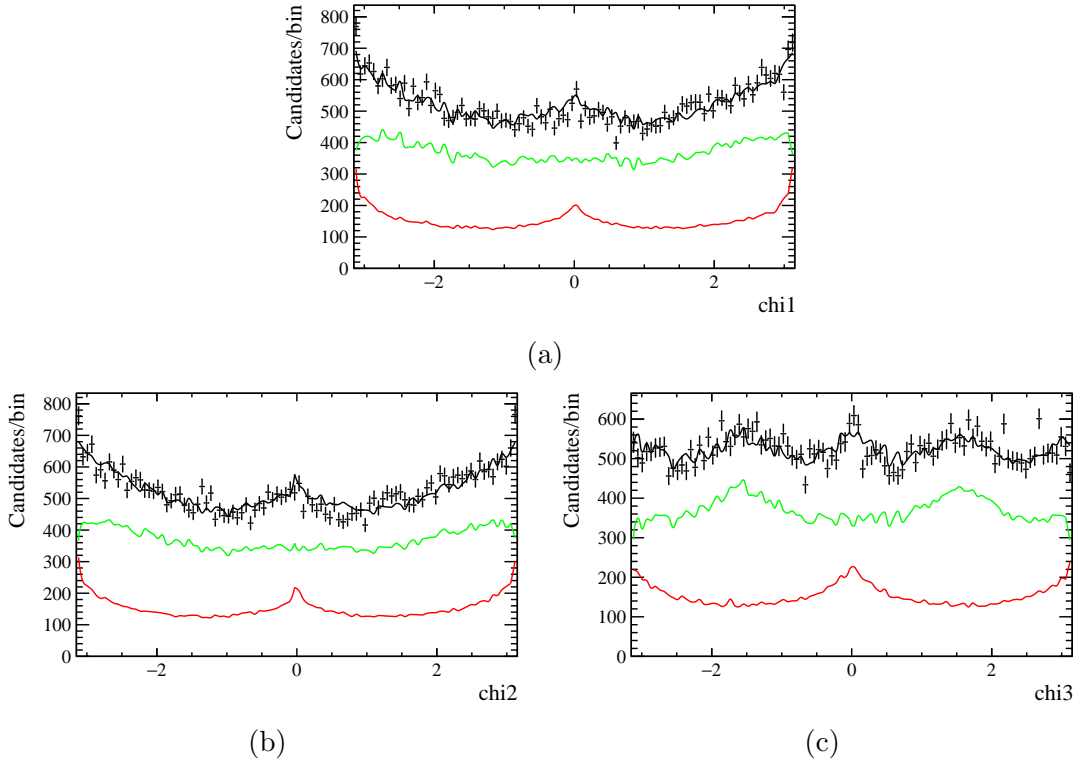


Figure 7.1: 2016 amplitude fits to the three  $\phi$  projections, (a)  $\phi(\rho_1\rho_2)$ , (b)  $\phi(\rho_3\rho_4)$ , (c)  $\phi(\rho_5\rho_6)$ —unphysical. Signal (Green) contributions and Background (Red) contributions are presented in the plots.

tions are three  $\phi$  projections that represent the helicity angle between the  $\rho(770)_i^0$  and  $\rho(770)_j^0$  planes for  $i \neq j$ . Six  $\cos(\theta)_{ij}$  ( $i \neq j$ ) projections that represent the helicity angle in the  $\rho(770)_i^0$  decay plane between the daughter pions. Six  $m(\pi_i\pi_j)$  ( $i \neq j$ ) projections for the invariant mass of the 2-body combinations, and four  $m(\pi_i\pi_j\pi_k)$  ( $i \neq j \neq k$ ) projections for the invariant mass of the 3-body combinations. Figures 7.1, 7.2, 7.3 and 7.4, are the projections for 2016. Figures 7.5, 7.6, 7.7 and 7.8, are the projections for 2017. Figures 7.9, 7.10, 7.11 and 7.12, are the projections for 2018 and Figures 7.13, 7.14, 7.15 and 7.16, are the projections for the full Run 2 data collected.

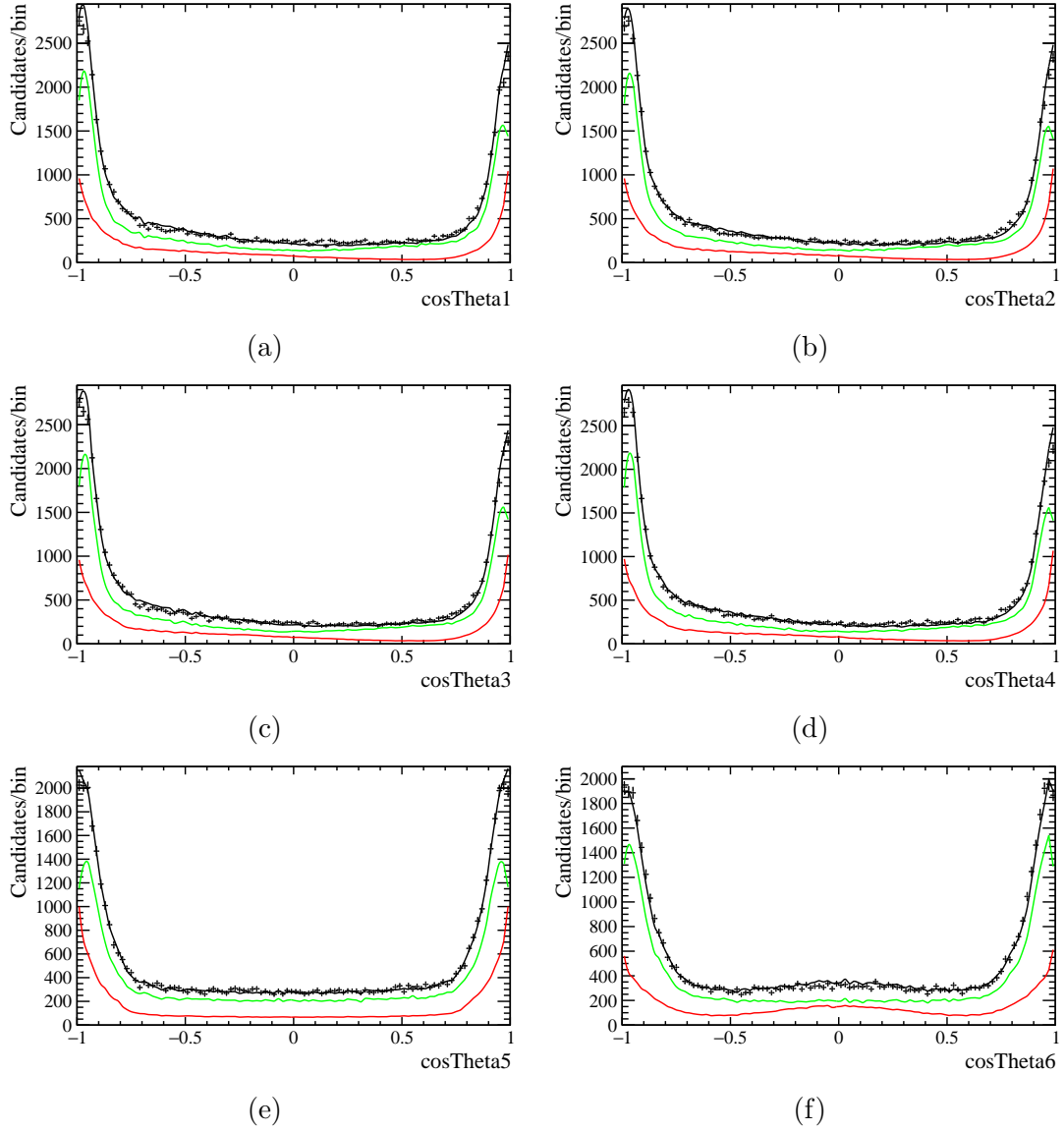


Figure 7.2: 2016 amplitude fits to the six  $\cos(\theta)_{ij}$  ( $i \neq j$ ) projections, (a)  $\cos(\theta(\pi_1^+ \pi_1^-))$ , (b)  $\cos(\theta(\pi_2^+ \pi_2^-))$ , (c)  $\cos(\theta(\pi_1^+ \pi_2^-))$ , (d)  $\cos(\theta(\pi_2^+ \pi_1^-))$ , (e)  $\cos(\theta(\pi_1^- \pi_2^-))$ —unphysical, (f)  $\cos(\theta(\pi_1^+ \pi_2^+))$ —unphysical. Signal (Green) contributions and Background (Red) contributions are presented in the plots.

Parameter	Description
xa1ppim	$B^0 \rightarrow a_1(1260)^\pm \pi^\mp$ amplitude real strong coupling
ya1ppim	$B^0 \rightarrow a_1(1260)^\pm \pi^\mp$ amplitude imaginary strong coupling
xa1_rpS	$a_1(1260)^\pm \rightarrow \rho(770)_S^0 \pi^\pm$ amplitude real strong coupling
ya1_rpS	$a_1(1260)^\pm \rightarrow \rho(770)_S^0 \pi^\pm$ amplitude imaginary strong coupling
xa1_rpD	$a_1(1260)^\pm \rightarrow \rho(770)_D^0 \pi^\pm$ amplitude real strong coupling
ya1_rpD	$a_1(1260)^\pm \rightarrow \rho(770)_D^0 \pi^\pm$ amplitude imaginary strong coupling
xa1_KMP1	$a_1(1260)^\pm \rightarrow \pi^\pm \pi^\mp \pi^\pm$ K-matrix production pole <sub>1</sub> real strong coupling
ya1_KMP1	$a_1(1260)^\pm \rightarrow \pi^\pm \pi^\mp \pi^\pm$ K-matrix production pole <sub>1</sub> imaginary strong coupling
xa1_KMP2	$a_1(1260)^\pm \rightarrow \pi^\pm \pi^\mp \pi^\pm$ K-matrix production pole <sub>2</sub> real strong coupling
ya1_KMP2	$a_1(1260)^\pm \rightarrow \pi^\pm \pi^\mp \pi^\pm$ K-matrix production pole <sub>2</sub> imaginary strong coupling
xa1_KMS1	$a_1(1260)^\pm \rightarrow \pi^\pm \pi^\mp \pi^\pm$ K-matrix $SV P_1$ production real strong coupling
ya1_KMS1	$a_1(1260)^\pm \rightarrow \pi^\pm \pi^\mp \pi^\pm$ K-matrix $SV P_1$ production imaginary strong coupling
xa1_KMS2	$a_1(1260)^\pm \rightarrow \pi^\pm \pi^\mp \pi^\pm$ K-matrix $SV P_2$ production real strong coupling
ya1_KMS2	$a_1(1260)^\pm \rightarrow \pi^\pm \pi^\mp \pi^\pm$ K-matrix $SV P_2$ production imaginary strong coupling
xa2ppim	$B^0 \rightarrow a_2(1320)^\pm \pi^\mp$ amplitude real strong coupling
ya2ppim	$B^0 \rightarrow a_2(1320)^\pm \pi^\mp$ amplitude imaginary strong coupling
xa2_rpD	$a_2(1320)^\pm \rightarrow \rho(770)_D^0 \pi^\pm$ amplitude real strong coupling
ya2_rpD	$a_2(1320)^\pm \rightarrow \rho(770)_D^0 \pi^\pm$ amplitude imaginary strong coupling
xa1640ppim	$B^0 \rightarrow a_1(1640)^\pm \pi^\mp$ amplitude real strong coupling
ya1640ppim	$B^0 \rightarrow a_1(1640)^\pm \pi^\mp$ amplitude imaginary strong coupling
xrho0omega	$\rho - \omega$ amplitude real strong coupling
yrho0omega	$\rho - \omega$ amplitude imaginary strong coupling
xrho0rho0_P	$B^0 \rightarrow [\rho(770)^0 \rho(770)^0]_P$ amplitude real strong coupling
yrho0rho0_P	$B^0 \rightarrow [\rho(770)^0 \rho(770)^0]_P$ amplitude imaginary strong coupling
xrho0rho0_D	$B^0 \rightarrow [\rho(770)^0 \rho(770)^0]_D$ amplitude real strong coupling
yrho0rho0_D	$B^0 \rightarrow [\rho(770)^0 \rho(770)^0]_D$ amplitude imaginary strong coupling
x_KMP1	$\rho(770)^0 \rightarrow \pi^+ \pi^-$ K-matrix production pole <sub>1</sub> real strong coupling
y_KMP1	$\rho(770)^0 \rightarrow \pi^+ \pi^-$ K-matrix production pole <sub>1</sub> imaginary strong coupling
x_KMP2	$\rho(770)^0 \rightarrow \pi^+ \pi^-$ K-matrix production pole <sub>2</sub> real strong coupling
y_KMP2	$\rho(770)^0 \rightarrow \pi^+ \pi^-$ K-matrix production pole <sub>2</sub> imaginary strong coupling
x_KMS1	$\rho(770)^0 \rightarrow \pi^+ \pi^-$ K-matrix $SV P_1$ production real strong coupling
y_KMS1	$\rho(770)^0 \rightarrow \pi^+ \pi^-$ K-matrix $SV P_1$ production imaginary strong coupling
x_KMS2	$\rho(770)^0 \rightarrow \pi^+ \pi^-$ K-matrix $SV P_2$ production real strong coupling
y_KMS2	$\rho(770)^0 \rightarrow \pi^+ \pi^-$ K-matrix $SV P_2$ production imaginary strong coupling
xrho0KM	$B^0 \rightarrow \rho(770)^0 \pi^+ \pi^-$ amplitude real strong coupling
yrho0KM	$B^0 \rightarrow \rho(770)^0 \pi^+ \pi^-$ amplitude imaginary strong coupling
xKMKM	$B^0 \rightarrow \pi^+ \pi^- \pi^+ \pi^-$ amplitude real strong coupling
yKMKM	$B^0 \rightarrow \pi^+ \pi^- \pi^+ \pi^-$ amplitude imaginary strong coupling

Table 7.1: Parameters floated in the amplitude fits.

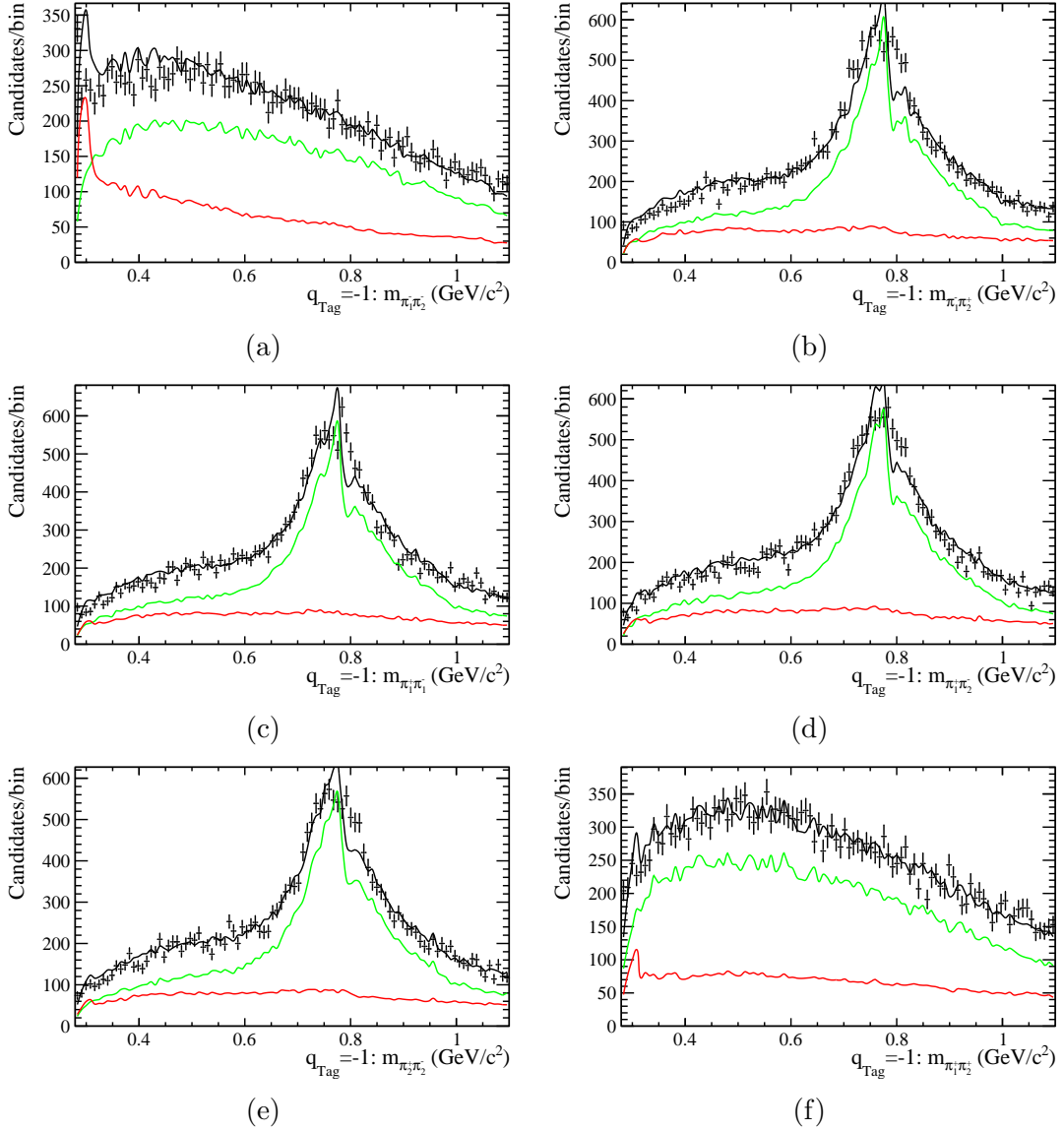


Figure 7.3: 2016 amplitude fits to the Six  $m(\pi_i \pi_j)$  ( $i \neq j$ ) projections, (a)  $\pi_1^- \pi_2^-$ —unphysical, (b)  $\pi_1^- \pi_2^+$ , (c)  $\pi_1^+ \pi_1^-$ , (d)  $\pi_1^+ \pi_2^-$ , (e)  $\pi_2^+ \pi_2^-$ , (f)  $\pi_1^+ \pi_2^+$ —unphysical. Signal (Green) contributions and Background (Red) contributions are presented in the plots.

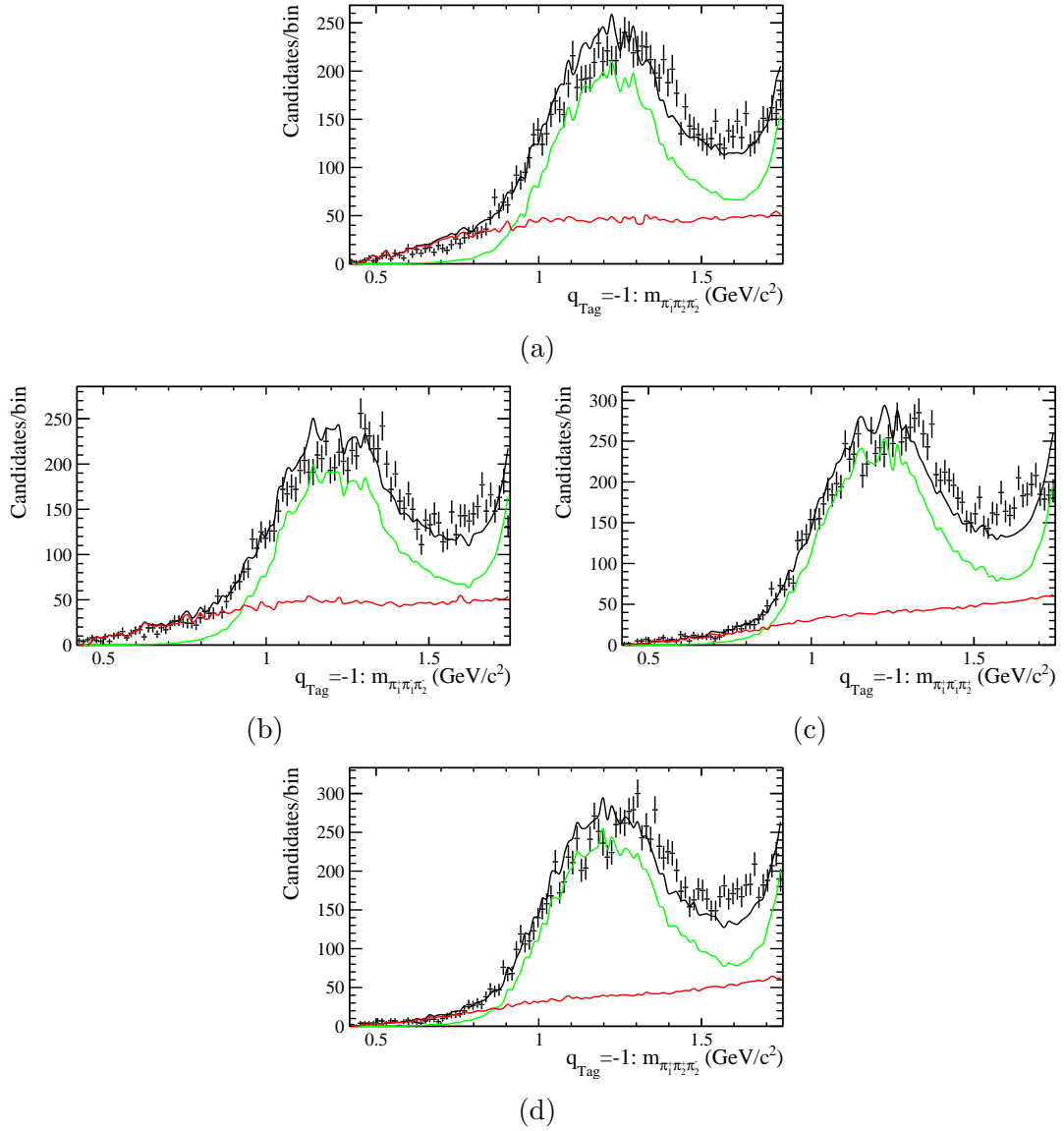


Figure 7.4: 2016 amplitude fits to the four  $m(\pi_i \pi_j \pi_k)$  projections, (a)  $\pi_1^- \pi_2^+ \pi_2^+$ , (b)  $\pi_1^+ \pi_1^- \pi_2^-$ , (c)  $\pi_1^+ \pi_1^- \pi_2^+$  and (d)  $\pi_1^+ \pi_2^+ \pi_2^-$ . Signal (Green) contributions and Background (Red) contributions are presented in the plots.

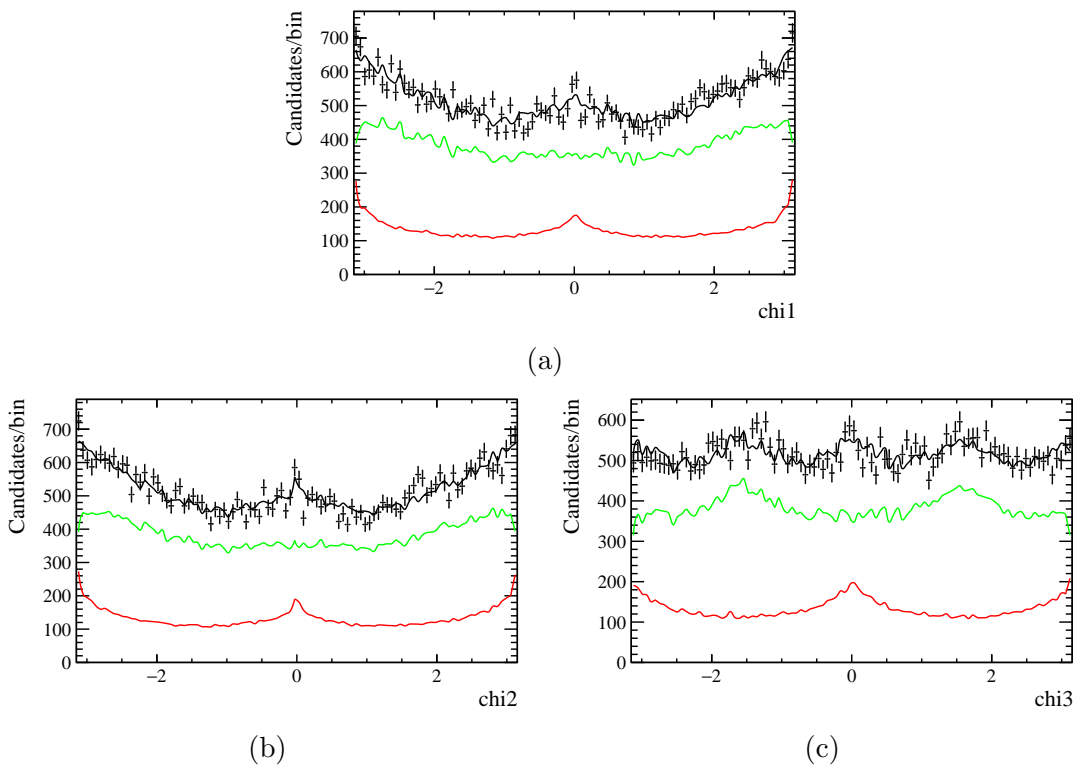


Figure 7.5: 2017 amplitude fits to the three  $\phi$  projections, (a)  $\phi(\rho_1\rho_2)$ , (b)  $\phi(\rho_3\rho_4)$ , (c)  $\phi(\rho_5\rho_6)$ —unphysical. Signal (Green) contributions and Background (Red) contributions are presented in the plots.

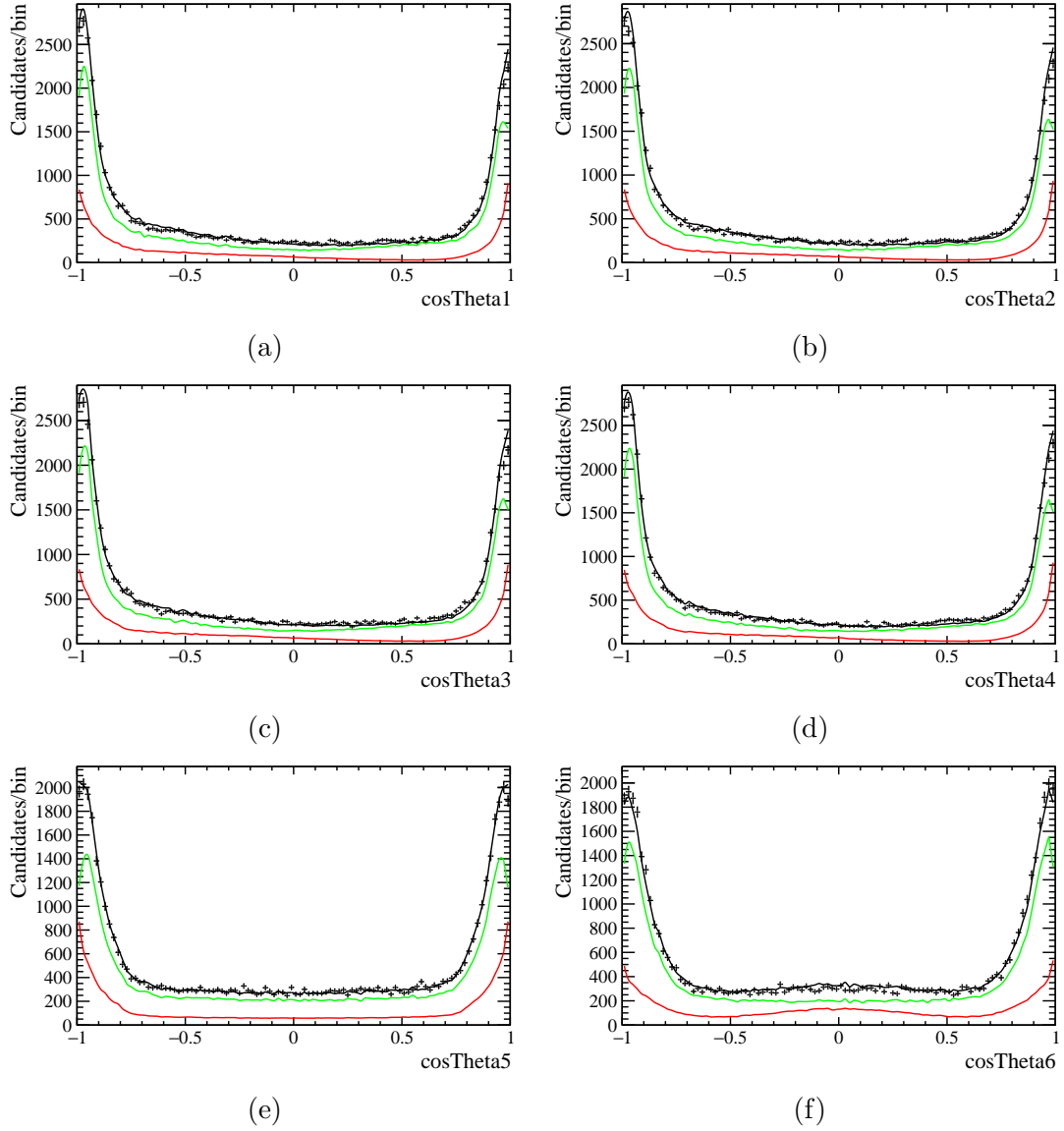


Figure 7.6: 2017 amplitude fits to the six  $\cos(\theta)_{ij}$  ( $i \neq j$ ) projections, (a)  $\cos(\theta(\pi_1^+ \pi_1^-))$ , (b)  $\cos(\theta(\pi_2^+ \pi_2^-))$ , (c)  $\cos(\theta(\pi_1^+ \pi_2^-))$ , (d)  $\cos(\theta(\pi_2^+ \pi_1^-))$ , (e)  $\cos(\theta(\pi_1^- \pi_2^-))$ —unphysical, (f)  $\cos(\theta(\pi_1^+ \pi_2^+))$ —unphysical. Signal (Green) contributions and Background (Red) contributions are presented in the plots.

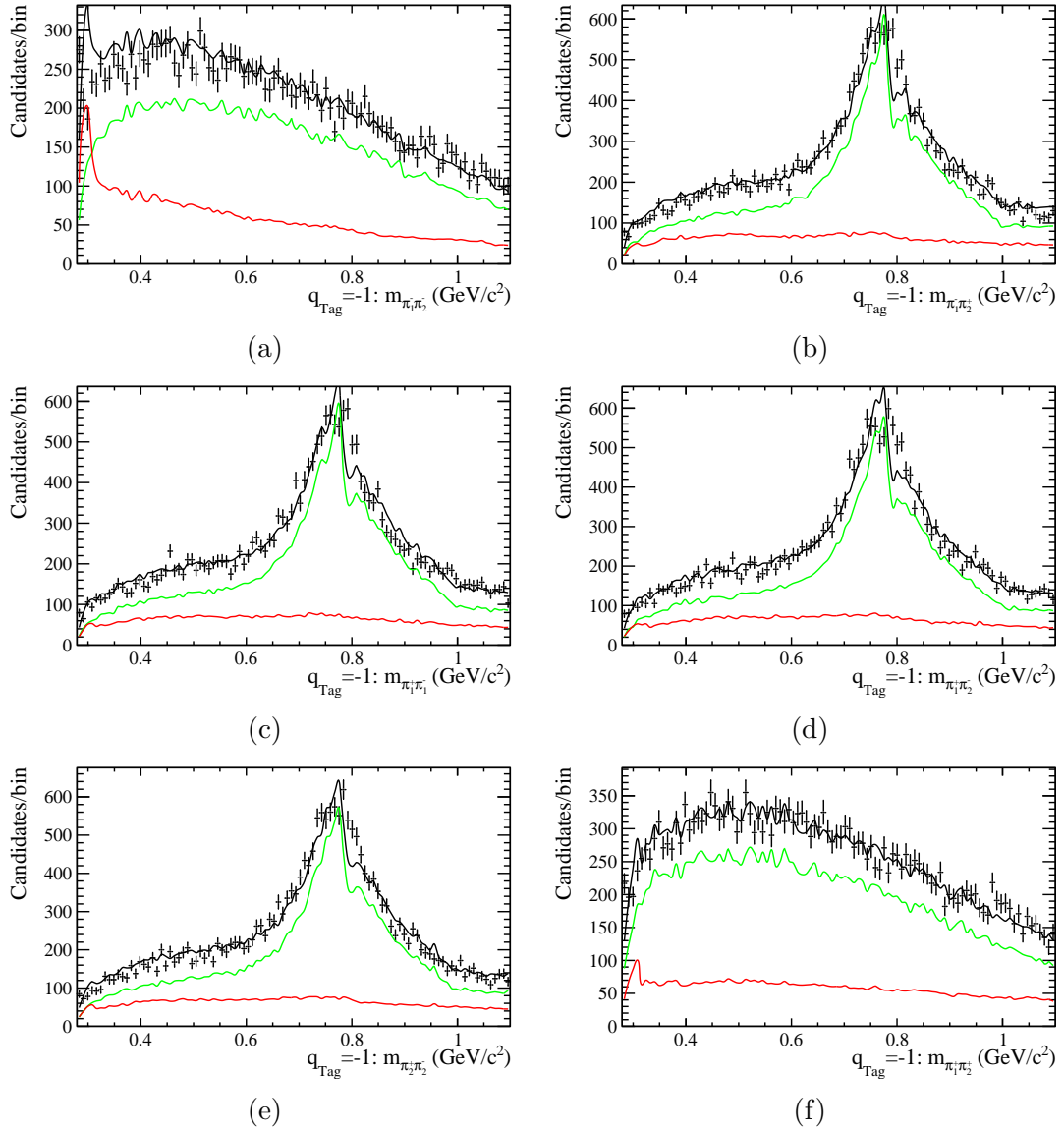


Figure 7.7: 2017 amplitude fits to the Six  $m(\pi_i \pi_j)$  ( $i \neq j$ ) projections, (a)  $\pi_1^- \pi_2^-$ —unphysical, (b)  $\pi_1^- \pi_2^+$ , (c)  $\pi_1^+ \pi_1^-$ , (d)  $\pi_1^+ \pi_2^-$ , (e)  $\pi_2^+ \pi_2^-$ , (f)  $\pi_1^+ \pi_2^+$ —unphysical. Signal (Green) contributions and Background (Red) contributions are presented in the plots.

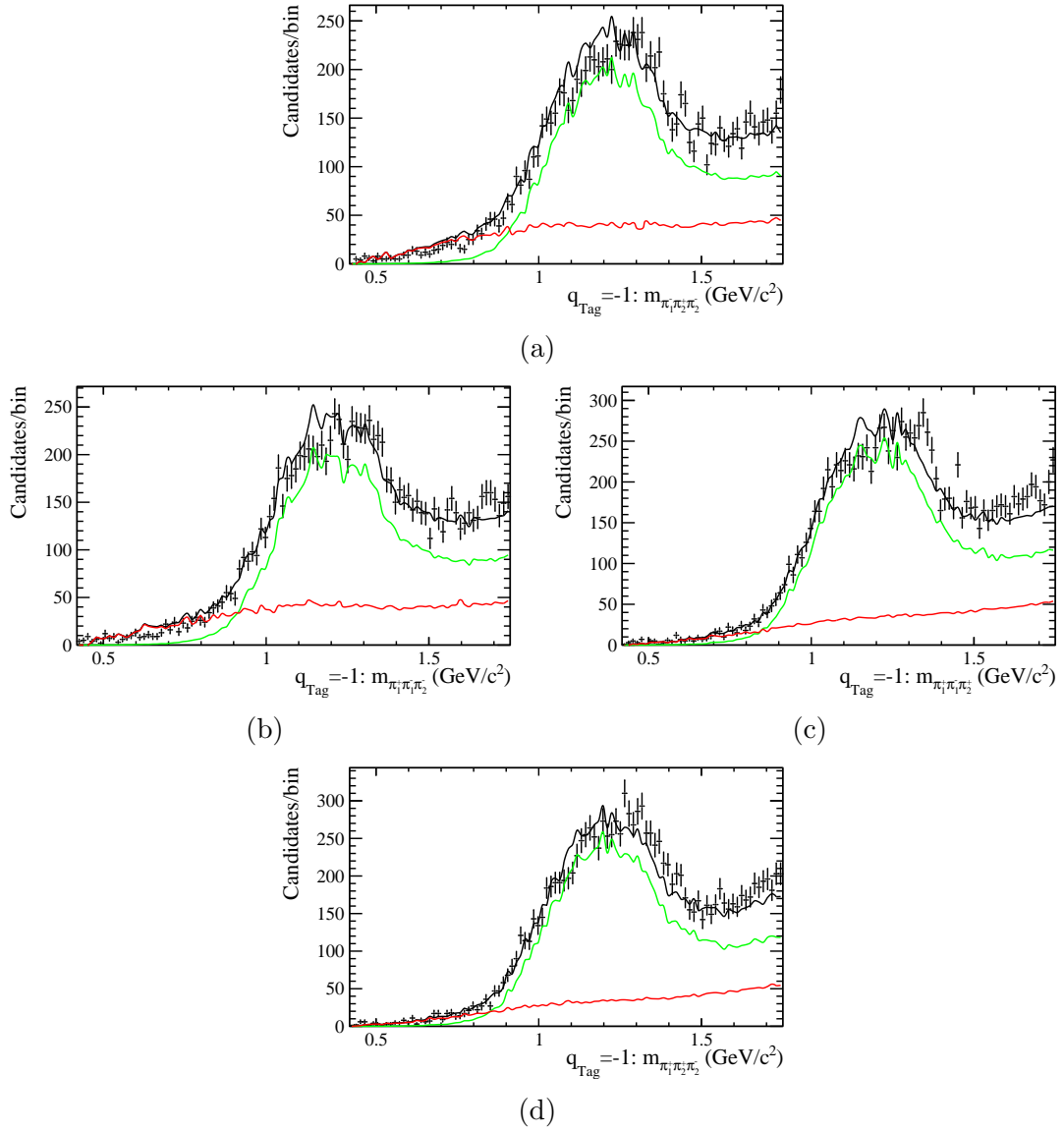


Figure 7.8: 2017 amplitude fits to the four  $m(\pi_i \pi_j \pi_k)$  projections, (a)  $\pi_1^- \pi_2^+ \pi_2^+$ , (b)  $\pi_1^+ \pi_1^- \pi_2^-$ , (c)  $\pi_1^+ \pi_1^- \pi_2^+$  and (d)  $\pi_1^+ \pi_2^+ \pi_2^-$ . Signal (Green) contributions and Background (Red) contributions are presented in the plots.

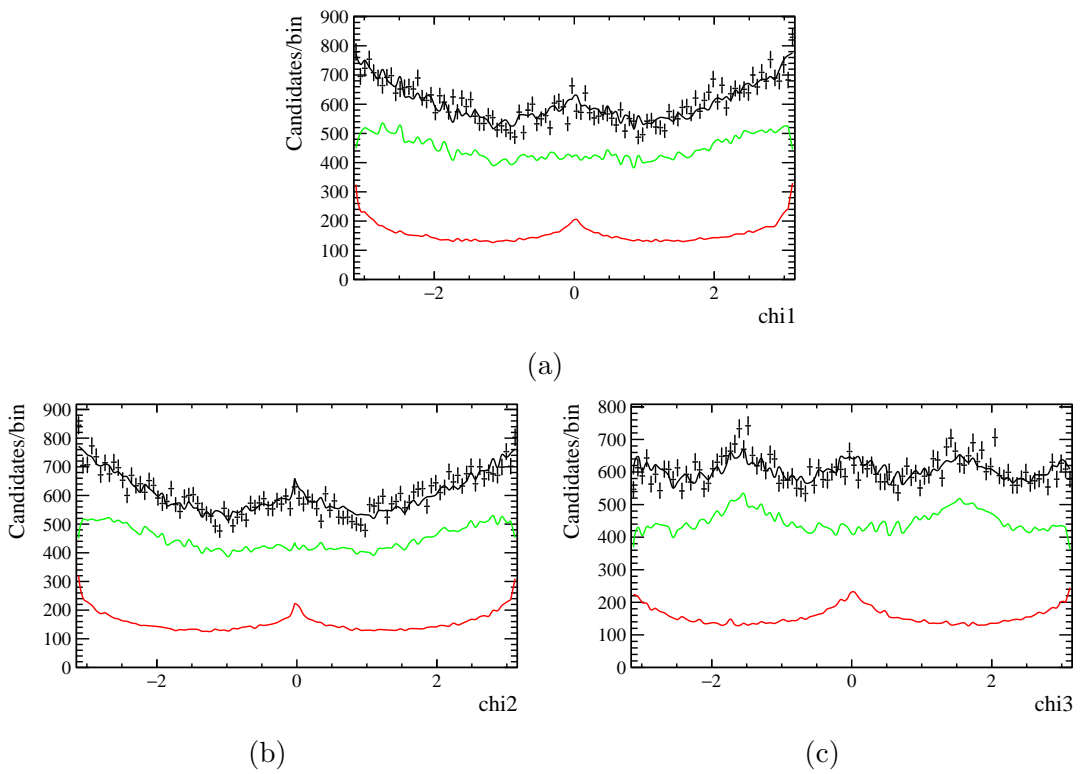


Figure 7.9: 2018 amplitude fits to the three  $\phi$  projections, (a)  $\phi(\rho_1\rho_2)$ , (b)  $\phi(\rho_3\rho_4)$ , (c)  $\phi(\rho_5\rho_6)$ —unphysical. Signal (Green) contributions and Background (Red) contributions are presented in the plots.

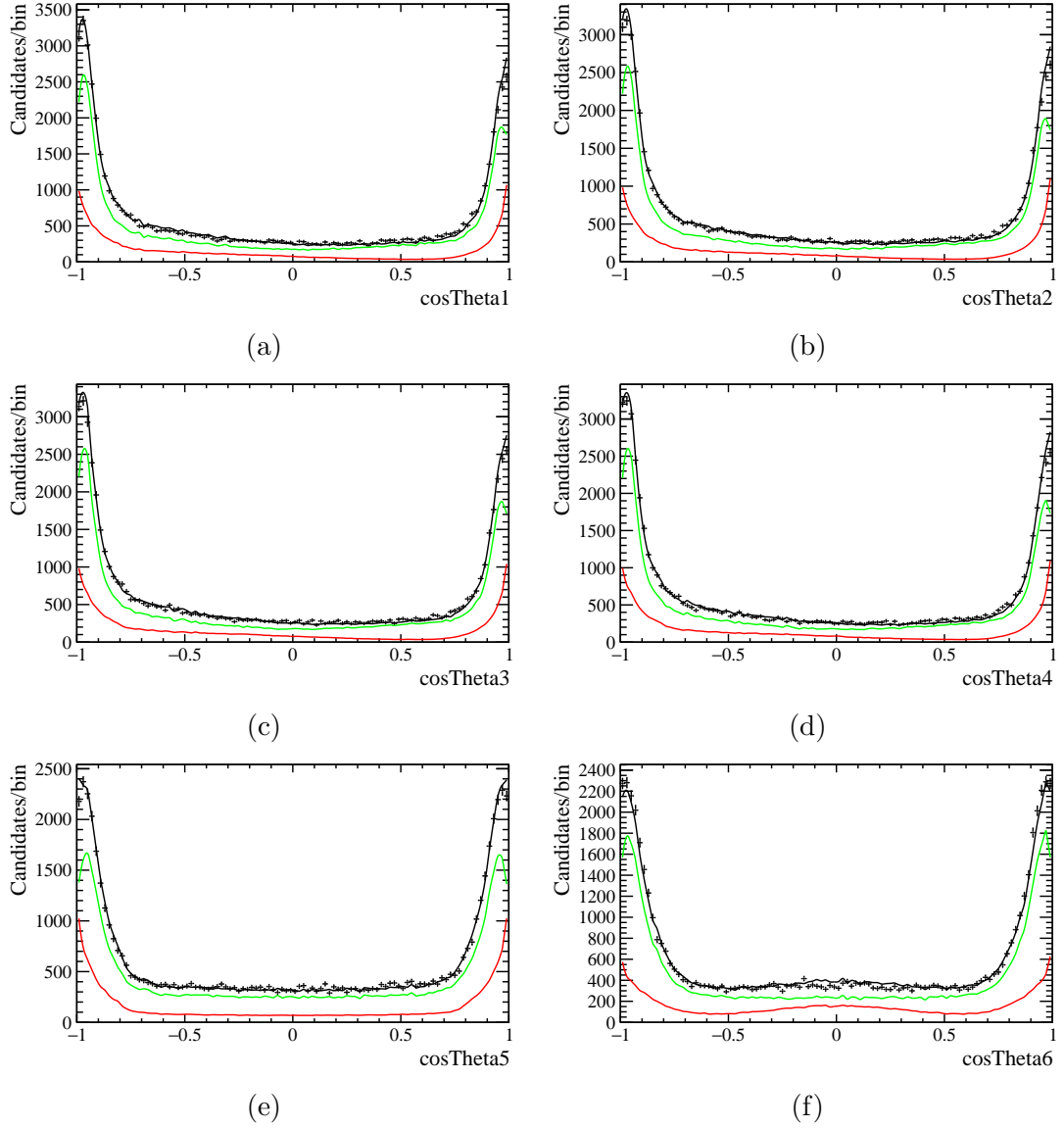


Figure 7.10: 2018 amplitude fits to the six  $\cos(\theta)_{ij}$  ( $i \neq j$ ) projections, (a)  $\cos(\theta(\pi_1^+ \pi_1^-))$ , (b)  $\cos(\theta(\pi_2^+ \pi_2^-))$ , (c)  $\cos(\theta(\pi_1^+ \pi_2^-))$ , (d)  $\cos(\theta(\pi_2^+ \pi_1^-))$ , (e)  $\cos(\theta(\pi_1^- \pi_2^-))$ —unphysical, (f)  $\cos(\theta(\pi_1^+ \pi_2^+))$ —unphysical. Signal (Green) contributions and Background (Red) contributions are presented in the plots.

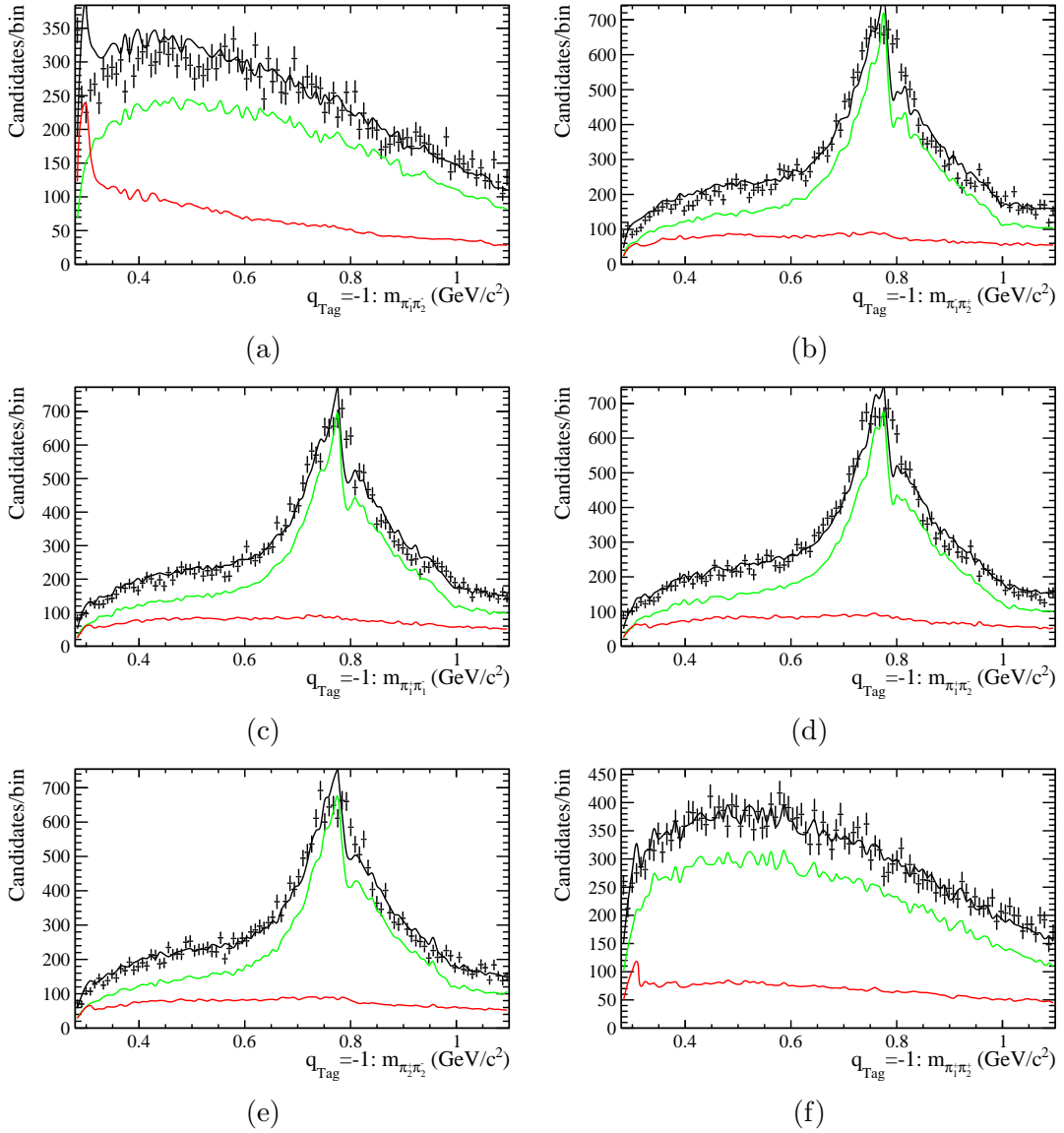


Figure 7.11: 2018 amplitude fits to the Six  $m(\pi_i \pi_j)$  ( $i \neq j$ ) projections, (a)  $\pi_1^- \pi_2^-$ —unphysical, (b)  $\pi_1^- \pi_2^+$ , (c)  $\pi_1^+ \pi_1^-$ , (d)  $\pi_1^+ \pi_2^-$ , (e)  $\pi_2^+ \pi_2^-$ , (f)  $\pi_1^+ \pi_2^+$ —unphysical. Signal (Green) contributions and Background (Red) contributions are presented in the plots.

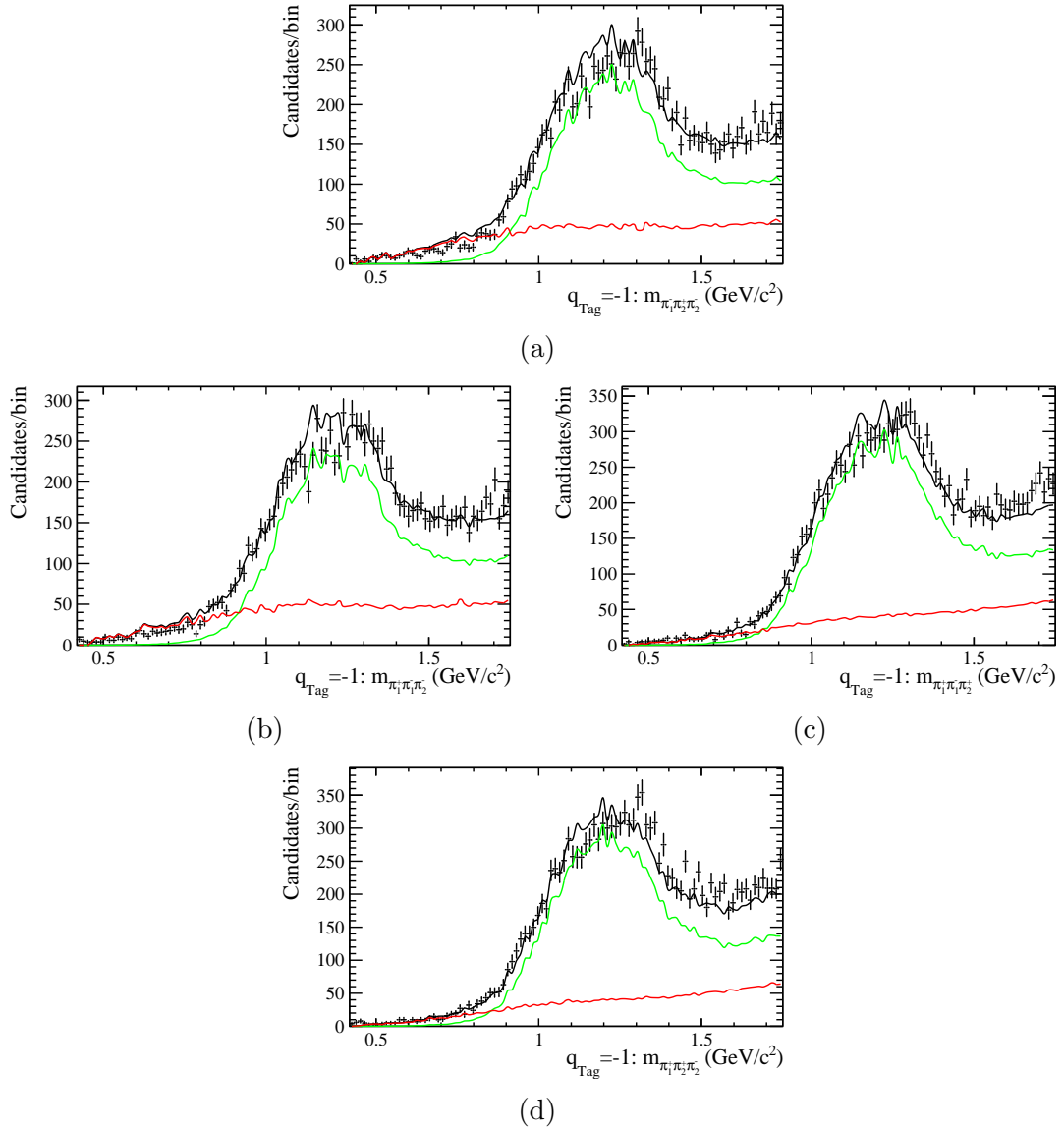


Figure 7.12: 2018 amplitude fits to the four  $m(\pi_i \pi_j \pi_k)$  projections, (a)  $\pi_1^- \pi_2^+ \pi_2^+$ , (b)  $\pi_1^+ \pi_1^- \pi_2^-$ , (c)  $\pi_1^+ \pi_1^- \pi_2^+$  and (d)  $\pi_1^+ \pi_2^+ \pi_2^-$ . Signal (Green) contributions and Background (Red) contributions are presented in the plots.

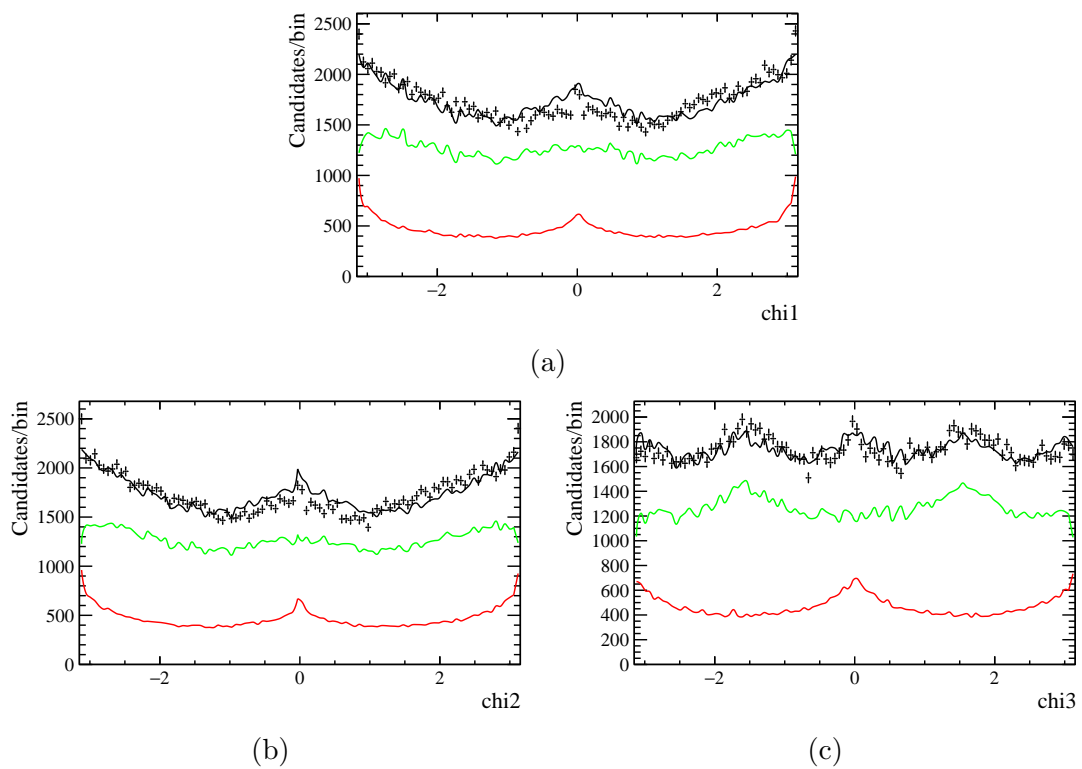


Figure 7.13: Run 2 amplitude fits to the three  $\phi$  projections, (a)  $\phi(\rho_1\rho_2)$ , (b)  $\phi(\rho_3\rho_4)$ , (c)  $\phi(\rho_5\rho_6)$ —unphysical. Signal (Green) contributions and Background (Red) contributions are presented in the plots.

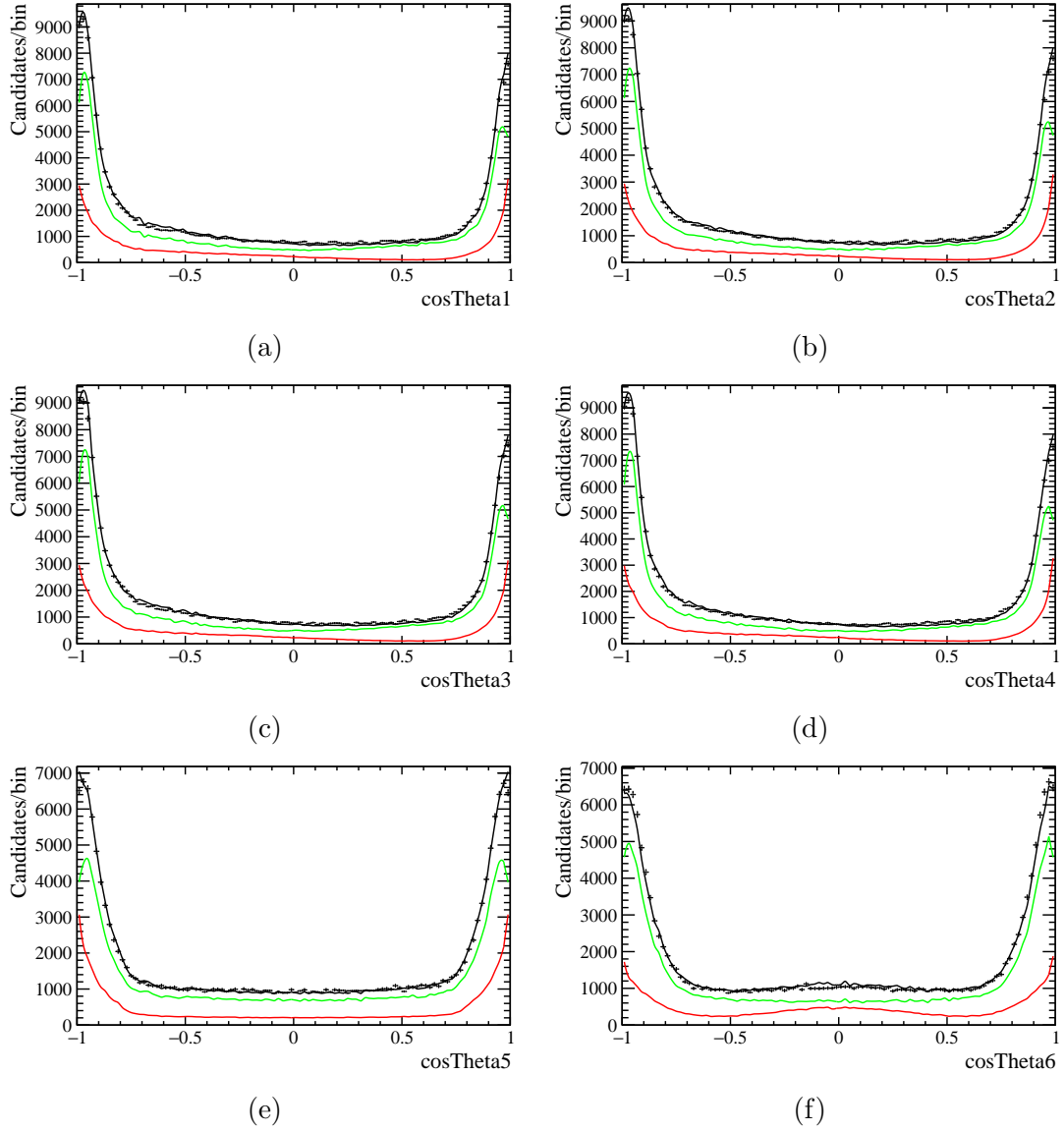


Figure 7.14: Run 2 amplitude fits to the six  $\cos(\theta)_{ij}$  ( $i \neq j$ ) projections, (a)  $\cos(\theta(\pi_1^+ \pi_1^-))$ , (b)  $\cos(\theta(\pi_2^+ \pi_2^-))$ , (c)  $\cos(\theta(\pi_1^+ \pi_2^-))$ , (d)  $\cos(\theta(\pi_2^+ \pi_1^-))$ , (e)  $\cos(\theta(\pi_1^- \pi_2^-))$ —unphysical, (f)  $\cos(\theta(\pi_1^+ \pi_2^+))$ —unphysical. Signal (Green) contributions and Background (Red) contributions are presented in the plots.

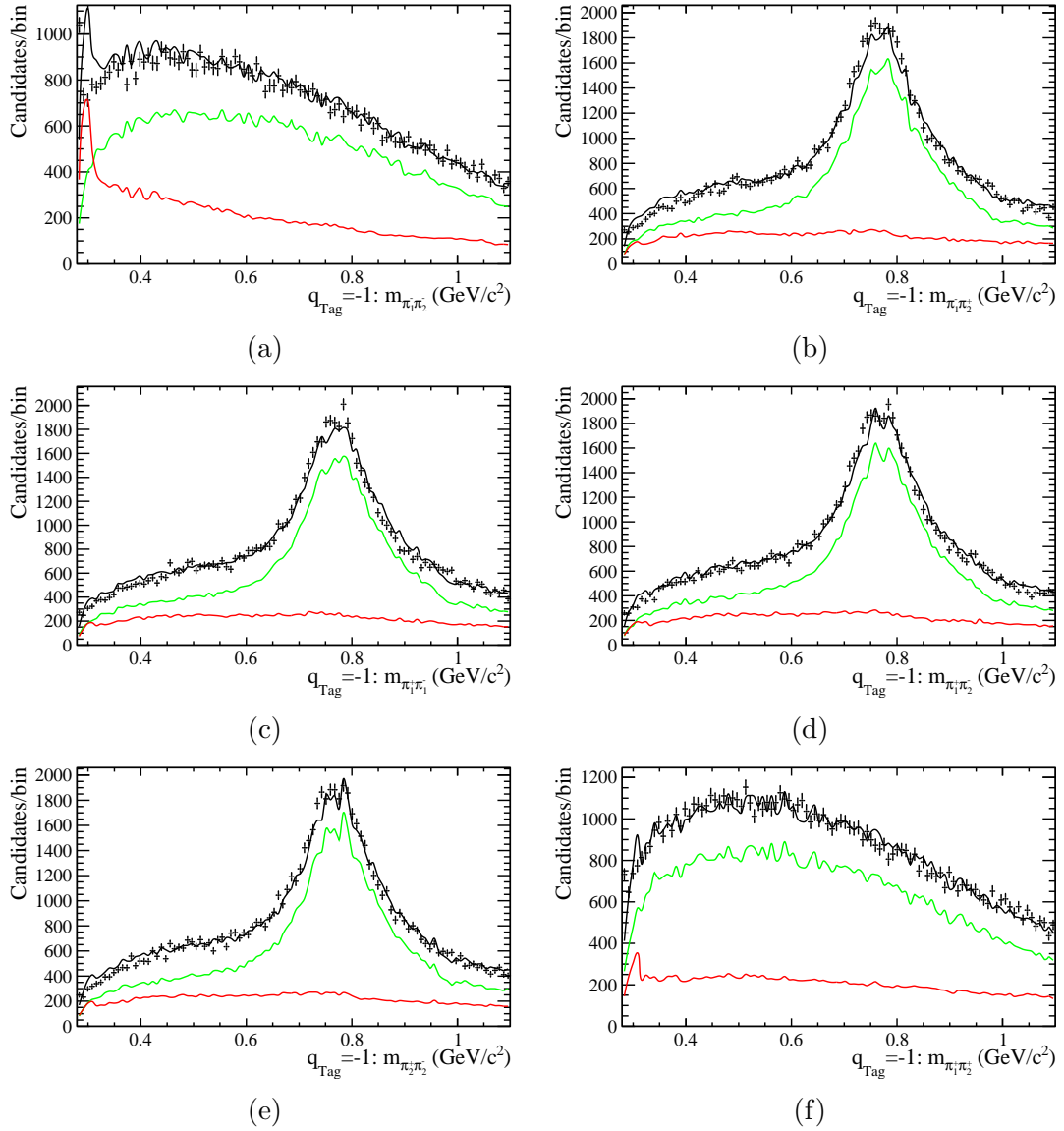


Figure 7.15: Run 2 amplitude fits to the Six  $m(\pi_i \pi_j)$  ( $i \neq j$ ) projections, (a)  $\pi_1^- \pi_2^-$ —unphysical, (b)  $\pi_1^- \pi_2^+$ , (c)  $\pi_1^+ \pi_1^-$ , (d)  $\pi_1^+ \pi_2^-$ , (e)  $\pi_2^+ \pi_2^-$ , (f)  $\pi_1^+ \pi_2^+$ —unphysical. Signal (Green) contributions and Background (Red) contributions are presented in the plots.

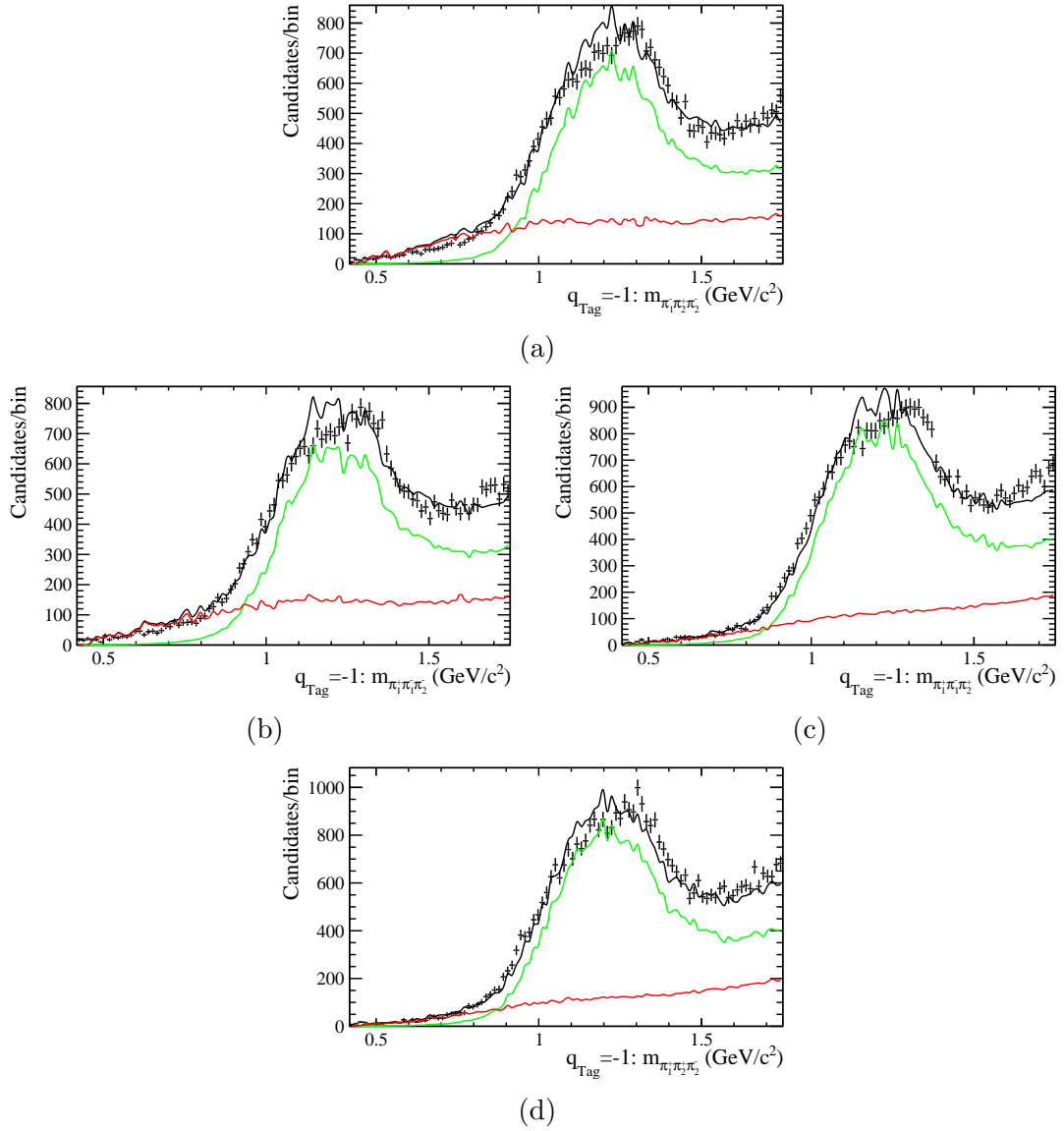


Figure 7.16: Run 2 amplitude fits to the four  $m(\pi_i \pi_j \pi_k)$  projections, (a)  $\pi_1^- \pi_2^+ \pi_3^+$ , (b)  $\pi_1^+ \pi_1^- \pi_2^-$ , (c)  $\pi_1^+ \pi_1^- \pi_2^+$  and (d)  $\pi_1^+ \pi_2^+ \pi_3^-$ . Signal (Green) contributions and Background (Red) contributions are presented in the plots.

From the full Run 2 fit, we extract the parameters presented with their statistical uncertainty in Table 7.3. These parameters fully define our amplitude model. It should be noted that the strong couplings can take large values since they are calculated in the model pre-normalisation. The parameters from this model are then used to calculate the Fit Fractions presented in Table 7.2, where we can see the dominant contribution of the  $a_1(1260)^\pm$ . The interference fractions (Figure 7.17) also show the distortions to the  $[\rho(770)^0\rho(770)^0]_{S,P,D}$  amplitudes induced by  $a_1(1260)^\pm$  of approximately 7% when using this extended phase space.

Parameter	Value
$a_1(1260)\pi$	$70.54 \pm 0.128\%$
$a_2(1320)\pi$	$0.56 \pm 1.34\%$
$[\rho(770)^0\rho(770)^0]_S$	$6.52 \pm 0.39\%$
$[\rho(770)^0\rho(770)^0]_P$	$0.68 \pm 1.21\%$
$[\rho(770)^0\rho(770)^0]_D$	$3.64 \pm 0.52\%$
$\rho(770)^0\pi^+\pi^-$	$3.39 \pm 0.54\%$
$\pi^+\pi^-\pi^+\pi^-$	$17.47 \pm 0.24\%$

Table 7.2: Fit Fractions—as percentages—from the full Run 2 amplitude fit. All uncertainties are statistical from the fit procedure. Interference fractions are not included in this table. They are presented separately in Figure 7.17.

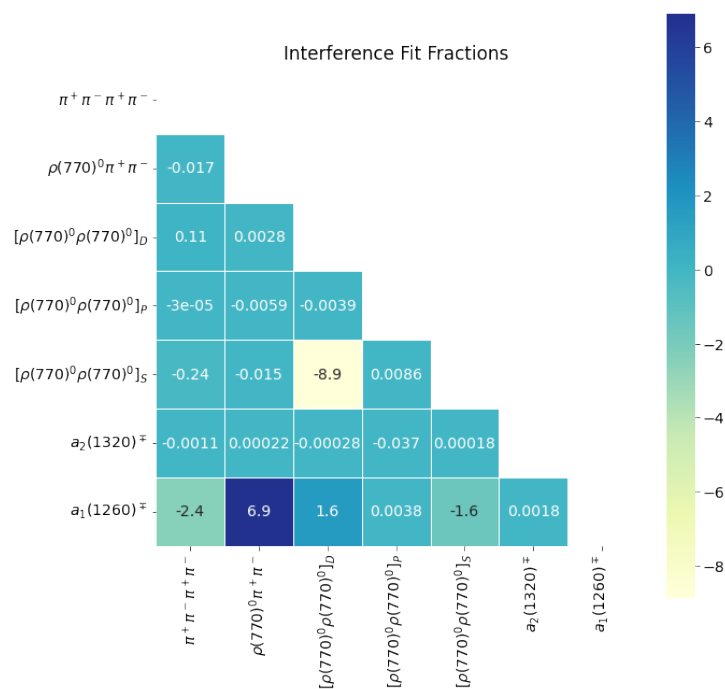


Figure 7.17: Interference Fit Fraction—as percentages—from the full Run 2 amplitude analysis.

Parameter	Value	Uncertainty
xa1ppim	5.9872	$\pm 0.1703$
ya1ppim	2.6620	$\pm 0.2239$
xa1_rpS	0.8652	$\pm 0.0197$
ya1_rpS	0.0489	$\pm 0.0236$
xa1_rpD	1.2780	$\pm 0.0727$
ya1_rpD	1.7156	$\pm 0.0917$
xa1_KMP1	0.3288	$\pm 0.0462$
ya1_KMP1	1.3133	$\pm 0.0507$
xa1_KMP2	-0.5406	$\pm 0.1258$
ya1_KMP2	4.3292	$\pm 0.1186$
xa1_KMS1	-0.8522	$\pm 0.0631$
ya1_KMS1	-1.5532	$\pm 0.06380$
xa1_KMS2	-1.3739	$\pm 0.2452$
ya1_KMS2	-3.727	$\pm 0.2954$
xa2ppim	1.926	$\pm 0.4160$
ya2ppim	0.6580	$\pm 0.3646$
xa2_rpD	0.9970	$\pm 0.1674$
ya2_rpD	-0.2449	$\pm 0.0754$
xa1640ppim	1.9264	$\pm 0.4165$
ya1640ppim	0.6580	$\pm 0.3646$
xrho0omega	-0.1611	$\pm 0.0247$
yrho0omega	-0.0776	$\pm 0.0247$
xrho0rho0_P	0.4019	$\pm 0.0174$
yrho0rho0_P	-0.0884	$\pm 0.0328$
xrho0rho0_D	0.7105	$\pm 0.0250$
yrho0rho0_D	0.3099	$\pm 0.0245$
x_KMP1	26.16	$\pm 43.37$
y_KMP1	311.0	$\pm 47.6$
x_KMP2	2423	$\pm 100$
y_KMP2	3466	$\pm 85$
x_KMS1	-2931	$\pm 58$
y_KMS1	-776.4	$\pm 79.5$
x_KMS2	-3181	$\pm 235$
y_KMS2	2880	$\pm 245$
xrho0KM	-0.0003286	$\pm 0.0000013$
yrho0KM	0.0002164	$\pm 0.0000021$
xKMKM	5.482e-08	$\pm 1.7570e-09$
yKMKM	-1.7424e-08	$\pm 2.7620e-09$

Table 7.3: Parameters from the full Run 2 amplitude fit.

## 7.2 Longitudinal Polarisation

The Longitudinal Polarisation Fraction,  $f_L$ , is used in the determination of the  $\rho(770)$  isospin decomposition [23], where all  $\rho(770)$  amplitudes only consider the Longitudinal contribution. The Longitudinal Polarisation Fraction,  $f_L$ , is defined as

$$f_L = \frac{|A_0|^2}{|A_0|^2 + |A_{\parallel}|^2 + |A_{\perp}|^2}, \quad (7.1)$$

where  $A_0$  is the unpolarised  $\rho(770)^0\rho(770)^0$  helicity amplitude and  $A_{\parallel}$ ,  $A_{\perp}$ , are the parallel and perpendicular helicity amplitudes respectively. This fraction provides important input to future measurements of  $\alpha$  using the methodology proposed in Chapter 2 [26]. However, access to this fraction is defined in a different spin-formalism to the models presented in this thesis. Our model presents the  $[\rho(770)^0\rho(770)^0]$  in terms of  $S, P$  and  $D$  wave contributions which, although convenient for the fit fractions and interference terms, it cannot be used, since the  $S$  and  $D$  waves are linear combinations of the parallel and unpolarised components. This can also be observed through their interference fractions in Figure 7.17.

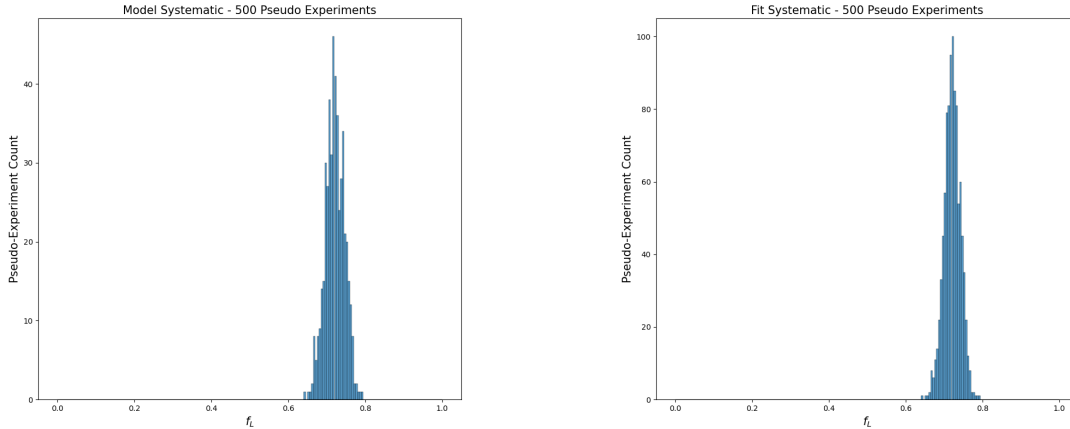
To resolve this, we generate sets of pseudo-experiments with the full amplitude model (Equation 6.9) simplified to contain only the  $[\rho(770)^0\rho(770)^0]_{S,P,D}$  amplitudes. A fit to these pseudo-experiments with the helicity amplitudes is then used to extract the Longitudinal Polarisation Fraction. The helicity amplitudes are defined in the following way. Firstly, we define each amplitude in terms of a modulus and phase coupling,

$$A_h = |A_h|e^{i\delta_h} f_h(\theta_1, \theta_2, \phi) g_h(m_1, m_2), \quad (7.2)$$

where  $|A_h|$  is the modulus,  $\delta_h$  is the phase,  $f_h(\theta_1, \theta_2, \phi)$  are the spherical harmonics with respect to the helicity angles  $\theta_1$ ,  $\theta_2$  and  $\phi$ , and  $g_h(m_1, m_2)$  are the mass propagators with respect to the invariant masses of  $\rho(770)_1^0$  and  $\rho(770)_2^0$ . From this, we can construct a three helicity amplitude,

$$\mathcal{A} = -\frac{3N}{4\pi} \left[ \left( A_0 \cos \theta_1 \cos \theta_2 + \frac{A_{\parallel}}{\sqrt{2}} \sin \theta_1 \sin \theta_2 \cos \phi + i \frac{A_{\perp}}{\sqrt{2}} \sin \theta_1 \sin \theta_2 \sin \phi \right) \mathcal{M}_0(m_1) \mathcal{M}_1(m_2) \right] \quad (7.3)$$

where  $\mathcal{M}_1$  are the spin-1 mass propagators and  $N$  is some normalisation. By squaring this



(a) systematic study output for the model uncertainty.

(b) systematic study output for the fit uncertainty.

Figure 7.18: Pseudo-Experiments for understanding the model and fit systematics.

amplitude and neglecting the imaginary terms—that can only be disentangled through time-dependent analyses since they embody a phase shift we are not sensitive to with this method—we have a PDF that can be used to extract  $f_L$ .

The pseudo-experiments for this fit are generated from the  $[\rho(770)^0\rho(770)^0]_{S,P,D}$  amplitudes, with the sample size matched to the Run II signal yield adjusted by the  $[\rho(770)^0\rho(770)^0]_{S,P,D}$  fit fractions, allowing us to extract statistical errors directly from the fit. Further to this, we run two systematic uncertainty studies (Figure 7.18). In the first of these studies, we generate 500 pseudo-experiments with the central values taken from the Run 2 fit. The distribution from this study is used to estimate the fit systematic uncertainty,  $[+0.021, -0.021]$ . We also generate pseudo-experiments floating the  $[\rho(770)^0\rho(770)^0]_{S,P,D}$  amplitude parameters within their statistical bounds. The distribution from this study is used to estimate the model systematics uncertainties,  $[+0.025, -0.025]$ . The final result for the Longitudinal Polarisation Fraction extracted from the full Run 2 dataset is,

$$f_L = 0.721 \pm 0.01 \pm 0.03$$

with the first error being statistical and the second being systematic. It should be noted that this preliminary result still requires a more detailed inspection of systematic uncertainties arising from the amplitude model and invariant mass fits. Systematics for the

invariant mass fits were discussed in Chapter 5, however, in terms of the amplitude model we still need to investigate the effect of different background levels, the effect of particle identification cuts, model dependent variations such as the inclusion and exclusion of resonances. Detailed work on the channel  $B^0 \rightarrow a_1(1260)^\pm \pi^\mp$  channel is currently being undertaken by colleagues at Instituto Galego de Física de Altas Enerxías (IGFAE), Santiago de Compostela. The inclusion of the modeling parameters from this work could reduce the ambiguity seen in the 3-body mass fits Figure 7.16 and by extension improve our systematic uncertainty. Comparison of this new preliminary result to previous measurements is presented in Figure 7.19.

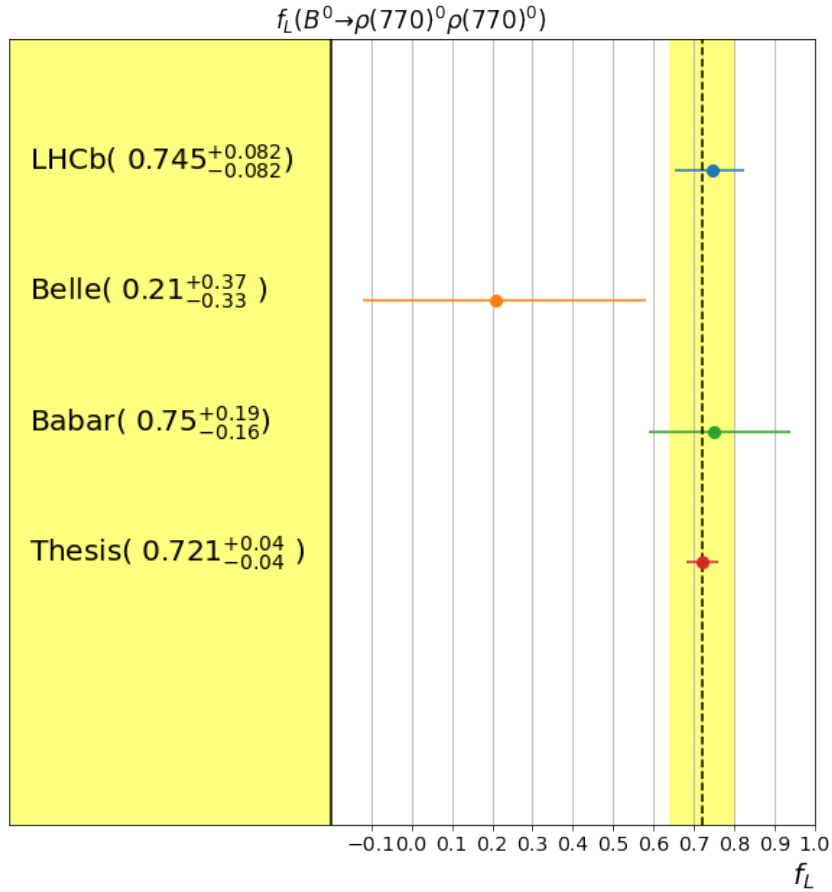


Figure 7.19: Longitudinal polarisation fraction measurements for the  $B^0 \rightarrow \rho(770)^0 \rho(770)^0$ . Measurements are included from Belle [28], BaBar [29] and LHCb [30]. Included errors are statistical and systematic. The measurement presented in this thesis falls inside the weighted average calculated against the PDG method [4].

### 7.3 Conclusions and Outlook

This measurement of the longitudinal polarisation fraction, and the relative strong couplings extracted directly from the amplitude fits will contribute directly to the time-dependent measurement of the unitarity angle  $\alpha$  as outlined in Ref. [26]. Further systematic uncertainty studies, and optimisation of the amplitude model, will lead to a final value of this input with greater precision than previous measurements in the  $B^0 \rightarrow \rho(770)^0 \rho(770)^0$  channel by Belle [28], BaBar [29] and LHCb [30].

The models and samples outlined in this thesis were developed with the extension to the time-dependent measurement in mind, hence the inclusion of the complex **CP** couplings and other time-dependent parameters within the model. For the extension of this model to the time-dependent measurement there are two further analysis tasks that need to be completed. Firstly, the phase space efficiency and background parametrisations will have to be recalculated inclusive of time. It will be particularly interesting in terms of the methodology to see how the KDE and reweighting methods respond to this increase to the six-dimensional phase space. Similarly, the flavour tagging [107] will need to be calibrated to provide meaningful  $B\bar{B}$  identification, After these flavour tagging calibrations, the sample size will be reduced by approximately 96% due to current limitations in flavour tagging efficiency.

The final inputs to fully constrain this single measurement will be taken from our current understanding of the  $B^0 \rightarrow a_1(1260)^\pm \pi^\mp$  channel. Work is currently being undertaken by colleagues at Instituto Galego de Física de Altas Enerxías (IGFAE), Santiago de Compostela, to extract a similar parameter set to this analysis using the methodology outlined in Ref. [108], a result I very much look forward to seeing.

# Chapter 8

## Summary

This book was written using 100% recycled words.

---

Terry Pratchett

The thesis opened with a theoretical overview of the Standard Model, relevant to the LHCb physics program, and the analysis presented in this thesis. Care was taken to fully describe the isospin decomposition that motivates the analysis of  $B^0 \rightarrow \pi^+\pi^-\pi^+\pi^-$ . The chapter also fully defined the formalism used in the amplitude analysis, with particular focus on the covariant spin formalism.

In Chapter 3, the LHCb experiment and its sub-detectors were fully described. The VELO was described in more detail, discussing alignment and the challenges facing the project in the High Luminosity LHC. The LGAD development, presented in Chapter 4, was motivated by this discussion. The software that gives analysts access to the experimental data was also discussed in this chapter.

Chapter 4 presented electrostatic and transient simulations for the LGAD project, a technology that is being developed for installation in the VELO during the High Luminosity LHC. Particular care was taken to describe the effects of high fluence environments, with novel simulations being presented that will be used to inform future developments of this technology. These LGAD simulations showed that under the high-fluence conditions projected for the High Luminosity LHC, the gain characteristics of LGAD could be compromised. The chapter also covered pixel termination with an extended look into how effective oxide trench termination is at the edge of the device, with trench performance

being consistent across a number of studies.

Chapter 5 detailed a full description of data selection for the  $B^0 \rightarrow \pi^+\pi^-\pi^+\pi^-$  analysis, presenting the full multivariate selection procedure, and invariant mass fits, for Run 2 data. The section discussed the three-panel optimisation used in the analysis to decide an optimum set of multivariate and physical selection criteria. Invariant mass fits to the data samples presented in this chapter provided an estimated total of  $126725 \pm 504$   $B^0 \rightarrow \pi^+\pi^-\pi^+\pi^-$  candidates, and were subsequently used in the remainder of the thesis.

Chapter 6 presented the KDE and reweighting methods for determining the efficiencies and background model respectively. Care was taken in the chapter to present the consistency in efficiency between data-taking runs of the LHCb experiment. This Chapter then presented the full amplitude model, inclusive of these modelled effects, and motivated the fixing of the complex **CP** couplings and other variables.

Chapter 7 closed out the time-independent amplitude analysis, presenting the results of the amplitude model in terms of fit fractions, and projections. It also presented a new time and flavour integrated measurement of the Longitudinal Polarisation Fraction for the  $\rho(770)^0\rho(770)^0$  decay channel that can contribute to a single determination of  $\alpha$ . Systematic studies to constrain the uncertainty on this measurement were also presented to provide a meaningful comparison with previous studies at Belle, BaBar, and LHCb. The final result for the Longitudinal Polarisation Fraction was given as

$$f_L = 0.721 \pm 0.01 \pm 0.03$$

where the first uncertainty is statistical and the second uncertainty is systematic.

# List of Tables

2.1	Lepton content of the Standard Model [4]. . . . .	6
2.2	Quark content of the Standard Model [4]. . . . .	7
2.3	CKM angle values [4]. . . . .	14
2.4	General Decomposition of the amplitudes observed in the $B \rightarrow hh$ decay modes for distinguishable mesons. . . . .	19
2.5	General Decomposition of the amplitudes observed in the $B \rightarrow hh$ decay modes for indistinguishable mesons. . . . .	20
2.6	Spin amplitudes for each decay topology considered in this analysis, where $P$ is a pseudoscalar, $S$ a scalar, $V$ a vector, $A$ an axial-vector and $T$ a tensor state. In cases where multiple orbital angular momentum configurations are present between states, the wave is indicated by a subscript. Note that the particle ordering is important as it sets the phase convention. . . . .	30
3.1	Integrated luminosity per year at LHCb [54]. . . . .	42
4.1	Heavy Ion parameters for use in transient simulations. . . . .	88
5.1	StrippingB2hhpipiPhsSpCcut4piLine selection criteria. . . . .	97
5.2	Decision Tree Variables used in the $B_d$ analysis. B0 ETA is the B0 pseudo-rapidity, B0 FD is the B0 Flight Distance, B0 Vertex Fit is a measure of the fit quality to the B0 vertex, B0 $P_T$ is the transverse momentum of the B0, B0 DIRA is the direction angle of the B0 with respect to the Primary Vertex, B0 AMAXDOCA is the maximum distance of closest approach from the daughter tracks, B0 IP is the impact parameter of the B0 with respect to the primary vertex and Daughter IP is the impact parameter of the daughters with respect to the B0. . . . .	99
5.3	Decision Tree Variables transforms used in the analysis. . . . .	101

5.4	BDT variable significance as calculated by the XDGBoost python library. The significance is an internal measure of a variables discrimination power with respect to the other variables. Significance always sums to unity. . . .	102
5.5	Fixed parameters for the $B^0 \rightarrow K\pi\pi\pi$ signal model. . . . .	105
5.6	Fixed parameters for the $B^0 \rightarrow KK\pi\pi$ signal model. . . . .	105
5.7	Fixed parameters for the $B^0 \rightarrow \pi\pi\pi\pi$ signal model. The value of $\sigma$ is not split in this DCB function as the reconstructed signal mode should be symmetric. . . . .	106
5.8	Yields of the three main contributions inside the $B_d$ mass window used for the analysis. . . . .	107
6.1	Kinematic selection cuts for MC particles. . . . .	114
6.2	Training variables for the KDE efficiency training. . . . .	115
6.3	Training variables for the hep-ml background reweighter. . . . .	122
6.4	Parameters fixed in the amplitude fits. . . . .	128
7.1	Parameters floated in the amplitude fits. . . . .	132
7.2	Fit Fractions—as percentages—from the full Run 2 amplitude fit. All uncertainties are statistical from the fit procedure. Interference fractions are not included in this table. They are presented separately in Figure 7.17. . .	147
7.3	Parameters from the full Run 2 amplitude fit. . . . .	149

# List of Figures

1.1	Asier Pereiro Castro, <i>Lost in phase space</i> . . . . .	2
2.1	Standard Model of particle physics. . . . .	5
2.2	Gamma anisotropy and beta asymmetry for polarizing field pointing up and pointing down, reproduced from [19]. . . . .	9
2.3	The CKM unitarity triangle in the $(\bar{\rho}, \bar{\eta})$ plane [22]. . . . .	13
2.4	David Friday <i>Artistic depiction of penguins at CERN</i> . . . . .	16
2.5	Tree (a) and Penguin (b) contributions in the $B^0 \rightarrow \pi\pi$ process [26]. . . . .	16
2.6	One-dimensional scan of $\alpha$ in the $[0,180]$ range (top) isospin analysis of the $B \rightarrow \pi\pi$ system. The zoom in the vicinity of 0 (bottom figure) displays the punctual discontinuity, whose width due to the scan binning has no physical meaning [27]. This is extracted from the branching fractions of each amplitude and their CP violating phases. . . . .	21
2.7	Isopin decomposition of the indistinguishable $B \rightarrow hh$ system. The red and blue arrows indicate the eight-fold degeneracy of the system while the green arrows indicate the phase offset due to penguin contributions in the system. In the $\rho\rho$ system this system collapses to a two-fold degeneracy. . . . .	22
2.8	One-dimensional scan of $\alpha$ in the $[0,180]$ range (top) isospin analysis of the $B \rightarrow \rho\rho$ system. The zoom in the vicinity of 0 (bottom figure) displays the punctual discontinuity, whose width due to the scan binning has no physical meaning [27]. . . . .	23
2.9	Two quasi-two-body decay paths for the $B^0$ , proceeding via either $B^0 \rightarrow \rho(770)^0 \rho(770)^0$ , or $B^0 \rightarrow a_1(1260)^\pm \pi^\mp$ . . . . .	25
2.10	energy-dependent partial width of the $a_1(1640)$ . . . . .	34
2.11	energy-dependent width of the $a_1(1640)$ . . . . .	35

3.1	Map of the CERN accelerator complex. Reproduced from [39]. . . . .	37
3.2	The LHCb detector layout, with the beam axis (z) going from left to right, the y-axis going from bottom to top, and the x-axis going into the page. Reproduced from [47]. . . . .	39
3.3	Angular distribution of the $b\bar{b}$ pair produced in $pp$ collisions at LHCb. The acceptance of the LHCb experiment appears as red on the plot. Reproduced from [48]. . . . .	40
3.4	Instantaneous luminosity plot against time(hours) for ATLAS, CMS and LHCb during LHC fill 2651. Reproduced from [51]. . . . .	41
3.5	A schematic of a VELO half showing the general configuration of the modules and RF foil. Note the module spacing increases as you move away from the interaction point (back of image). Reproduced from [47]. . . . .	43
3.6	An overview of the layout of the VELO modules with the R sensors (red) and $\phi$ sensors (blue). Reproduced from [47]. . . . .	44
3.7	$IP_x$ and $IP_y$ resolution as a function of momentum (left) and $IP_x$ as a function of $1/p_T$ and compared with simulation (right). Determined with 2012 data. Reproduced from [47]. . . . .	45
3.8	Example of unbiased sensor residuals as a function of the $\phi$ coordinate using only the survey information (left) and using the track-based software alignment (right). Results are given for two different example sensors. Reproduced from [49]. . . . .	46
3.9	Reconstructed secondary vertices (SV) in the Run 1 data sample showing the $zr$ plane integrated over $\phi$ , where a positive (negative) $r$ value denotes that the SV is closest to material in the right (left) half of the VELO. Reproduced from [55]. . . . .	46
3.10	Orientation of the sub planes of the TT. Reproduced from [60]. . . . .	48
3.11	Schematic of the tracking station (T1 - T3) inner silicon tracker. Reproduced from [60]. . . . .	48
3.12	Perspective view of the LHCb magnet Reproduced from [47]. . . . .	49
3.13	Reconstructed Cherenkov angle as a function of track momentum in the $C_4F_{10}$ radiator of RICH-1. Reproduced from [61]. . . . .	51

3.14	Kaon identification efficiency (red) and kaon-pion misidentification rate (black) as a function of track momentum, in GeV/c, from 2011 data. The plot was reproduced from [61]. The two $\Delta LL$ ranges demonstrate the trade off between identification efficiency and misidentification within the RICH.	52
3.15	Energy deposition of (a) 50 GeV electrons and (b) pions in the PS. The plot was reproduced from [47]. . . . .	54
3.16	The layout of an HCAL module. Reproduced from [47]. . . . .	54
3.17	Side view of the muon system. Reproduced from [47]. . . . .	55
3.18	Schematic cross section of a triple-GEM detector. Reproduced from [47]. . . . .	56
3.19	HLT1 track and vertex reconstruction [63]. . . . .	58
3.20	HLT2 track and vertex reconstruction [63]. . . . .	58
3.21	LHCb Event Display reconstructing a real event using the GEANT4 framework. Image provided by CERN. . . . .	60
4.1	Silicon Miller index orientations for HEP, reproduced from [77]. . . . .	64
4.2	Schematic illustration of a p-n junction (a) and its band diagram to illustrate built-in voltage. Reproduced from [78]. . . . .	65
4.3	Comparison of CCE between n-in-p detector (non-oxygenated p-bulk), oxygenated and non-oxygenated p-in-n detectors. Reproduced from [83]. . . . .	70
4.4	Schematic cross-section of the LGAD pad design. Reproduced from [82]. . . . .	71
4.5	Measured absolute collected charge as a function of the applied bias for a LGAD sample irradiated to different fluences. Reproduced from [82]. . . . .	71
4.6	Absolute collected charge (up) and noise (bottom) signals for two LGAD samples after Sr-90 source MIPs exposure. Measurements are compared with the response of a conventional non-multiplying pad diode (2328-10). Reproduced from [82]. . . . .	72
4.7	Schematic view of the pixel structures studied in this work. (a) Conventional p-type stripped detector. (b) “Polytrench” variation, including a polysilicon trench, doped with phosphorus, along the centre of the strip pitch. (c) “P-layer” variation, including a p-type diffusion below the $N^+$ electrode; (d) “OxideTrench” variation, including an oxide filled trench along the centre of the strip and a p-type implantation through the trench. Reproduced from [85]. . . . .	73

4.8	JTE probe dopant concentration fit with a sum of Gaussian functions used to approximate the JTE structure in TCAD simulations. . . . .	75
4.9	Oxide trench used in an inter-pixel region. . . . .	76
4.10	Doping profile for a general LGAD device using both JTE and oxide trench termination for use in electrostatic and transient device simulation. N1, N2 and N3 each represent individual pixels. . . . .	77
4.11	Electric field simulations at 320V for an LGAD device and a PiN Diode. Simulated in TCAD [89]. . . . .	78
4.12	Breakdown Scan of a simulated LGAD device. The device design has a generic 50 $\mu\text{m}$ thickness. The dashed line indicates the estimated point of device breakdown. Simulated in TCAD [89]. . . . .	79
4.13	Sample of LGAD termination scenarios: floating JTE (top left), oxide covered JTE with no termination trench (top right), variable JTE offset (bottom left), terminated with only a trench (bottom right). Simulated in TCAD [89]. . . . .	80
4.14	IV Scan of a simulated LGAD device with floating JTE and oxide trench termination. The breakdown is consistent between pixels N1 and N2. Simulated in TCAD [89]. . . . .	81
4.15	Comparison of main termination configurations across edge pixel N1. Trench parameters were kept constant between termination modes for meaningful comparison. Simulated in TCAD [89]. . . . .	82
4.16	Comparison of breakdown voltage across different trench depths with constant width of 2 $\mu\text{m}$ . Simulated in TCAD [89]. . . . .	83
4.17	Interface level trap distributions (left), bulk trap level distributions (right). Reproduced from [91]. . . . .	85
4.18	Analytical multiplication profiles in high fluence environments, optimised for phosphorous doping using values extracted from [94]. . . . .	87
4.19	Evolution of charge density during transient device simulation. Simulated in TCAD [89]. . . . .	89
4.20	Transient current plots for a MIP charge injected at 0 ps in the centre of pixel N1. The simulation terminates after 1000 ps. The current is given in arbitrary units to blind true charge characteristics. Simulated in TCAD [89].	90

4.21	Relative gain for different a device simulated at varying fluences. Simulated in TCAD [89]. . . . .	91
4.22	Simulated charge collection in LGAD devices with profile outlined in Figure 4.10. Scans are carried out from the JTE over pixels N1 and N2. Fluences are given in $\phi_{eq}/\text{cm}^{-2}$ . Simulated in TCAD [89]. . . . .	92
4.23	Simulated breakdown characteristics of LGAD devices. Simulated in TCAD [89]. . . . .	93
4.24	Simulated gain recovery for a selection of fluences. The device breakdown at a fluence of $8 \times 10^{14} \phi$ is at a approximately 510 V limiting the range of this experiment. Simulated in TCAD [89]. . . . .	94
5.1	2012 dataset without radial flight distance cuts (left). Radial flight distance cut applied to the 2012 dataset. Units of both axis are cm. . . . .	98
5.2	Logarithmic and power transforms applied to several training variables. The left plots are the original variables, the second from the left are the same variables with a Yeo-Johnson transform, the third column consists of the Box-Cox transform and the right plots are the logarithmic transforms of the variables. As can be seen, transform efficiency varies by variable. In the case of $B0_{PT}$ a suitable $\lambda$ could not be resolved to run the Yeo Johnson transform. . . . .	100
5.3	Pull plot of B0 DIRA OWNPV significance over random training seeds to monitor stability. Fold 1 refers to the variable significance extracted from a single k-fold. . . . .	101
5.4	ROC curve showing the performance of the selected XDGBoost classifier. . . . .	102
5.5	Three panel optimisations for the 2016 (a), 2017 (b) and 2018 (c) datasets. The left plots are optimised for the $S/\sqrt{S+B}$ FoM, the middle plots are optimised for the purity $S/B$ and the right plots are optimised for $\chi^2$ , where a lower $\chi^2$ indicates a better convergence with a simplified invariant mass model. Characteristics of the optimisation are consistent between samples. . . . .	108
5.6	Misidentified MC events reconstruced under a $B^0 \rightarrow \pi\pi\pi\pi$ hypothesis. . . . .	109
5.7	Invariant mass fits for the full 2015 (a), 2016 (b), 2017 (c) and 2018 (d) datatsets. . . . .	110

6.1	Demonstration of a 1D KDE method compared to alternative binning schemes. Underlying data is given in red. . . . .	112
6.2	Demonstration of a 1D KDE method overestimating variance in data generated from three distinct Gaussian distributions. . . . .	113
6.3	Correlation plot for the normalisation sample. . . . .	116
6.4	Correlation plot for the sideband sample. . . . .	117
6.5	Correlation plot for the LHCb flat phase space sample. . . . .	118
6.6	KS tests for the training variables used in the KDE efficiency training. . .	119
6.7	Null test validation plots (pt 1). The magenta plots indicate the training variables and the blue plots indicate the reconstructed projections. The overlay plots represent the kinematic cuts $[\pi\pi]_S < 1.1 GeV$ and $[\pi\pi\pi]_S < 3.06 GeV$ . . . . .	120
6.8	Null test validation plots (pt 2). The magenta plots indicate the training variables and the blue plots indicate the reconstructed projections. The overlay plots represent the kinematic cuts $[\pi\pi]_S < 1.1 GeV$ and $[\pi\pi\pi]_S < 3.06 GeV$ . . . . .	121
6.9	Helicity formalism for the $B_d \rightarrow \rho(770)^0 \rho(770)^0$ system reproduced from [30]. The $\theta$ angles represent the decay topology of the $\rho$ , while the angle $\phi$ represents the angle between the decay planes. Angles used in the reweighting are considered over all possible pion combinations. . . . .	123
6.10	Sample of the training variables used in the multivariate reweighting to model the background . . . . .	124
6.11	Background model reproduced from the training variables in the four possible 3-body combinations, (a) $\pi_1^- \pi_2^+ \pi_2^+$ , (b) $\pi_1^+ \pi_1^- \pi_2^-$ , (c) $\pi_1^+ \pi_1^- \pi_2^+$ and (d) $\pi_1^+ \pi_2^+ \pi_2^-$ . The fit is completed to Run 2 upper sideband data. . . . .	125
7.1	2016 amplitude fits to the three $\phi$ projections, (a) $\phi(\rho_1 \rho_2)$ , (b) $\phi(\rho_3 \rho_4)$ , (c) $\phi(\rho_5 \rho_6)$ —unphysical. Signal (Green) contributions and Background (Red) contributions are presented in the plots. . . . .	130
7.2	2016 amplitude fits to the six $\cos(\theta)_{ij}$ ( $i \neq j$ ) projections, (a) $\cos(\theta(\pi_1^+ \pi_1^-))$ , (b) $\cos(\theta(\pi_2^+ \pi_2^-))$ , (c) $\cos(\theta(\pi_1^+ \pi_2^-))$ , (d) $\cos(\theta(\pi_2^+ \pi_1^-))$ , (e) $\cos(\theta(\pi_1^- \pi_2^-))$ —unphysical, (f) $\cos(\theta(\pi_1^+ \pi_2^+))$ —unphysical. Signal (Green) contributions and Background (Red) contributions are presented in the plots. . . . .	131

7.3	2016 amplitude fits to the Six $m(\pi_i\pi_j)(i \neq j)$ projections, (a) $\pi_1^-\pi_2^-$ —unphysical, (b) $\pi_1^-\pi_2^+$ , (c) $\pi_1^+\pi_1^-$ , (d) $\pi_1^+\pi_2^-$ , (e) $\pi_2^+\pi_2^-$ , (f) $\pi_1^+\pi_2^+$ —unphysical. Signal (Green) contributions and Background (Red) contributions are presented in the plots. . . . .	133
7.4	2016 amplitude fits to the four $m(\pi_i\pi_j\pi_k)$ projections, (a) $\pi_1^-\pi_2^+\pi_2^+$ , (b) $\pi_1^+\pi_1^-\pi_2^-$ , (c) $\pi_1^+\pi_1^-\pi_2^+$ and (d) $\pi_1^+\pi_2^+\pi_2^-$ . Signal (Green) contributions and Background (Red) contributions are presented in the plots. . . . .	134
7.5	2017 amplitude fits to the three $\phi$ projections, (a) $\phi(\rho_1\rho_2)$ , (b) $\phi(\rho_3\rho_4)$ , (c) $\phi(\rho_5\rho_6)$ —unphysical. Signal (Green) contributions and Background (Red) contributions are presented in the plots. . . . .	135
7.6	2017 amplitude fits to the six $\cos(\theta)_{ij}$ ( $i \neq j$ ) projections, (a) $\cos(\theta(\pi_1^+\pi_1^-))$ , (b) $\cos(\theta(\pi_2^+\pi_2^-))$ , (c) $\cos(\theta(\pi_1^+\pi_2^-))$ , (d) $\cos(\theta(\pi_2^+\pi_1^-))$ , (e) $\cos(\theta(\pi_1^-\pi_2^-))$ —unphysical, (f) $\cos(\theta(\pi_1^+\pi_2^+))$ —unphysical. Signal (Green) contributions and Background (Red) contributions are presented in the plots. . . . .	136
7.7	2017 amplitude fits to the Six $m(\pi_i\pi_j)$ ( $i \neq j$ ) projections, (a) $\pi_1^-\pi_2^-$ —unphysical, (b) $\pi_1^-\pi_2^+$ , (c) $\pi_1^+\pi_1^-$ , (d) $\pi_1^+\pi_2^-$ , (e) $\pi_2^+\pi_2^-$ , (f) $\pi_1^+\pi_2^+$ —unphysical. Signal (Green) contributions and Background (Red) contributions are presented in the plots. . . . .	137
7.8	2017 amplitude fits to the four $m(\pi_i\pi_j\pi_k)$ projections, (a) $\pi_1^-\pi_2^+\pi_2^+$ , (b) $\pi_1^+\pi_1^-\pi_2^-$ , (c) $\pi_1^+\pi_1^-\pi_2^+$ and (d) $\pi_1^+\pi_2^+\pi_2^-$ . Signal (Green) contributions and Background (Red) contributions are presented in the plots. . . . .	138
7.9	2018 amplitude fits to the three $\phi$ projections, (a) $\phi(\rho_1\rho_2)$ , (b) $\phi(\rho_3\rho_4)$ , (c) $\phi(\rho_5\rho_6)$ —unphysical. Signal (Green) contributions and Background (Red) contributions are presented in the plots. . . . .	139
7.10	2018 amplitude fits to the six $\cos(\theta)_{ij}$ ( $i \neq j$ ) projections, (a) $\cos(\theta(\pi_1^+\pi_1^-))$ , (b) $\cos(\theta(\pi_2^+\pi_2^-))$ , (c) $\cos(\theta(\pi_1^+\pi_2^-))$ , (d) $\cos(\theta(\pi_2^+\pi_1^-))$ , (e) $\cos(\theta(\pi_1^-\pi_2^-))$ —unphysical, (f) $\cos(\theta(\pi_1^+\pi_2^+))$ —unphysical. Signal (Green) contributions and Background (Red) contributions are presented in the plots. . . . .	140
7.11	2018 amplitude fits to the Six $m(\pi_i\pi_j)$ ( $i \neq j$ ) projections, (a) $\pi_1^-\pi_2^-$ —unphysical, (b) $\pi_1^-\pi_2^+$ , (c) $\pi_1^+\pi_1^-$ , (d) $\pi_1^+\pi_2^-$ , (e) $\pi_2^+\pi_2^-$ , (f) $\pi_1^+\pi_2^+$ —unphysical. Signal (Green) contributions and Background (Red) contributions are presented in the plots. . . . .	141

7.12	2018 amplitude fits to the four $m(\pi_i\pi_j\pi_k)$ projections, (a) $\pi_1^-\pi_2^+\pi_2^+$ , (b) $\pi_1^+\pi_1^-\pi_2^-$ , (c) $\pi_1^+\pi_1^-\pi_2^+$ and (d) $\pi_1^+\pi_2^+\pi_2^-$ . Signal (Green) contributions and Background (Red) contributions are presented in the plots. . . . .	142
7.13	Run 2 amplitude fits to the three $\phi$ projections, (a) $\phi(\rho_1\rho_2)$ , (b) $\phi(\rho_3\rho_4)$ , (c) $\phi(\rho_5\rho_6)$ —unphysical. Signal (Green) contributions and Background (Red) contributions are presented in the plots. . . . .	143
7.14	Run 2 amplitude fits to the six $\cos(\theta)_{ij}$ ( $i \neq j$ ) projections, (a) $\cos(\theta(\pi_1^+\pi_1^-))$ , (b) $\cos(\theta(\pi_2^+\pi_2^-))$ , (c) $\cos(\theta(\pi_1^+\pi_2^-))$ , (d) $\cos(\theta(\pi_2^+\pi_1^-))$ , (e) $\cos(\theta(\pi_1^-\pi_2^-))$ —unphysical, (f) $\cos(\theta(\pi_1^+\pi_2^+))$ —unphysical. Signal (Green) contributions and Background (Red) contributions are presented in the plots.	144
7.15	Run 2 amplitude fits to the Six $m(\pi_i\pi_j)$ ( $i \neq j$ ) projections, (a) $\pi_1^-\pi_2^-$ —unphysical, (b) $\pi_1^-\pi_2^+$ , (c) $\pi_1^+\pi_1^-$ , (d) $\pi_1^+\pi_2^-$ , (e) $\pi_2^+\pi_2^-$ , (f) $\pi_1^+\pi_2^+$ —unphysical. Signal (Green) contributions and Background (Red) contributions are presented in the plots. . . . .	145
7.16	Run 2 amplitude fits to the four $m(\pi_i\pi_j\pi_k)$ projections, (a) $\pi_1^-\pi_2^+\pi_2^+$ , (b) $\pi_1^+\pi_1^-\pi_2^-$ , (c) $\pi_1^+\pi_1^-\pi_2^+$ and (d) $\pi_1^+\pi_2^+\pi_2^-$ . Signal (Green) contributions and Background (Red) contributions are presented in the plots. . . . .	146
7.17	Interference Fit Fraction—as percentages—from the full Run 2 amplitude analysis. . . . .	148
7.18	Pseudo-Experiments for understanding the model and fit systematics. . . .	151
7.19	Longitudinal polarisation fraction measurements for the $B^0 \rightarrow \rho(770)^0\rho(770)^0$ . Measurements are included from Belle [28], BaBar [29] and LHCb [30]. Included errors are statistical and systematic. The measurement presented in this thesis falls inside the weighted average calculated against the PDG method [4]. . . . .	152

# Bibliography

- [1] CMS collaboration, S. Chatrchyan *et al.*, *Observation of a new boson at a mass of 125 GeV with the CMS experiment at the LHC*, Physics Letters B **716** (2012), no. 1 30.
- [2] ATLAS collaboration, G. Aad *et al.*, *Observation of a new particle in the search for the Standard Model Higgs boson with the ATLAS detector at the LHC*, Physics Letters B **716** (2012), no. 1 1.
- [3] Muon  $g-2$  collaboration, B. Abi *et al.*, *Measurement of the Positive Muon Anomalous Magnetic Moment to 0.46 ppm*, Phys. Rev. Lett. **126** (2021) 141801.
- [4] K. Olive, *Review of Particle Physics*, Chinese Physics C **40** (2016) 100001.
- [5] Y. Fukuda *et al.*, *Evidence for Oscillation of Atmospheric Neutrinos*, Physical Review Letters **81** (1998) 1562.
- [6] LHCb collaboration, R. Aaij *et al.*, *Test of lepton universality in beauty-quark decays*, 2021. doi: 10.48550/ARXIV.2103.11769.
- [7] M. E. Peskin and D. V. Schroeder, *An Introduction to quantum field theory*. Addison-Wesley, Reading, USA, 1995.
- [8] M. Kobayashi and T. Maskawa, *CP Violation in the Renormalizable Theory of Weak Interaction*, Prog. Theor. Phys. **49** (1973) 652.
- [9] ATLAS collaboration, G. Aad *et al.*, *Observation of Light-by-Light Scattering in Collisions with the ATLAS Detector*, Physical Review Letters **123** (2019) .
- [10] F. Englert and R. Brout, *Broken Symmetry and the Mass of Gauge Vector Mesons*, Phys. Rev. Lett. **13** (1964) 321.

- [11] P. W. Higgs, *Broken Symmetries and the Masses of Gauge Bosons*, Phys. Rev. Lett. **13** (1964) 508.
- [12] G. S. Guralnik, C. R. Hagen, and T. W. B. Kibble, *Global Conservation Laws and Massless Particles*, Phys. Rev. Lett. **13** (1964) 585.
- [13] G. Arnison *et al.*, *Experimental observation of isolated large transverse energy electrons with associated missing energy at  $s=540$  GeV*, Physics Letters B **122** (1983), no. 1 103.
- [14] G. Arnison *et al.*, *Experimental observation of lepton pairs of invariant mass around 95 GeV/c<sup>2</sup> at the CERN SPS collider*, Physics Letters B **126** (1983), no. 5 398.
- [15] M. Banner *et al.*, *Observation of single isolated electrons of high transverse momentum in events with missing transverse energy at the CERN pp collider*, Physics Letters B **122** (1983), no. 5 476.
- [16] T. D. Lee and C. N. Yang, *Question of Parity Conservation in Weak Interactions*, Phys. Rev. **104** (1956) 254.
- [17] G. Harris, J. Orear, and S. Taylor, *Lifetimes of the  $\tau^+$  and  $K_L^+$ -mesons*, Phys. Rev. **100** (1955) 932.
- [18] R. W. Birge, J. R. Peterson, D. H. Stork, and M. N. Whitehead, *Mass Values of the K Mesons*, Phys. Rev. **100** (1955) 430.
- [19] C. S. Wu *et al.*, *Experimental Test of Parity Conservation in Beta Decay*, Phys. Rev. **105** (1957) 1413.
- [20] N. Cabibbo, *Unitary Symmetry and Leptonic Decays*, Phys. Rev. Lett. **10** (1963) 531.
- [21] L. Wolfenstein, *Parametrization of the Kobayashi-Maskawa Matrix*, Phys. Rev. Lett. **51** (1983) 1945.
- [22] R. Van de Water, *The CKM matrix and flavor physics from lattice QCD*, arXiv (2009).

- [23] M. Gronau and D. London, *Isospin analysis of CP asymmetries in B decays*, Phys. Rev. Lett. **65** (1990) 3381.
- [24] G. Karleskint, R. Turner, and J. Small, *Introduction to Marine Biology*. Cengage Learning, 2012.
- [25] LHCb collaboration, A. A. Alves Jr. *et al.*, *The LHCb detector at the LHC*, JINST **3** (2008), no. LHCb-DP-2008-001 S08005.
- [26] J. Dalseno, *Resolving the  $\alpha$  ambiguity in  $B^0 \rightarrow \rho\rho$* , Journal of High Energy Physics **2018** (2018) .
- [27] J. Charles, O. Deschamps, S. Descotes-Genon, and V. Niess, *Isospin analysis of charmless B-meson decays*, The European Physical Journal C **77** (2017) .
- [28] Belle I collaboration, I. Adachi *et al.*, *Study of  $B^0 \rightarrow \rho^0\rho^0$  decays, implications for the CKM angle  $\phi_2$  and search for other  $B^0$  decay modes with a four-pion final state*, Phys. Rev. D **89** (2014), no. 7 072008, [arXiv:1212.4015](#), [Addendum: Phys.Rev.D 89, 119903 (2014)].
- [29] BABAR collaboration, B. Aubert *et al.*, *Measurement of the branching fraction, polarization, and CP asymmetries in  $B^0 \rightarrow \rho^0\rho^0$  decay, and implications for the CKM angle  $\alpha$* , Phys. Rev. D **78** (2008) 071104.
- [30] LHCb collaboration, R. Aaij *et al.*, *Observation of the  $B^0 \rightarrow \rho(770)^0\rho(770)^0$  decay from an amplitude analysis of  $B^0 \rightarrow (\pi^+\pi^-)(\pi^+\pi^-)$  decays*, Physics Letters B **747** (2015) 468.
- [31] J. M. Blatt and V. F. Weisskopf, *Theoretical nuclear physics*. Courier Corporation, 1991.
- [32] W. Rarita and J. Schwinger, *On a theory of particles with half-integral spin*, Physical Review **60** (1941), no. 1 61.
- [33] G. J. Gounaris and J. J. Sakurai, *Finite-Width Corrections to the Vector-Meson-Dominance Prediction for  $\rho \rightarrow e^+e^-$* , Phys. Rev. Lett. **21** (1968) 244.

- [34] P. E. Rensing, *Single electron detection for SLD CRID and multi-pion spectroscopy in  $K^-p$  interactions at 11 GeV/c*, PhD thesis, Stanford Univ., Stanford, CA, 1993, Presented on Aug 1993, SLAC-R-0421.
- [35] LHCb collaboration, A. A. Alves *et al.*, *The LHCb Detector at the LHC*, JINST **3** (2008), no. LHCb-DP-2008-001 S08005, Also published by CERN Geneva in 2010.
- [36] LHCb collaboration, R. Aaij *et al.*, *A search for  $\Xi_{cc}^{++} \rightarrow D^+pK^-\pi^+$  decays*, Journal of High Energy Physics **2019** (2019) .
- [37] LHCb collaboration, R. Aaij *et al.*, *Search for the doubly charmed baryon  $\Xi_{cc}^+$  in the  $\Xi_c^+\pi^-\pi^+$  final state*, Journal of High Energy Physics **2021** (2021) .
- [38] LHCb collaboration, R. Aaij *et al.*, *First observation of the decay  $B_s^0 \rightarrow K^-\mu^+\nu_\mu$  and measurement of  $|V_{ub}|/|V_{cb}|$* , Phys. Rev. Lett. **126** (2020) 081804. 11 p, arXiv:2012.0514.
- [39] C. Lefèvre, *The CERN accelerator complex. Complexe des accélérateurs du CERN*, Accessed September 2022, Dec, 2008.
- [40] ATLAS collaboration, A. Airapetian *et al.*, *ATLAS detector and physics performance: Technical Design Report*, CERN-LHCC-99-014.
- [41] CMS collaboration, S. Chatrchyan *et al.*, *The CMS magnet project: Technical Design Report*, CERN-LHCC-97-010.
- [42] ALICE collaboration, S. Acharya *et al.*, *ALICE: Technical proposal for a Large Ion collider Experiment at the CERN LHC*, CERN-LHCC-95-71.
- [43] R. Aaij *et al.*, *LHCb : Technical Proposal*, CERN-LHCC-98-004.
- [44] S. Acharya *et al.*, *Direct observation of the dead-cone effect in quantum chromodynamics*, Nature **605** (2022) 440.
- [45] BaBar collaboration, D. Boutigny *et al.*, *BaBar Technical Design Report*, SLAC-R-0457.
- [46] N. Toge, *KEK B-factory Design Report*, KEK-Report-95-7.

- [47] LHCb collaboration, A. A. Alves *et al.*, *The LHCb Detector at the LHC*, JINST **3** (2008) S08005, Also published by CERN Geneva in 2010.
- [48]  $\bar{b}b$  production angle plots, [https://lhcb.web.cern.ch/lhcb/speakersbureau/html/bb\\_ProductionAngles.html](https://lhcb.web.cern.ch/lhcb/speakersbureau/html/bb_ProductionAngles.html). Accessed September 2022.
- [49] LHCb collaboration, R. Aaij *et al.*, *Performance of the LHCb Vertex Locator*, Journal of Instrumentation **9** (2014) P09007–P09007.
- [50] B. Muratori and T. Pieloni, *Luminosity levelling techniques for the LHC*, arXiv:1410.5646.
- [51] LHCb collaboration, R. Aaij *et al.*, *Lhcb detector performance*, International Journal of Modern Physics A **30** (2015) 1530022.
- [52] LHCb collaboration, R. Aaij *et al.*, *Precision luminosity measurements at LHCb*, JINST **9** (2014), no. 12 P12005, arXiv:1410.0149.
- [53] LHCb collaboration, R. Aaij *et al.*, *Measurement of the  $b$ -Quark Production Cross Section in 7 and 13 TeV  $pp$  Collisions*, Physical Review Letters **118** (2017) .
- [54] LHCb collaboration, R. Aaij *et al.*, *LHCb standard set of performance numbers*, <https://lhcb.web.cern.ch/speakersbureau/html/PerformanceNumbers.html>. Accessed September 2022.
- [55] M. Alexander *et al.*, *Mapping the material in the LHCb Vertex Locator using secondary hadronic interactions*, JINST **13** (2018), no. 06 P06008, arXiv:1803.0746.
- [56] S. Borghi *et al.*, *First spatial alignment of the LHCb VELO and analysis of beam absorber collision data*, Nucl. Instrum. Meth. A **618** (2010) 108.
- [57] LHCb collaboration, R. Aaij *et al.*, *Search for Dark Photons Produced in 13 TeV  $pp$  Collisions*, Physical Review Letters **120** (2018) .
- [58] M. Agari and O. Steinkamp, *The Design of the LHCb Silicon Tracker*, tech. rep., CERN, Geneva, 2004.
- [59] LHCb collaboration, P. d'Argent *et al.*, *Improved performance of the LHCb outer tracker in LHC run 2*, Journal of Instrumentation **12** (2017) P11016.

- [60] *lhcb silicon tracker material for publications*, <https://lhcb.physik.uzh.ch/ST/public/material/index.php>. Accessed September 2022.
- [61] M. Adinolfi *et al.*, *Performance of the LHCb RICH detector at the LHC*, The European Physical Journal C **73** (2013) .
- [62] L. Anderlini *et al.*, *The PIDCalib package*, LHCb-PUB-2016-021, CERN-LHCb-PUB-2016-021.
- [63] LHCb collaboration, R. Aaij *et al.*, *Design and performance of the LHCb trigger and full real-time reconstruction in Run 2 of the LHC*, JINST **14** (2019), no. 04 P04013, [arXiv:1812.1079](https://arxiv.org/abs/1812.1079).
- [64] *The MOORE project*, <https://lhcbdoc.web.cern.ch/lhcbdoc/moore/>. Accessed February 2021.
- [65] *The BRUNEL project*, <https://lhcbdoc.web.cern.ch/lhcbdoc/brunel/>. Accessed February 2021.
- [66] *The DAVINCI project*, <https://lhcbdoc.web.cern.ch/lhcbdoc/davinci/>. Accessed February 2021.
- [67] T. Sjöstrand *et al.*, *An introduction to PYTHIA 8.2*, Computer Physics Communications **191** (2015) 159.
- [68] M. Clemencic *et al.*, *The LHCb Simulation Application, Gauss: Design, Evolution and Experience*, Journal of Physics: Conference Series **331** (2011) 032023.
- [69] S. Agostinelli *et al.*, *Geant4—a simulation toolkit*, Nuclear Instruments and Methods in Physics Research Section A: Accelerators, Spectrometers, Detectors and Associated Equipment **506** (2003), no. 3 250.
- [70] D. J. Lange, *The EvtGen particle decay simulation package*, *journal = Nuclear Instruments and Methods in Physics Research Section A: Accelerators, Spectrometers, Detectors and Associated Equipment*, , BEAUTY2000, Proceedings of the 7th Int. Conf. on B-Physics at Hadron Machines.
- [71] P. Golonka and Z. Was, *PHOTOS Monte Carlo: a precision tool for QED corrections in Z and W decays*, The European Physical Journal C **45** (2006) 97.

- [72] A. Vasilescu and G. Lindstroem, *Displacement damage in silicon*, online compilation (2000), <https://rd50.web.cern.ch/niel/>.
- [73] L. Collaboration, *LHCb VELO Upgrade Technical Design Report*, Tech. Rep. CERN-LHCC-2013-021. LHCb-TDR-013, CERN-LHCC-2013-021. LHCb-TDR-013, CERN, Nov, 2013.
- [74] N. Moffat *et al.*, *Low Gain Avalanche Detectors (LGAD) for particle physics and synchrotron applications*, Journal of Instrumentation **13** (2018) C03014.
- [75] D. Renker, *New trends on photodetectors*, Nuclear Instruments and Methods in Physics Research Section A: Accelerators, Spectrometers, Detectors and Associated Equipment **571** (2007), no. 1 1.
- [76] G. Lindstroem, *Radiation damage in silicon detectors*, Nuclear Instruments and Methods in Physics Research Section A: Accelerators, Spectrometers, Detectors and Associated Equipment **512** (2003) 30–43.
- [77] R. Wittmann, *Semiconductor Doping Technology*, Miniaturization Problems in CMOS Technology: Investigation of Doping Profiles and Reliability (2007), <https://www.iue.tuwien.ac.at/phd/wittmann/node7.html> .
- [78] L. Rossi, P. Fischer, T. Rohe, and N. Wermes, *Pixel detectors: From fundamentals to applications*. Springer Science & Business Media, 2006.
- [79] W. Maes, K. M. D. Meyer, and R. V. Overstraeten, *Impact ionization in silicon: A review and update*, Solid-state Electronics **33** (1990) 705.
- [80] S. Sze, *Semiconductor Devices: Physics and Technology*. John Wiley & Sons Singapore Pte. Limited, 2012.
- [81] S. Ramo, *Currents Induced by Electron Motion*, Proceedings of the IRE **27** (1939), no. 9 584.
- [82] G. Pellegrini *et al.*, *Technology developments and first measurements of Low Gain Avalanche Detectors (LGAD) for high energy physics applications*, Nuclear Instruments and Methods in Physics Research Section A: Accelerators, Spectrometers, Detectors and Associated Equipment **765** (2014) 12, HSTD-9 2013 - Proceedings of

the 9th International “Hiroshima” Symposium on Development and Application of Semiconductor Tracking Detectors.

- [83] G. Casse *et al.*, *First results on charge collection efficiency of heavily irradiated microstrip sensors fabricated on oxygenated p-type silicon*, Nuclear Instruments and Methods in Physics Research Section A: Accelerators, Spectrometers, Detectors and Associated Equipment **518** (2004), no. 1 340, Frontier Detectors for Frontier Physics: Proceedings.
- [84] P. Fernández-Martínez *et al.*, *Simulation of new p-type strip detectors with trench to enhance the charge multiplication effect in the n-type electrodes*, Nuclear Instruments and Methods in Physics Research Section A: Accelerators, Spectrometers, Detectors and Associated Equipment **658** (2011), no. 1 98, RESMDD 2010.
- [85] P. Fernández-Martínez *et al.*, *Simulation of new p-type strip detectors with trench to enhance the charge multiplication effect in the n-type electrodes*, Nuclear Instruments and Methods in Physics Research Section A: Accelerators, Spectrometers, Detectors and Associated Equipment **658** (2011), no. 1 98, RESMDD 2010.
- [86] G. Paternoster *et al.*, *Trench-Isolated Low Gain Avalanche Diodes (TI-LGADs)*, IEEE Electron Device Letters **41** (2020), no. 6 884.
- [87] V. Temple, *Increased avalanche breakdown voltage and controlled surface electric fields using a junction termination extension (JTE) technique*, IEEE Transactions on Electron Devices **30** (1983), no. 8 954.
- [88] Williams, C. C., *Two-Dimensional Dopant Profiling By Scanning Capacitance Microscopy*, Annual Review of Materials Science **29** (1999), no. 1 471.
- [89] Synopsis, *Synopsis Sentaurus Device Manual*. Synopsis, 2010.
- [90] N. Moffat and R. Bates, *Simulation of the small pixel effect contributing to a low fill factor for pixellated Low Gain Avalanche Detectors (LGAD)*, Nuclear Instruments and Methods in Physics Research Section A: Accelerators, Spectrometers, Detectors and Associated Equipment **1018** (2021) 165746.
- [91] D. Passeri and A. Morozzi, *TCAD radiation damage model*, AIDA-2020 (2019), <http://cds.cern.ch/record/2705944>.

- [92] J.M. McGarrity, F.R. McLean, T.R. Oldham, H.E. Boesch, *Ionizing radiation effects in MOS-devices*. Springer, 1989.
- [93] M. Moll, *Displacement Damage in Silicon Detectors for High Energy Physics*, IEEE Transactions on Nuclear Science **65** (2018), no. 8 1561.
- [94] M. Ferrero *et al.*, *Radiation resistant LGAD design*, Nuclear Instruments and Methods in Physics Research Section A: Accelerators, Spectrometers, Detectors and Associated Equipment **919** (2019) 16.
- [95] N. C. H. F-W Sadrozinski, A. Seiden, *4D tracking with ultra-fast silicon detectors*, Reports on Progress in Physics **81** (2018) .
- [96] E. Currás, M. Fernández, and M. Moll, *Gain reduction mechanism observed in Low Gain Avalanche Diodes*, Nuclear Instruments and Methods in Physics Research Section A: Accelerators, Spectrometers, Detectors and Associated Equipment **1031** (2022) 166530.
- [97] M. Ferrero *et al.*, *Radiation resistant LGAD design*, Nuclear Instruments and Methods in Physics Research Section A: Accelerators, Spectrometers, Detectors and Associated Equipment **919** (2019) 16.
- [98] T. Chen and C. Guestrin, *XGBoost: A Scalable Tree Boosting System*, [arXiv:1603.0275](https://arxiv.org/abs/1603.0275).
- [99] H. Albrecht *et al.*, *Search for hadronic  $b \rightarrow u$  decays*, Physics Letters B **241** (1990), no. 2 278.
- [100] T. Skwarnicki, *A study of the radiative CASCADE transitions between the Upsilon-Prime and Upsilon resonances*, PhD thesis, Cracow, INP, 1986.
- [101] F. Pedregosa *et al.*, *Scikit-learn: Machine learning in Python*, Journal of Machine Learning Research **12** (2011) 2825.
- [102] N. Smirnov, *Table for Estimating the Goodness of Fit of Empirical Distributions*, The Annals of Mathematical Statistics **19** (1948), no. 2 279 .
- [103] *The HEP-ML project*, [https://arogozhnikov.github.io/hep\\_ml/](https://arogozhnikov.github.io/hep_ml/). Accessed September 2022.

- [104] F. a. James, *MINUIT: Function Minimization and Error Analysis Reference Manual*, 1998. CERN Program Library Long Writeups.
- [105] S. Chung *et al.*, *Partial wave analysis in K-matrix formalism*, *Annalen der Physik* **507** (1995), no. 5 404.
- [106] Y. Xie, *sfit: a method for background subtraction in maximum likelihood fit*, 2009. doi: 10.48550/ARXIV.0905.0724.
- [107] LHCb collaboration, R. Aaij *et al.*, *New algorithms for identifying the flavour of  $B^0$  mesons using pions and protons*, *The European Physical Journal C* **77** (2017) .
- [108] J. Dalseno, *Resolving the  $\phi_2$  ( $\alpha$ ) ambiguity in  $B^0 \rightarrow a_1^\pm \pi^\mp$* , *JHEP* **10** (2019) 191, [arXiv:1907.0923](https://arxiv.org/abs/1907.0923).